UNIVERSITEIT VAN PRETORIA
UNIVERSITY OF PRETORIA
YUNIBESITHI YA PRETORIA

Faculty of Engineering, Built Environment and Information Technology

Fakulteit Ingenieurswese, Bou-omgewing en Inligtingtegnologie / Lefapha la Boetšenere, Tikologo ya Kago le Theknolotši ya Tshedimošo

OPTIMAL CONTROL SURFACE MIXING OF A RHOMBOID-WING UAV

by

Elizna Miles

Submitted in partial fulfilment of the requirements for the degree

MASTER OF ENGINEERING

In the Department of Mechanical and Aeronautical Engineering

University of Pretoria

December 2015

Supervisor: Dr B.A. Broughton

Co-supervisor: Prof J.P. Meyer

Abstract

Title:	Optimal Control Surface Mixing of a Rhomboid-Wing UAV
Supervisor:	Dr B.A. Broughton
Co-supervisor:	Prof J.P. Meyer
Department:	Mechanical and Aeronautical Engineering
Degree:	Master of Engineering (Mechanical Engineering)

This thesis describes the development of an open-loop control allocation function – also known as a 'mixing function' – for aircraft with an unconventional control surface setup (*i.e.* not consisting of a conventional elevator, rudder and ailerons) by using mathematical optimisation. The techniques used to design the control allocation and mixing used on the unconventional configuration when flying it without artificial stability or control augmentation is provided. A typical application of this control mixing would be to enable a pilot to operate an unconventional unmanned aerial vehicle (UAV) as if it was a conventional model aircraft during flight testing or as a backup mode should any sensor failures occur during a typical flight test program. The allocation can also be used to simplify the inner control structure of a UAV autopilot or stability augmentation system. Although this type of mixing would be straightforward on a conventional airframe, an unconventional configuration has several unique characteristics that complicate the modelling and design process.

A custom six degree of freedom (6DOF) formulation for flight simulation was made available to model the aircraft and run various scripts to evaluate the aircraft response when the control allocation function is implemented. The simulation model was used to develop the mixing function that maps conventional input commands to the unconventionally situated control surfaces in the most optimal way.

The design process was formulated as a multi-objective optimisation problem, which was solved using a custom sequential quadratic programming and custom leapfrog programming method. A methodology was proposed to define the constraints, which can be customised for a particular aircraft or application.

The control allocation function was implemented in two different simulation environments to investigate the suitability of candidate designs. A robustness study was performed to evaluate the impact of actuator failures on the aircraft control response using the designed control allocation system. The proposed control allocation design methodology can also be used to design the inner control loops of more sophisticated control systems such as stability augmentation and automatic flight control, which is also briefly discussed in this thesis.

Publications

The following papers were produced and presented as part of this study:

Published in a conference proceedings

1. Miles, E., Broughton, B.A., Optimal Control Surface Mixing of a Rhomboid Wing UAV, 29th Congress of the International Council of the Aeronautical Sciences, St. Petersburg, Russia, 7-12 September, 2014.

Presented at conferences (no proceedings)

2. Miles, E., Broughton, B.A., Optimal Control Surface Scheduling of an Unconventional UAV, International Symposium of South Africa, Stellenbosch, South Africa, 14-16 September, 2015.
3. Miles, E., Broughton, B.A., Optimal Control Surface Mixing of a Rhomboid Wing UAV, International Symposium of South Africa, Irene, South Africa, 24 & 25 November, 2014.
4. Miles, E., Broughton, B.A., Optimal Control Surface Mixing of a Rhomboid Wing UAV, 29th Congress of the International Council of the Aeronautical Sciences, St. Petersburg, Russia, 7-12 September, 2014.

Submitted to the AIAA Journal of Aircraft

5. Miles, E., Broughton, B.A., Optimal control surface mixing of a rhomboid-wing UAV, AIAA Journal of Aircraft, 15 February 2016.

Acknowledgements

Firstly, I would like to thank God for giving me the strength and ability to finish this project.

I would also like to express my deepest appreciation to the following people for their help and support:

- Dr B.A. Broughton for continuously sharing his knowledge and guiding me throughout this project and for investing so much time and effort into the research.
- Prof J.P. Meyer for his time and effort during the finalisation of this project.
- My family for their love and support throughout this project.
- The Council for Scientific and Industrial Research (CSIR) and the Aerospace Industry Support Initiative (AISI) in South Africa that funded and supported this project.
- Paramount Advanced Technologies (PAT) for providing the UAV and the related design data.

Contents

List of figures

List of tables

Nomenclature

Abbreviations

AVL	Athena Vortex Lattice
CAD	Computer-aided design
CFD	Computational fluid dynamics
CSIR	Council for Scientific and Industrial Research
DCM	Direction Cosine Matrix
DOF	Degrees of freedom
ISA	International standard atmospheric
LFOP	Leapfrog optimisation programming
MDOE	Modern Design of Experiments
MIT	Massachusetts Institute of Technology
PAT	Paramount Advanced Technologies
RPM	Revolutions per minute
RPV	Remotely piloted vehicle
SQP	Sequential quadratic programming
TAS	True airspeed
UAV	Unmanned aerial vehicle

Control surfaces

δ_a	Aileron deflection
δ_e	Elevator deflection
δ_r	Rudder deflection
δ_1	Left front wing outer control surface deflection
δ_2	Right front wing outer control surface deflection
δ_3	Left rear wing outer control surface deflection
δ_4	Right rear wing outer control surface deflection
δ_5	Left rear wing inner control surface deflection

δ_6	Right rear wing inner control surface deflection
δ_7	Left front wing inner control surface deflection
δ_8	Right front wing inner control surface deflection
r_p	Pitch command
r_r	Roll command
r_y	Yaw command

Aerodynamics

C_L	Lift coefficient
C_{Lu}	Change in lift coefficient with respect to speed
$C_{L\alpha}$	Lift slope, change in lift coefficient with angle of attack
$C_{L\dot{\alpha}}$	Change in lift coefficient with respect to angle of attack rate
$C_{L_{\alpha h}}$	Change in lift coefficient with respect to angle of attack at the horizontal tail
C_D	Drag coefficient
$C_{D\alpha}$	Change in drag coefficient with angle of attack
C_{Du}	Change in drag coefficient with respect to speed
C_Y	Force coefficient for the y_b-component of aerodynamic force
C_l	Aircraft rolling moment coefficient about the aircraft centre of gravity
C_m	Aircraft pitching moment coefficient about the aircraft centre of gravity
$C_{m\dot{\alpha}}$	Change in pitching moment coefficient with respect to angle of attack rate
C_n	Aircraft yawing moment coefficient about the aircraft centre of gravity
$C_{l\delta a}$	Change in C_l with respect to δ_a
$C_{m\delta a}$	Change in C_m with respect to δ_a
$C_{n\delta a}$	Change in C_n with respect to δ_a
$C_{l\delta e}$	Change in C_l with respect to δ_e
$C_{m\delta e}$	Change in C_m with respect to δ_e
$C_{n\delta e}$	Change in C_n with respect to δ_e
$C_{l\delta r}$	Change in C_l with respect to δ_r

$C_{m\delta r}$	Change in C_m with respect to δ_r
$C_{n\delta r}$	Change in C_n with respect to δ_r
C_{m0}	Aircraft pitching moment coefficient at zero fuselage angle of attack and zero elevator deflection
$C_{m\alpha}$	Change in pitching moment coefficient with respect to angle of attack
$C_{m_{TU}}$	Thrust pitching moment coefficient with speed
C_{mq}	Change in C_m with respect to q
$C_{l\beta}$	Change in C_l with respect to β
C_{lp}	Change in C_l with respect to p
C_{lr}	Change in C_l with respect to r
$C_{n\beta}$	Change in C_n with respect to β
C_{np}	Change in C_n with respect to p
C_{nr}	Change in C_n with respect to r
$C_{T_{XU}}$	X-thrust coefficient with speed

Forces and moments

D	Drag force
L	Lift force
Y	Side force
m	Pitching moment
n	Yawing moment
l	Rolling moment
p	Roll rate
q	Pitch rate
r	Yaw rate
$\dot{p}$	Roll acceleration
$\dot{q}$	Pitch acceleration
$\dot{r}$	Yaw acceleration

Greek letters

α	Angle of attack
$\dot{\alpha}$	Time rate of change of angle of attack
β	Angle of sideslip
$\dot{\beta}$	Sideslip acceleration
δ	Control surface deflection angle
ε	Downwash angle
Δ	Incremental value
η_h	Dynamic pressure ratio at the horizontal tail
θ	Pitch attitude angle
λ	Taper ratio
Λ	Sweep angle
κ	Ratio of actual lift curve slope to 2π
φ	Bank angle
ψ	Heading angle
ω	Frequency

Matrix notation

$\mathbf{A}$	Quadratic mixing matrix coefficients
B	Linear mixing matrix coefficients
$\mathbf{T}$	Trim bias vector
$\mathbf{x}$	Design variable vector
[]	Square or rectangular matrix
$[]^T$	Row or transposed column matrix

Natural constants

ρ	Air density
g	Gravitational acceleration

Optimisation

f(x)	Objective function
g(x)	Inequality constraints
h(x)	Equality constraints
w	Objective function weights
α_k	Step size
d^k	Search direction

Physical

A	Aspect ratio
b	Wingspan
c	Reference chord
$\bar{c}$	Mean aerodynamic chord
CG	Centre of gravity
e	Oswald's efficiency factor
F_i	An inertial reference frame
F_b	A body-fixed frame in the rigid vehicle
h	Angular momentum vector
I_{xx}	Moment of inertia about X-axis
I_{yy}	Moment of inertia about Y-axis
I_{zz}	Moment of inertia about Z-axis
I_{xz}	Product of inertia
I	Inertia matrix
l_h	Distance measured parallel to the wing root chord
m	Mass
NP	Neutral point
$\bar{q}$	Dynamic pressure

S	Surface area
V	Working motor voltage
$\overline{V}_h$	Horizontal tail volume coefficient
X_{ac_H}	Location of aerodynamic centre of the horizontal tail

Velocity

a	Speed of sound
TAS	True airspeed
V_T	True airspeed
$\dot{V}_T$	Acceleration of relative airspeed
$\omega_{b/I}$	Angular velocity of F_b with respect to F_i

Subscripts

b	Body axes
i	Inertial frame
k	Iteration number

Superscripts

b	Body axes
i	The i^{th} design variable

1. Introduction

1.1. Background

Paramount Advanced Technologies (PAT) is currently developing an unmanned aerial vehicle (UAV) called the Roadrunner. This UAV has a rhomboid configuration and has already flown in prototype form. A photograph of the Roadrunner is shown in Figure 1.1.

Figure 1.1: PAT Roadrunner UAV with turbine engine

A rhomboid-wing configuration is a type of joined-wing [1] concept where the two forward wings are swept back, while the two rear wings are swept forward, the wing tips of this configuration are interconnected (front view of the aircraft in Figure 1.2) which also leads to the term box-wing aircraft. The fundamentals of this unconventional airframe are discussed in [2], with conceptual design process of such airframe discussed in [3]. The rhomboid wing configuration is one example of the family of configurations called joined-wing aircraft; another example is the PrandtlPlane concept shown in Figure 1.2. Research has continued in the field of joined-wing aircraft by the USAF [4], papers published such as [5], with further collaborations between NASA and Boeing on highly nonplanar lifting systems [6].

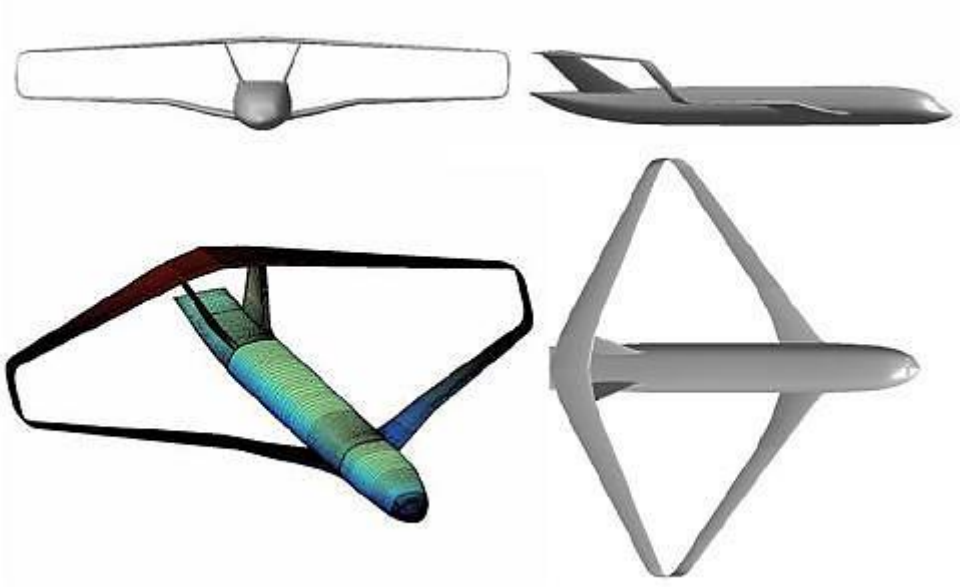

Figure 1.2: PrandtlPlane configuration [7]

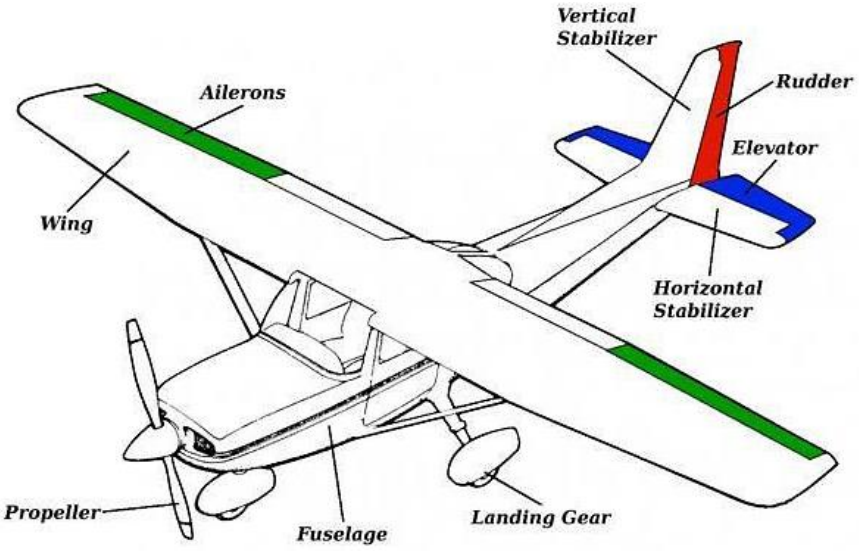

Figure 1.3: Conventional single-engine propeller aircraft [8]

Rhomboid-wing configurations are among many other unconventional configurations currently being investigated in the aviation industry. For more types of unconventional aircraft, see [9]. The amount of resources invested in doing research on unconventional aircraft has increased over the past few years, due to its advantages over conventional aircraft configurations such as the one illustrated in Figure 1.3. However, various challenges arose when engineers tried to incorporate conventional control laws on these unconventional aircraft, which led to investigating the possibilities of designing a methodology to simplify the integration process.

One of the control challenges presented by some of these layouts deals with allocating pitch, roll and yaw control on an aircraft with an unconventional control setup, or in some cases, the lack of a vertical control surface. Various unconventional configurations are discussed in the next section, together with existing control allocation methods.

1.2. Literature review

During the Vietnam War and afterwards, a UAV was referred to as a 'remotely piloted vehicle' (RPV) – until the early 1990s, when it was replaced with the term 'unmanned aerial vehicle' [10]. In Armitage [11], a UAV is defined as "a powered, aerial vehicle that does not carry a human operator, uses aerodynamic forces to provide vehicle lift, can fly autonomously or be piloted remotely, can be expendable or recoverable, and can carry a lethal or nonlethal payload".

The UAV sector is one of the fastest growing sectors in the aerospace industry. Various resources are being invested into the further development of new technologies and low-cost UAVs that can provide low-risk solutions to numerous requirements. The control and configuration aspect of some of these new developments in UAVs is discussed below.

Davidson, Lallman and Bundick [12] developed a real-time adaptive control allocation method for an aircraft with a large number of control surfaces. The control allocation method was capable of taking two different types of input commands: desired aircraft moments or

desired angular acceleration. The input commands were then mapped to the physical control surfaces.

The first step in the control allocation process was to investigate the possibility of using a linear control allocation function, but this would only be valid if there was minimal or no control coupling. Increasing the number of control surfaces resulted in a significant number of control interaction and nonlinearities, which led to the investigation of an extended control allocation function. Two additional terms were added to the linear control allocation function that contained the linear control effectiveness matrix. The second term was used to model the control moment due to the control surface deflection magnitude, and the third term was used to model the reduction in the control effectiveness of a specific control surface.

The optimisation objective was to maximise the aircraft mission performance. The optimisation was performed using a MATLAB® built-in optimisation function to obtain the extended control allocation function while satisfying the objective function. The control surface deflections were limited by using constraints in the optimisation process. The nonlinear control allocation function was dependent on accurate feedback measurements from the sensors – in the case of a sensor failure the aircraft might be uncontrollable and an airframe might be lost. This issue is still under investigation.

Due to increased demands on aircraft performance and efficiency, aircraft are no longer limited to conventional control surface setups; on the contrary, various aircraft make use of more control surfaces in order to meet the increased requirements, as well as for redundancy purposes.

The aircraft used to demonstrate the methodology developed in this thesis made use of an unconventional control surface setup similar to the aircraft that was used by Zhang, Suresh, Jiang and Theilliol [13]. Zhang *et al.* developed a control allocation function that can reallocate controls in the case of an aircraft control effector failure. The control allocation function was reconfigured when a failure occurred, but the control law was kept constant. Two numerical analysis methods were used to design the control allocation function that was responsible for the control reallocation: a pseudo-inverse method and a fixed-point algorithm. The flight control system made use of two closed-loop feedback loops; a problem was encountered when a sensor failure occurred, which resulted in inaccurate information being fed to the autopilot and control allocation functions. The physical control surface deflections were restricted by constrained optimisation techniques.

The first constrained optimisation technique investigated in this study exposed some limitations. The solution was not feasible for all virtual input commands in the presence of actuator position or actuator rate constraints. Due to this limitation, it was considered to truncate the control surface equation by removing the components that violate some of the constraints. The disadvantage of using the second constrained optimisation technique was that it could only find a solution if none of the constraints were active. Further investigation into the control reallocation function and algorithms has been considered.

Buffington [14] designed a control allocation module based on a closed-loop feedback control system. The control system was developed for a tailless aircraft with conventional and unconventional control effectors. The conventional effectors consisted of elevons, pitch flaps, thrust-vectoring and outboard leading edge flaps. The unconventional effectors included spoiler-slot deflectors and all moving tips. The objective of the constrained parameter optimisation was to obtain the maximum aircraft accelerations as a function of the angle of attack, sideslip angle, roll rate, pitch rate, yaw rate and control surface deflections. Instead of limiting the actual control surface deflections, the input command was limited. The input command was clipped, so that the input command given by the pilot would never result in a control surface deflection that would exceed the mechanical deflection limit. Further investigation into past command-limiting strategies was required, since this strategy produced an unacceptable axes coupling. The aim to minimise a linear approximation of drag was however, successfully demonstrated on a tailless fighter aircraft with conventional and unconventional control effectors.

Härkegård and Glad [15] investigated the differences between distributing the control effort among a redundant set of actuators using optimal control design and control allocation. Two design strategies were used in this study. The first consisted of using optimal control to limit or decide the control input. The second strategy consisted of using optimal control to decide the amount that each effector will be deflected and then using a control allocation method to calculate the control input. The control surface deflections were restricted by limiting the input commands. The second strategy, however, showed that the actuator constraints could be handled to some extent, but further investigation was required. The main results showed that the same degrees of design freedom were obtained using optimal control design and control allocation to shape the closed-loop response and distribute the control effort. However, the use of a separate control allocator was still under investigation.

Various other resources have been invested in doing research related to control allocation for over-actuated systems due to the amount of redundancy for the flight control system. Another control allocation example for over-actuated systems is provided in a report by Oppenheimer and Doman [16]. Oppenheimer and Doman investigated the use of a closed-loop linear control allocation method. The objective was to obtain a control allocation function that would produce the desired aircraft moments or accelerations while incorporating the control surface rate and position limits. The control surface rate and position limits were incorporated by using inequality constraints in the optimisation process. Differential control was not considered for the ailerons, but a linear combination for the left and right ailerons was implemented. The linear programming technique that was developed in this study proved to be a feasible method to solve online control allocation problems.

In another study, Doman and Oppenheimer [17] investigated the possibility of improving control allocation accuracy for nonlinear aircraft dynamics. They used the linear control allocation scheme developed in [16] and added an additional term to the control allocation scheme to help improve the fit, since fitting errors affect the preciseness of the control system. Using a linear control allocation function in nonlinear aircraft regions produce inaccurate results, and therefore the authors investigated making the control allocation

function nonlinear. The results obtained from using the nonlinear control allocation function showed that the aircraft pitch rate error was reduced significantly. Doman and Oppenheimer therefore recommended that a nonlinear control allocation function be used instead of a linear function.

Furthermore, Doman and Oppenheimer assisted Poonamallee, Yurkovich and Serrani [18] to develop a nonlinear control allocation method by using the linear control allocation developed in [16] as a basis. The aim was to compare the performance of the nonlinear control allocation function to other control allocation approaches.

The first step in the process was to compare the control allocation methods under consideration using open-loop measures. One of the measures consisted of commanding a manoeuvre and studying the aircraft's ability to attain the response using four control allocation functions. These functions included an open-loop measure of the nonlinear control allocation function compared to a mixed optimisation scheme, a redistributed pseudo-inverse approach and a direct geometric allocation method. The nonlinear control allocation method minimised the sum of the weighted square distances between the commanded pitch, roll and yaw moments, and corresponding moment functions, respectively. The control surface deflections and rates were limited through inequality constraints. The nonlinear control allocation function developed in this study gave the best results, compared to the mixed optimisation scheme, the redistributed pseudo-inverse approach and the direct geometric allocation methods in the nonlinear regions and in the presence of failures.

The above research areas were discussed to emphasise the focus of previous control allocation work, which mostly investigated the respective control allocation areas using closed-loop feedback. Some of the studies discussed above had an open-loop component, but it was mostly used as a starting point for the closed-loop feedback system. There were many other topics in literature that investigated closed-loop feedback, such as fault-tolerant control [19], adaptive control [12] and fuzzy logic control [20] systems, which are discussed in further detail below.

Basson [19] presented the development of a control allocation system that was used as part of a fault-tolerant control system in UAVs. The aim of the research was to reduce the likelihood of a fault that might originate at the reconfiguration of the control, guidance or navigation systems of the aircraft.

The objective was to minimise the difference between the desired and achievable aircraft performance parameters. Minimising the differences was accomplished by optimising the control allocation commanded inputs to the physical actuators present on the aircraft. The multi-objective optimisation problem formulated as a result was solved using the sequential quadratic programming method. The objective function contained the forces and moment terms, and each term's importance was emphasised by using weights. The actuators' usages were limited by using inequality constraints, and the trim equations were set to zero by using equality constraints in the optimisation process. The control allocation function was capable of dealing with both single and multiple actuator failures. The importance of actuator

redundancy as an influencing factor in the efficiency of control allocation was emphasised. The effects of actuator failures had been reduced by employing optimal control allocation. Redundant actuators were used to maximise the possible level of performance that could be achieved by the actuators and control reallocation. It was concluded that, with little difficulty and no alteration to the system, the control allocation system was capable of handling very different aircraft configurations.

Many control allocation schemes were based on closed-loop systems, which were not the topic of this research, but several of the optimisation techniques and control allocation approaches that were investigated were similar to what was done and considered in this thesis. Alwi and Edwards [21] investigated fault-tolerant control using sliding modes with online control allocation.

Sliding mode control is a nonlinear control method that forces the aircraft to ‘slide’ along a cross-section of the aircraft’s normal behaviour. The accuracy of the control allocation function depended on the fault estimator and weighting algorithm. The controller was kept constant while the feedback loop sent signals to the control allocation function to correct for any errors or failures that might occur. The weighting algorithm was changed online to compensate for any actuator failures. The advantage of using an online correction algorithm was that, at any given time, the system could correct for a failure that might take place by applying a discontinuous control signal. The results showed that good performance was obtained from the aircraft in different fault and failure scenarios. The control allocation scheme was thus able to handle the failures directly without reconfiguring the controller.

Voskuijl, La Rocca and Dircken [22] performed multidisciplinary design optimisation on a blended-wing body. The aircraft trim condition was calculated empirically. The trim condition was used to linearise the aircraft model via the numerical perturbation of the nonlinear model. The controllability of this blended-wing body was investigated, together with the handling qualities in normal operation and with failure states present. The model that was developed through multidisciplinary design optimisation was used as a baseline for the control allocation scheme. It was decided to investigate the control allocation scheme later.

The research of Peterson and Bodson [23] was aimed at optimally allocating redundant actuators under constraints. Constrained quadratic programming techniques for control allocation were investigated. The results of three optimisation algorithms were compared. They compared two objectives. The first was to determine the components of the control vector that resulted in the desired roll, pitch and yaw acceleration. The second optimisation objective was to minimise the magnitude of the control vector. The two objectives were implemented by using the weighted-sum optimisation method. The first objective was seen as the primary objective and had to receive priority throughout the flight envelope. The second objective had a weight assigned to it and was varied for specified scenarios. This is one possible variation to the weighted-sum method that can be used in optimisation. The study by Peterson and Bodson was dedicated to comparing optimisation techniques, whereas in this thesis, the focus is not on optimisation techniques, but on control allocation.

Various other studies investigated constrained control allocation with a different focus. Härkegård [24] investigated dynamic control allocation using constrained quadratic programming. 'Dynamic control allocation' in this context refers to the resulting control distribution that is a function of the current and previous sampling instant. A static control allocation only depends on the current control command. The actuator positions and rates were limited through constraints, and a weighting matrix was used to affect the distribution of control effort. The optimisation problem was formulated using a linearly constrained quadratic programming algorithm. Härkegård [25] also investigated an efficient active set algorithm; the algorithm actively searched for the optimal control allocation combination. The objective function consisted of optimising the moments or angular accelerations as a function of actuator positions. The aim of the study was to compare various active set algorithms.

Dang-Vu and Brocas [26] studied closed-loop constrained control allocation for a super-manoeuvrable aircraft. The aim was to incorporate an open-loop control allocation function inside a closed-loop function. The process consisted of two parts: the maximum moments the aircraft could produce were obtained in the first part, while the second part consisted of finding the control combination that would produce those moments. This approach ensured that the control allocation method would produce maximum aircraft moment within the control constraints.

Johansen, Fossen and Berge [27] studied constrained nonlinear control allocation with singularity avoidance, particularly avoiding the loss of controllability. Most of these constrained control allocation studies approached the initial optimisation process in a similar way, but they focused either on comparing different optimisation techniques or using closed-loop constrained control allocation. The objective of the study of Johansen *et al.* was to minimise the use of control effort in order to ensure that a maximum amount of control authority remained for controllability. A nonlinear control allocation function was chosen, together with a penalty term to avoid singularities.

Luo, Serrani, Yurkovich, Doman and Oppenheimer [28] studied the inner loop of a model-predictive dynamic control allocation, with the emphasis on the sampling period. The flight control system was seen as a sampled-data system, and therefore the sampling period was taken into account while designing the control allocation function. The actuator rate limits were restricted by using inequality constraints, which were divided by the sampling period.

The first part of the work consisted of optimising an open-loop control objective over a future time interval at each control step. The open-loop control refers to obtaining the maximum moment the aircraft can generate if a maximum desired input command is given without any feedback to correct for unwanted effects. A sequential quadratic programming algorithm with dynamic constraints was used, which was cast into a linear complementary problem. A nonlinear dynamic control allocation scheme was used to map input commands to a redundant set of actuators. The desired aircraft moment was given as input to the actuator dynamics where the control mapping took place, and that produced the actual aircraft response. The amplitude of the control surface deflection and the rate at which the control

surfaces deflected were limited through constraints in the optimisation process. The objective was to distribute control power among redundant control effectors, with the sub-objective of minimising the drag and control energy. The aircraft and actuator performance was under consideration in the study of Luo *et al.*, whereas in this thesis, the objective is to efficiently allocate controls in order to maximise the aircraft response for a roll pitch and yaw input command.

Various studies have previously been conducted in control allocation design. Most of the studies emphasised closed-loop feedback functions, but some considered the open-loop function to obtain the specific information needed to proceed with the closed-loop function. The control allocation strategy developed in this thesis differs from literature as follows:

- An open-loop control allocation methodology was developed that can be used to map any unconventional control surface setup to conventional control input commands.
- The open-loop control allocation function can be used as a foundation for a closed-loop feedback system that makes use of conventional input commands.

1.3. Motivation

The stability of an aircraft is referred to as the aircraft's tendency to return to straight and level flight after a disturbance. 'Control of an aircraft' refers to the ability to steer the aircraft on an arbitrary flight path. The term 'flying qualities' is used to designate the aircraft characteristics that are relevant to the stability and control behaviour of the aircraft. One of the challenges encountered during the early 1900s, and the last to be overcome, was to achieve satisfactory flying qualities throughout the envelope of flight.

The flying qualities of an aircraft can be determined using various methods such as mathematical analysis, machine computation, wind tunnel testing and flight testing. The complex equations that describe the behaviour of the aircraft in flight can be solved using mathematical analysis and machine computation. The aerodynamic forces required as input data for the equations of motions can accurately be obtained through wind tunnel tests. In order to verify that the flying qualities actually achieved are satisfactory, or to find and eliminate imperfections in them, it is necessary to perform flight tests [29].

During the first few flights of a new design, it is often desirable to fly the UAV in an open-loop configuration to evaluate the stability and control of the aircraft. 'Open loop' in this context refers to no data being fed back from the sensors, and the pilot flying the aircraft remotely. The aircraft can be flown in open-loop configurations, where the pilot can give simple input commands to evaluate the aircraft handling and comment on the stability and control. During initial flight testing, and even later during operational flight, the failure of certain sensors may require the aircraft to be reverted to an open-loop backup mode. The work described here represents one methodology for designing the control allocation for such an open-loop backup mode.

The flight testing of an aircraft with a conventional control surface setup is fairly straightforward, as the elevators are dedicated to pitch the aircraft, the ailerons are dedicated to roll the aircraft and the rudder is dedicated to yaw the aircraft. The flight testing of an

aircraft with an unconventional control surface setup is a lot more complex, since it might not be clear which control surface would be most optimal to execute the input command given by the pilot. The problem with allocating an unconventional number of control surfaces to produce the desired moments is that they become non-unique. The control surfaces need to be mapped to pitch, roll and yaw input commands to produce the desired aircraft response. The control allocation function is responsible for mapping the control surfaces to the input commands in the most optimum way.

Various aircraft have been equipped with closed-loop feedback systems to ensure a safe ability to fly, but not without the difficulty of mapping the unconventional control surface setup to conventional inputs. The open-loop control system proposed in this thesis addressed the following shortcomings:

- The control system gains may be incorrect if there is something wrong with the computational fluid dynamics (CFD), wind tunnel or other analysis data. Therefore, it is a good idea to have a backup/reversion mode for additional safety.
- Those control allocation algorithms that are dynamic are dependent on control feedback. This means that a failure in any of those sensors can cause the loss of the aircraft. Once again, an open-loop reversion mode may be very useful.
- The use of control allocation in the inner loop to ‘distribute’ the commands to the relevant control surfaces can make the control system design process considerably easier. The control engineer may have other ideas, but it is a useful option.

The open-loop system developed in this study can be used as a foundation for a closed-loop system, or it can be used as an independent backup mode or a completely separate control methodology for recovery or flight testing.

In Figure 1.4, there is no dedicated control allocation function. The autopilot is therefore responsible for the control assignment of the eight control surfaces, including protection against control saturation. It would be difficult for the designer to implement the autopilot in such a way that control authority is allocated in the most optimal way without saturating the control surfaces.

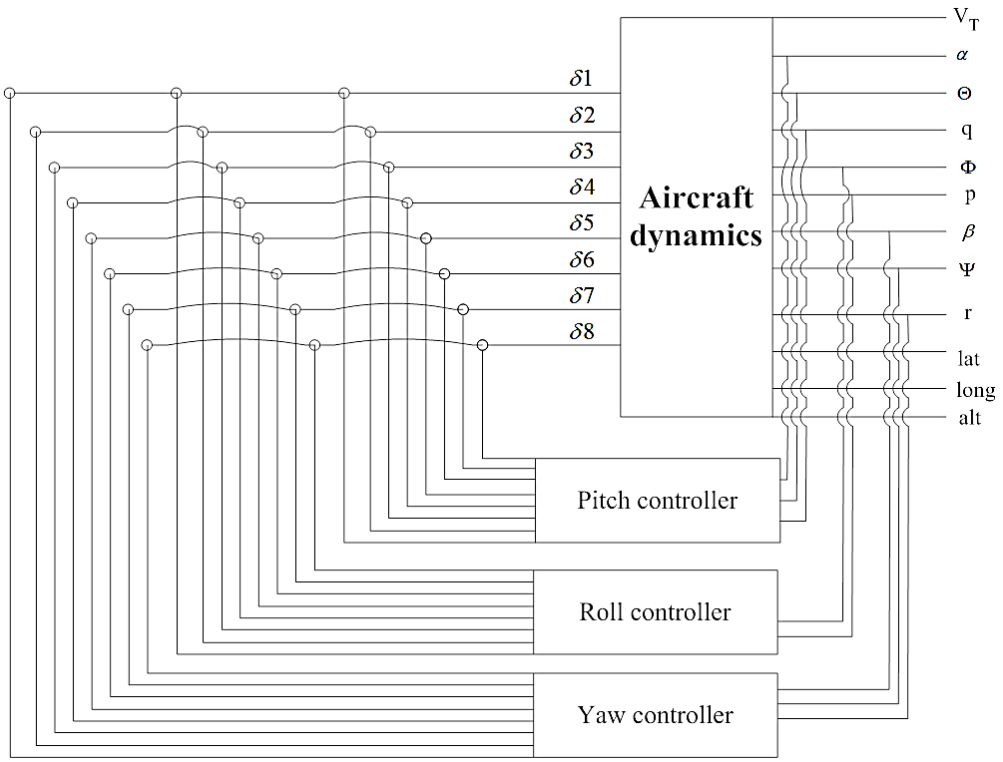

Figure 1.4: Example of implementation where the autopilot is directly responsible for control assignment

The aim of the current work was to develop a methodology for designing a mixer that would allocate the available control surfaces so the aircraft would respond to conventional pitch, roll and yaw command combinations in the most optimal way. Figure 1.5 illustrates the concept where a closed-loop feedback system is implemented with a control allocation or 'mixing' function inside the inner loops. The autopilot design process can therefore proceed as if it was for a conventional aircraft with dedicated elevators, ailerons and rudder. The mixer is solely responsible for the control allocation in this case. This approach, although by no means the only way to design an autopilot for an unconventional aircraft, could simplify the autopilot design process considerably.

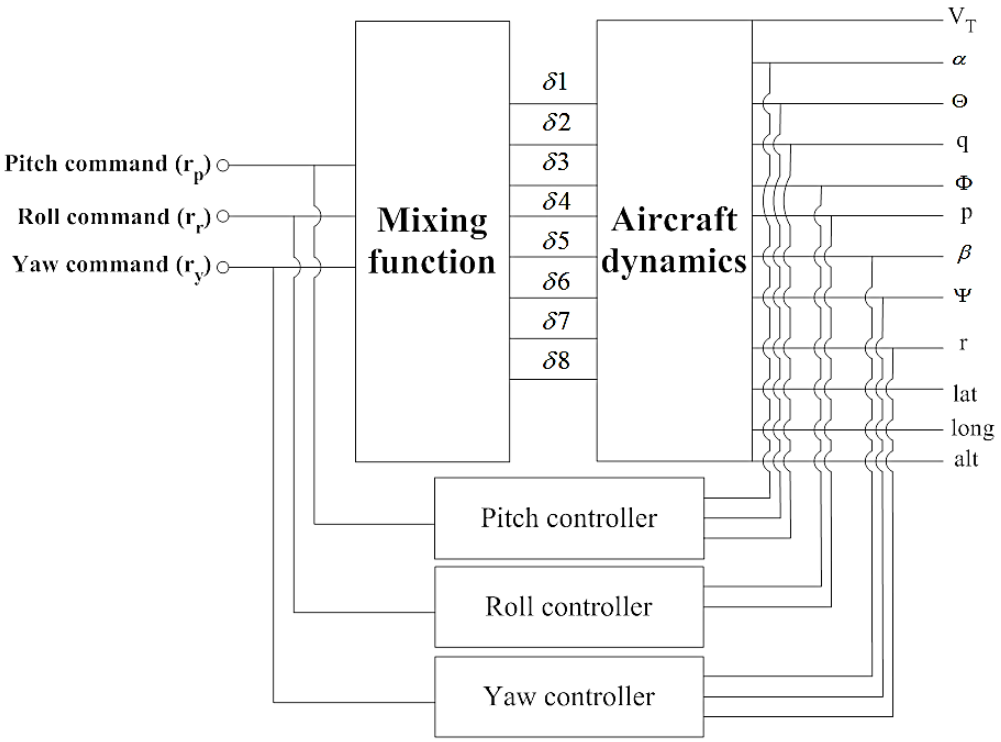

Figure 1.5: Example of implementation where a mixer is directly responsible for control assignment

One goal of the project was therefore to develop a methodology to design an open-loop system to act as the foundation for closed-loop feedback systems, while mapping any number of control surfaces to the desired pitch, roll and yaw commands in the most optimal way. Further advantages of the methodology introduced in this thesis involve the following:

- The control system enables manual flight for safe airframe recovery by eliminating unwanted control coupling.
- The control usage is optimised in an open-loop configuration.
- A methodology is developed to map the unconventional control surface setup to conventional inputs when flying the aircraft as part of a closed-loop feedback system.

The design strategy is applicable to almost any type of aircraft that makes use of control surfaces other than a conventional elevator, rudder and ailerons.

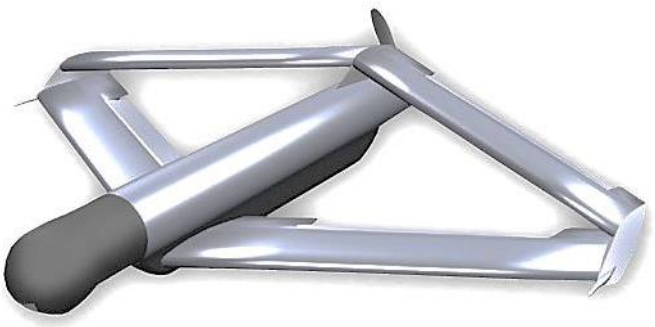

Figure 1.6: PAT Roadrunner UAV with propeller

The rhomboid UAV shown in Figure 1.6 uses eight control surfaces, of which any individual control surface can contribute to pitch, roll and yaw, and for this reason, it serves as an ideal platform to develop a design methodology for the open-loop system.

1.4. Project objectives

The aim of the project was to develop a methodology that could be used to design an open-loop control system for any type of aircraft. The research outcomes include the following:

- A methodology to map an unconventional control surface setup for any type of aircraft to conventional inputs and describing it as an optimisation problem.
- The selection of a relevant objective function that will result in satisfactory handling qualities.
- A method to determine the optimisation constraints based on the user's specific requirements.

1.5. Thesis overview

Chapter 1 provides an overall introduction and motivation for the project, setting out the aims and objectives of the study, together with the context of the work done. Chapter 2 describes the simulation environment and aspects needed for six-degrees-of-freedom (6DOF) modelling. It also describes how a detailed, nonlinear flight model of the rhomboid UAV was developed. Chapters 2 and 3 explain the tools required to implement the proposed solution strategy. Chapter 3 also provides a basic overview of optimisation and the optimisation tools used in the methodology presented in Chapter 4. Chapter 5 provides sample results of the methodology developed, as applied to the rhomboid UAV chosen as platform for this research. Chapters 6 and 7 conclude with a discussion of the design methodology and results, together with recommendations for further research on this topic.

2. Modelling and simulation

2.1 Introduction

This chapter introduces some of the fundamentals used during the modelling and simulation of this project, and explains the tools required to implement the solution methodology mentioned in section 1.4. The rigid-body equations of motion that were used to build a 6DOF flight-dynamic model of the aircraft are then defined, followed by a description of the simulation environments that were used.

The dynamics of the prototype aircraft were evaluated using a mathematical model in conjunction with computer simulation. The mathematical model incorporated the experimental data of the aircraft and was also used to improve the design of the control system. The simulation was not only used for design purposes; it allowed the designer to reconstruct the flight conditions and study the effects of modifications to the design without the risk of building a real aircraft at high cost and damaging the airframe during flight testing. The mathematical model was used in all aspects of the aircraft design.

2.2 Notation and conventions

This section introduces some of the notations and definitions used throughout the analysis and control system design of this project. Various axis systems are defined, followed by the force and moment conventions used in this project. The section concludes with a brief description of a conventional and unconventional control surface setup.

2.2.1 Axis system definitions

Before the mathematical model of the aircraft can be developed, it is necessary to define a framework according to which the equations of motion can be developed. Four different reference frames will be described: inertial, body, wind and stability axis systems [30]. The orientation of a vehicle relative to the airflow is expressed in terms of angle of attack (α) and the sideslip angle (β). The aerodynamic coefficients and forces are either relative to, or in terms of α or β. The significance of angle of attack and sideslip is that the aerodynamic forces are generally functions of (but not limited to) these quantities.

Inertial axis system

An inertial axis system is required when Newton's equations of motion are to be applied. The North-East-Down Axis System is one possible choice for an inertial axis system, and chosen for the purpose of this project. A random starting position for x and y, and sea level for z, can be chosen for the centre of the axis system or the axis system can be chosen to coincide with a convenient reference point on the earth's surface, usually located on the runway. The inertial axis system is illustrated in Figure 2.1 below [31].

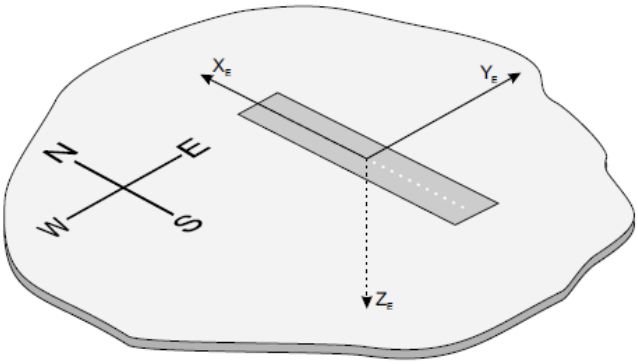

Figure 2.1: Inertial axis system

Body axis system

The body axis is fixed to the aircraft, so that the origin coincides with the centre of mass of the aircraft. Gravity is assumed to be uniform; hence, the centre of mass and the centre of gravity are the same point. The x-axis lies in the plane of symmetry and points along some convenient reference line, such as the zero angle-of-attack line of the wing or watermark line of the fuselage. The y-axis lies perpendicular to the plane of symmetry in the direction of the starboard wing. The z-axis points downwards relative to the aircraft cockpit. The body axes are preferred when performing dynamic simulations. This simplifies the analysis with regard to the angular rates and moments of inertia. If the aircraft is symmetrical with respect to the xz plane, the following products of inertia can be set to zero: $I_{xy} = I_{zy} = 0$.

Wind axis system

The wind axes are similar to the body axes in that their origin coincides with the centre of mass of the aircraft, and they thus move with the aircraft. The difference, however, is that the x-axis of the wind axes points in the direction of the velocity vector, while the z-axis lies in the aircraft's plane of symmetry and points in the down direction relative to the cockpit. The y-axis completes the right-hand axis system and points in the direction of the starboard wing. The main reason for the use of the wind axis system is that it is more convenient for calculating aerodynamic forces and moments. The wind axis is used to obtain aircraft properties relative to the wind vector.

Stability axis system

The stability axes are a variation of the body axes, and they coincide with the body axes when the angle of attack is zero. The wind axes and the stability axes coincide when the sideslip is zero. A variation of the wind axis system arises when β (sideslip angle) is assumed to be zero during aerodynamic modelling, since stability derivatives are modelled in this axis system. Three of the axes are illustrated in Figure 2.2.

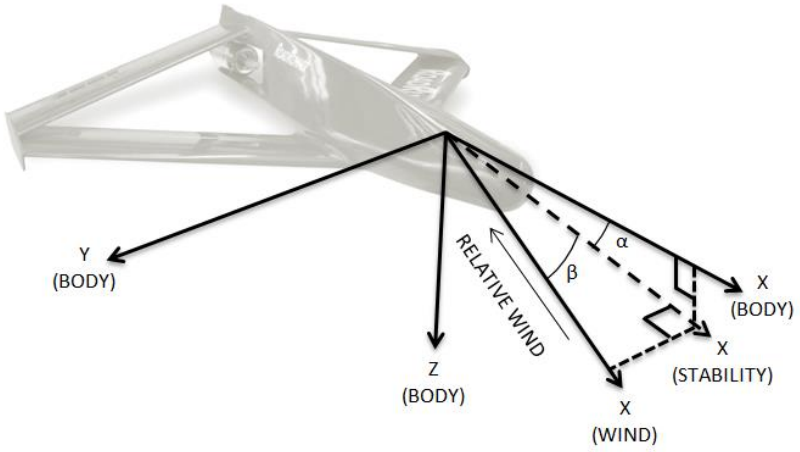

Figure 2.2: Definition of aircraft axes

2.2.2 Forces and moments

The aerodynamic forces and moments are central to the study of aircraft motion. In order to study the flight mechanics, an understanding of the fundamentals of aerodynamics is a prerequisite. The body axis system and notation used for the forces and moments acting on the aircraft are shown in Figure 2.3 below. The pitching moment is defined as the moment about the lateral axis. The rolling moment is defined as the moment about the longitudinal axis and the yawing moment is about the normal axis. The symbols given in Figure 2.3 are defined in Table 2.1. These symbols will be used throughout the thesis.

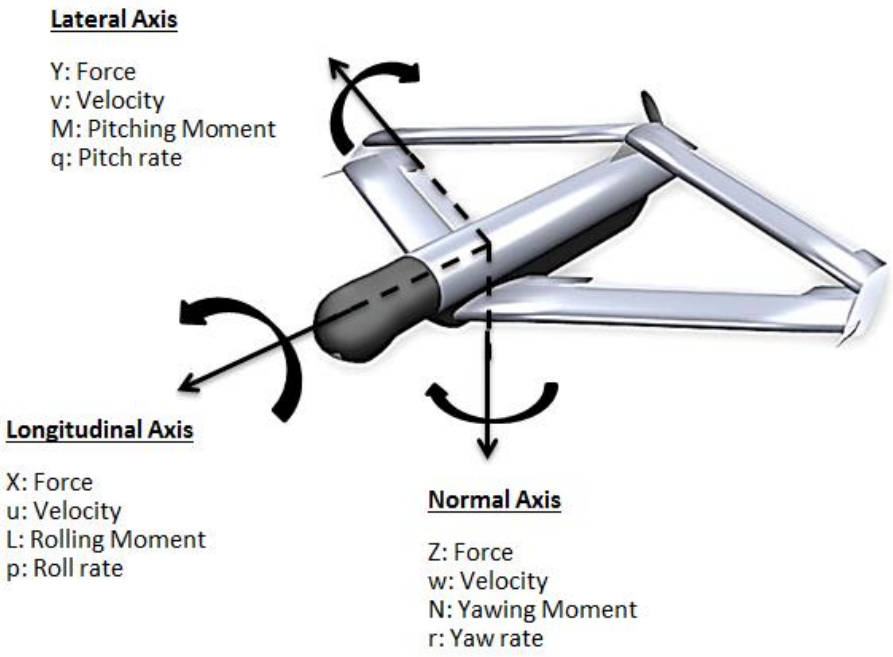

Figure 2.3: Body axis force, moment, velocity and angular rate definitions

Table 2.1: Force, moment, velocity and angular rate definitions

X Y Z	Axial force Lateral force Normal force	The sum of the components of aerodynamic, thrust and weight forces
L **M** **N**	Rolling moment Pitching moment Yawing moment	The sum of the components of aerodynamic, thrust and weight moments
u **v** **w**	Axial velocity Lateral velocity Normal velocity	The total linear velocity components of the centre of gravity position
p **q** **r**	Roll rate Pitch rate Yaw rate	The components of angular velocity

Figure 2.4 illustrates the pitch, roll and yaw conventions used in the modelling and analysis of the aircraft response. A positive pitching moment is assumed to be one that will pitch the aircraft nose up. A positive rolling moment is assumed to be one that will bank the aircraft to the right, and a positive yawing moment is assumed to be one that will yaw the nose to the right. These moment definitions would create positive rotations as for a right-handed axis system.

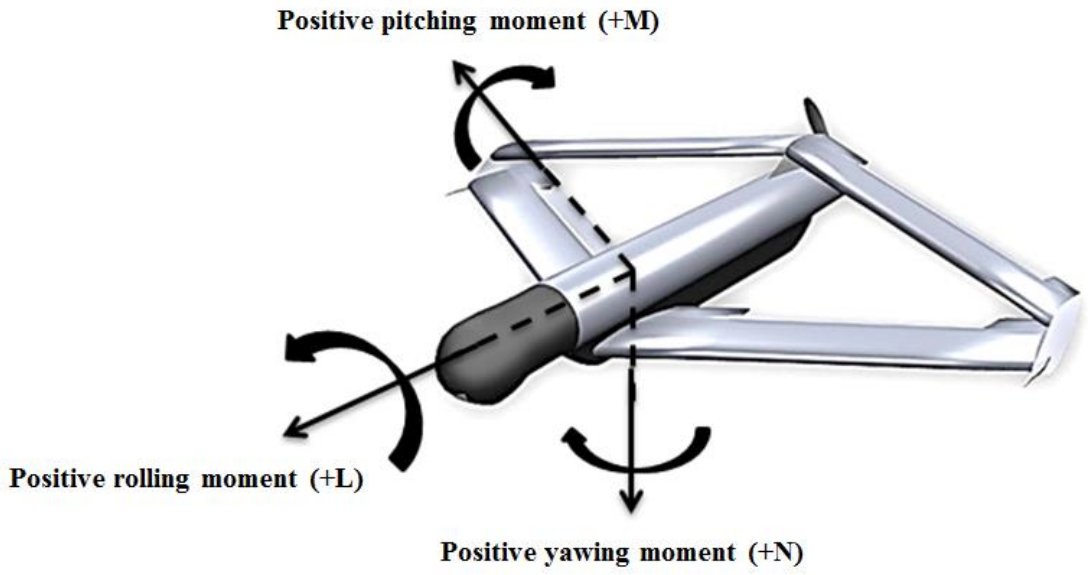

Figure 2.4: Aircraft moment convention and notation

2.2.3 Conventional control setup

A typical conventional aircraft control setup is shown in Figure 2.5, as defined in [31].

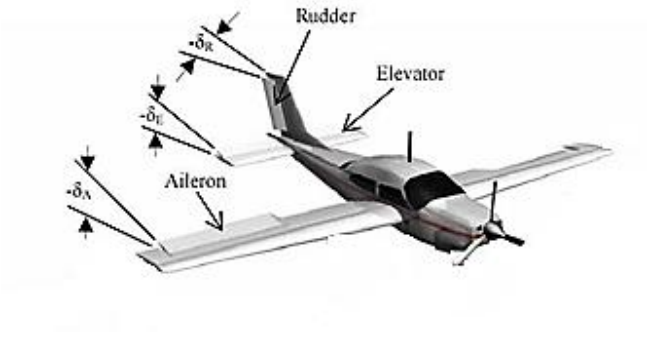

Figure 2.5: Conventional aircraft control surface sign convention

A conventional aircraft is equipped with various control surfaces, each dedicated to perform either a pitching, rolling or yawing moment about the corresponding axes. The elevator is dedicated to pitch the aircraft, the ailerons are dedicated to roll the aircraft, and the rudder is dedicated to yaw the aircraft about their respective axes. An unconventional control setup will be discussed in the next section.

2.2.4 Unconventional control setup

Unconventional control setups refer to aircraft that have multifunctional control surfaces where it may not be obvious which control surfaces would affect roll, pitch or yaw in the most optimal way. Flying wings, for example, may sometimes use control surfaces with dual functions, for example by mixing roll and pitch functions using so-called ‘elevons’ [32]. The Roadrunner UAV that was chosen as a platform for this project uses an unconventional control setup, as illustrated in Figure 2.6.

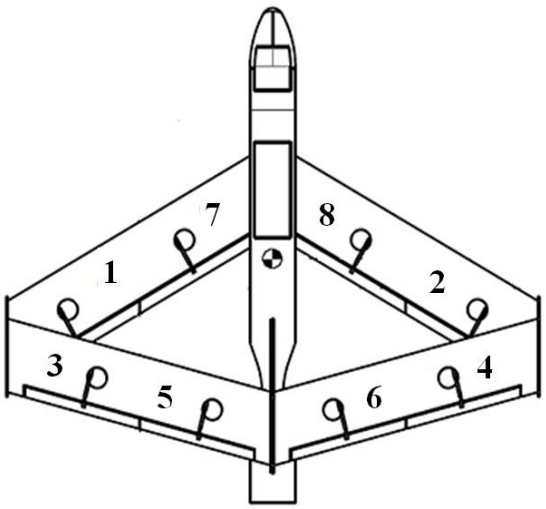

Figure 2.6: Roadrunner control surface setup

This UAV was equipped with eight multifunctional control surfaces, which could all contribute to the rolling, pitching or yawing of the aircraft. The eight control surfaces predominantly resided in the same plane of the aircraft; there was no vertical stabiliser and no

dedicated yaw control surface. In the case of the Roadrunner, the eight control surfaces had to be mixed in some complex way in order to attain the same yawing moment that would normally be provided by a dedicated rudder. As stated in the introduction, the methodology developed in this project can be used on any type of unconventional aircraft and is most suitable for cases where there are redundant control surfaces or where there is no obvious dedicated control surface to provide one of the primary flight control functions.

2.3 Six-degrees-of-freedom flight modelling

This section presents the 6DOF equations of motion that were used to mathematically model the Roadrunner UAV. A general layout of the Roadrunner airframe with dimensions is given below. The balance reference illustrated in Figure 2.7 was used during the wind tunnel tests, which is discussed later in the thesis.

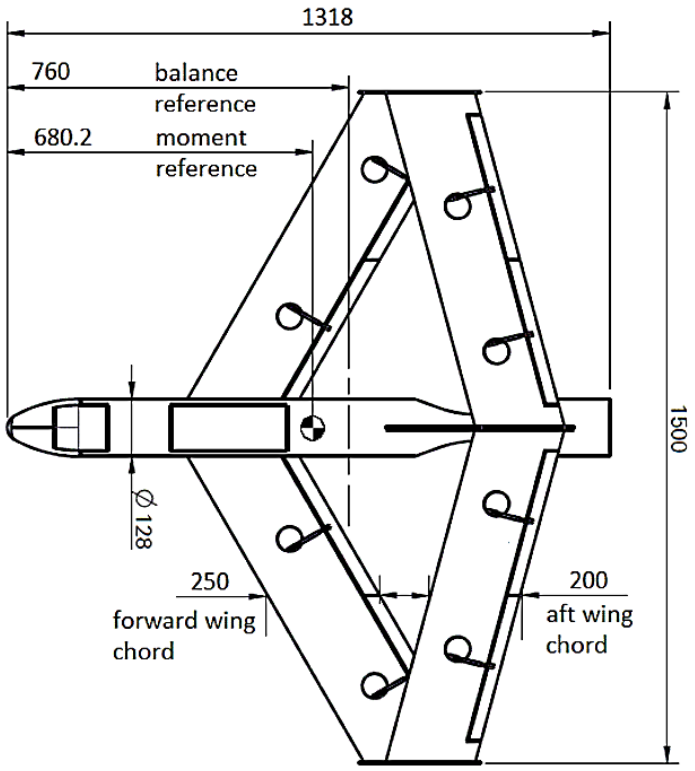

Figure 2.7: Plan view of the Roadrunner UAV

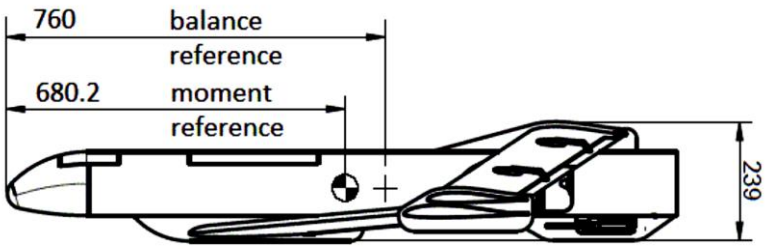

Figure 2.8: Side view of the Roadrunner UAV

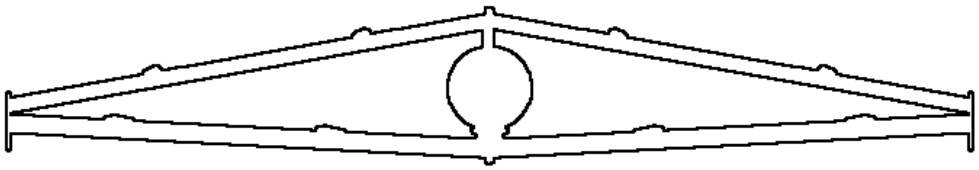

Figure 2.9: Front view of the Roadrunner UAV

The system features for the Roadrunner UAV found in [34] are listed as follows:

- Electric motor flight time > 45min
- Fuel engine flight time > 2hours
- Optional turbine motor
- Weight < 15kg
- Automatic Flight Control
- Operational range up to 40km line of sight (fuel engine)
- Ground Control Unit compatible with other Mini UAVs
- Ready to operate in less than 10min – no pilot
- Compact airframe – 1.5m wingspan

Typical applications for the Roadrunner include, but are not limited to:

- Path clearance
- Mobile observation
- Pursuit/chase of moving vehicle
- Short range intelligence missions and tactical awareness
- Border patrol
- Infrastructure and site surveillance
- Disaster image gathering
- Game observation
- Transport and delivery of light cargo
- Coastal surveillance
- Ship borne applications
- Operational speeds from stall to 55 m/s were considered

A 6DOF flight-dynamic model is required to fully understand the control allocation problem encountered. The three translational degrees of freedom and the three rotational degrees of freedom form the six degrees of freedom of the aircraft. The 6DOF equations of motion are graphically depicted in Figure 2.10 [31]. The flight-dynamic model looks like a typical aircraft flight simulation. In order to test the accuracy and validity of the aircraft model, a simulation can be very helpful in unveiling effects that have been unaccounted for.

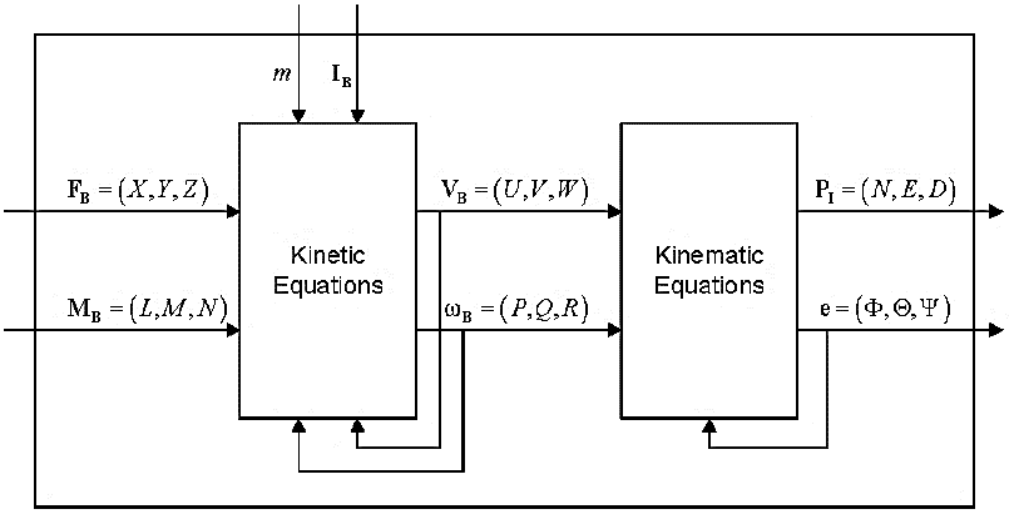

Figure 2.10: Six-degrees-of-freedom equations of motion block diagram

The main assumptions made during the flight dynamics modelling were that the aircraft is a rigid body with six degrees of freedom moving in inertial space. A rigid body implies that the position of each mass element (continuous mass distribution) on the aircraft remains fixed, relative to the body axis system, at all times. Furthermore, it was assumed that the earth is flat and the earth is an inertial frame, neglecting the centripetal and Coriolis terms when developing the equations of motion. The latter assumptions are valid, since no prerequisite for precise simulation of position is required for the low-speed flight simulation of an aircraft flying over a small region of the earth [33].

2.3.1 Aircraft forces and moments

The aerodynamic forces and moments depend on the orientation and velocity of the aircraft with respect to the airflow, and not on the velocity of the aircraft relative to the ground. The aerodynamic forces and moments are therefore produced by the relative motion with respect to the air. Uniform airflow was assumed in the simulation environment (in other words: no wind or a constant wind, no turbulence, and all parts of the aircraft experienced the same external flow).

In order to describe the mathematical models for the forces and moments on a wing, a body of a given shape with a given orientation to the freestream flow needs to be considered. The two orientation angles needed to specify the aerodynamic forces, and moments are the angle of attack (α) and the sideslip angle (β). The forces and moments are proportional to the product of freestream mass density (ρ), the square of the freestream airspeed (V_T) and a characteristic area of the body. The product of the first two quantities has the dimensions of pressure and it is convenient to define the dynamic pressure ($\bar{q}$) by:

$$\bar{q} = \frac{1}{2}\rho {V_T}^2 \qquad (2.1)$$

The aerodynamic forces and moments are complex to model, and this is where most of the uncertainties are introduced into the aircraft model. The aerodynamic forces and moments, as used in the simulation, are given below:

$$X = \bar{q}SC_X \tag{2.2}$$

$$Y = \bar{q}SC_Y \tag{2.3}$$

$$Z = \bar{q}SC_Z \tag{2.4}$$

$$l = \bar{q}SbC_l \tag{2.5}$$

$$m = \bar{q}S\bar{c}C_m \tag{2.6}$$

$$n = \bar{q}SbC_n \tag{2.7}$$

S is the wing area, b is the wingspan, $\bar{c}$ is the mean aerodynamic chord and $\boldsymbol{C_{(.)}}$ is the non-dimensional aerodynamic force and moment coefficients as defined in the body axes. Equations (2.2) to (2.4) state the aerodynamic forces in the body axis system, while aerodynamic data is more often given in the wind axis (C_L, C_D and C_Y). Conversions from wind to body are therefore usually required.

Aerodynamic coefficients

The non-dimensional coefficients are used to describe the aerodynamic properties of a specific airframe and to determine the force and moments experienced by the airframe. The static aerodynamic coefficients can be measured in a wind tunnel by using a scaled or full-scale model of the aircraft, or can be obtained through flight tests, analyses or numerical modelling. Usually, a combination of these methods is used. The following aerodynamic force and moment coefficient equations were used:

$$C_X = C_{X_0}(\alpha,\beta) + C_{X_\delta}(\alpha,\beta,\delta) + \frac{\bar{c}}{2V_T}C_{X_q}(\alpha,\beta)q \tag{2.8}$$

$$C_Y = C_{Y_0}(\alpha,\beta) + C_{Y_\delta}(\alpha,\beta,\delta) + \frac{b}{2V_T}\left[C_{Y_r}(\alpha,\beta)r + C_{Y_p}(\alpha,\beta)p\right] \tag{2.9}$$

$$C_Z = C_{Z_0}(\alpha,\beta) + C_{Z_\delta}(\alpha,\beta,\delta) + \frac{\bar{c}}{2V_T}C_{Z_q}(\alpha,\beta)q \tag{2.10}$$

$$C_l = C_{l_0}(\alpha,\beta) + C_{l_\delta}(\alpha,\beta,\delta) + \frac{b}{2V_T}\left[C_{l_r}(\alpha,\beta)r + C_{l_p}(\alpha,\beta)p\right] \tag{2.11}$$

$$C_m = C_{m_0}(\alpha,\beta) + C_{m_\delta}(\alpha,\beta,\delta) + \frac{\bar{c}}{2V_T}C_{m_q}(\alpha,\beta)q \tag{2.12}$$

$$C_n = C_{n_0}(\alpha,\beta) + C_{n_\delta}(\alpha,\beta,\delta) + \frac{b}{2V_T}\left[C_{n_r}(\alpha,\beta)r + C_{n_p}(\alpha,\beta)p\right] \tag{2.13}$$

The aerodynamic coefficients have a complex dependence on a large number of variables. This creates both measurement and modelling problems. The aerodynamic force and moment coefficient equations presented in equations (2.8) to (2.13) are modelled by using a constant term and a selection of derivative terms. The derivative terms are nonlinear functions of several independent variables such as angle of attack, sideslip angle and control surface deflection angle. The derivatives relate the increments in the moments or forces to the yawing, pitching and rolling rates. The effects of some of the other independent variables, such as the Reynolds number and Mach number, were left out of the equations given above. The Reynolds number is significant, but the wind tunnel tests were only performed at one Reynolds number and therefore a simplification was made, as the wind tunnel data was used. The Mach number is not significant here, as the aircraft will fly at low speed, and the compressibility can thus be ignored.

2.3.2 Aerodynamic derivatives

As previously mentioned, the aerodynamic forces and moments are dependent on the orientation of the aircraft, as well as the angular rates. These forces and moments can be modelled as linearly proportional to the angular rates that produced them. Linearisation is usually associated with taking a partial derivative, and in this case the coefficient of proportionality is called an 'aerodynamic derivative'. The aerodynamic derivatives can be subdivided into two categories: the damping and the acceleration derivatives.

Damping derivatives

The mathematical model for the dimensionless damping force or moment ΔC used in this project is defined in Equation (2.14) below:

$$\Delta C_{(.)} = C_{(.)}(\alpha, \beta) \times \frac{k}{2V_T} \times rate \qquad (2.14)$$

The constant k in the dimensionless rate in Equation (2.14) is either the wingspan (b) for roll and yaw rates, or the wing mean aerodynamic chord ($\bar{c}$) for pitch rate. The coefficient $\boldsymbol{C_{(.)}}$ is one of the following: roll (p), pitch (q) or yaw (r) derivatives listed in Table 2.2.

Table 2.2: Damping derivative definitions

Coefficients	Description
C_{lr}	Change in rolling moment with respect to yaw rate
C_{nr}	Change in yawing moment with respect to yaw rate
C_{xq}	Change in axial force with respect to pitch rate
C_{yp}	Change in side force with respect to roll rate
C_{yr}	Change in side force with respect to yaw rate
C_{zq}	Change in normal force with respect to pitch rate
C_{lp}	Change in rolling moment with respect to roll rate
C_{mq}	Change in pitching moment with respect to pitch rate
C_{np}	Change in yawing moment with respect to roll rate

The dimensionless forces and moments are converted to dimensional forces and moments by using equations (2.2) to (2.7). The moment derivatives are the source of the damping effects on the natural modes of the aircraft.

Acceleration derivatives

The second category of aerodynamic derivatives to be considered is the acceleration derivatives. The equations used to obtain the acceleration derivatives are given below. The angle-of-attack acceleration is represented by $\dot{\alpha}$, the sideslip-angle acceleration is presented by $\dot{\beta}$ and the acceleration of relative airspeed (TAS) is presented by $\dot{V}_T$.

$$\dot{\alpha} = \frac{U\dot{W} - W\dot{U}}{U^2 + W^2} \tag{2.15}$$

$$\dot{\beta} = \frac{\dot{V}V_T + V\dot{V}_T}{V_T[U^2 + W^2]^{1/2}} \tag{2.16}$$

$$\dot{V}_T = \frac{U\dot{U} + V\dot{V} + W\dot{W}}{V_T} \tag{2.17}$$

In deriving the equations for the simulation, it is possible to use the set u, v and w, or α, β and V_T. The simulation program primarily utilises u, v and w, and it may occasionally be necessary to calculate α, β, V_T and their derivatives in order to utilise aerodynamic data tabulated against the angles instead. In that case, equations (2.15) to (2.17) are needed to do the conversion. The acceleration derivatives given in Equation (2.18) are commonly used:

$$\text{alpha} - \text{dot derivatives:} \qquad C_{L_{\dot{\alpha}}} \; C_{m_{\dot{\alpha}}} \tag{2.18}$$

The alpha-dot derivatives were not used in the simulation, because they were not captured in the wind tunnel due to the way in which the wind tunnel tests were performed. The beta-dot derivatives are less commonly used.

2.3.3 Equations of motion

The aerodynamic force and moment models were combined with the vector equations of motion to obtain a set of equations that could be used to simulate the motion of an aircraft. The flat-earth, body axes' 6DOF equations are presented below. The aerodynamic or thrust effects in the equations below are indicated by using subscripts A or T respectively.

Euler 3-2-1 attitude parameterisation

The attitude angles used in the equations in this chapter are illustrated in Figure 2.11 [31]. There are a variety of different ways to describe the attitude of a body relative to the earth or inertial reference system, with the most commonly used being the Euler angles. The major drawback with Euler angles is that they result in a singularity in the attitude dynamics, whereas alternative attitude parameterisations, such as Quaternions and Direction Cosine Matrix (DCM) parameters avoid singularity, which is preferable, but more complex to model. The singularities occur at $\theta = \pm 90°$, where no distinction is possible between roll and yaw.

The singularities were never encountered in this study due to the types of manoeuvres that were performed. The Euler 3-2-1 sequence is the most commonly used, whereby three angles and a predefined order of rotation are used to describe the attitude of the body axis system with respect to the inertial axis system. These angles are defined as follows:

- yaw – the body axis system rotates through the heading angle ψ
- pitch – the body axis system rotates through the pitch angle θ
- roll – the body axis system rotates through the roll angle φ

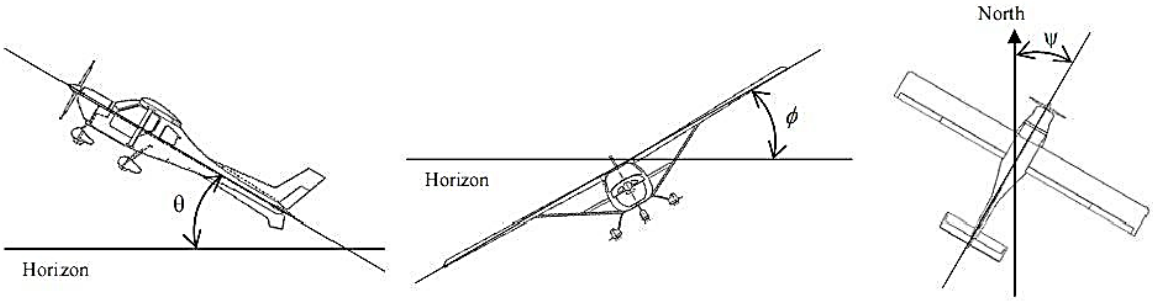

Figure 2.11: Basic illustration of Euler attitude angles [31]

It can be shown that Equation (2.19) is an orthogonal matrix, and its inverse is thus simply its transpose. Equation (2.19) gives the transformation from the body axis to the inertial axis, C represents the cosine trigonometric function of the angle indicated in the subscript, and S represents the sine trigonometric function.

$$\begin{bmatrix} \dot{p_N} \\ \dot{p_E} \\ \dot{h} \end{bmatrix} = \begin{bmatrix} C_\psi C_\theta & C_\psi S_\theta S_\phi - S_\psi C_\phi & C_\psi S_\theta C_\phi + S_\psi S_\phi \\ S_\psi C_\theta & S_\psi S_\theta S_\phi + C_\psi C_\phi & S_\psi S_\theta C_\phi - C_\psi S_\phi \\ -S_\theta & C_\theta S_\phi & C_\theta C_\phi \end{bmatrix} \begin{bmatrix} U \\ V \\ W \end{bmatrix} \tag{2.19}$$

Force equations

In equations (2.20) to (2.22), the time rate of change of the x-component of the airspeed is represented by $\dot{u}$, the time rate of change of the y-component of the airspeed is represented by $\dot{v}$, and the time rate of change of the z-component of the airspeed is represented by $\dot{w}$, and the magnitude of the gravitational acceleration is presented by g_D.

$$\dot{u} = rV - qW - g_D \sin\theta + (X_A + X_T)/m \tag{2.20}$$

$$\dot{v} = pW - rU + g_D \sin\Phi \cos\theta + Y_A/m \tag{2.21}$$

$$\dot{w} = qU - pV + g_D \cos\Phi \cos\theta + Z_A/m \tag{2.22}$$

Moment equations

In the equations below, the roll acceleration is presented by $\dot{p}$, the yaw acceleration is presented by $\dot{r}$, and the pitch acceleration is presented by $\dot{q}$.

$$\dot{p} = \frac{I_{xz}(I_{xx} - I_{yy} + I_{zz})pq - (I_{zz}(I_{zz} - I_{yy}) + {I_{xz}}^2)qr}{\gamma} + \frac{I_{zz}(l + torque) + I_{xz}n + I_{xz}qh_x}{\gamma} \tag{2.23}$$

$$\dot{r} = \frac{\left((I_{xx} - I_{yy})I_{xx} + {I_{xz}}^2\right)pq - I_{xz}(I_{xx} - I_{yy} + I_{zz})qr}{\gamma} + \frac{I_{xz}(l + torque) + I_{xx}n + I_{xx}qh_x}{\gamma} \tag{2.24}$$

$$\dot{q} = \frac{(I_{zz} - I_{xx})pr - I_{xz}(p^2 - r^2) + m - rh_x}{I_{yy}} \tag{2.25}$$

Where $\gamma = I_{xx}I_{zz} - {I_{xz}}^2$, note that this equation must be modified slightly if the angular momentum of the rotating rotor/propeller has components in the y- and z- body axes.

Kinematic equations

The Euler rates are calculated by using the equations below. The time rate of change of yaw angle is represented by $\dot{\psi}$, the time rate of change of pitch angle is represented by $\dot{\theta}$, and the time rate of change of roll angle is represented by $\dot{\Phi}$.

$$\dot{\Phi} = P + \tan\theta\,(\mathrm{Q}\sin\Phi + \mathrm{R}\cos\Phi) \tag{2.26}$$

$$\dot{\theta} = Q\cos\Phi - R\sin\Phi \tag{2.27}$$

$$\dot{\psi} = (Q\sin\Phi + R\cos\Phi)/\cos\theta \tag{2.28}$$

Navigation equations

In the equations below, the velocity component in the northerly direction is represented by $\dot{p}_N$, the velocity component in the easterly direction by $\dot{p}_E$ and the rate of climb by $\dot{h}$.

$$\dot{p}_N = U\cos\theta\cos\psi + V(-\cos\Phi\sin\psi + \sin\Phi\sin\theta\cos\psi) + W(\sin\Phi\sin\psi + \cos\Phi\sin\theta\cos\psi) \tag{2.29}$$

$$\dot{p_E} = U\cos\theta\sin\psi + V(\cos\Phi\cos\psi + \sin\Phi\sin\theta\sin\psi) + W(-\sin\Phi\cos\psi + \cos\Phi\sin\theta\sin\psi) \tag{2.30}$$

$$\dot{h} = U\sin\theta - V\sin\Phi\cos\theta - W\cos\Phi\cos\theta \tag{2.31}$$

2.4 MATLAB® 6DOF simulation environment

A locally developed simulation environment was made available to model the aircraft based on the principles discussed in section 2.3. A mathematical understanding of how the simulation environment works was required in order to correctly model the aircraft. A diagram of the MATLAB® 6DOF simulation environment is illustrated in Figure 2.12. It consisted of a nonlinear aerodynamic model, an electric motor/propeller propulsion model and a 1976 standard atmospheric model. The equations and parameters used to create the atmospheric model are documented in [35].

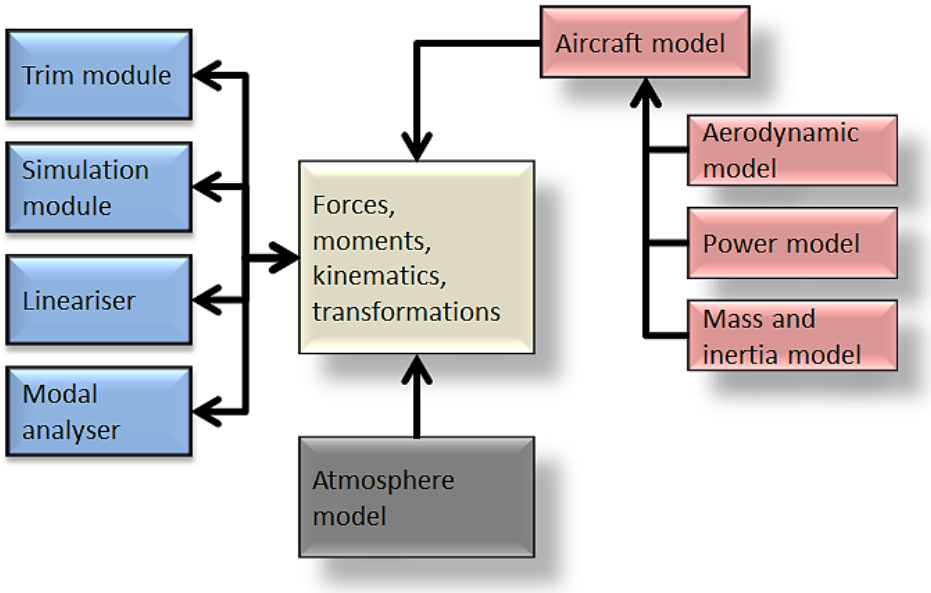

Figure 2.12: Locally developed MATLAB® 6DOF simulation model

A 6DOF aircraft model, consisting of an aerodynamic model and a propulsion model, was implemented in the existing simulation environment in MATLAB® in order to develop and test the control system design. Candidate control system designs were tested through scripted manoeuvres within the simulation environment. The simulation modules that were used to analyse the aircraft response are discussed in section 2.5, while a detailed description of the way in which the aircraft data was obtained and implemented in MATLAB® is provided in section 2.6. The chapter proceeds with section 2.7, which gives a description of the atmospheric model used in the MATLAB® simulation model, and concludes with section 2.8, which provides information on the way in which the aircraft models were validated.

2.5 Simulation modules

The simulation modules were used to initialise the aircraft at a given state, and execute scripted inputs. A 4^{th}-order Runge-Kutta [34] integrator was available in the simulation to solve the nonlinear simulation equations. Various scripts were designed to test the Roadrunner's response, such as simulated coordinated turns, pitch, roll and yaw doublets, step pitch, and roll and yaw inputs. The modules save the time history, which allow the response to be analysed or plotted afterwards. The analysis modules circled in Figure 2.13 below will be discussed in the subsections that follow.

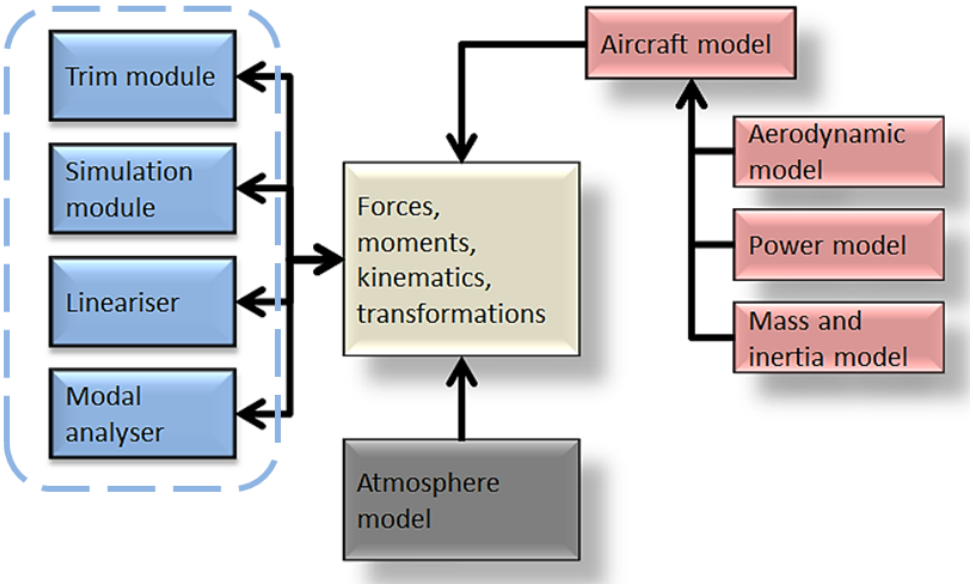

Figure 2.13: Custom 6DOF analysis modules

2.5.1 Steady-state flight

Steady-state flight is usually used as an initial condition for flight simulation. It also provides fixed conditions about which the aircraft dynamics can be linearised. The steady-state behaviour of an aircraft can be investigated thoroughly from a set of trimmed flight conditions. The trimmer module available in the MATLAB® environment was able to set up a function minimisation problem to determine the steady-state trim condition for the aircraft.

A set of initial conditions were required to start the trim solver. The required parameters depended on the trim state required, but typically included a state vector and approximate control positions. The nonlinear system of equations was solved using a multidimensional Newton-Raphson [34] solver to obtain the steady-state condition. The steady-state trim conditions that were important for control system design consisted of setting the time derivatives of the relative airspeed ($\dot{V}_T, \dot{\alpha}$ *and* $\dot{\beta}$) and the three body rotational accelerations ($\dot{p}, \dot{q}$ *and* $\dot{r}$) to zero for the control fixed steady dynamic system. The trim algorithm was used to model the following additional conditions:

1. Steady, wings-level flight (climb/descent allowed): $\Phi, \dot{\Phi}, \dot{\theta}, \dot{\psi} \equiv 0$ ($\therefore$ p, q and r $\equiv 0$)
2. Steady turning flight (climb/descent allowed): $\dot{\Phi}, \dot{\theta} \equiv 0, \dot{\psi} \equiv$ turn rate (specify $\dot{\psi}$ or Φ)
3. Steady symmetrical pull-up: $\Phi, \dot{\Phi}, \dot{\psi} \equiv 0, \dot{\theta} \equiv$ specified pitch rate
4. Steady roll: $\dot{\theta}, \dot{\psi} \equiv 0, \dot{\Phi} \equiv$ roll rate. For a steady roll it is better to set $\psi = 0$.

The steady-state conditions $\dot{p}, \dot{q}$ and $\dot{r} \equiv 0$ specify that the angular accelerations must be zero. The conditions $\dot{V}_T, \dot{\alpha}, \dot{\beta} \equiv 0$ require the derivative of airspeed, angle of attack and sideslip angle respectively to be zero. The linearisation will be discussed in the next section.

2.5.2 Lineariser

Linearisation is the process of finding a linear model that approximates a nonlinear one, which is usually valid for small perturbations about some reference condition [35]. Nonlinear

system characteristics can be approximated by linear models for which many powerful methods of design and analysis exist [36]. These powerful tools of linear systems theory can be used to analyse the system and perform control system design once the nonlinear model has been linearised around a design point [33].

A numerical linearisation algorithm was made available that can be applied to various nonlinear models. The linearisation tool assumed that the aircraft had already been trimmed to a steady-state condition. The lineariser was then able to extract linear state-space and transfer function descriptions of an aircraft model to perform linear control system design. The linear state ($\dot{x}$) and output equations (y) of the aircraft model are given in equations (2.32) and (2.33).

$$\dot{x} = Ax + Bu \tag{2.32}$$

$$y = Cx + Du \tag{2.33}$$

The lineariser makes small perturbations to each state variable at a time to compute the elements of the A, B, C and D matrices. The program allows the user to specify the states of interest, which means he or she can, for example, create separate longitudinal and lateral linear models. The linearised state-space model obtained in this section was converted to transfer functions in order to analyse the longitudinal and lateral modes of the aircraft, as discussed in the next section.

2.5.3 Modal analyser

The modal analyser was used to obtain the aircraft's frequencies and damping ratios for the various rigid body aircraft modes. The modes are a result of the longitudinal and lateral motion of the aircraft. The different modes are described below.

Longitudinal motion

A longitudinal motion is a motion that is constrained in the longitudinal plane of symmetry of the aircraft. The motion is described by the axial force X, the normal force Z and the pitching moment M.

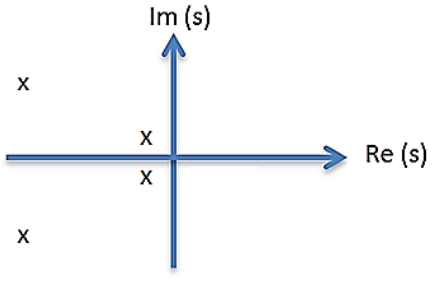

Figure 2.14: Longitudinal pole plot

The higher frequency poles in the left-hand plane are associated with the short period mode. The lower frequency poles in the right-hand plane are associated with the 'phugoid' mode. The short-period mode describes the aircraft's tendency to realign itself with the velocity

vector when disturbed. The phugoid mode is a largely kinematic mode of motion and describes the exchange of potential and kinetic energy when the aircraft is disturbed from trimmed flight. The periods of these modes are usually separated by more than an order of magnitude, which makes them fairly easy to identify as the short-period and phugoid modes. The phugoid mode is usually very lightly damped, whereas the short period mode is typically well damped.

Lateral motion

The lateral motion considers all natural aircraft modes outside the plane of symmetry. Lateral motion therefore deals with rolling and yawing motions, as well as sideways motion along the y-axis.

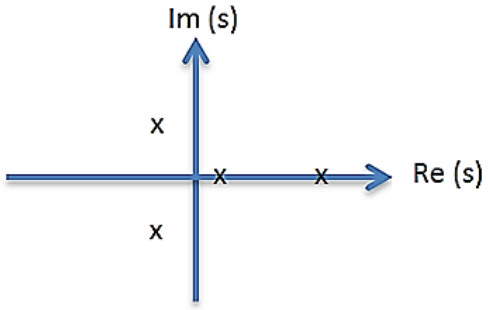

Figure 2.15: Lateral pole plot

There are typically two real modes and one oscillatory mode associated with lateral motion, although it is possible (but rare) for the two real modes to merge into a secondary roll-spiral mode. The real pole with the larger magnitude is associated with the 'roll' mode. There is usually a second real pole very close to origin that is associated with the 'spiral' mode. It may be stable or unstable; it is unstable in Figure 2.15. The complex pole pair is associated with the 'Dutch roll' mode. The roll mode describes the roll dynamics of an aircraft. The Dutch roll mode can be described by an out-of-phase combination of sideslipping, rolling and yawing oscillation that can be very unpleasant. The Dutch roll mode is almost the directional equivalent of the short-period mode. The spiral mode describes the aircraft's tendency to restore itself to wings-level flight or diverge from wings-level flight when laterally disturbed, *i.e.* in roll angle. It is not uncommon for this mode to be unstable.

The modal analyser made use of the lineariser to create a linear model from which the individual rigid body modes could be identified using conventional eigenvector and eigenvalue analysis. The equations of motion were linearised about a steady-state condition described under two sets – one as the longitudinal motion of an aircraft, and the other as the lateral/directional motion. The modal analysis tool was only used for verification purposes during the initial design phase of the project [33]. As mentioned before, the lineariser was used to linearise the nonlinear state-space model into a linear state-space model in order to use the MATLAB® built-in function state-space to transfer function 'ss2tf'. The MATLAB® function converts a linear state-space model (equations (2.32) and (2.33)) to a transfer function model in the form given in Equation (2.34).

$$H(s) = \frac{Num(s)}{Den\ (s)} \tag{2.34}$$

The Den(s) vector contained the coefficients of the denominator in descending powers of s, whereas the numerator coefficients were returned in matrix Num(s) with as many rows as there were outputs, y. The motion of a linear system is governed by the poles (s) of the system. Determining the open-loop poles of a system is equivalent to determining the natural modes of motion of a system, as discussed below. The open-loop poles were determined by calculating the eigenvalues of the system matrix [37]. The eigenvalues of each pole of the system matrix were obtained using the 'eig' MATLAB® built-in function; the complex poles were defined in terms of their real (σ) and imaginary parts ($j\omega_d$), as illustrated in Equation (2.35).

$$s = -\sigma \pm j\omega_d \tag{2.35}$$

The MATLAB® built-in function 'poly' converts the roots to polynomials in order to write the transfer function in polynomial form, as illustrated in Equation (2.36).

$$H(s) = \frac{{\omega_n}^2}{s^2 + 2\zeta\omega_n s + {\omega_n}^2} \tag{2.36}$$

The transfer function in polynomial form is used to determine the natural frequencies and damping ratio by using Equations.

$$\sigma = \zeta\omega_n \tag{2.37}$$

$$\omega_d = \omega_n\sqrt{1-\zeta^2} \tag{2.38}$$

The damping ratio is defined by the parameter ζ, the undamped natural frequency is defined by the parameter ω_n, and the damped natural frequency is defined by the parameter ω_d. The modes are obtained by analysing the eigenvectors of the lateral and longitudinal motion of the aircraft. Two complex-conjugate pairs of eigenvalues are obtained from the four states of longitudinal dynamics, which correspond to two stable oscillatory modes. The two modes are identified as the short-period and phugoid mode. The periods of these modes are separated by more than an order of magnitude. The phugoid mode was usually very lightly damped and the period is long, compared to the short period, whereas the short-period mode was reasonably well damped.

The lateral aircraft dynamics produced two real eigenvalues and a complex-conjugate pair. The oscillatory mode in these eigenvectors is called the Dutch roll mode. The eigenvalues show that the Dutchroll mode period was quite short and the oscillation was usually very lightly damped. The second lateral dynamic mode was a stable exponential mode known as the roll mode. The third lateral dynamic mode, known as the spiral mode, was also a stable exponential mode, but has a much longer time constant than the roll mode. In some aircraft, the spiral mode may be unstable, and additional calculations are required for stability.

2.6 Aircraft data

The aircraft model consisted of a complete 6DOF nonlinear aerodynamic model, propulsion model and mass and inertia model, as indicated in Figure 2.16.

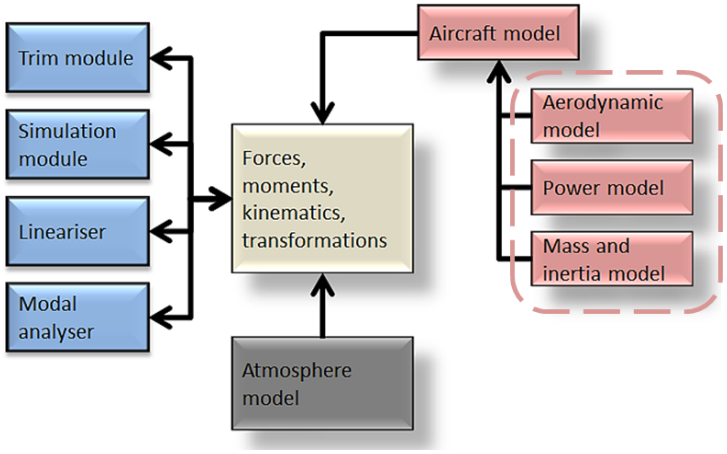

Figure 2.16: Custom 6DOF aircraft model

The method by which the data was obtained and implemented in the simulation environment is discussed in the subsections that follow.

2.6.1 Aerodynamic model

The aerodynamic model consisted of implementing the data required to complete the equations given in section 2.3. The stability derivatives consisted of the static and dynamic aerodynamic coefficients, which are discussed below.

Static aerodynamic coefficients

A wind tunnel test series was conducted at the Council for Scientific and Industrial Research (CSIR). This preceded the work reported here [38]. These tests were performed using a full-scale model of the aircraft in the low-speed wind tunnel at the CSIR. The airframe characterisation tests were executed by using the Modern Design of Experiments (MDOE) technique [39]. MDOE is aimed at extracting as much information as possible from a limited number of tests [40]. In order to limit the amount of wind tunnel testing necessary, a test matrix was designed to capture the response of the airframe utilising a response surface approach. Characteristic response surfaces were derived in the form of mathematical models that were statistically defensible [41]. To determine the response surfaces characterising the airframe, the MDOE technique was used as a function of 10 factors, *i.e.* angle of attack, angle of sideslip and the deflections of the eight individual control surfaces. The commercially available package Design-Expert®, from Stat-Ease, was used to analyse the test data [38]. The static stability was experimentally determined from wind tunnel data using the MDOE approach [42].

The MDOE models for the various aerodynamic forces and moments were provided in the form of coefficients of polynomial expressions. The design space was divided into three angle-of-attack ranges, which resulted in separate MDOE models that were valid over each individual range. The low alpha region spanned $-6° \leq \alpha \leq 6°$, the high alpha region spanned

$4° \leq \alpha \leq 11°$ and the post-stall region spanned $14° \leq \alpha \leq 18°$. The design test envelope for the angle-of-attack range therefore covered the range $-6° \leq \alpha \leq 18°$ so that the combined MDOE model was defined over the same range. The sideslip design test envelope consisted of a range of $-10° \leq \beta \leq 10°$.

The low alpha and high alpha range MDOE models were expressed as second-order polynomials with pure third-order terms, whereas the post-stall region was reduced to a linear model with two additional squared terms. Several asymmetric terms were detected in the MDOE models, which – although statistically significant – were undesirable for the flight dynamics modelling of the physically symmetrical airframe. The MDOE models were therefore modified for implementation in the simulation environment by eliminating the asymmetries that resulted from the experimental testing and MDOE analysis technique. Further modification involved taking the average weighted effect of the corresponding control surfaces on the left and right to ensure a perfectly symmetrical modelled aircraft. The corresponding control surfaces are illustrated in Figure 2.17.

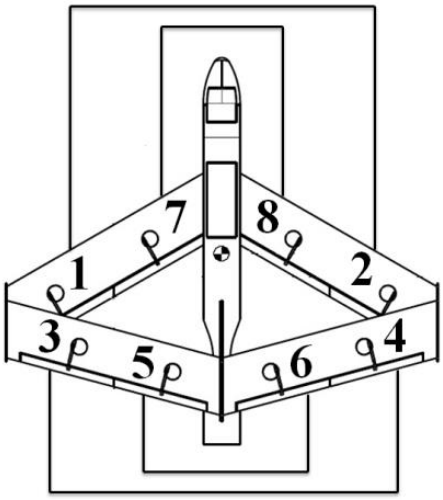

Figure 2.17: Corresponding control surfaces

In addition, the low, medium and high angle-of-attack aerodynamic models were combined into a single model using blending functions over the overlapping angles of attack (between the low and high angle-of-attack regions) and to span the range from 11- to 14-degree angles of attack, which was not covered by the MDOE models at all. The final model gave each of the six body-axis static aerodynamic coefficients as functions of angle of attack, angle of sideslip and a combination of deflections of the eight control surfaces.

The blending functions used were interpolating functions that agreed exactly with the given data where that data was defined, and assumed a smooth transition between the separate regions. The three sets of polynomials for the low, high and post-stall angle-of-attack regions were respectively joined together smoothly for all the force and moment MDOE models. The polynomial equations were joined using an interpolation function between the low, high and post-stall angle-of-attack regions, respectively. An extract of how the angle of attack regions for the axial-force coefficient were blended is illustrated in Appendix C. Note that all the force and moment coefficients were blended using the same approach.

The figures below illustrate the method used for blending all six the aerodynamic coefficients. The difference between the blending function and the MDOE models is evident in the overlapping region between 4° and 6° angles of attack, and in the region between 11° and 14° where no data existed, as illustrated by the dashed lines respectively. A smooth transition between the three angle-of-attack regions for the axial force coefficient is illustrated in Figure 2.18. The blending function was especially useful in the region between the low and high, and high and post-stall angle-of-attack regions. Although an overlap existed between low and high angle-of-attack regions, it was still necessary to blend the function, as the two regions did not agree. Interpolation between the high and post-stall regions was necessary due to the missing information.

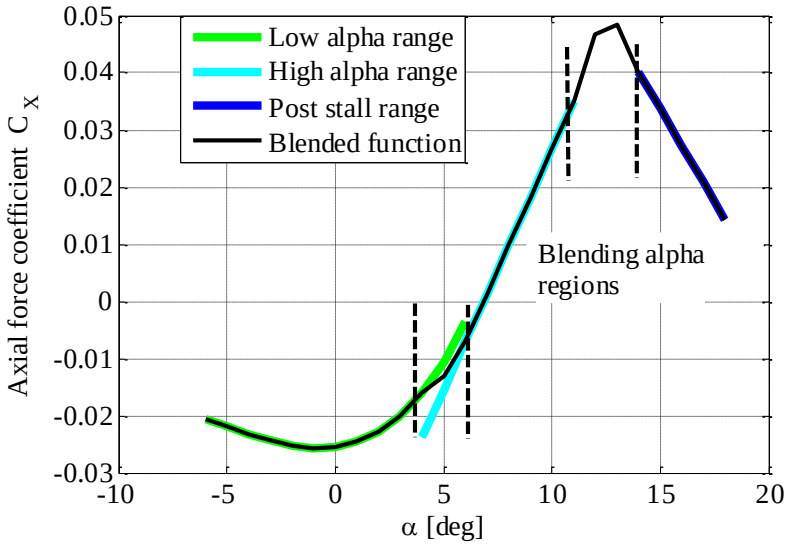

Figure 2.18: Blending function effect on axial-force coefficient for β = 0°

Blending of the normal force coefficient is illustrated in Figure 2.19. The blending function once again ensured a smooth transition between the high and post-stall regions, illustrating the overlap between the low and high angle-of-attack regions.

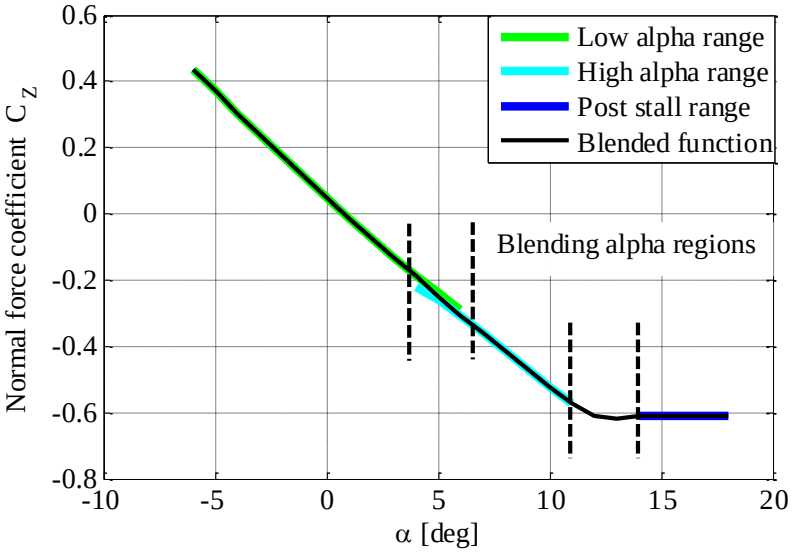

Figure 2.19: Blending function effect on normal-force coefficient for β = 0°

The MDOE model for the pitching moment coefficient was not consistent between the different angle-of-attack regions; large variations existed, as shown in Figure 2.20. The blending function was unavoidable for the pitching moment coefficient, due to the inconsistencies in the high angle-of-attack range, as illustrated in Figure 2.20. The blending function ensured a continuous function for the pitching moment coefficient between the low and post-stall angle of attack by using the gradient of the high angle-of-attack region.

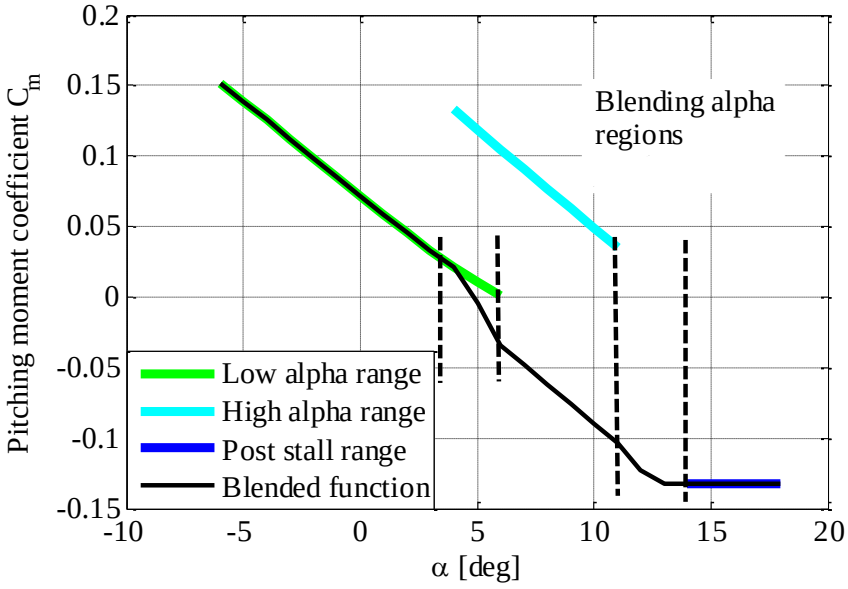

Figure 2.20: Blending function effect on pitching moment coefficient for β = 0°

Blending functions were required for the side-force, rolling and yawing moment coefficients when the sideslip angle was not zero. The blending functions for the rolling, yawing moment and side-force coefficients are illustrated in Figure 2.21, Figure 2.22 and Figure 2.23 for a sideslip angle of two degrees.

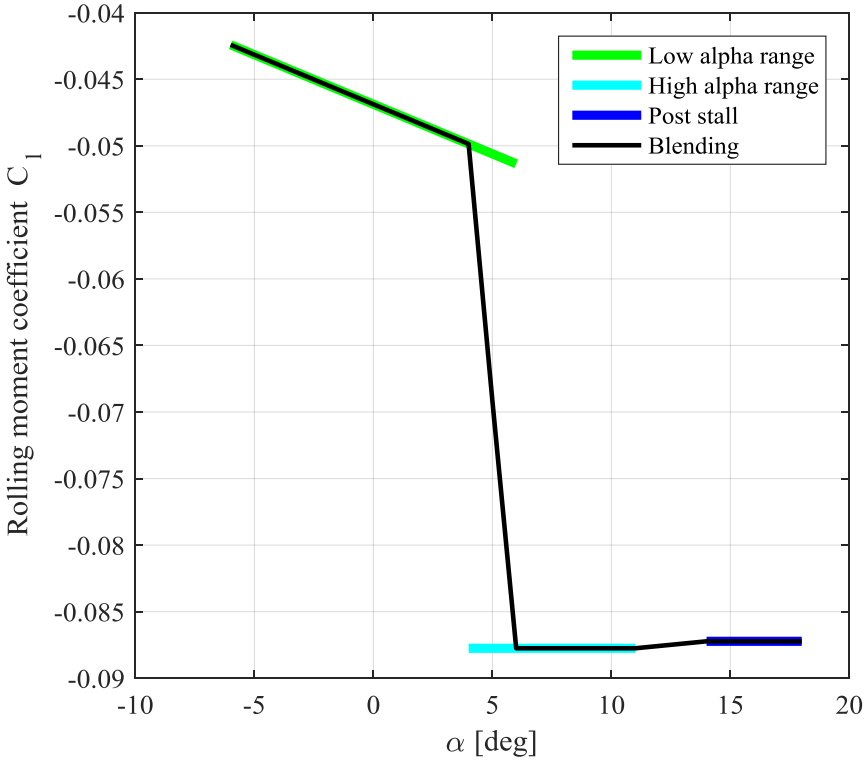

Figure 2.21: Blending function effect on rolling moment coefficient for β = 10°

In Figure 2.21, Figure 2.22 and Figure 2.23, it can be seen that blending was necessary when sideslip was present. In Figure 2.22, it is clear that the blending function used the slopes of the respective alpha regions, but neglected to pass through the actual data set of the low and high alpha regions. The aerodynamic model made use of these blending functions to ensure a smooth transition between the different angle-of-attack regions. The function did not pass through all the data sets, but the function was still acceptable for simulation purposes. MATLAB® has various built-in functions, such as polyval and polyfit, which could be used to fit the data and ensure a smooth transition between regions. The MATLAB® function or MATLAB® curve-fitting toolbox can be used to generate a higher order polynomial that passes through all the data sets.

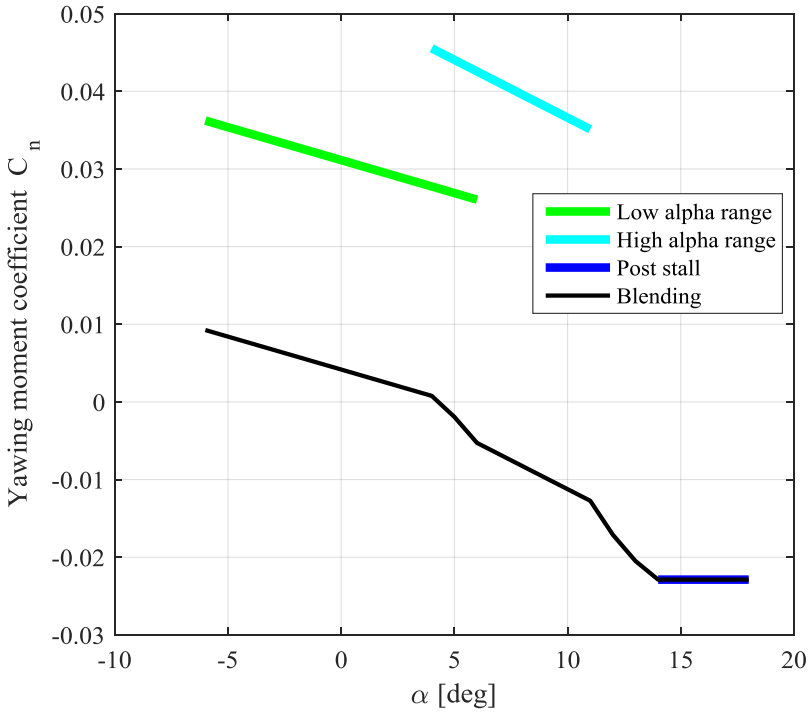

Figure 2.22: Blending function effect on yawing moment coefficient for β = 10°

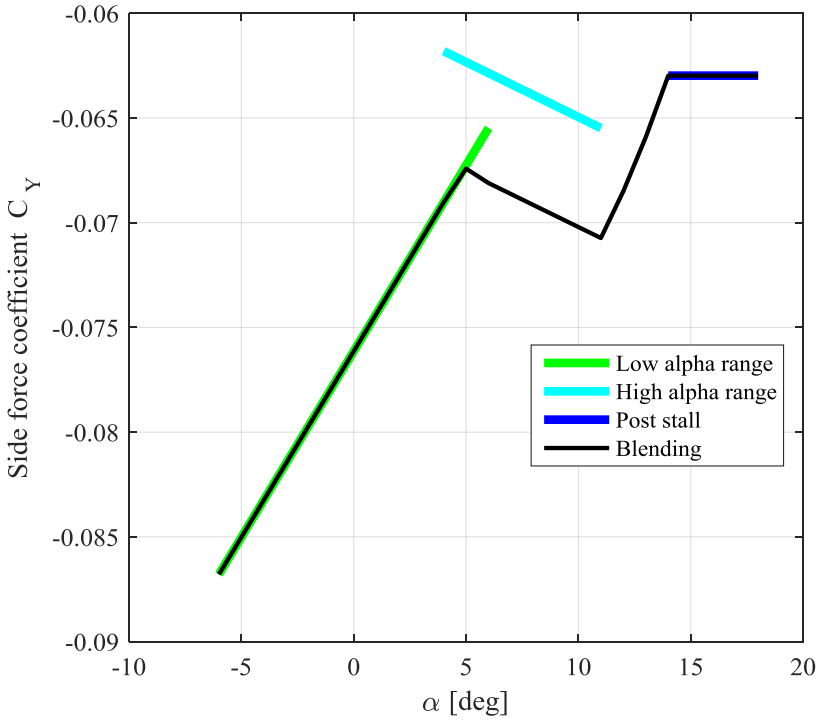

Figure 2.23: Blending function effect on side force coefficient for β = 10°

Dynamic aerodynamic coefficients

The Athena Vortex Lattice (AVL) [43] is a software package developed at the Massachusetts Institute of Technology (MIT) that is suitable for the aerodynamic and flight dynamics analysis of rigid aircraft in inviscid, incompressible flow. The software package uses a vortex lattice method to model an aircraft and calculate the stability and control derivatives. Vortex lattice methods are a numerical, CFD method used in the early stages of aircraft design. Vortex lattice methods are similar to panel methods and provide insight into wing aerodynamics and component interaction. They are also based on solutions to Laplace's Equation. AVL assumed quasi-steady flow, which means that unsteady vorticity shedding was neglected in the simulation. AVL assumes the limit of small reduced frequencies, *i.e.* if there is an oscillatory motion in pitch, it must be slow enough so that the period of oscillation is much longer than the time it takes the flow to traverse an aerofoil chord. The vortex-lattice modelling principles on which AVL is based are discussed in detail in [43]. The AVL modelling limitations are briefly listed below.

AVL modelling limitations

AVL is best suited to aerodynamic configurations that consist mainly of, but are not limited to, thin lifting surfaces at small angles of attack and sideslip. The flow is modelled based on the assumption of 2D potential flow, and it is therefore acceptable to ignore some of the flow effects, and to model the aircraft using this tool. The limitations are summarised below:

- Stall and separation cannot be modelled.
- Thickness is not modelled.
- Viscous effects are not modelled.

The stability derivatives that were not obtained from the previously described wind tunnel tests were calculated using AVL. The aircraft was modelled utilising four different methods, as illustrated below. The wings were modelled using different numbers of span-wise and chord-wise horseshoe vortices for each section in order to accurately model the aerodynamics. The lifting surfaces were straightforward to model, since they are exactly what AVL was designed for. AVL has limitations when modelling non-lifting surfaces, such as a fuselage of an aircraft. The fuselage can be modelled by its side-view and top-view profiles, but the moment of the fuselage will still only be captured reasonably well. The fuselage is therefore challenging to model, since it can generate some side force and yawing moment, but it would be less than an equivalent wing in the vertical plane. In this project, the aircraft was modelled using four different configurations to evaluate which model captured the moments and forces best. The configurations are discussed and illustrated below.

The first vortex lattice model made use of a vertical lifting panel to represent the fuselage of the aircraft, as illustrated in Figure 2.24. The second vortex lattice model used sources and doublets to represent the fuselage of the aircraft, as illustrated in Figure 2.25. The third model used sources and doublets to represent the nose of the aircraft and a vertical lifting panel to represent the rest of the fuselage, as illustrated in Figure 2.26. The fourth model was implemented without a fuselage, as illustrated in Figure 2.27.

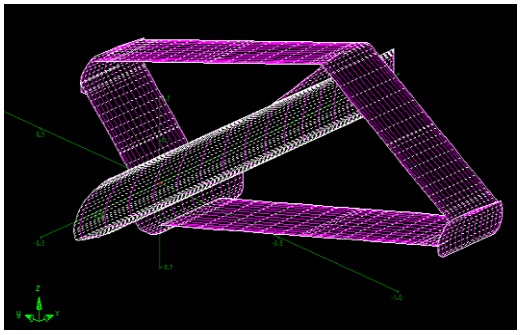

Figure 2.24: Fuselage modelled as a vertical lifting panel

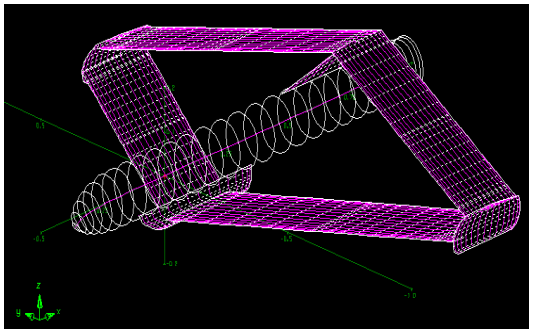

Figure 2.25: Fuselage modelled using sources and doublets

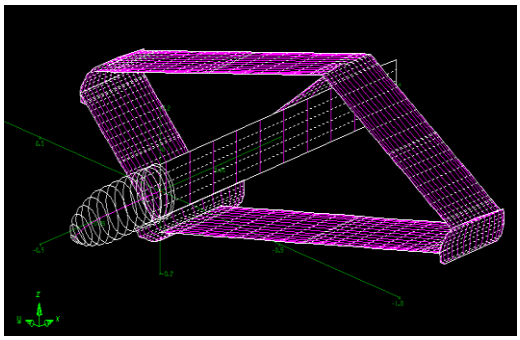

Figure 2.26: Fuselage modelled using sources and doublets and a vertical lifting panel

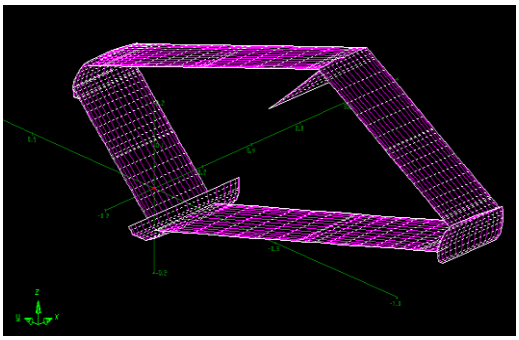

Figure 2.27: Aircraft modelled without a fuselage

In order to verify the AVL model, static coefficients predicted by the AVL model were compared to the wind tunnel results in the low angle-of-attack range. The results obtained from the wind tunnel and AVL for the lift coefficient are compared in Figure 2.28.

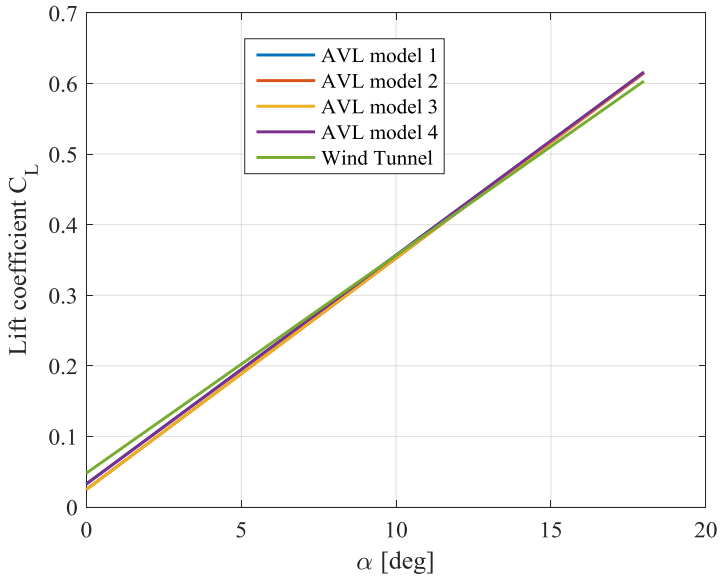

Figure 2.28: Lift coefficient comparison between wind tunnel and AVL data

As can be seen in Figure 2.28, the results obtained from the four AVL models correspond to the results obtained from the wind tunnel. The results obtained from the wind tunnel and AVL for the yawing moment coefficient are compared in Figure 2.29.

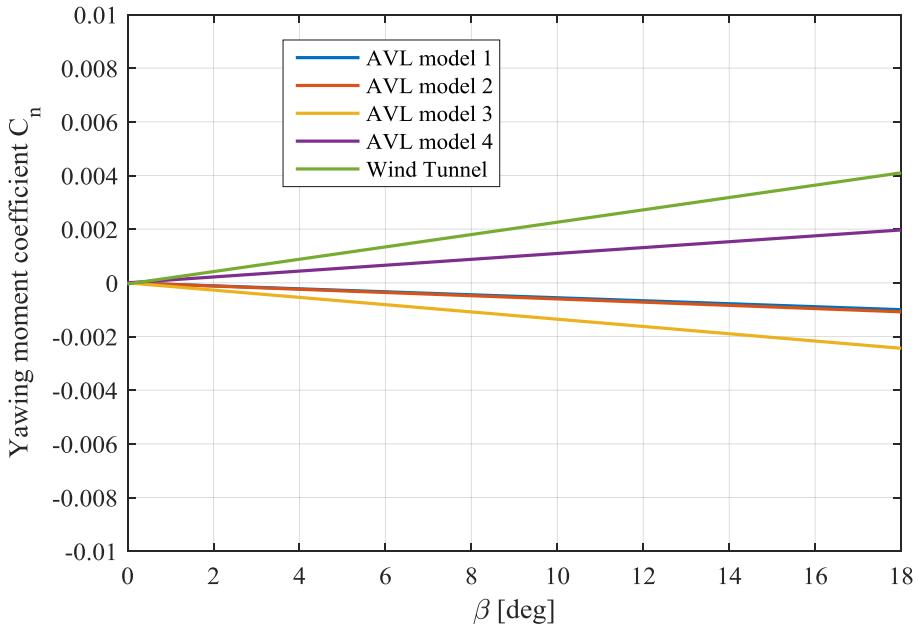

Figure 2.29: Yawing moment coefficient comparison between wind tunnel and AVL data

Figure 2.29 shows that AVL Model 4 was the only model that produced a positive yawing moment coefficient slope, which corresponded with the positive slope obtained from the wind tunnel. The model that therefore provided the best correlation with the wind tunnel test results was the fourth vortex lattice model, where the aircraft was modelled without a fuselage. Despite the expected differences related to the use of a vortex lattice program, the agreement between the AVL and the wind tunnel results was considered sufficiently accurate to justify the use of the damping derivatives (that were not obtained in the wind tunnel) in the simulation. The static derivatives obtained from AVL are given in Appendix A: Static derivatives, and the dynamic derivatives are given in

Appendix B: Dynamic derivatives.

2.6.2 Power model

The Roadrunner UAV used for demonstration purposes in this project was powered by an electric motor and a pusher propeller, as illustrated in Figure 1.6. The propulsion force and propeller torque were calculated using a custom model of a brushless motor, combined with measured propeller coefficient tables. The propeller manufacturer published data tables that could be used directly for this analysis. A function was written in MATLAB® to calculate the thrust, revolutions per minute (RPM) and torque, as required by the 6DOF simulation. The methodology described in [44] was used to calculate the thrust and torque of the motor/propeller combination. The function that was written to calculate the thrust, RPM and torque made use of an iterative solution method. The initial RPM was used as a starting value to calculate the advance ratio (J) given in Equation (2.39) below, where V_T is the true airspeed, and n is the rotational speed multiplied by the propeller diameter, D.

$$J = \frac{V_T}{nD} \tag{2.39}$$

The advance ratio was used to calculate the thrust and power coefficients of the propeller, which, in turn, were used to calculate the thrust and torque of the motor. The equation that was used to calculate the torque is given in Equation (2.40) below; the power is represented by P in the equation.

$$Q = \frac{P}{2n\pi} \tag{2.40}$$

The thrust was obtained using Equation (2.41) below, where C_T is the propeller thrust coefficient, ρ is the density, n is the rotational speed and D the propeller diameter.

$$T = C_T \rho n^2 D^4 \tag{2.41}$$

The motor RPM was obtained using the calculated RPM subtracted from the initial guessed RPM in an iterative process until the error was reduced to an acceptable value. The RPM was calculated using Equation (2.42) below.

$$n = \frac{K_v(V - IR_m)}{60} \tag{2.42}$$

In Equation (2.42) above, K_v is the RPM per volt, I is the torque current and R_m is the motor resistance. The torque current was calculated using Equation (2.43) below.

$$I = \frac{Q}{K_q} + I_0 \tag{2.43}$$

In Equation (2.43) above, I_0 is the no-load current and Kq is the torque constant, calculated using Equation (2.44) below.

$$K_q = \frac{30}{\pi K_v} \tag{2.44}$$

2.6.3 Mass and inertia model

The angular momentum vector (represented by **h**) of the propeller causes gyroscopic effects that were also modelled using Equation (2.45) below [33].

$$\mathbf{h} = \boldsymbol{I\omega} \tag{2.45}$$

The matrix **I** is referred to as the 'inertia matrix of the rigid body'. An expansion of the first term in the equation above is given below:

$$\mathbf{h} = \begin{bmatrix} I_{xx} & -I_{xy} & -I_{xz} \\ -I_{xy} & I_{yy} & -I_{yz} \\ -I_{xz} & -I_{yz} & I_{zz} \end{bmatrix} \begin{bmatrix} p \\ q \\ r \end{bmatrix} \equiv \boldsymbol{I\omega} \tag{2.46}$$

The aircraft mass moment of inertia was calculated by the aircraft manufacturer using CFD.

2.7 Atmospheric model

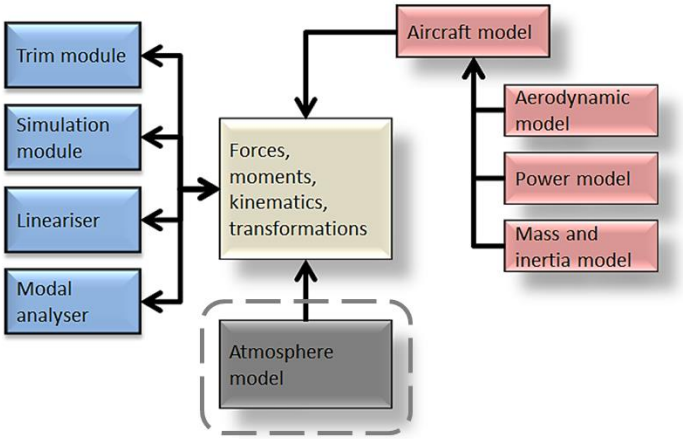

Figure 2.30: Custom 6DOF atmospheric model

The atmospheric model that was available in the MATLAB® simulation is based on the international standard atmospheric (ISA) model, 1976 Standard Atmosphere. The ISA model, as implemented in the MATLAB® simulation, required the following inputs:

- The geometric altitude
- The temperature offset used for non-ISA conditions
- Altitude inputs (the function has the facility to take these in metres or feet)

The following outputs can be obtained after providing the model with the required inputs listed above:

- Temperature in Kelvin
- Pressure in Pascal
- Density in kilogram per cubic meter
- Local speed of sound in Mach

- Kinematic viscosity in metre squared per second

Although the atmospheric module was capable of many functions that are usually used in more complex simulations – such as conversions between true, equivalent and calibrated airspeed – its main role in the context of the current research was to provide realistic air density values for the calculation of dynamic pressure, which, in turn, is used to convert coefficients into dimensional forces and moments.

2.8 Validation of aircraft models

2.8.1 Introduction

The aircraft models in this project were only verified qualitatively. The verification process, for example, helped to ensure that the directions or signs of inputs and responses were correct. Further verification checks consisted of comparing the stability results with qualitative pilot comments. The verification was limited, and further verification should be conducted in future in parallel with flight testing. The quantitative flight test data should, in turn, be used to update the simulation.

2.8.2 Simulation models

Up to this point, this chapter has introduced the fundamentals needed for flight dynamics modelling. The emphasis was placed on the MATLAB® simulation environment. A second aircraft model was developed in an existing flight dynamics-modelling program called JSBSim to conduct a pilot in the loop simulations of the resulting design [45]. One of the limitations of the locally developed MATLAB® simulation is the fact that it does not allow for real-time, man-in-the-loop qualitative evaluations of the final design, and therefore it was necessary to simulate the final design in JSBSim, which allows for real-time evaluations.

JSBSim is an open-source, platform-independent flight dynamics modelling program. It is supplied with input files in XML format that contain descriptions of the aerodynamics of the vehicle, controls, systems, propulsion and scripts for preprogrammed manoeuvres or tests. It was possible to utilise JSBSim along with FlightGear for piloted simulation and as independent verification of the design obtained in the MATLAB® simulation environment.

Flight-dynamic characteristics are most often stored in tables, and therefore JSBSim was designed in such a way to make it possible to use data tables instead of equations. It is possible to insert if-statements and various arbitrary algebraic equations, but this complicates the modelling process to a great extent. The wind tunnel tests, however, were conducted using MDOE techniques, which provide the various aerodynamic forces and moments in the form of coefficients of polynomial expressions, as discussed in section 2.6.1. The design space in which the forces and moments were characterised consisted of three angle-of-attack regions, as mentioned in section 2.6.1.

The MATLAB® model was therefore used to generate the lookup tables for all six the aerodynamic coefficients. The aerodynamic coefficients obtained from the wind tunnel were all a function of 10 factors respectively, *i.e.* angle of attack, angle of sideslip, and the deflections of the eight individual control surfaces, as mentioned in section 2.6.1. Note that

the Reynolds number and Mach number effects were not considered. The process of generating these tables was fairly complicated. Each aerodynamic coefficient was characterised by nine tables respectively, *i.e.* a nonlinear base table that is a lookup table against angle of attack and sideslip angle. The contribution of each control surface was then added. The control surface contributions were also tabulated in nonlinear tables against angle of attack and sideslip angle.

2.8.3 Static stability

Actual flight tests of a prototype airframe used for the current research confirmed that the aircraft was statically stable, with the centre of gravity (CG) in the nominal position. The slope of the pitching moment curve could therefore be used as a first-order check that the simulation model was stable, just as the actual UAV. A quantitative static stability check was therefore conducted by plotting the pitching moment coefficient as a function of angle of attack, as illustrated in Figure 2.31. It can be seen in Figure 2.31 that the slope of this coefficient was negative, as expected.

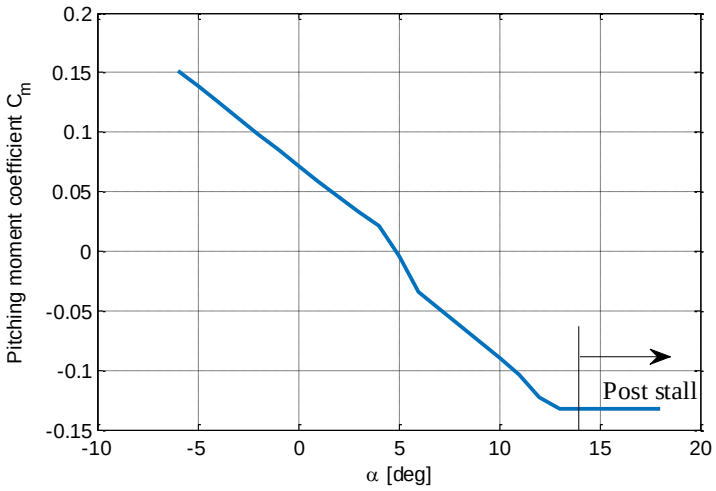

Figure 2.31: Variation of pitching moment coefficient with angle of attack

The post-stall data obtained from the wind tunnel tests was limited, which resulted in less realistic simulations in that region. Insufficient data was available to realistically simulate the post-stall behaviour of the aircraft, and therefore the post-stall behaviour seemed to be unchanged for an increase in angle of attack.

2.8.4 Dynamic stability

Rudder and pitch doublet verification scripts were performed for the JSBSim model. The results of these excitations were compared to the results obtained from the locally developed 6DOF MATLAB® model. The results for the two cases are illustrated and discussed below. The pitch doublet excitation results are given in Figure 2.32. The response obtained from the comparison was regarded as satisfactory. The rudder doublet excitation results for a yaw input command (r_y) are given in Figure 2.33. The trim offset observed in the rudder command in Figure 2.33 is a result of the different methods that MATLAB® and JSBSim implement to calculate the trim state of the aircraft. JSBSim adjusts the roll angle (φ) to obtain the trim

state, while MATLAB® adjusts the sideslip angle (β). The dynamic response of the aircraft is, however, very similar, despite the small offset in trim position and therefore initial conditions.

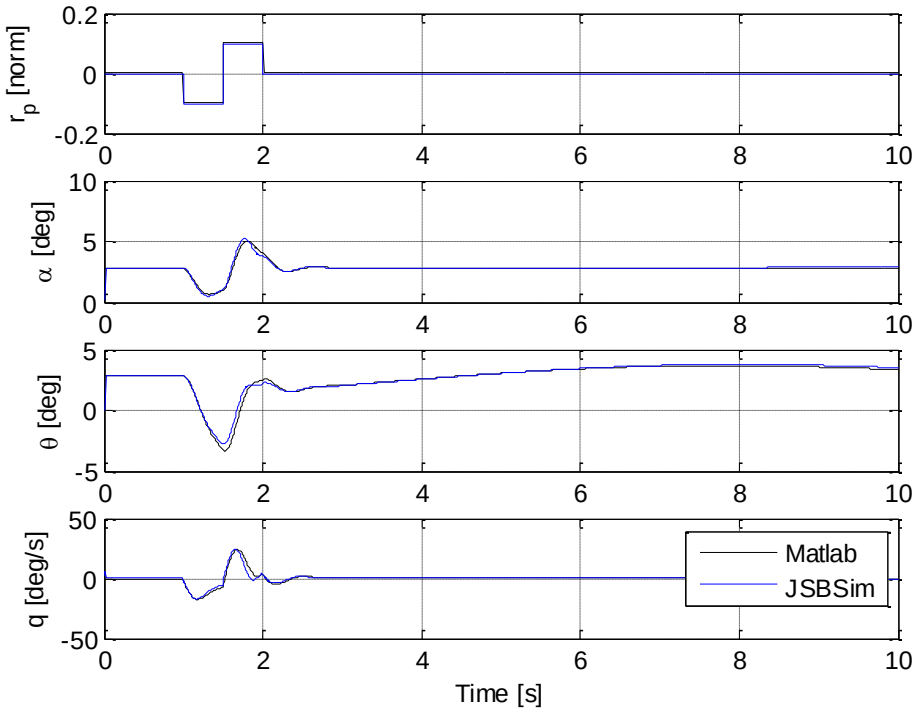

Figure 2.32: Pitch doublet comparison between MATLAB® and JSBSim models

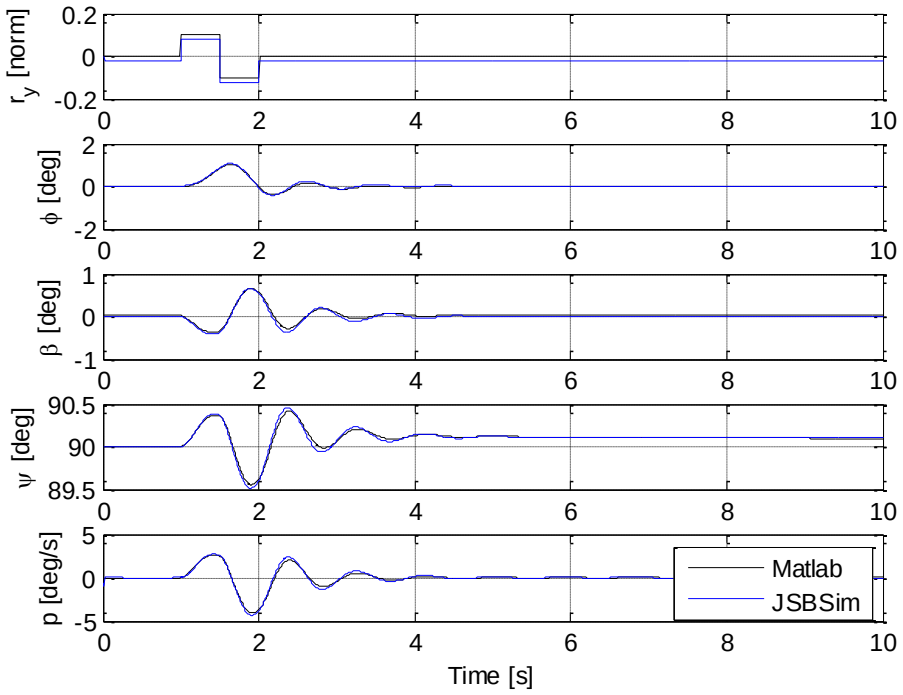

Figure 2.33: Rudder doublet comparison between MATLAB® and JSBSim models

2.8.5 Stall

The post-stall data obtained from the wind tunnel tests was limited, which resulted in less realistic simulations in that region. Because of the insufficient amount of data available to realistically simulate the post-stall behaviour of the aircraft, its post-stall behaviour seemed to be unchanged for an increase in angle of attack.

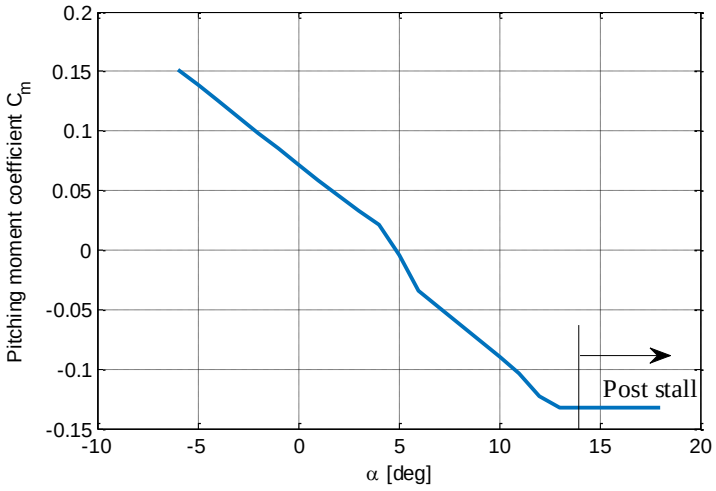

Figure 2.34: Post-stall behaviour

2.8.6 Summary

The aircraft responses in the pitch and lateral-directional axes were evaluated by comparing the aircraft response to doublets, which provided a cross-check and, in particular, allowed a real-time, man-in-the-loop qualitative evaluation of the final design. A slope of the pitching

moment coefficient was evaluated as a function of angle of attack. The slope was negative, and therefore the aircraft was statically stable. A rudder and a pitch doublet were simulated to evaluate the dynamic stability of the aircraft. The results showed that the JSBSim and MATLAB® results correlated very well, which was expected, since the JSBSim aerodynamic model was created using MATLAB®. The post-stall behaviour of the aircraft was not very realistic, but this was due to a lack of data at very high post-stall angles of attack.

3. Optimisation principles

3.1 Introduction

This chapter introduces some of the fundamentals of optimisation used during the control system design of this project. Optimisation is defined as a "process to maximise or minimise a user-specified objective" [46]. Optimisation methods are usually iterative, where the solution process is started by selecting a trial design or a set of trial designs [46]. The trial designs are analysed and evaluated, and a new trial design is generated. This iterative process is continued until an optimum solution is reached. The first step in the process is to formulate an optimum design problem, which involves translating a descriptive statement of the physical requirement into a well-defined mathematical statement. The concepts behind a well-defined mathematical optimisation statement are defined in this chapter.

3.2 Design variables

The next step in the formulation process is to identify the unknown design variables that need to be optimised. These are assembled into a design vector. The design variables are sometimes also referred to as 'optimisation variables'. They should be independent of each other to avoid constraints between them. The design degrees of freedom are equal to the number of independent design variables. A minimum number of design variables required to properly formulate a design optimisation problem must exist [46].

3.3 Objectives

The second-last step in the formulation process is to identify a criterion that associates a number with each design. The objective function must be a function of the design variable vector and it must be a scalar function of which the numerical value can be determined once a design has been specified.

3.3.1 Basic concepts

The criterion mentioned in the previous section can consist of optimising one or more objectives that are functions of some real or integer variables. A single-objective function involves optimising one objective that is expressed in the form of a function, whereas a multiple-objective function involves optimising two or more objectives simultaneously. Single-objective function optimisation is time-consuming when the design requires more than one objective to be optimised. Equation (3.1) illustrates the case where one objective function is optimised as a function of an n-vector **(x)** of design variables.

$$f(\boldsymbol{x}) = f(x_1, x_2, \dots, x_n) \tag{3.1}$$

This project dealt with both cases – a single-objective function, as illustrated in Equation (3.1), and a multiple-objective function case, which is discussed in the next section.

3.3.2 Multiple objectives

The multiple-objective optimisation problem formulation is explained and mathematically articulated in this section. There are many practical applications where the designer may want to optimise two or more objective functions simultaneously, such as in this specific project.

The general design optimisation model for multiple-objective optimisation problems are formulated in Equation (3.2).

$$\boldsymbol{f}(\boldsymbol{x}) = (f_1(\boldsymbol{x}), f_2(\boldsymbol{x}), \dots, f_k(\boldsymbol{x}) \tag{3.2}$$

In Equation (3.2), k is defined as the number of objective functions and x as the design variable vector mentioned in the previous section. The most common approach to multiple-objective optimisation, and the approach followed in this project, is the weighted-sum method, which scales the objective functions, also known as 'scalarised multiple-objective functions', illustrated in Equation (3.3) [46].

$$\boldsymbol{f}(\boldsymbol{x}) = \sum_{i=1}^{k} w_i f_i(\boldsymbol{x}) \tag{3.3}$$

The weights (w_i) are a reflection of the importance of the objectives. The weights for normalised objective functions preferably need to add up to 1, as illustrated in Equation (3.4), whereas the weights for a non-normalised objective function can be random.

$$\sum_{i=1}^{k} w_i = 1 \tag{3.4}$$

Optimising a single-objective function requires identifying a local maximum or minimum that is also the global optimum. The following definitions apply:

- Global optimum: the absolute minimum at the solution if the value of the function at the solution is less than or equal to the value of the function at any other point in the feasible set.
- Local minimum: a relative minimum at the solution if the value of the function is a minimum in a small vicinity of the solution in the feasible set.

3.4 Constraints

Optimisation problems are mainly categorised under constrained or unconstrained problems; all the restrictions placed on the design are collectively called 'constraints'. The final step in the formulation process is therefore to identify all the constraints placed on the design. Design problems may have equality and inequality constraints, which will be discussed in the next two subsections.

3.4.1 Equality constraints

An equality constraint, defined by h(x), is a constraint that needs to be equal to a specific value, Δ, determined by the design.

$$\boldsymbol{h}(\boldsymbol{x}) = \Delta \tag{3.5}$$

The preferred equality constraints form is illustrated in Equation (3.6), where p is the number of equality constraints. It is possible to rewrite any equality constraint into this form.

$$h_i(\boldsymbol{x}) = 0;\ \mathrm{i} = 1 \text{ to } \mathrm{p} \tag{3.6}$$

3.4.2 Inequality constraints

An inequality constraint, defined by g(x) in Equation (3.7), is a constraint that needs to be more or less than a certain value, where m is the number of inequality constraints.

$$g_j(\boldsymbol{x}) \leq \Delta; \mathrm{j} = 1 \text{ to } \mathrm{m} \tag{3.7}$$

Once again, it is possible to rewrite all inequality constraints into the standard form given in Equation (3.8) below.

$$g_j(\boldsymbol{x}) \leq 0; \mathrm{j} = 1 \text{ to } \mathrm{m} \tag{3.8}$$

3.5 Normalisation

In scalarised multiple-objective optimisation, multiple objectives are placed into one objective function where they are related by weightings, as mentioned in section 3.3.2. In numerical calculations, it is desirable to normalise the objectives in the objective function when these objectives have different units. It would be difficult to determine the magnitude of the weights assigned to each objective function term if the objective function was not normalised and the terms in the function had different units. A number of normalisation approaches are available. The method chosen in this work was to normalise the objectives with respect to their limit values. This made comparison between the different objectives meaningful. The limit values here refer to the maximum value obtainable by the objectives respectively. The normalised mathematical expression is given in Equation (3.9), where $f_i(x)$ represents the objective function to be optimised and f_i^{max} the maximum/limit value that the objective function is able to reach.

$$f_i(x)_{norm} = \frac{f_i(x)}{f_i^{max}} \tag{3.9}$$

Normalisation results in a well-conditioned system that avoids numerical instability and ensures that each objective in the function is in the same order of magnitude.

3.6 Optimisation algorithms

3.6.1 Basic concepts

Various aspects have to be considered when choosing an optimisation algorithm. The nature of the objective function and constraints has an influence on the type of optimisation algorithm; the main requirements that should be taken into account are listed below:

- Is the problem constrained or unconstrained?
- Are the objective function and constraints linear or nonlinear?
- Are the objective function and constraints continuous and differentiable?

The secondary requirements that assist the designer in the choice of optimisation algorithms are as follows:

- Robustness
- Efficiency
- Generality
- Ease of use

This section provides a brief description of the sequential quadratic programming (SQP) and leapfrog (lfopcv3) optimisation algorithms that were utilised in this project. The methods were implemented in MATLAB® prior to commencement of the project described in this thesis, and were therefore selected for this work due to their availability. Other constrained, nonlinear gradient-based methods may also be suitable.

3.6.2 Sequential quadratic programming

An SQP optimisation algorithm was considered because of its efficiency as a general optimiser for constrained optimisation problems. In general, the SQP algorithm was preferred, due to its speed and efficiency [46]. The aim of the study was not to investigate potential optimisation algorithms, and therefore only a brief discussion of the basic concepts and steps associated with SQP methods is provided. SQP basically implements an iterative concept in component form [46].

$$x_i{}^{k+1} = x_i{}^{k} + \Delta x_i{}^{k}; k = 0,1,2 \ldots; i = 1{:}n \tag{3.10}$$

The superscript k in Equation (3.10) represents the iteration or design cycle number, and the change in design $\Delta \boldsymbol{x}^k$ is decomposed in Equation (3.11), where α_k is a step size in the search direction $\boldsymbol{d}^k$.

$$\Delta \boldsymbol{x}^k = \alpha_k \boldsymbol{d}^k \tag{3.11}$$

The optimisation algorithm follows two steps iteratively to obtain an optimum value. The first step consists of calculating a search direction in the design space by utilising the values and gradients of the problem function; a quadratic programming subproblem is then defined and solved. The second step involves calculating a step size along the search direction to minimise a descent function; a step size calculation subproblem is then defined and solved.

The line search method that was implemented included bracketing and used Brent's method, although the golden line search method was also available [46].

3.6.3 Leapfrog optimisation algorithm

An alternative leapfrog type of optimisation algorithm was also used in selected cases. The custom leapfrog method was used as a slower, but slightly more robust alternative to the SQP algorithm that was also available. The leapfrog method only required the gradient vector ∇F(x) to be explicitly known. The difference between the leapfrog and other gradient methods is that it approaches the problem by considering the analogous physical problem of the motion of a particle of unit mass in an n-dimensional conservative force field, where the

potential energy of the particle is represented by the function $F(x)$. The motion of the particle is simulated by monitoring its kinetic energy and adopting an interfering strategy, ensuring that the potential energy is systematically reduced. The particle is forced to follow a trajectory towards a local minimum in potential energy following the way discussed above [47].

The leapfrog method consisted of implementing the improved version (see [48]) of the one described above in MATLAB®. Further modifications that were made to the leapfrog method found in [48] consisted of the following:

- Implementing ‘single file’ user functions
- Adding changes to make diagnostics easier
- Adding variable scaling

This is a completely general implementation where the objective function and constraints may be linear or nonlinear. The algorithm solves linear programming, quadratic programming or nonlinear programming problems.

3.6.4 SQP and leapfrog comparison

Both these methods were tested using existing functions with known optimum values. The verification process consisted of providing both algorithms with starting values inside and outside the feasible range, and both these algorithms converged to the local optimum values without fail. Both methods proved to be robust and reliable, although the particular implementation of the SQP algorithm had difficulty dealing with very large numbers of constraints.

4. Methodology

The previous chapters provided some of the fundamental principles required to implement the solution methodology introduced in this chapter. Some of the general aspects of flight dynamics and optimisation were discussed. However, this chapter integrates the theory to create a design methodology that can be applied to various configurations. The Roadrunner platform will be used to demonstrate the technique.

4.1 Requirements

As described in section 1.4, the rhomboid UAV chosen for this project is equipped with eight multifunctional control surfaces. The difficulty arises when trying to allocate these control surfaces to act as elevators, ailerons and rudders in the most optimal way. The challenge often arises when trying to allocate controls to obtain the best aircraft response when dealing with aircraft with an unconventional layout of control surfaces.

One of the requirements was to design an open-loop control allocation program that is as general as possible, so that it can be applied to various types of aircraft with minimal alterations. A further requirement involved designing a control allocation system that would allow a pilot to fly the aircraft giving conventional inputs, which are then allocated to an unconventional control surface configuration that would respond optimally. Still another requirement that was considered was designing a control allocation program that would enable the pilot to manually recover the UAV during flight testing, should a failure, such as a sensor or an actuator failure, occur. The control allocation program, also referred to as the 'mixing function', is developed in this chapter, with the aim of meeting the requirements mentioned above. The mixing function design that was chosen to perform the control allocation is discussed in section 4.2, followed by a description of the way in which the solution strategy was implemented to obtain the necessary terms required by the mixing function.

4.2 Mixing function

As mentioned above, the aim was to develop a control allocation program that would optimally allocate controls to provide the desired aircraft response throughout the flight envelope. The mixing function transforms the conventional roll, pitch and yaw commands into the required physical deflections of each of the eight control surfaces. The input command vector $[r_p, r_r, r_y]'$ represents the pitch, roll and yaw input commands. These commands were normalised to the range -1 to 1. For example, a roll input $r_r = -1$ represented a full left-roll command, while $r_r = 1$ represented a full right-roll command. A nose-up pitch command is represented by $r_p = 1$, and nose-down by $r_p = -1$. A nose-left-yaw command is represented by $r_y = -1$, and a nose-right–yaw command by $r_y = 1$. The control convention illustrating the pitch command explanation is given in Figure 4.1.

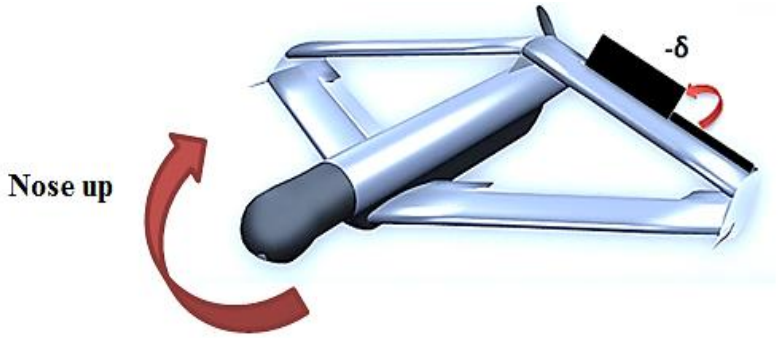

Figure 4.1: Actuator deflection for a nose-up pitching command

The simplest linear control allocation function would take on the mathematical form stated in Equation (4.1).

$$[\boldsymbol{\delta}] = [\boldsymbol{B}] \begin{bmatrix} r_p \\ r_r \\ r_y \end{bmatrix} \tag{4.1}$$

The control allocation function in Equation (4.1) transforms the input commands (r_p, r_r and r_y) into physical control surface deflections through a gain matrix, B. The control allocation function described in Equation (4.1) does not allow for differential control, which is needed on conventional aircraft for aileron control, and desired on aircraft with an unconventional control setup to allow for control surfaces to fulfil the role of ailerons.

A few control allocation requirements were considered when designing the mixing function. The aim was to design a mixing function with the following capabilities:

- Add a bias term for the control surface trim states
- Allow for differential control surface deflections between the left and right sides of the aircraft

With regard to the first requirement mentioned above, the objective was to map the zero input case (no pitch, roll or yaw command) to a nominal trimmed aircraft state. Since the mixing function determines the physical control surface deflections (δ), it needs to have a constant vector, which will be referred to as the 'trim bias vector'. The trim bias vector for the Roadrunner would therefore contain the eight control surface (see Figure 4.2) deflection angles that would initialise the aircraft in a trimmed state.

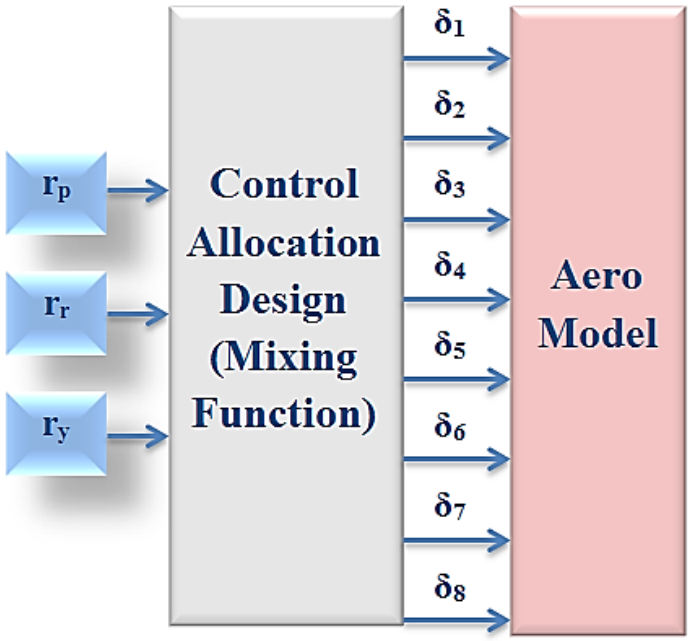

Figure 4.2: Mapping of conventional input commands to control surface deflections

The control allocation function illustrated in Equation (4.1) can be modified to include the trim bias vector, as illustrated in Equation (4.2).

$$[\boldsymbol{\delta}] = [\boldsymbol{B}]\begin{bmatrix} r_p \\ r_r \\ r_y \end{bmatrix} + [\boldsymbol{T}] \tag{4.2}$$

In the case of the second requirement, the objective was to design the mixing function with the capability of allowing differential control. Differential control implies that the control deflections may be asymmetric in the aircraft plane, *e.g.* more up on the left than down on the right, and vice versa, as illustrated in Figure 4.3.

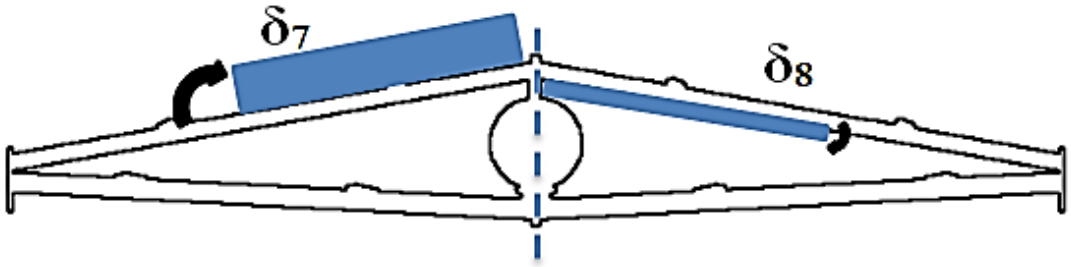

Figure 4.3: Differential control illustration

The mixing function expressed in Equation (4.2) does not allow for differential control, since the input-output relationship is linear. In order to allow for the possibility of differential control, a quadratic term had to be added through a gain matrix, A.

$$[\boldsymbol{\delta}] = [\boldsymbol{A}]\begin{bmatrix} {r_p}^2 \\ {r_r}^2 \\ {r_y}^2 \end{bmatrix} + [\boldsymbol{B}]\begin{bmatrix} r_p \\ r_r \\ r_y \end{bmatrix} + [\boldsymbol{T}] \tag{4.3}$$

The mixing function therefore consisted of three terms: quadratic, linear and constant. The quadratic and linear terms allowed for differential control. The solution strategy to determine the trim bias vector and matrices A and B will be discussed in the next section.

4.3 Solution strategy

As mentioned in the previous section, the first objective was to initialise the aircraft in a trimmed condition. Since the input commands are all zero for the trimmed case, the bias vector can be solved independently. The process could therefore be divided into two phases: Phase 1 was dedicated to obtaining the trim vector and Phase 2 to obtaining the A and B matrices to allocate the controls for manoeuvring and steady states other than the nominal trim condition.

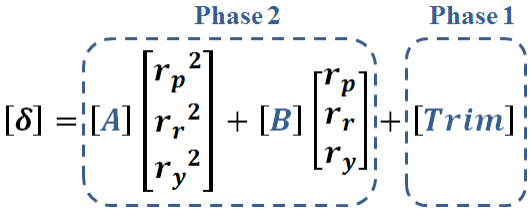

Figure 4.4: Mixing function process breakdown

The complex and often conflicting mixing requirements necessitated the use of constrained mathematical optimisation for both design phases. Note that there are various ways in which a solution can be obtained, although it would be more efficient to make use of optimisation, since it provides the best possible solution, while satisfying the stated requirements. The optimisation techniques for the respective phases are discussed in the next two sections.

4.4 Solution of trim variables

Phase 1 consisted of determining the trim bias vector for a specific steady-state flight condition. The optimisation objective for this phase was to obtain the eight control surface deflections that would trim the aircraft, while the individual deflections would deviate as little as possible from the nominal positions. The optimisation problem is formulated in the subsections that follow.

4.4.1 Design variables

There were 11 unknowns that had to be solved in order to trim the aircraft: the eight control surface positions, throttle position ($\delta_{throttle}$), angle of attack (α) and sideslip angle (β). The 11 unknowns forming the design vector are given in Equation (4.4).

$$\boldsymbol{x} = [\delta_1, \delta_2, \delta_3, \delta_4, \delta_5, \delta_6, \delta_7, \delta_8, \delta_{throttle}, \alpha, \beta] \tag{4.4}$$

4.4.2 Objective function

As described earlier, the aim was to find a trim setting where each individual control surface was as close as possible to neutral. The objective function was therefore defined as the sum of the squares of the control surface positions as shown in Equation (4.5).

$$\boldsymbol{f}(\boldsymbol{x}) = \sum_{\boldsymbol{i=1}}^{\boldsymbol{8}} [\delta_i{}^2] \tag{4.5}$$

4.4.3 Constraints

The final step in the formulation process was to identify all the constraints placed on the design. Design problems may have both equality and inequality constraints, as described in section 3.4. However, the first optimisation phase only required equality constraints. In order to trim the aircraft, the time derivatives of the relative airspeed ($\dot{V}, \dot{\alpha}$ *and* $\dot{\beta}$) and the three body rotational accelerations ($\dot{p}, \dot{q}$ *and* $\dot{r}$) were required to be zero. Therefore, equality constraints could be used.

The problem could be expressed as six equality constraints – roll acceleration ($\dot{p}$), yaw acceleration ($\dot{r}$), pitch acceleration ($\dot{q}$), angle-of-attack acceleration ($\dot{\alpha}$), sideslip-angle acceleration ($\dot{\beta}$) and acceleration of true airspeed (TAS) ($\dot{V}_T$) – which were all required to be zero. The equality constraint vector is mathematically expressed below:

$$\boldsymbol{h}(\boldsymbol{x}) = [\dot{p}, \dot{r}, \dot{q}, \dot{\alpha}, \dot{\beta}, \dot{V}_T] = \boldsymbol{0} \tag{4.6}$$

4.5 Solution of control surface mixing variables

Phase 2 consisted of various optimisation design trials to find the optimal mixing coefficient matrices A and B. The optimisation objective for this phase was to maximise the aircraft response in all three axes. The optimisation problem is formulated in the subsections that follow.

4.5.1 Design variables

The design variables in Phase 2 consisted of the coefficients that make up the mixing matrices A and B. The eight control surfaces and three input commands resulted in an 8 x 3 matrix. The aircraft was geometrically symmetrical, but not always aerodynamically symmetrical, due to the torque effects. One of the simplifications and assumptions involved modelling the aircraft as if it were an aerodynamically symmetrical aircraft to combine the control surfaces. The assumption of symmetry assumes that the inputs for a left command are exactly symmetrical to the inputs for a right command.

The control surfaces were combined to use the same design variables for the left and right corresponding control surface in order to reduce the number of design variables in the optimisation. The optimisation problem therefore comprised 24 design variables in Phase 2. Note that, in the absence of the symmetry assumptions, each control surface would have its own design variable, increasing the number of design variables to 48. Mixing matrix A contained the first 12 design variables, as demonstrated in Equation (4.7), and mixing matrix B contained the remaining 12 design variables, as demonstrated in Equation (4.8). The negative signs in matrix B allowed the control surfaces to deflect to opposite sides for roll and yaw commands.

$$\boldsymbol{A} = \begin{bmatrix} x_1 & x_2 & x_3 \\ x_1 & x_2 & x_3 \\ x_4 & x_5 & x_6 \\ x_4 & x_5 & x_6 \\ x_7 & x_8 & x_9 \\ x_7 & x_8 & x_9 \\ x_{10} & x_{11} & x_{12} \\ x_{10} & x_{11} & x_{12} \end{bmatrix} \tag{4.7}$$

$$\boldsymbol{B} = \begin{bmatrix} x_{13} & x_{14} & x_{15} \\ x_{13} & -x_{14} & -x_{15} \\ x_{16} & x_{17} & x_{18} \\ x_{16} & -x_{17} & -x_{18} \\ x_{19} & x_{20} & x_{21} \\ x_{19} & -x_{20} & -x_{21} \\ x_{22} & x_{23} & x_{24} \\ x_{22} & -x_{23} & -x_{24} \end{bmatrix} \tag{4.8}$$

4.5.2 Objective function

The objective for Phase 2 was to maximise the aircraft response in all three axes (lateral, directional and longitudinal). The objective function was a scalarised multiple-objective optimisation problem because multiple objectives were placed in one objective function where they were related by weightings. In section 3.3.2 it was mentioned that the weights, when using the weighted-sum method, should typically be selected to add up to one. In this thesis however, the approach was modified slightly as indicated in Equation (4.9), as experience with the method showed that it was more intuitive to apply adjustments to the weights in this manner.

$$f(x) = -(2w_1\dot{p}_{(cond1)} + 2w_2\beta_{(cond2)} + w_3\dot{q}1_{(cond3)} - w_4\dot{q}2_{(cond4)}) \tag{4.9}$$

In Equation (4.9), $\dot{p}$ was the roll acceleration corresponding to a maximum roll control input, β represented the steady-state sideslip generated by a maximum yaw control input, $\dot{q}_1$ was the pitch acceleration for a maximum positive pitch input (nose up) and $\dot{q}_2$ for a maximum negative pitch input (nose down). The first condition involved a full roll input command to the simulation to obtain the maximum achievable roll acceleration, while the pitch and yaw commands remained zero (r_r = 1, r_p = 0, r_y = 0). The second condition involved finding the steady-state sideslip condition using a solver implemented in the trim module of the simulation with a full yaw command (r_r = 0, r_p = 0, r_y = 1) in order to obtain the maximum sideslip achievable by the aircraft, while the pitch and roll input commands remained zero. The third condition involved a full positive pitch command to obtain the maximum achievable pitch acceleration, while the roll and yaw input commands remained zero (r_r = 0, r_p = 1, r_y = 0). The fourth condition involved a full negative pitch command to obtain the maximum achievable negative (or nose-down) pitch acceleration, while the roll and yaw input commands remained zero (r_r = 0, r_p = -1, r_y = 0).

The factor 2 for the roll and yaw cases was used, so that the left and right cases could be considered simultaneously, as their responses were symmetrical, except for the small difference made by the torque of the propeller. The responses obtained for a nose-up pitch command and a nose-down pitch command had different requirements and was therefore separated. The importance of the objectives is reflected by the weights (w) in Equation (4.9) and the negative sign outside the brackets before the objective function was used to convert the maximisation problem into a minimisation problem, as expected by the optimisation program.

4.5.3 Equality constraints

The equality constraints were imposed on the second phase, with the goal to decouple the initial responses. Responses to be reduced included secondary effects such as adverse yaw and control coupling. The equality constraints consisted of two parts. The purpose of the first part was to minimise the pitch and sideslip coupling due to a roll command. The maximum pitch rate and sideslip for a roll command was observed at 0.5 seconds. The simulation was run for 0.5 seconds, after which the equality constraints were imposed to minimise the secondary responses that occurred at that time step. The first equality constraint in Equation (4.10) constrained the initial pitch rate, which occurred at 0.5 seconds after the initial input. The second equality constraint expressed in Equation (4.11) constrained the sideslip response to a maximum roll command 0.5 seconds after the input was given, thereby minimising the adverse yaw. Although these equality constraints usually minimise the initial response that may result from roll inputs, it cannot control the longer-term response that may result without the use of a feedback control system.

$$h(1)_{(r_r = 1)} = q \tag{4.10}$$

$$h(2)_{(r_r = 1)} = \beta \tag{4.11}$$

The purpose of the second part was to minimise the pitch and roll coupling for a maximum yaw command. The third equality constraint given in Equation (4.12) constrained the initial pitch response to a maximum yaw input. The fourth equality constraint given in Equation (4.13) constrained the initial roll response for a maximum yaw input; the simulation was called and allowed to run for 0.5 seconds, after which the fourth equality constraint was applied.

$$h(3)_{(r_y = 1)} = q \tag{4.12}$$

$$h(4)_{(r_y = 1)} = p \tag{4.13}$$

4.5.4 Inequality constraints

The control surface deflections were constrained by considering all the possible command combinations that could be given to this UAV. If the control surface deflections were restricted for every possible input command, it would over-constrain the optimisation problem, which would result in reduced aircraft performance. The realistic input command combinations that were applicable or that would be encountered during the application of the

aircraft were considered and mathematically expressed as inequality constraints. The possible input combinations that were considered are discussed below.

Before the control surface constraints could be defined, all the control input combinations had to be closely examined. The aim was to eliminate all the unnecessary constraints in order to prevent an artificial reduction of the design space, and to identify the input commands that could possibly be encountered when flying the Roadrunner.

Note that the possible input commands may be unique to the aircraft and are a function of the type of mission for which it would be used. This approach can be used as a tool to determine the realistic command combinations for any type of aircraft application once the design requirements are known. Being a high-speed UAV, the Roadrunner was designed to operate in a surveillance role. The input commands were thus assessed according to these types of missions. There were 27 combinations of inputs that contained maximum values of one or more of the commands. These had to be considered for the three input commands (pitch, roll and yaw), since only the maximum input is considered for each command. The 27 command combinations are listed in Table 4.1. The first column is simply a number to identify the case, while the second, third and fourth columns contain the possible pitch, roll and yaw control inputs, respectively. The fifth column states whether a particular combination should be considered in the constraint function. The sixth column is a motivation for the decision to include or exclude a particular combination. Each of the 27 combinations was considered, and when it was clear that a particular combination was unlikely to occur within the Roadrunner's typical mission profile, it was removed from the constraint function. Table 4.1 was used to determine the command combinations that might result in control surface saturation, and each combination pair is discussed below.

Table 4.1: Input command combinations

Combinations	r_p	r_r	r_y	Required	Comment
1	-1	0	-1	×	Not a realistic input
2	-1	0	0	✓	Full down pitch
3	-1	0	1	-	Unlikely combination
4	-1	1	-1	×	Not a realistic input
5	-1	1	0	-	Unlikely combination
6	-1	1	1	×	Not a realistic input
7	-1	-1	-1	×	Not a realistic input
8	-1	-1	0	-	Unlikely combination
9	-1	-1	1	×	Not a realistic input
10	0	0	-1	✓	Left-yaw command
11	0	0	0	×	Neutral control
12	0	0	1	✓	Right-yaw command
13	0	1	-1	✓	Roll + yaw

14	0	1	0	✓	Right-roll command
15	0	1	1	✓	Roll + yaw
16	0	-1	-1	✓	Roll + yaw
17	0	-1	0	✓	Left-roll command
18	0	-1	1	✓	Steady-heading sideslip
19	1	0	-1	✓	Positive pitch + yaw
20	1	0	0	✓	Full positive pitch
21	1	0	1	✓	Positive pitch + yaw
22	1	1	-1	×	Not a realistic input
23	1	1	0	✓	Pitch + roll
24	1	1	1	×	Not a realistic input
25	1	-1	-1	×	Not a realistic input
26	1	-1	0	✓	Pitch + roll
27	1	-1	1	×	Not a realistic input

In the first nine lines in Table 4.1, it can be seen that only one realistic command combination was identified. This was line 2: a full nose-down pitch command with no roll or yaw command. The first nine lines all correspond to full nose-down pitch combinations. The Roadrunner was not intended to be an aerobatic UAV and was therefore unlikely to encounter a scenario where a combination of nose-down pitch together with roll or yaw, or both, would be required for either left or right commands. A combination that had to be considered was the full nose-down pitch command in line 2, since these constraints determine the maximum control surface deflections that correspond with maximum inputs. If this constraint was neglected, a full nose-down pitch command could result in some control surfaces deflecting more than the prescribed angles.

With regard to lines 10 to 18 in Table 4.1 on left- and right-roll and yaw command combinations, it is clear that all the combinations were regarded as realistic command combinations. Since the Roadrunner has no vertical control surface, it is hard to determine how much yaw control might be required during roll commands to eliminate the adverse yaw, and therefore the roll and yaw combinations were all included, as it was not impossible that they could be encountered at some time during a given mission. Table 4.1 further indicates that a full pitch-up (line 20) and -down (line 2), a full roll left (line 17) and right (line 14), and a full yaw left (line 10) and right (line 12) were all included in the constraint functions. The neutral control combination in line 11 required no consideration, since Phase 1 of the optimisation already took that scenario into account during the design of the trim bias vector, for which no input commands were given.

The remaining lines in Table 4.1, lines 19 to 27, indicate that a full nose-up pitch (line 20) command needs to be considered in order to ensure a sufficient amount of control authority..

The combinations of full nose-up pitch command and roll, or full nose-up pitch command and yaw, should also be considered, as they may be required when manoeuvring the aircraft at high angles of attack. It was not deemed necessary to consider the combination of pitch up together with roll and yaw command combinations, as these would almost never be encountered for the missions for which this type of UAV was designed, and are normally associated with aerobatic manoeuvres.

Fourteen possible combinations were identified and are indicated with a tick (✓) in Table 4.1, which meant that each control surface would require 14 constraints. The trim variables obtained from Phase 1 were very similar for the control surface pairs illustrated in Figure 2.17. A small offset in left and right variables was observed – this was due to the propeller torque that was also modelled in the simulation, and not due to a geometrical asymmetry. Since the bias values were small, it was possible to reduce the number of constraints by averaging the left and right offsets in the trim vector. Equations (4.14) to (4.17) provide a mathematical expression of the averaging.

$$T_{12} = \frac{1}{2}(T_1 + T_2) \tag{4.14}$$

$$T_{34} = \frac{1}{2}(T_3 + T_4) \tag{4.15}$$

$$T_{56} = \frac{1}{2}(T_5 + T_6) \tag{4.16}$$

$$T_{78} = \frac{1}{2}(T_7 + T_8) \tag{4.17}$$

Figure 4.5 illustrates the left and right control surfaces that were combined to reduce the number of constraints.

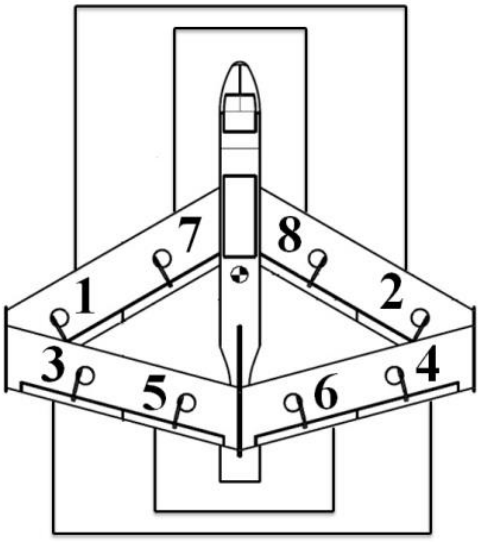

Figure 4.5: Corresponding control surfaces

Averaging the trim values reduced the number of inequality constraints from 112 (14 combinations x 8 control surface pairs) to 56 (14 combinations x 4 control surface pairs). The inequality constraints were obtained by substituting the 14 realistic command combinations into the mixing function in order to obtain the control surface positions in terms of the design variables. The final mixing function is expressed in Equation (4.18) below.

$$\begin{bmatrix}\delta_1\\ \delta_2\\ \delta_3\\ \delta_4\\ \delta_5\\ \delta_6\\ \delta_7\\ \delta_8\end{bmatrix} = \begin{bmatrix} x_1 & x_2 & x_3\\ x_1 & x_2 & x_3\\ x_4 & x_5 & x_6\\ x_4 & x_5 & x_6\\ x_7 & x_8 & x_9\\ x_7 & x_8 & x_9\\ x_{10} & x_{11} & x_{12}\\ x_{10} & x_{11} & x_{12}\end{bmatrix}\begin{bmatrix}{r_p}^2\\ {r_r}^2\\ {r_y}^2\end{bmatrix} + \begin{bmatrix} x_{13} & x_{14} & x_{15}\\ x_{13} & -x_{14} & -x_{15}\\ x_{16} & x_{17} & x_{18}\\ x_{16} & -x_{17} & -x_{18}\\ x_{19} & x_{20} & x_{21}\\ x_{19} & -x_{20} & -x_{21}\\ x_{22} & x_{23} & x_{24}\\ x_{22} & -x_{23} & -x_{24}\end{bmatrix}\begin{bmatrix}r_p\\ r_r\\ r_y\end{bmatrix} + \begin{bmatrix}T_{12}\\ T_{12}\\ T_{34}\\ T_{34}\\ T_{56}\\ T_{56}\\ T_{78}\\ T_{78}\end{bmatrix} \tag{4.18}$$

Due to the large number of inequality constraints, only one example of the process is given below, providing a step-by-step breakdown of how the first inequality constraint for a full nose-down pitch command was obtained. The pitch command ($\mathbf{r}_p$) was replaced by a negative pitch input, and the roll and yaw commands were set to zero, as illustrated in Equation (4.19).

$$\begin{bmatrix}\delta_1\\ \delta_2\\ \delta_3\\ \delta_4\\ \delta_5\\ \delta_6\\ \delta_7\\ \delta_8\end{bmatrix} = \begin{bmatrix} x_1 & x_2 & x_3\\ x_1 & x_2 & x_3\\ x_4 & x_5 & x_6\\ x_4 & x_5 & x_6\\ x_7 & x_8 & x_9\\ x_7 & x_8 & x_9\\ x_{10} & x_{11} & x_{12}\\ x_{10} & x_{11} & x_{12}\end{bmatrix}\begin{bmatrix}(-1)^2\\ 0\\ 0\end{bmatrix} + \begin{bmatrix} x_{13} & x_{14} & x_{15}\\ x_{13} & -x_{14} & -x_{15}\\ x_{16} & x_{17} & x_{18}\\ x_{16} & -x_{17} & -x_{18}\\ x_{19} & x_{20} & x_{21}\\ x_{19} & -x_{20} & -x_{21}\\ x_{22} & x_{23} & x_{24}\\ x_{22} & -x_{23} & -x_{24}\end{bmatrix}\begin{bmatrix}-1\\ 0\\ 0\end{bmatrix} + \begin{bmatrix}T_{12}\\ T_{12}\\ T_{34}\\ T_{34}\\ T_{56}\\ T_{56}\\ T_{78}\\ T_{78}\end{bmatrix} \tag{4.19}$$

After performing a matrix multiplication, the control surface deflections could be represented by the mathematical expression given in Equation (4.20).

$$\begin{bmatrix}\delta_1\\ \delta_2\\ \delta_3\\ \delta_4\\ \delta_5\\ \delta_6\\ \delta_7\\ \delta_8\end{bmatrix} = \begin{bmatrix} x_1 & 0 & 0\\ x_1 & 0 & 0\\ x_4 & 0 & 0\\ x_4 & 0 & 0\\ x_7 & 0 & 0\\ x_7 & 0 & 0\\ x_{10} & 0 & 0\\ x_{10} & 0 & 0\end{bmatrix} + \begin{bmatrix} -x_{13} & 0 & 0\\ -x_{13} & 0 & 0\\ -x_{16} & 0 & 0\\ -x_{16} & 0 & 0\\ -x_{19} & 0 & 0\\ -x_{19} & 0 & 0\\ -x_{22} & 0 & 0\\ -x_{22} & 0 & 0\end{bmatrix} + \begin{bmatrix}T_1\\ T_2\\ T_3\\ T_4\\ T_5\\ T_6\\ T_7\\ T_8\end{bmatrix} \tag{4.20}$$

The inequality constraints derived from the realistic command combinations in equations (4.19) and (4.20) were manipulated to take on the standard form, as illustrated in section 3.4.2 (see standard representation in Equations (4.21) to (4.34). The approximate indication of maximum deflection a control surface will experience during a typical flight is given by the term *k* in the equation below; this is typically 30° for the Roadrunner. Note that it is theoretically possible to use a different limit for each control surface. The inequality constraint terms were squared to remove the necessity of considering the positive and

negative deflections as separate constraints. The inequality constraint pair for control surfaces 1 and 2 is expressed in equations (4.21) to (4.34).

$$g_1 = (x_3 - x_{15} + T_{12})^2 - k^2 \quad (4.21)$$

$$g_2 = (x_3 + x_{15} + T_{12})^2 - k^2 \quad (4.22)$$

$$g_3 = (x_2 + x_3 + x_{14} - x_{15} + T_{12})^2 - k^2 \quad (4.23)$$

$$g_4 = (x_2 + x_3 + x_{14} + x_{15} + T_{12})^2 - k^2 \quad (4.24)$$

$$g_5 = (x_2 + x_{14} + T_{12})^2 - k^2 \quad (4.25)$$

$$g_6 = (x_2 - x_{14} + T_{12})^2 - k^2 \quad (4.26)$$

$$g_7 = (x_2 + x_3 - x_{14} - x_{15} + T_{12})^2 - k^2 \quad (4.27)$$

$$g_8 = (x_2 + x_3 - x_{14} + x_{15} + T_{12})^2 - k^2 \quad (4.28)$$

$$g_9 = (x_1 + x_3 + x_{13} - x_{15} + T_{12})^2 - k^2 \quad (4.29)$$

$$g_{10} = (x_1 + x_3 + x_{13} + x_{15} + T_{12})^2 - k^2 \quad (4.30)$$

$$g_{11} = (x_1 + x_{13} + T_{12})^2 - k^2 \quad (4.31)$$

$$g_{12} = (x_1 - x_{13} + T_{12})^2 - k^2 \quad (4.32)$$

$$g_{13} = (x_1 + x_2 + x_{13} + x_{14} + T_{12})^2 - k^2 \quad (4.33)$$

$$g_{14} = (x_1 + x_2 + x_{13} - x_{14} + T_{12})^2 - k^2 \quad (4.34)$$

The remaining three pairs of constraints are given in Appendix D: Inequality constraints.

4.6 Normalisation

The design variables were internally normalised by the optimisation algorithms used in this project. However, the objective function terms were normalised based on the principles described in section 3.5. The objective function terms had different units, which made it difficult to determine what the optimal weights should be, and therefore normalisation was required. The normalisation process consisted of four optimisation runs, since each term in the objective function had to be normalised. The runs were done to obtain the maximum/limit values to perform normalisation, based on section 3.5.

The first term of the objective function in Equation (4.9) was the roll rate of the aircraft. In order to obtain the maximum roll rate achievable by the aircraft, the weight for this term had to be set to 1, and the weights for the remaining three terms in the equation had to be set to very small values, as illustrated in Table 4.2, Run 1. The second normalisation run consisted of obtaining the maximum sideslip achievable by the aircraft, and therefore the second weight was set to 1, whereas the other three weights were set to very small values. The same method

was followed to obtain the maximum positive and negative pitch rate the aircraft could achieve. The weights accompanying all four the normalisation runs are summarised in Table 4.2. These runs were executed at specific flight conditions. The flight conditions that were chosen for this study involved airspeeds of 20, 30 and 40 m/s respectively.

Table 4.2: Normalisation runs with accompanying weights

Run	Objective	Weights
1	$\dot{p}^{max}$	$w_1 = 1, w_2 = 0.0001, w_3 = 0.0001, w_4 = 0.0001$
2	β^{max}	$w_1 = 0.0001, w_2 = 1, w_3 = 0.0001, w_4 = 0.0001$
3	$(\dot{q}_{pos})^{max}$	$w_1 = 0.0001, w_2 = 0.0001, w_3 = 1, w_4 = 0.0001$
4	$(\dot{q}_{neg})^{max}$	$w_1 = 0.0001, w_2 = 0.0001, w_3 = 0.0001, w_4 = 1$

Once the maximum rates and sideslip values had been obtained through the runs summarised in Table 4.2, the objective function was normalised using these values. The normalised objective function is illustrated in Equation (4.35), and a breakdown of the normalised terms is given in equations (4.36) to (4.39) below.

$$f(x) = -(2w_1 f_1 + 2w_2 f_2 + w_3 f_3 + w_4 f_4) \tag{4.35}$$

$$f_1 = \frac{\dot{p}}{|\dot{p}_{\max}|} \tag{4.36}$$

$$f_2 = -\frac{\beta}{|\beta_{\min}|} \tag{4.37}$$

$$f_3 = \frac{\dot{q}_{pos}}{|\dot{q}_{\max}|} \tag{4.38}$$

$$f_4 = -\frac{\dot{q}_{neg}}{|\dot{q}_{\min}|} \tag{4.39}$$

Constraints may also have different units, similar to those of the objective functions. In that case, the constraint normalisation method in [46] can be implemented. The constraints defined in this project, however, have the same units and did not require normalisation.

4.7 Evaluation of designs

A description of whether the design met the requirements, and how it was determined, is given in the sections below. The evaluation consisted of a numerical and a qualitative testing of the design.

4.7.1 Numerical simulation

In order to perform a numerical evaluation of the control allocation design, the mixing function designed in this chapter was simulated in the 6DOF simulation environment

discussed in section 0. The dynamic response of the aircraft was simulated to determine whether the design complied with the handling qualities set out in [49]. The dynamic response evaluation consisted of simulating a full roll and yaw command and assessing the rates, sideslip angles and accelerations obtained as a result. Full negative and positive pitch commands were simulated to determine the amount of control authority required to execute the command.

Further numerical evaluations consisted of simulating the mixing function over the entire airspeed range to determine if the aircraft could be trimmed at different airspeeds using the same mixing function and how the handling qualities were affected at various airspeeds. The selected aircraft responses were plotted to assess the magnitude of the responses to determine whether rates complied with the handling quality specifications set out in [49].

4.7.2 Qualitative testing

The control allocation function was implemented in JSBSim, as discussed in section 2.8. JSBSim was used in real time as the flight dynamics module for FlightGear, and a pilot was given the opportunity to fly the aircraft using a joystick. The pilot was requested to fly a set-out pattern, create a pitch doublet and yaw doublet, and perform a coordinated turn. In order to evaluate the control allocation design from a man-in-the-loop perspective, the pilot assessed the aircraft's response and behaviour, handling qualities and secondary effects as a result of the inputs.

4.8 Scheduling

4.8.1 Basic concept

UAV control systems are often scheduled; in other words, different gains or control system elements may be used, depending on the flight condition or state of the aircraft. In the context of the current work, scheduling refers to the use of different mixing functions. The control system can be scheduled against the centre of gravity of the aircraft, against airspeed, against altitude or against any other desired variable.

4.8.2 Scheduling against airspeed

In this work, only scheduling against airspeed will be considered, which is the type of scheduling most often used for UAVs. The aircraft response at various airspeeds using the same mixing function was firstly investigated to determine if scheduling would be necessary at all. Following this, different mixing functions were designed for specific airspeeds to compare the aircraft responses. The goal was to determine whether scheduling was necessary or if there was one mixing function that could provide a satisfactory aircraft response over the entire airspeed envelope.

4.9 Robustness of design

The robustness of the mixing function design was tested for actuator failures. The aircraft's response was evaluated by failing an actuator and then performing the same tests as described in section 4.7, which consisted of testing the aircraft's response in the simulation

environment followed by tests conducted in FlightGear. The assumptions that were made regarding the actuator failures were as follows:

- Single actuator failure at a time
- Actuator fail at zero-degree deflection ($\delta = 0°$)

The tests were performed to determine whether the aircraft could be trimmed when an actuator failure occurred. A further assessment consisted of an evaluation of the aircraft's dynamic response and handling qualities to determine whether the aircraft would still be controllable when it experienced a failure, and which actuator failures were more hazardous. Pitch and yaw doublets were used to excite and assess the respective dynamic modes of the aircraft.

5. Results

5.1 Introduction

Chapters 1 to 4 described the modelling, simulation, optimisation and design principles of the control allocation methodology. The previous chapter provided a detailed description of the way in which the control allocation methodology was developed, implemented and tested. Various optimisation runs were conducted before a baseline of results could be obtained at specified flight conditions. The optimisation iterative process, as well as a description of the various runs performed, is given in Appendix E: Optimisation summary. The control allocation design methodology was implemented and evaluated at three flight conditions, resulting in three control configurations, as defined below:

- Configuration 1: mixing function designed at 20 m/s, baseline weighting
- Configuration 2: mixing function designed at 30 m/s, baseline weighting
- Configuration 3: mixing function designed at 40 m/s, baseline weighting

The optimisation results for the three configurations using the baseline weights are given in the section below, followed by the scheduling investigation, robustness study and qualitative testing. The impact of relative objective weighting will be investigated in section 5.8, followed by a summary of the results obtained.

The specifications of the computer system that was used to perform the optimisation runs and the simulations are given in Table 5.1 below.

Table 5.1: System specifications

Windows edition	Windows 7 Enterprise
System	Dell Latitude E6530
Rating	5.9
Processor	Intel® Core™ i7-3740QM CPU @ 2.70 GHz
Installed memory (RAM)	8.00 GB (7.88 GB useable)
System type	64-bit operating system
MATLAB® version	64-bit, 8.3.0.532 (R2014a)

5.2 Control Configuration 1

5.2.1 General

In this configuration, the control allocation design process was conducted for a typical low-speed flight condition for the Roadrunner UAV – in this case a nominal airspeed of 20 m/s. The optimisation results for Phase 1 are given in Table 5.2.

Table 5.2: Configuration 1 optimisation overview for Phase 1

Phase 1	
Convergence time [sec]	8.90
Function evaluations	2501
Iterations	90
Optimisation algorithm	SQP

The convergence time is defined as the amount of time required for the optimisation algorithm to reach an optimum point. The number of function evaluations is defined as the number of times the algorithm directly and indirectly evaluated the objective function during an optimisation run for a specific set of design variable values. This included function evaluations required for calculating gradients using a finite difference scheme. The iterations refer to the number of steps the algorithm took before reaching the minimum. The optimisation results for Phase 2 are given in Table 5.3. The active inequality constraints are discussed in section 5.2.4.

Table 5.3: Configuration 1 optimisation overview for Phase 2

Phase 2	Weight set 1
Convergence time [sec]	51283.6 (14.3 hours)
Function evaluations	52471
Iterations	1097
Number of active inequality constraints	24
Optimisation algorithm	LFOPCV3

The primary aim of Phase 1 was to obtain the control surface deflections at trim and to ensure that these deflections are as close as possible to the neutral position for each control surface. The trim bias vector is given in Equation (5.1).

$$\boldsymbol{T} = \begin{bmatrix} 3.1429 \\ 2.9037 \\ -11.1477 \\ -9.8692 \\ -14.5891 \\ -14.2895 \\ 12.5722 \\ 13.1457 \end{bmatrix} \tag{5.1}$$

The control allocation design process for Configuration 1 was conducted at a relatively low airspeed. Flying a normal aircraft at a trimmed condition at low airspeeds requires a high angle of attack, which necessitates relatively large deflections of the elevators to maintain the altitude of the aircraft. The trim bias vector indicates that control surfaces 1 and 2 (outer control surfaces on the front wing) were close to neutral, whereas the other control surfaces had relatively large deflections. Relatively large control surface deflections were expected since the airspeed was fairly low. The control surfaces were restricted to ±30°. Note that control surfaces 5 and 6 were deflected to almost half of the maximum value. The position of control surfaces 5 and 6, which is on the inner rear wings, can be compared to the position of conventional elevators, which is on the tail of the aircraft close to the fuselage. It can be concluded that control surfaces 5 and 6 were predominantly responsible for pitching the aircraft, and acted like conventional elevators. All the control surfaces on the front wing were deflected downwards, whereas all the control surfaces on the rear wing were deflected upwards to trim the aircraft. The asymmetric terms for the corresponding control surfaces observed in the trim bias vector served to compensate for the propeller gyroscopic effects that were taken into account by the simulation.

5.2.2 Control allocation

The optimal mixing values for the coefficient matrices A and B of Configuration 1 are given in Equation (5.2). The mixing function given in Equation (5.2) was implemented in the simulation environment to evaluate how it performs the control allocation.

$$\begin{bmatrix}\delta_1\\ \delta_2\\ \delta_3\\ \delta_4\\ \delta_5\\ \delta_6\\ \delta_7\\ \delta_8\end{bmatrix} = \begin{bmatrix}-17.4450 & 0.0000 & -4.8899\\ -17.4450 & 0.0000 & -4.8899\\ 12.0124 & 7.9435 & -1.9270\\ 12.0124 & 7.9435 & -1.9270\\ 12.9424 & 2.4510 & 6.4830\\ 12.9424 & 2.4510 & 6.4830\\ -20.7691 & -6.5505 & 6.1539\\ -20.7691 & -6.5505 & 6.1539\end{bmatrix}\begin{bmatrix}r_p{}^2\\ r_r{}^2\\ r_y{}^2\end{bmatrix} + \begin{bmatrix}17.4450 & 0.0000 & -30.0000\\ 17.4450 & 0.0000 & 30.0000\\ -24.0041 & 19.9353 & 10.0647\\ -24.0041 & 19.9353 & -10.0647\\ -30.0000 & 2.4510 & 6.4830\\ -30.0000 & -2.4510 & -6.4830\\ 26.9230 & 12.7044 & 0.0000\\ 26.9230 & -12.7044 & 0.0000\end{bmatrix}\begin{bmatrix}r_p\\ r_r\\ r_y\end{bmatrix} + \begin{bmatrix}3.1429\\ 2.9037\\ -11.1477\\ -9.8692\\ -14.5891\\ -14.2895\\ 12.5722\\ 13.1457\end{bmatrix} \quad (5.2)$$

The control allocation plots for the pitch, roll and yaw command ranges – using the mixing function given in Equation (5.2) – are illustrated in the figures below. Figure 5.1 presents the control surface positions resulting from a range of pitch commands from a full nose-down pitch command on the left to a full nose-up pitch command on the right. Note that a negative pitch command *(r_p = -1)* is to pitch the aircraft nose down and a positive command corresponds to a nose-up pitch command. A positive pitch command corresponds to a nose-up pitching moment, as illustrated in Figure 4.1. The aircraft figures on either side of the control allocation graph illustrate where the respective control surfaces are situated on the UAV. The red and green arrows indicate whether the respective control surface is moving up or down for the given input command. Figure 5.1 shows that, for a nose-up pitch command *(r_p = 1*, or on the right-hand side of the figure*)*, the control surfaces on the front wing were not contributing significantly to the required nose-up pitching moment. It appears that control surfaces 1 and 2 were reserved for other functions, while control surfaces 7 and 8 were deflected slightly downward, contributing somewhat to the required pitching moment. The control surfaces on the rear wing were assigned by the optimiser as the primary pitch control surfaces. Control surfaces 5 and 6 were mainly responsible for pitching the aircraft, although the optimiser also made use of control surfaces 3 and 4.

In the case of a nose-down pitch command, it can be seen that control surfaces 5 and 6, together with control surfaces 7 and 8, exceeded the maximum deflection amount. Control surfaces 1 and 2, together with control surfaces 3 and 4, were deflected to the maximum amount. The maximum amount of control authority was therefore required for a nose-down pitch command. In order to reduce the amount of control authority required to perform the same manoeuvre, the objective function weight for the nose-down pitch command should be increased and the optimisation run should be re-run.

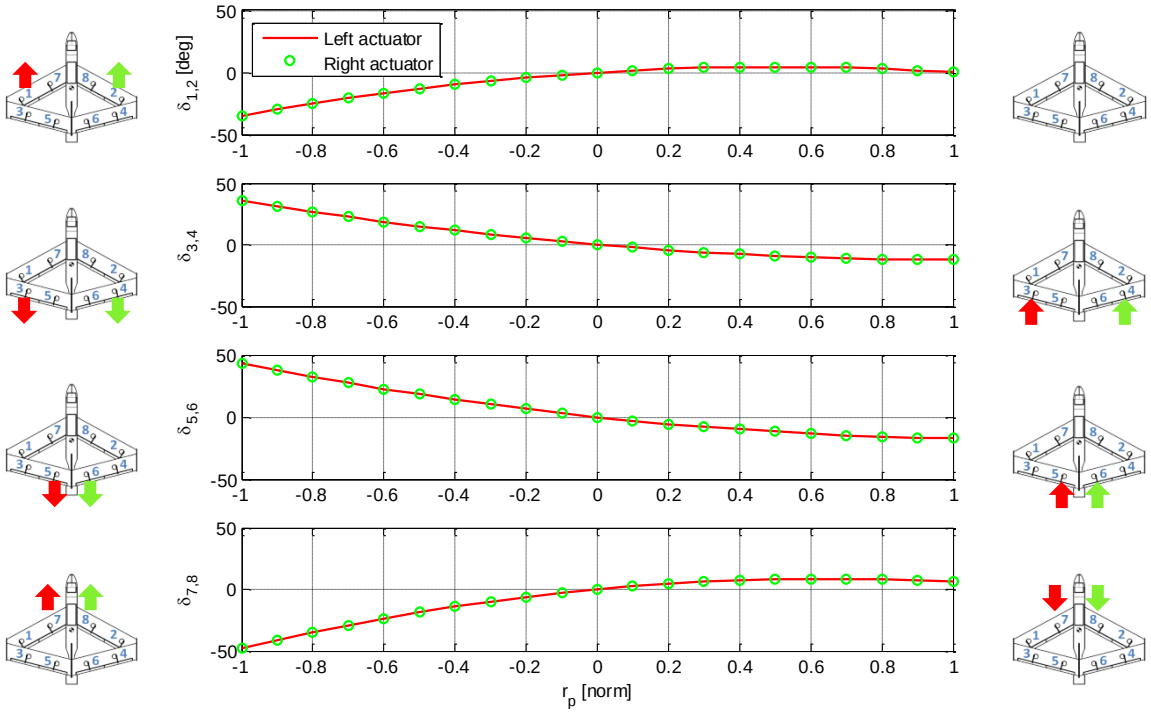

Figure 5.1: Pitch command control allocation for Configuration 1

The control allocation plot for the roll command range is illustrated in Figure 5.2. The control allocation for a full left-roll command ($r_r = -1$) is illustrated on the left and the control allocation for a full right-roll command ($r_r = 1$) is illustrated on the right.

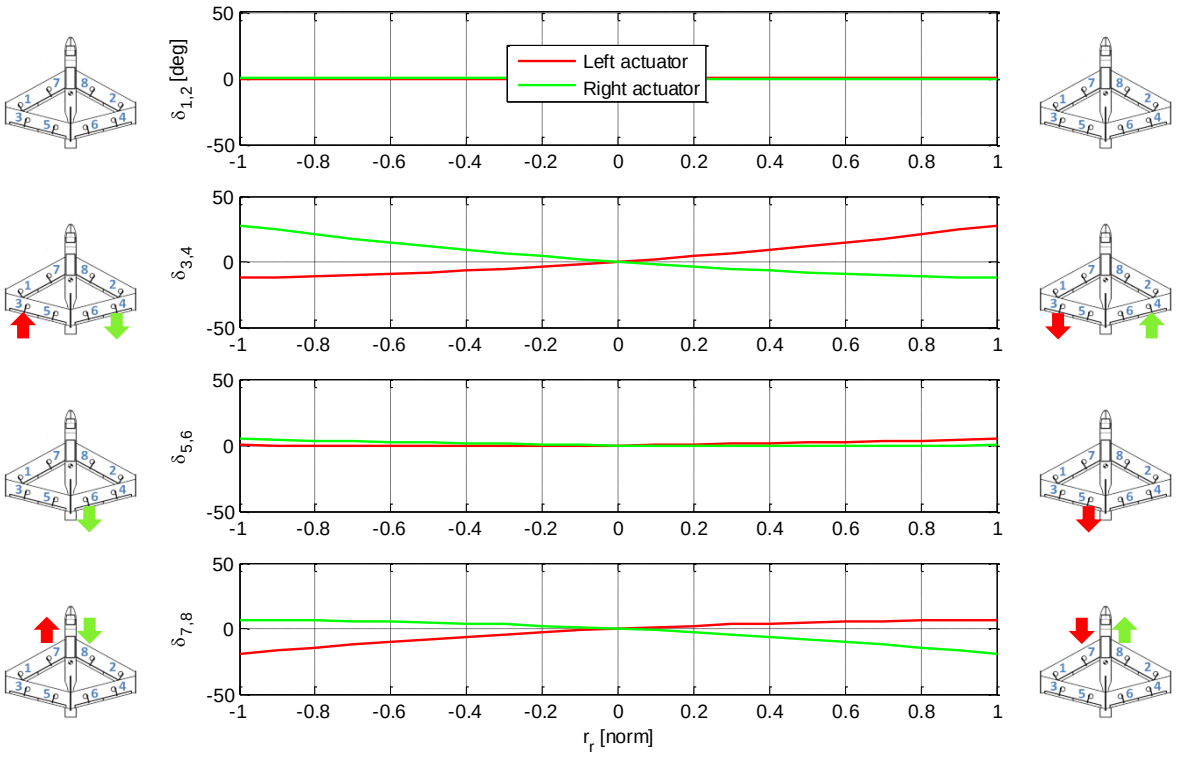

Figure 5.2: Roll command control allocation for Configuration 1

As shown in Figure 5.2, a symmetrical effect was obtained for a left- and right-roll command. Further evaluation shows that control surfaces 3, 4, 7 and 8 were mostly used when rolling

the aircraft, whereas control surfaces 1 and 2 were completely reserved for other functions. It will later be shown that these were used primarily for yaw control. Control surfaces 5 and 6 were also not allocated a significant rolling function by the optimiser, although a slight deflection was observed.

Figure 5.3 illustrates the control allocation for a range of yaw control input commands. The control allocation for a full left-nose-yaw command ($r_y = -1$) is illustrated on the left and the control allocation for a full right-yaw command ($r_y = 1$) is illustrated on the right.

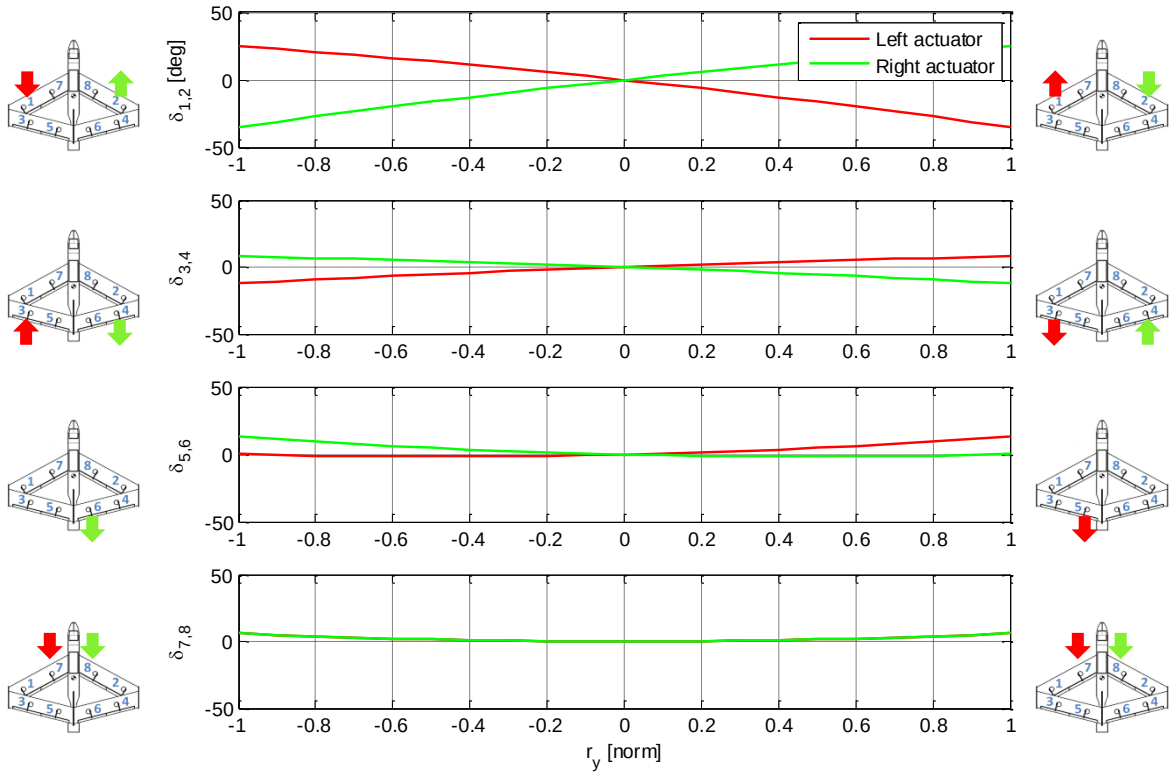

Figure 5.3: Yaw command control allocation for Configuration 1

The yaw control mixing was relatively complex and would have been very difficult to design manually. Control surfaces 1 and 2 were primarily used for yaw control, and these two were reserved during a pitch and roll command by the optimiser specifically for yaw control. Control surfaces 3 and 4 were also used during a yaw command. What is evident from Figure 5.3, is that the outer control surfaces on the front and rear wing were mostly used to yaw the aircraft. Control surfaces 5 and 6 were slightly deflected and then only one at a time. Control surfaces 7 and 8 were both deflected slightly downwards for a nose-left and right-yaw command.

5.2.3 Objective function solution

The optimal accelerations and optimal sideslip corresponding to the objective function terms obtained for Configuration 1 are shown in Table 5.4. The weights were all set to 1 to give the same importance to all the terms in the objective function in turn in order to establish a baseline as reference.

Table 5.4: Objective function solution obtained for Configuration 1

$\dot{p}$ [°/s^2]	22.2
β [°]	-0.957
$\dot{q}_{pos}$[°/s^2]	7.02
$\dot{q}_{neg}$[°/s^2]	-22.6
F(x)	-4.34

In Table 5.4, $\dot{p}$ denotes the maximum roll acceleration for a roll step input, β denotes the maximum sideslip for a yaw step input, $\dot{q}_{pos}$ denotes the maximum pitch acceleration for a nose-up pitch step input, $\dot{q}_{neg}$ denotes the maximum pitch acceleration for a nose-down pitch step input and F(x) denotes the objective function value at the optimal point. The values listed in Table 5.4 represent the maximum values obtained at the optimal point using the normalised objective function with all the weights equal to 1 (see section 4.6).

5.2.4 Constraints at solution

The constraint requirements, as specified in section 3.4, state that the equality constraints need to be equal to zero and the inequality constraints need to be smaller than or equal to zero for an optimum point to exist. The six equality constraints for Phase 1 and the four equality constraints for Phase 2 were all equal to zero at the solution, as expected. This is shown in Table 5.5 and Table 5.6.

Table 5.5: Phase 1 equality constraint results at optimum point for Configuration 1

h_final(1) = 0.00
h_final(2) = 0.00
h_final(3) = 0.00
h_final(4) = 0.00
h_final(5) = 0.00
h_final(6) = 0.00

Table 5.6: Phase 2 equality constraint results at optimum point for Configuration 1

h_final(1) = 0.00
h_final(2) = 0.00
h_final(3) = 0.00
h_final(4) = 0.00

The inequality constraint results at the optimum point for Configuration 1 are given in Table 5.7. The inequality constraints active at the optimum point are highlighted in the table.

Table 5.7: Inequality constraint results at solution for Configuration 1

g (1) = 0.000	g (15) = -575.7	g (29) = -732.5	g (43) = -331.4
g (2) = 0.000	g (16) = -895.5	g (30) = -899.9	g (44) = -331.4
g (3) = 0.000	g (17) = -802.6	g (31) = -835.4	g (45) = 0.000
g (4) = 0.000	g (18) = 0.000	g (32) = -875.7	g (46) = 0.000
g (5) = -876.1	g (19) = -422.0	g (33) = -835.4	g (47) = -331.4

g (6) = -876.1	g (20) = -575.7	g (34) = -732.5	g (48) = -897.6
g (7) = 0.000	g (21) = 0.000	g (35) = -732.5	g (49) = -878.9
g (8) = 0.000	g (22) = -802.6	g (36) = -899.9	g (50) = -878.9
g (9) = 0.000	g (23) = 0.000	g (37) = 0.000	g (51) = 0.000
g (10) = 0.000	g (24) = -802.6	g (38) = -609.8	g (52) = 0.000
g (11) = -876.1	g (25) = -575.7	g (39) = 0.000	g (53) = -331.4
g (12) = 0.000	g (26) = 0.000	g (40) = 0.000	g (54) = 0.000
g (13) = -876.1	g (27) = -802.6	g (41) = -270.1	g (55) = 0.000
g (14) = -876.1	g (28) = 0.000	g (42) = 0.000	g (56) = -878.9

The active inequality constraints highlighted in Table 5.7 at Configuration 1 for the respective control surface pairs are given in Table 5.8. The first column in Table 5.8 represents the inequality constraints that were active at the optimum point. The control command combinations corresponding to the active constraint are given in the next three columns, together with a short description of the command in the last column.

Table 5.8: Active inequality constraints for Configuration 1

Active inequality constraints for control surfaces 1 and 2				
# g(x)	**r_p**	**r_r**	**r_y**	**Comment**
1	0	0	-1	Left-yaw command
2	0	0	1	Right-yaw command
3	0	1	-1	Roll + yaw cross control
4	0	1	1	Roll + yaw
7	0	-1	-1	Roll + yaw
8	0	-1	1	Roll + yaw cross control
9	1	0	-1	Pitch + yaw
10	1	0	1	Pitch + yaw
12	-1	0	0	Full down pitch
Active inequality constraints for control surfaces 3 and 4				
# g(x)	**r_p**	**r_r**	**r_y**	**Comment**
18	0	1	1	Roll + yaw
21	0	-1	-1	Roll + yaw
23	1	0	-1	Pitch + yaw
26	-1	0	0	Full down pitch
28	1	-1	0	Pitch + roll
Active inequality constraints for control surfaces 5 and 6				
# g(x)	**r_p**	**r_r**	**r_y**	**Comment**
37	1	0	-1	Pitch + yaw
39	1	0	0	Full positive pitch
40	-1	0	0	Full down pitch
42	1	-1	0	Pitch + roll
Active inequality constraints for control surfaces 7 and 8				
# g(x)	**r_p**	**r_r**	**r_y**	**Comment**
45	0	1	-1	Roll + yaw
46	0	1	1	Roll + yaw
51	1	0	-1	Pitch + yaw

52	1	0	1	Pitch + yaw
54	-1	0	0	Full down pitch
55	1	1	0	Pitch + roll

5.2.5 Simulated aircraft response

The aircraft dynamic responses were simulated to evaluate the results for a full roll and yaw command using Configuration 1. Figure 5.4 illustrates the aircraft dynamic response to a full right-roll step command *(r_r = 1)*.

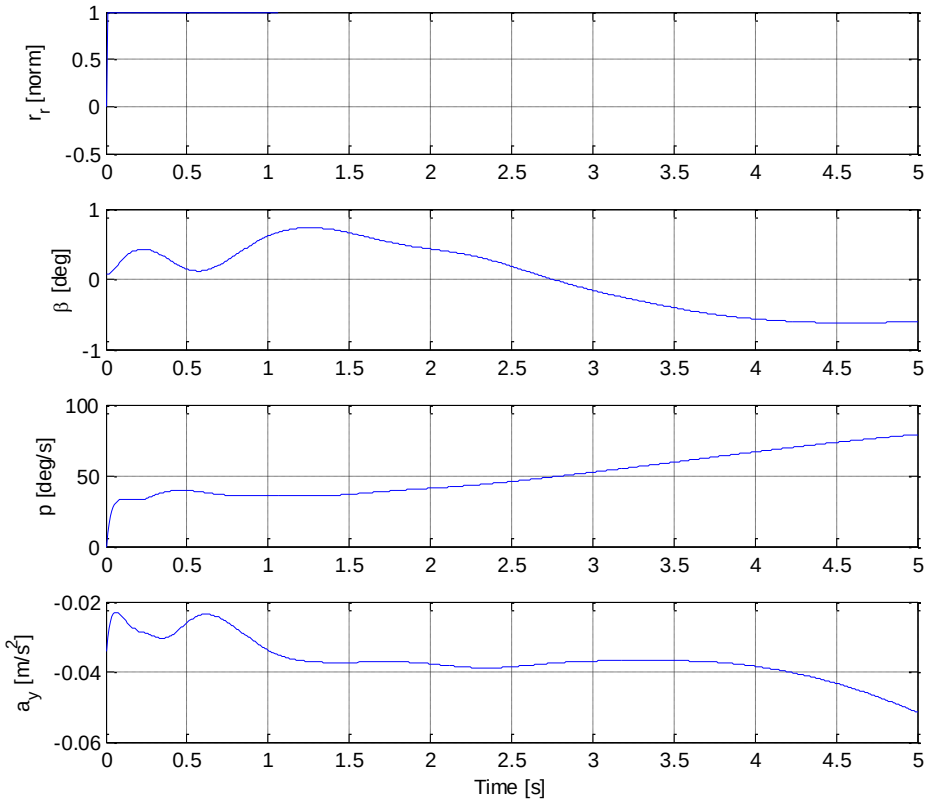

Figure 5.4: Dynamic response for a pure roll input for Configuration 1

A steady roll rate (p) of 35°/s was reached within 0.1 seconds after the control input had been given. A sideslip between -1° and 1° was generated, together with a small side acceleration compared to 1 g. A roll input command would excite the Dutch roll mode and therefore the sideslip was not constant; it was relatively small and positive for the first 2.7 seconds.

The aircraft lateral response for a pure yaw step command is illustrated in Figure 5.5. A maximum yaw input command generated an approximate steady-state sideslip of -0.9°. A positive yaw rate was generated, together with a negative sideslip, for a right-yaw input command. There was no initial roll response to a yaw input, although a longer-term roll response was observed, which was probably caused by the dihedral effect. The dihedral effect is a characteristic of the airframe aerodynamics and would typically require a feedback system to change. In this case, however, a nose-right-yaw command resulted in a negative sideslip angle, which is conventional, and a positive roll rate (bank to the right) resulted, which implies a positive dihedral effect, which is therefore also conventional.

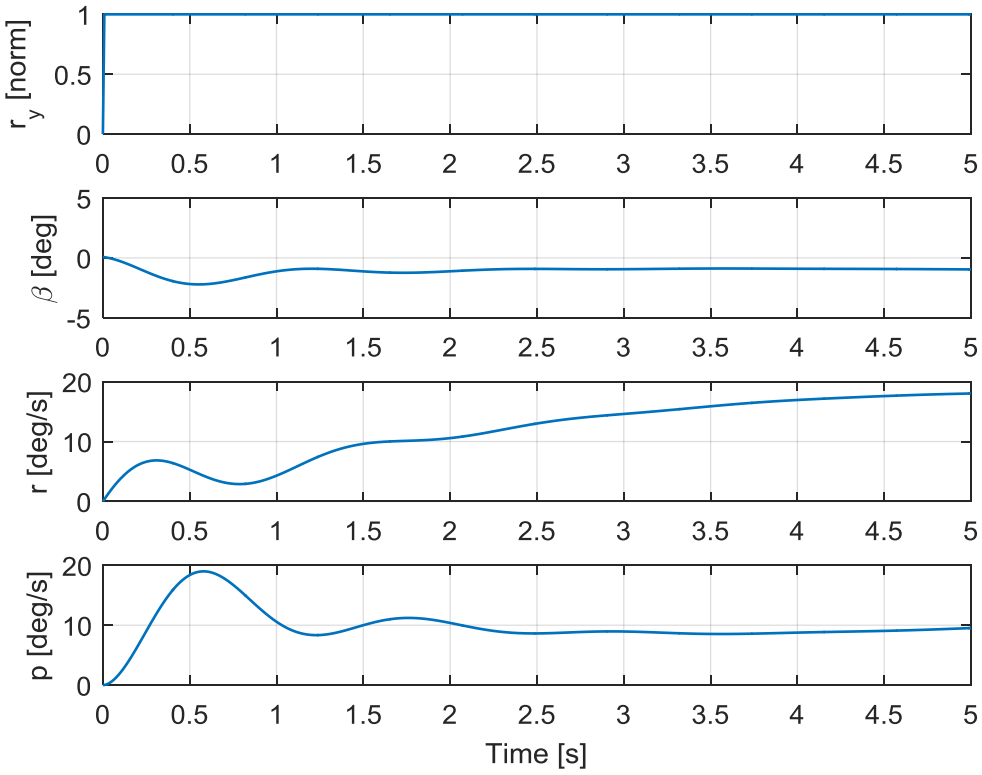

Figure 5.5: Dynamic response for a pure yaw input for Configuration 1

5.2.6 Off-design response

The amount of pitch input required to trim the UAV using Configuration 1 over the entire flight envelope is shown in Figure 5.6. The blue dot in Figure 5.6 represents the design airspeed.

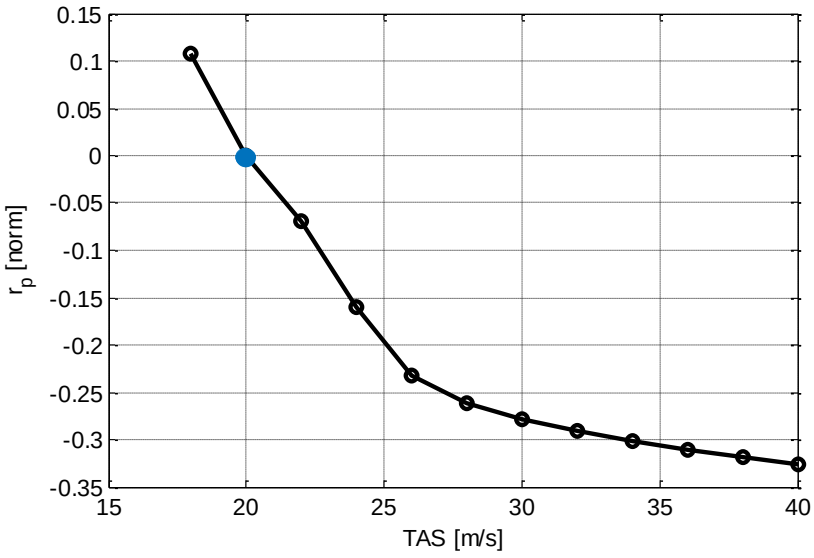

:

Figure 5.6: Pitch authority required to trim UAV over flight envelope for Configuration 1

Figure 5.6 indicates that a maximum amount of 11% positive input at low speed and 30% negative input at high speed were required to trim the aircraft. A sufficient control margin remained for low and high speeds, which was as desired. An adequate amount of control authority therefore remains to trim the aircraft throughout the speed envelope.

The maximum pitch rate (q) the aircraft could achieve over the flight envelope using Configuration 1 is given in Table 5.9 below. The first column represents the respective airspeeds at which the pitch rates were determined, and the second column contains the maximum pitch rates achieved at the respective airspeeds. The third column contains the pitch commands (r_p) required to reach the respective pitch rates, and the last column shows the load factor (n_z) experienced by the airframe at the respective pitch rates.

Table 5.9: Maximum obtainable pitch rate using Configuration 1 over the flight envelope

TAS [m/s]	q [°/s]	r_p [norm]	n_z[g]
18	4.40	0.503	-1.12
20	11.66	0.631	-1.39
25	27.40	0.586	-2.17
30	41.30	0.610	-3.14
35	54.08	0.622	-4.28
40	66.13	0.612	-5.59
45	77.80	0.641	-7.08

5.3 Control Configuration 2

5.3.1 General

In this configuration, the control allocation design process was conducted for a typical UAV medium-speed flight condition. The optimisation results for Phase 1 at a nominal airspeed of 30 m/s are given in Table 5.10.

Table 5.10: Configuration 2 optimisation overview for Phase 1

Phase 1	
Convergence time [sec]	6.23
Function evaluations	1160
Iterations	19
Optimisation algorithm	SQP

The optimisation results for Phase 2 are given in Table 5.11. The active inequality constraints are discussed in section 5.3.4.

Table 5.11: Configuration 2 optimisation overview for Phase 2

Phase 2	Weight set 1
Convergence time [sec]	91418.5 (25.4 hours)
Function evaluations	99367
Iterations	2074

Number of active inequality constraints	22
Optimisation algorithm	LFOPCV3

The primary aim of Phase 1 was to obtain the control surface deflections at trim as close as possible to neutral. The trim bias vector is given in Equation (5.3).

$$Trim\ bias\ vector = \begin{bmatrix} 0.7408 \\ 0.9968 \\ -3.4925 \\ -2.7357 \\ -4.4211 \\ -4.1108 \\ 3.5589 \\ 3.7138 \end{bmatrix} \tag{5.3}$$

The control allocation design process for Configuration 2 was conducted at a slightly higher airspeed compared to Configuration 1. The trim bias vector for Configuration 1 required almost 50% of control surface deflections to trim the aircraft, whereas a maximum of 15% control surface deflection was required for Configuration 2 to trim the aircraft. It can therefore be seen that as the airspeed increased, the angle of attack decreased, which resulted in less control authority required to trim the aircraft. Control surfaces 5 and 6 were mostly used for pitch control. All the control surfaces on the front wing were again deflected downwards, whereas all the control surfaces on the rear wing were deflected upwards to trim the aircraft. The asymmetric terms for the corresponding control surfaces observed in the trim bias vector were to compensate for the propeller gyroscopic effects that were taken into account by the simulation.

5.3.2 Control allocation

The optimal mixing values for the coefficient matrices A and B of Configuration 2 are given in Equation (5.4).

$$\begin{bmatrix} \delta_1 \\ \delta_2 \\ \delta_3 \\ \delta_4 \\ \delta_5 \\ \delta_6 \\ \delta_7 \\ \delta_8 \end{bmatrix} = \begin{bmatrix} -15.4344 & 0 & -0.8688 \\ -15.4344 & 0 & -0.8688 \\ 16.5570 & -7.4705 & 10.5846 \\ 16.5570 & -7.4705 & 10.5846 \\ 10.9190 & -13.3061 & -2.2038 \\ 10.9190 & -13.3061 & -2.2038 \\ -9.4046 & -11.0499 & 5.7683 \\ -9.4046 & -11.0499 & 5.7683 \end{bmatrix} \begin{bmatrix} {r_p}^2 \\ {r_r}^2 \\ {r_y}^2 \end{bmatrix} + \begin{bmatrix} 15.4344 & 0 & -30.00 \\ 15.4344 & 0 & 30.00 \\ -16.5570 & 19.4154 & 10.5846 \\ -16.5570 & -19.4154 & -10.5846 \\ -23.3470 & 0 & 7.2649 \\ -23.3470 & 0 & -7.2649 \\ 24.2317 & 22.5864 & -5.7683 \\ 24.2317 & -22.5864 & 5.7683 \end{bmatrix} \begin{bmatrix} r_p \\ r_r \\ r_y \end{bmatrix} + \begin{bmatrix} 0.7408 \\ 0.9968 \\ -3.4925 \\ -2.7357 \\ -4.4211 \\ -4.1108 \\ 3.5589 \\ 3.7138 \end{bmatrix} \tag{5.4}$$

The control allocation plots for the pitch, roll and yaw command ranges – using the mixing function given in Equation (5.4) – are illustrated in the figures below. Figure 5.7 presents the control surface positions resulting from a range of pitch commands, from a full nose-down pitch command on the left to a full nose-up pitch command on the right. The aircraft figures on either side of the control allocation graph illustrate where the respective control surfaces are situated on the UAV. The red and green arrows show whether the respective control surfaces are moving up or down for the given input command.

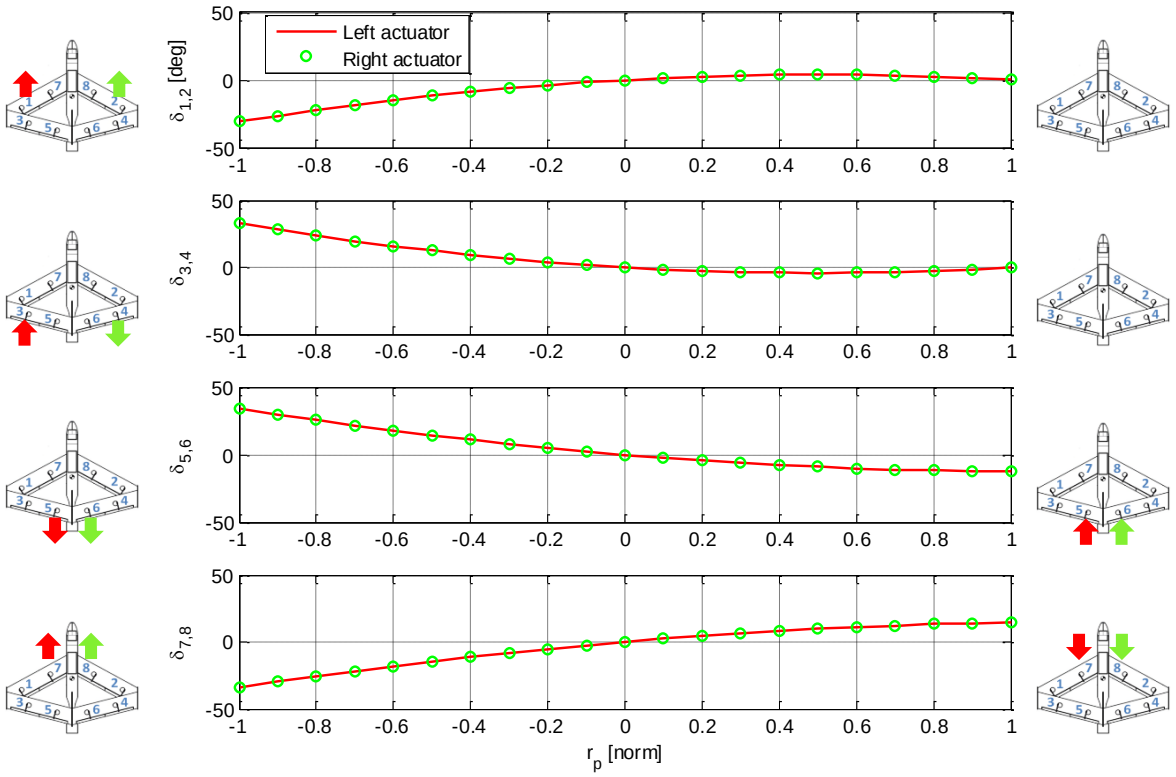

Figure 5.7: Pitch command control allocation for Configuration 2

Figure 5.7 illustrates the case for a nose-up pitch command *(r_p = 1)*. It can be seen that the outer control surfaces (1, 2, 3 and 4) were not used to obtain a nose-up pitching moment. The inner control surfaces on the front and rear wings were used for a nose-up pitch command. Control surfaces 5 and 6 acted like typical elevators. In the case of a nose-down pitch command, it can be seen that all the control surface pairs were deflected to the maximum amount. In the case of Configuration 1, control surfaces 5 and 6, and 7 and 8 violated the deflection constraint, whereas in Configuration 2, these control surfaces were all deflected to the maximum amount without violating the constraint.

The control allocation plot for the roll command range is illustrated in Figure 5.8. The control allocation for a full left-roll command ($r_r = -1$) is illustrated on the left and the control allocation for a full right-roll command ($r_r = 1$) is illustrated on the right. Figure 5.8 shows that control surfaces 1 and 2 were reserved for yaw control, while making very little use of control surfaces 5 and 6. Note that control surfaces 5 and 6 were both deflected upwards for a full left- and right-roll command. The differential control can be seen on close inspection by considering the degree to which the corresponding control surfaces on the left and right deflected.

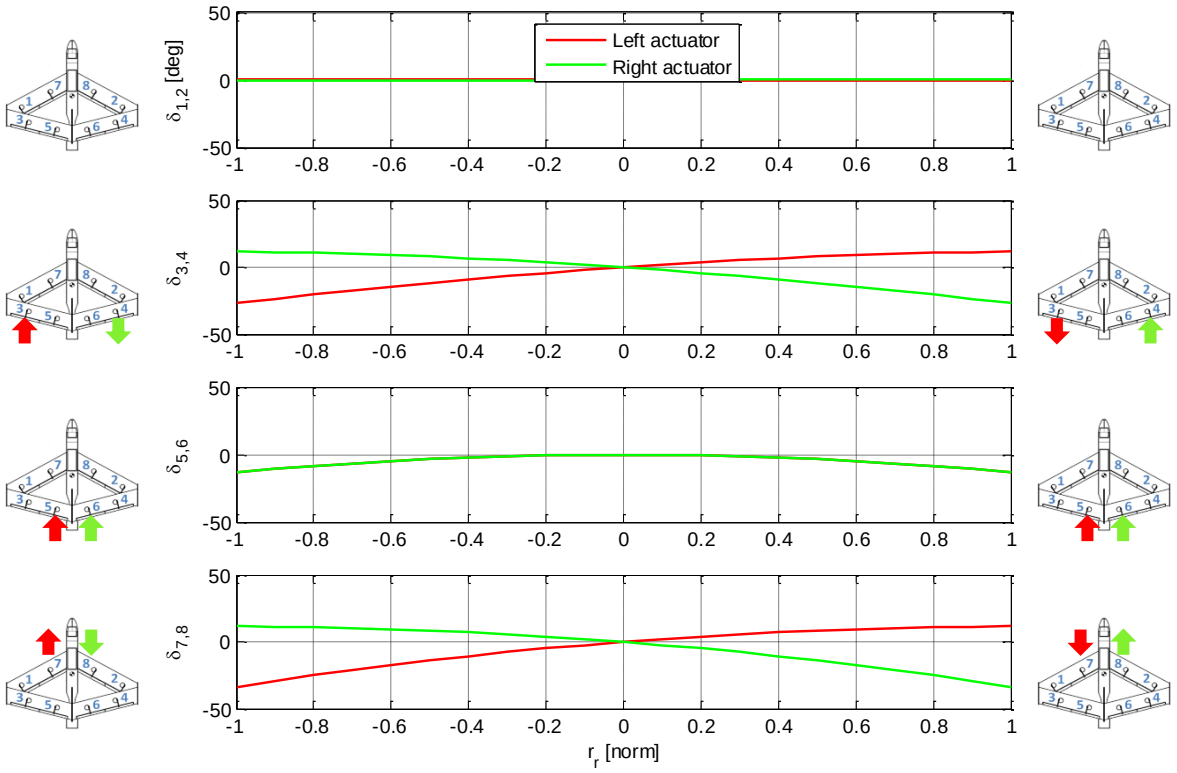

Figure 5.8: Roll command control allocation for Configuration 2

Figure 5.9 illustrates the control allocation for a range of yaw control input commands. The control allocation for a full left-nose-yaw command ($r_y = -1$) is illustrated on the left and the control allocation for a full right-yaw command ($r_y = 1$) is illustrated on the right.

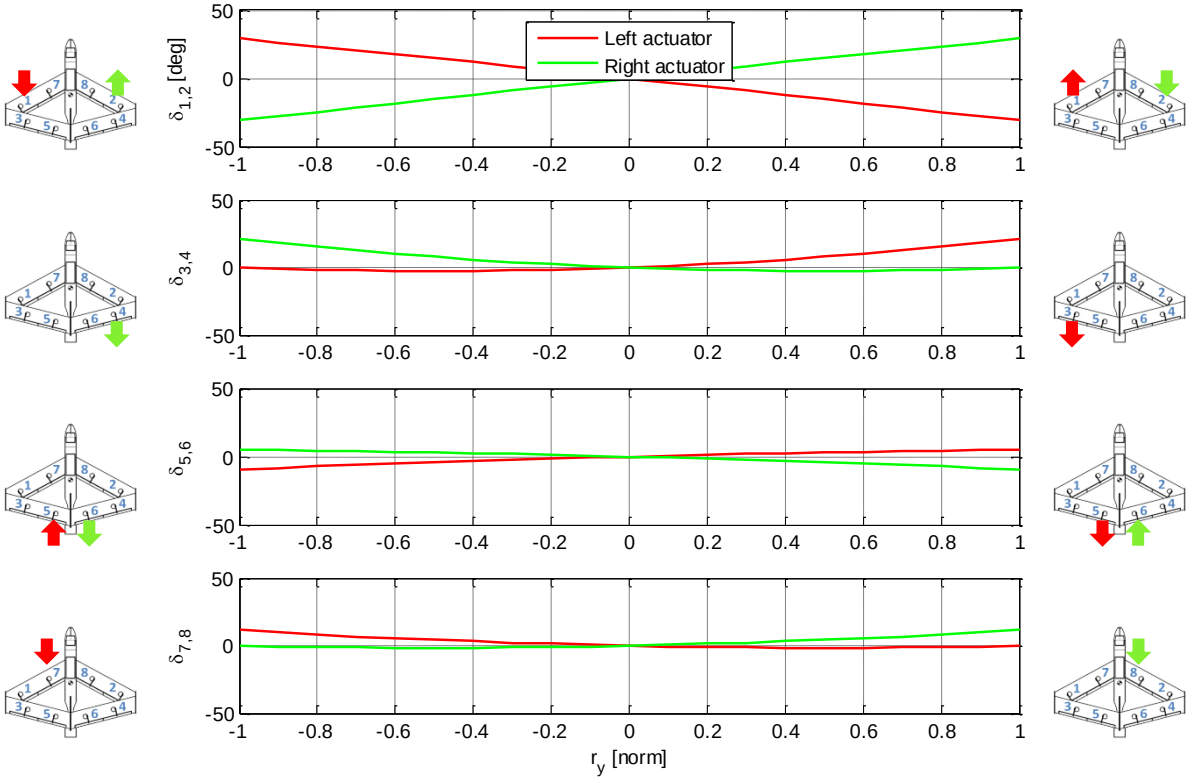

Figure 5.9: Yaw command control allocation for Configuration 2

Figure 5.9 shows that the yaw control mixing was once again fairly complex and would have been difficult to design manually. The optimiser mainly used control surfaces 1, 2, 3 and 4 when a yaw input command was given. The optimiser made little use of control surfaces 5, 6, 7 and 8.

5.3.3 Objective function solution

The optimal accelerations and optimal sideslip corresponding to the objective function terms obtained for Configuration 2 are shown in Table 5.12. The weights were all set to 1 to give the same importance to all the terms in the objective function in order to establish a baseline as reference.

Table 5.12: Objective function solution obtained for Configuration 2

$\dot{p}$ [°/s^2]	62.3
β [°]	-1.35
$\dot{q}_{pos}$[°/s^2]	11.4
$\dot{q}_{neg}$[°/s^2]	-46.6
F(x)	-3.73

In Table 5.12, $\dot{p}$ denotes the maximum roll acceleration for a roll step input, β denotes the maximum sideslip for a yaw step input, $\dot{q}_{pos}$ denotes the maximum pitch acceleration for a nose-up pitch step input, $\dot{q}_{neg}$ denotes the maximum pitch acceleration for a nose-down pitch step input and F(x) denotes the objective function value at the optimal point.

5.3.4 Constraints at solution

The constraint requirements, as specified in section 3.4, state that the equality constraints need to be equal to zero and the inequality constraints need to be smaller than or equal to zero for an optimum point to exist. The six equality constraints for Phase 1 and the four equality constraints for Phase 2 were all equal to zero at the solution, which was a partial confirmation of convergence, as indicated in Table 5.13 and Table 5.14.

Table 5.13: Phase 1 equality constraint results at optimum point for Configuration 2

h_final(1) = 0.00
h_final(2) = 0.00
h_final(3) = 0.00
h_final(4) = 0.00
h_final(5) = 0.00
h_final(6) = 0.00

Table 5.14: Phase 2 equality constraint results at optimum point for Configuration 2

h_final(1) = 0.00
h_final(2) = 0.00
h_final(3) = 0.00
h_final(4) = 0.00

The inequality constraint results at the solution for Configuration 2 are given in Table 5.15, and the inequality constraints that are active at the optimum point are highlighted in Table 5.15.

Table 5.15: Inequality constraint results at solution for Configuration 2

g (1) = 0.000	g (15) = -890.3	g (29) = -711.4	g (43) = -669.8
g (2) = 0.000	g (16) = -574.0	g (30) = -899.4	g (44) = -886.8
g (3) = 0.000	g (17) = -822.0	g (31) = -168.8	g (45) = -186.6
g (4) = 0.000	g (18) = 0.000	g (32) = -743.5	g (46) = -669.8
g (5) = -899.3	g (19) = -822.0	g (33) = -591.2	g (47) = -669.8
g (6) = -899.3	g (20) = 0.000	g (34) = -591.2	g (48) = 0.000
g (7) = 0.000	g (21) = 0.000	g (35) = -168.8	g (49) = -559.1
g (8) = 0.000	g (22) = -822.0	g (36) = -743.5	g (50) = 0.000
g (9) = 0.000	g (23) = -890.3	g (37) = -215.5	g (51) = 0.000
g (10) = 0.000	g (24) = -574.0	g (38) = -764.7	g (52) = -559.1
g (11) = -899.3	g (25) = -890.3	g (39) = -621.3	g (53) = -559.1
g (12) = 0.000	g (26) = 0.000	g (40) = 0.000	g (54) = 0.000
g (13) = -899.3	g (27) = -822.0	g (41) = 0.000	g (55) = 0.000
g (14) = -899.3	g (28) = 0.000	g (42) = 0.000	g (56) = -669.8

The active inequality constraints for Configuration 2 for the respective control surface pairs are given in Table 5.16. The active inequality constraints highlighted in Table 5.15 for Configuration 2 for the respective control surface pairs are given in Table 5.16. The first column in Table 5.16 represents the inequality constraints that are active at the optimum point. The control command combinations corresponding to the active constraints are given in the following three columns, together with a short description of the command in the last column.

Table 5.16: Description of active inequality constraints for Configuration 2

Active inequality constraints for control surfaces 1 and 2				
# g(x)	**r_p**	**r_r**	**r_y**	**Comment**
1	0	0	-1	Yaw command
2	0	0	1	Right-yaw command
3	0	1	-1	Roll + yaw
4	0	1	1	Roll + yaw
7	0	-1	-1	Roll + yaw
8	0	-1	1	Roll + yaw
9	1	0	-1	Positive pitch + yaw
10	1	0	1	Pitch + yaw
12	-1	0	0	Full down pitch
Active inequality constraints for control surfaces 3 and 4				
# g(x)	**r_p**	**r_r**	**r_y**	**Comment**
18	0	1	1	Roll + yaw
20	0	-1	0	Left-roll command
21	0	-1	-1	Roll + yaw

26	-1	0	0	Full down pitch
28	1	-1	0	Pitch + roll
Active inequality constraints for control surfaces 5 and 6				
# g(x)	r_p	r_r	r_y	Comment
40	-1	0	0	Full down pitch
41	1	1	0	Pitch + roll
42	1	-1	0	Pitch + roll
Active inequality constraints for control surfaces 7 and 8				
# g(x)	r_p	r_r	r_y	Comment
48	0	-1	0	Left-roll command
50	0	-1	1	Roll + yaw
51	1	0	-1	Positive pitch + yaw
54	-1	0	0	Full down pitch
55	1	1	0	Pitch + roll

When the active inequality constraints for Configuration 2 were compared to the active constraints for Configuration 1, the following was detected. Fewer constraints were active at the higher airspeed configuration. The same constraints were active for the two configurations for control surface pair 1 and 2. For control surfaces 5 and 6, the positive pitch and positive roll command case was active at a higher airspeed, whereas the nose-up pitch and nose-left-yaw command combination, together with the full nose-up pitch command constraint, was active at the lower airspeed. For control surfaces 7 and 8, the right-roll and left-yaw combination and right-roll and right-yaw combination constraints were active at the lower airspeed and not at the higher airspeed. The constraints that were active at the higher airspeed but not at the lower airspeed included the left-roll command, the left-roll and right-yaw command combination, a full nose-down pitch command and the nose-up pitch and right-roll command combination.

5.3.5 Simulated aircraft response

The aircraft dynamic responses were simulated to evaluate the results for a full roll and yaw command using Configuration 2. Figure 5.10 illustrates the aircraft dynamic response to a full right-roll step command *($r_r = 1$)*:

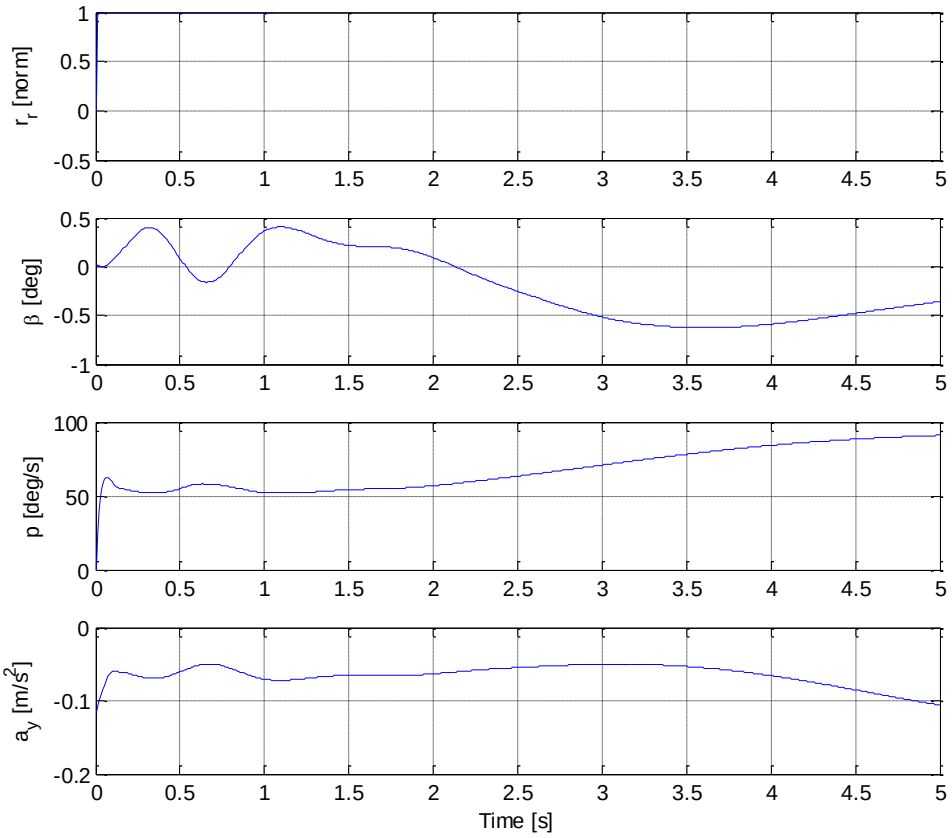

Figure 5.10: Dynamic response to a pure roll input for Configuration 2

A steady roll rate (p) of 50°/s was reached within 0.1 seconds after the control input was given. Very little rudder control was needed to coordinate the aircraft for the small sideslip and lateral acceleration (a_y) generated during a roll manoeuvre. A roll input command would excite the Dutch roll mode and therefore the sideslip was not constant.

Figure 5.11 illustrates the aircraft dynamic response to a full right-yaw command *(r_y = 1)*. The controls were not particularly effective to yaw the aircraft, since a maximum yaw input was only able to generate an approximate steady-state sideslip angle of -2.2°, as shown in Figure 5.11. Dutch roll manifested as a slight wallowing/wavering effect, but it was well damped, as it died out within 1.3 seconds. There was no initial roll response to a yaw input. In this case, however, a nose-right-yaw command resulted in a negative sideslip angle, which is conventional, and a positive roll rate (bank to the right), which implies a positive dihedral effect, which is therefore also conventional.

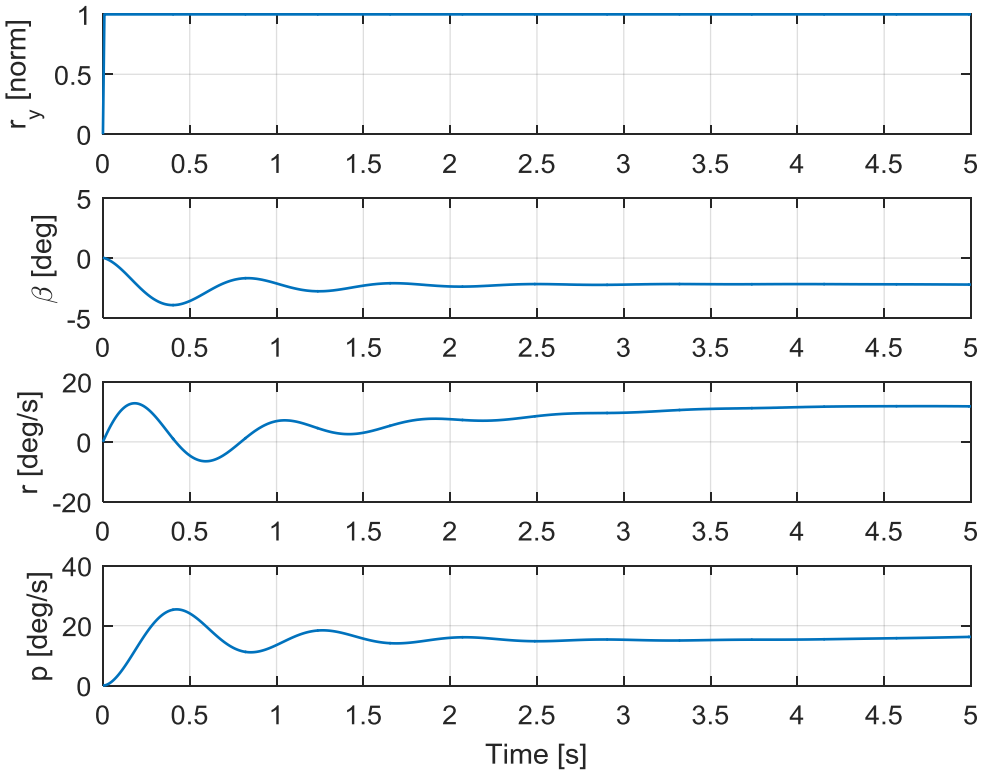

Figure 5.11: Dynamic response for a pure yaw input for Configuration 2

5.3.6 Off-design response

The amount of pitch input was investigated to determine whether the aircraft had a sufficient amount of control authority for trimming it at the lowest flyable airspeed, which was 18 m/s for this particular UAV. Figure 5.12 illustrates the amount of pitch command required to trim the aircraft over the flight envelope. The blue dot indicates the on-design condition for Configuration 2.

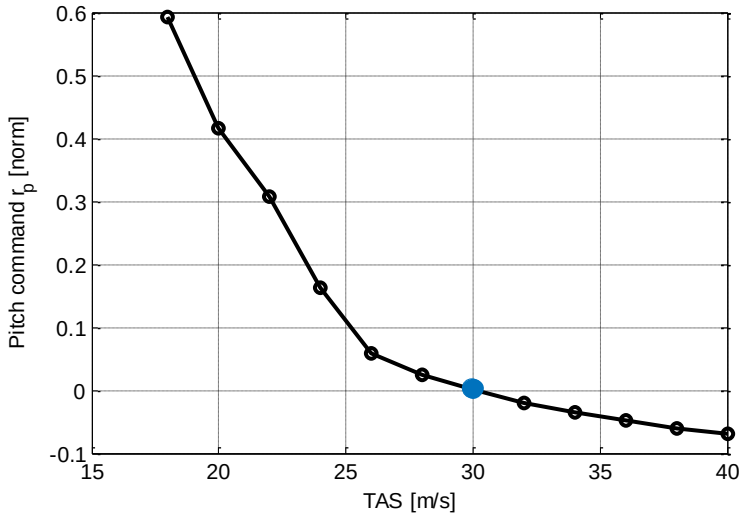

Figure 5.12: Pitch authority required to trim UAV over flight envelope for Configuration 2

Figure 5.12 indicates that a maximum amount of 60% positive input at low speed and 8% negative input at high speed were required to trim the aircraft. An adequate amount of control authority therefore remains to trim the aircraft throughout the speed envelope.

The maximum pitch rate (q) that the aircraft can achieve over the flight envelope using Configuration 2 is given in Table 5.17 below. The first column represents the respective airspeeds at which the pitch rates were determined, and the second column contains the maximum pitch rates achieved at the respective airspeeds. The third column shows the pitch commands (r_p) required to reach the respective pitch rates and the last column contains the load factor (n_z) experienced by the airframe at the respective pitch rates.

Table 5.17: Maximum obtainable pitch rate using Configuration 2 over the flight envelope

TAS [m/s]	q [°/s]	r_p [norm]	n_z [g]
18	-	-	-
20	1.67	0.857	-1.05
25	13.74	0.854	-1.60
30	24.11	0.869	-2.27
35	33.48	0.862	-3.06
40	42.24	0.864	-3.97
45	50.56	0.851	-5.01

5.4 Control Configuration 3

5.4.1 General

In this configuration, the control allocation design process was conducted for a typical UAV high-speed flight condition. The optimisation results for Phase 1 at a nominal airspeed of 40 m/s are given in Table 5.18.

Table 5.18: Configuration 3 optimisation overview for Phase 1

Phase 1	
Convergence time [sec]	3.09
Function evaluations	751
Iterations	25
Optimisation algorithm	SQP

The optimisation results for Phase 2 are given in Table 5.19. The active inequality constraints are discussed in section 5.4.4.

Table 5.19: Configuration 3 optimisation overview for Phase 2

Phase 2	Weight set 1
Convergence time [sec]	100308.3 (27.9 hours)
Function evaluations	89239
Iterations	1863
Number of active inequality constraints	18
Optimisation algorithm	LFOPCV3

The primary aim of Phase 1 was to obtain the control surface deflections at trim as close as possible to neutral. The trim bias vector is given in Equation (5.1).

$$Trim\ bias\ vector = \begin{bmatrix} 0.2674 \\ 0.6345 \\ -1.9112 \\ -1.2623 \\ -2.2601 \\ -1.9677 \\ 1.8300 \\ 1.9244 \end{bmatrix} \tag{5.5}$$

It can be seen that the trim values obtained for Configuration 3 are much lower than those obtained for configurations 1 and 2. Configuration 1 required almost 50% of the maximum amount of control surface deflection to trim the aircraft, and Configuration 2 required 15%. Configuration 3 required a maximum of 7.53% of the maximum control surface deflection to trim the aircraft. It was therefore concluded that the amount of control authority required to trim the aircraft decreased as the airspeed increased. The asymmetric terms for the corresponding control surfaces observed in the trim bias vector was to compensate for the propeller gyroscopic effects that were taken into account by the simulation.

5.4.2 Control allocation

The optimal mixing values for the coefficient matrices A and B of Configuration 3 are given in Equation (5.4). The control allocation plots for the pitch, roll and yaw command ranges – using the mixing function given in Equation (5.4) – are illustrated in the figures below.

$$\begin{bmatrix} \delta_1 \\ \delta_2 \\ \delta_3 \\ \delta_4 \\ \delta_5 \\ \delta_6 \\ \delta_7 \\ \delta_8 \end{bmatrix} = \begin{bmatrix} -8.5337 & 6.6917 & -7.1426 \\ -8.5337 & 6.6917 & -7.1426 \\ 8.6901 & -2.9179 & 0.1430 \\ 8.6901 & -2.9179 & 0.1430 \\ 3.7301 & -3.2261 & 4.1580 \\ 3.7301 & -3.2261 & 4.1580 \\ -8.9079 & -8.9079 & 7.0307 \\ -8.9079 & -8.9079 & 7.0307 \end{bmatrix} \begin{bmatrix} {r_p}^2 \\ {r_r}^2 \\ {r_y}^2 \end{bmatrix} + \begin{bmatrix} 21.9172 & 6.6917 & -23.3083 \\ 21.9172 & -6.6917 & 23.3083 \\ -22.8967 & 11.2887 & 14.3496 \\ -22.8967 & -11.2887 & -14.3496 \\ -28.3838 & 0.0063 & -7.3904 \\ -28.3838 & -0.0063 & 7.3904 \\ 22.9693 & 22.9693 & -7.0307 \\ 22.9693 & -22.9693 & 7.0307 \end{bmatrix} \begin{bmatrix} r_p \\ r_r \\ r_y \end{bmatrix} + \begin{bmatrix} 0.2674 \\ 0.6345 \\ -1.9112 \\ -1.2623 \\ -2.2601 \\ -1.9677 \\ 1.8300 \\ 1.9244 \end{bmatrix} \tag{5.6}$$

Figure 5.13 presents the control surface positions resulting from a range of pitch commands from a full nose-down pitch command on the left to a full nose-up pitch command on the right. The aircraft figures on either side of the control allocation graph illustrate where the respective control surfaces are situated on the UAV. The red and green arrows show whether the respective control surfaces are moving up or down for the given input command. In the case of a full nose-down pitch command, it can be seen that the control surfaces were all

deflected to the maximum amount. Figure 5.13 illustrates the case for a nose-up pitch command *(r_p = 1)*. It can be seen that the optimiser primarily allocated control surfaces 5 and 6 to be responsible for pitch control, while using all the remaining control surfaces by more or less the same amount. For a full nose-down pitch command, the control surfaces were all deflected to the maximum degree.

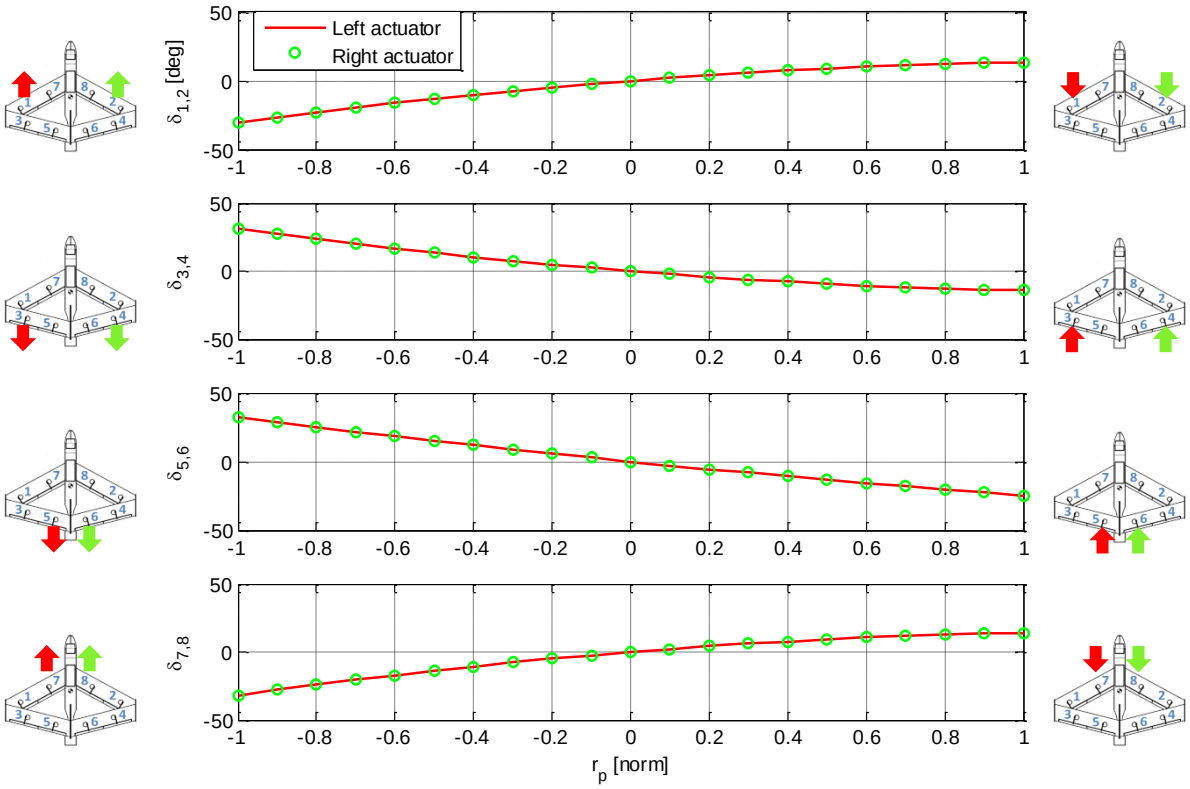

Figure 5.13: Pitch command control allocation for Configuration 3

The control allocation plot for the roll command range is illustrated in Figure 5.14. The control allocation for a full left-roll command ($r_r = -1$) is illustrated on the left and the control allocation for a full right-roll command ($r_r = 1$) is illustrated on the right. Figure 5.14 shows that control surfaces 1, 2, 3, 4, 7 and 8 were primarily used when a roll input command was given; the optimiser reserved control surfaces 5 and 6 mainly for pitching the aircraft, since they act like conventional elevators.

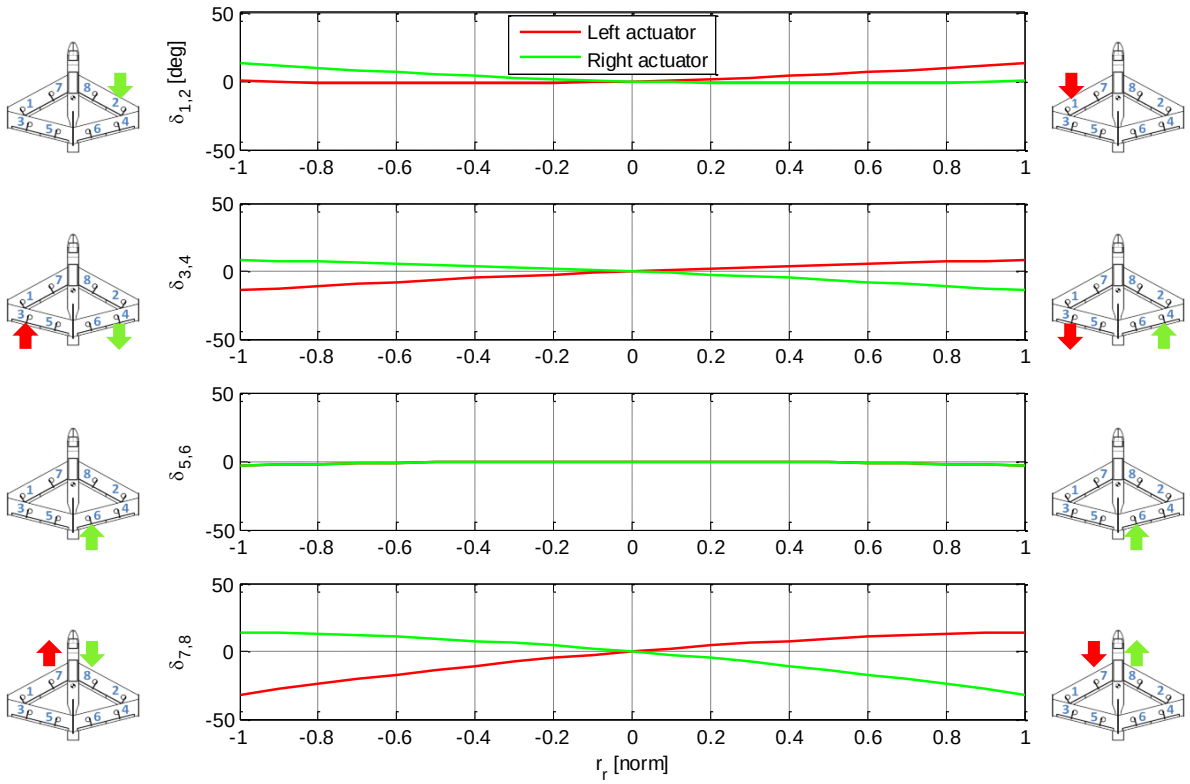

Figure 5.14: Roll command control allocation for Configuration 3

Figure 5.15 illustrates the control allocation for a range of yaw control input commands. The control allocation for a full nose-left-yaw command ($r_y = -1$) is illustrated on the left and the control allocation for a full nose-right-yaw command ($r_y = 1$) is illustrated on the right.

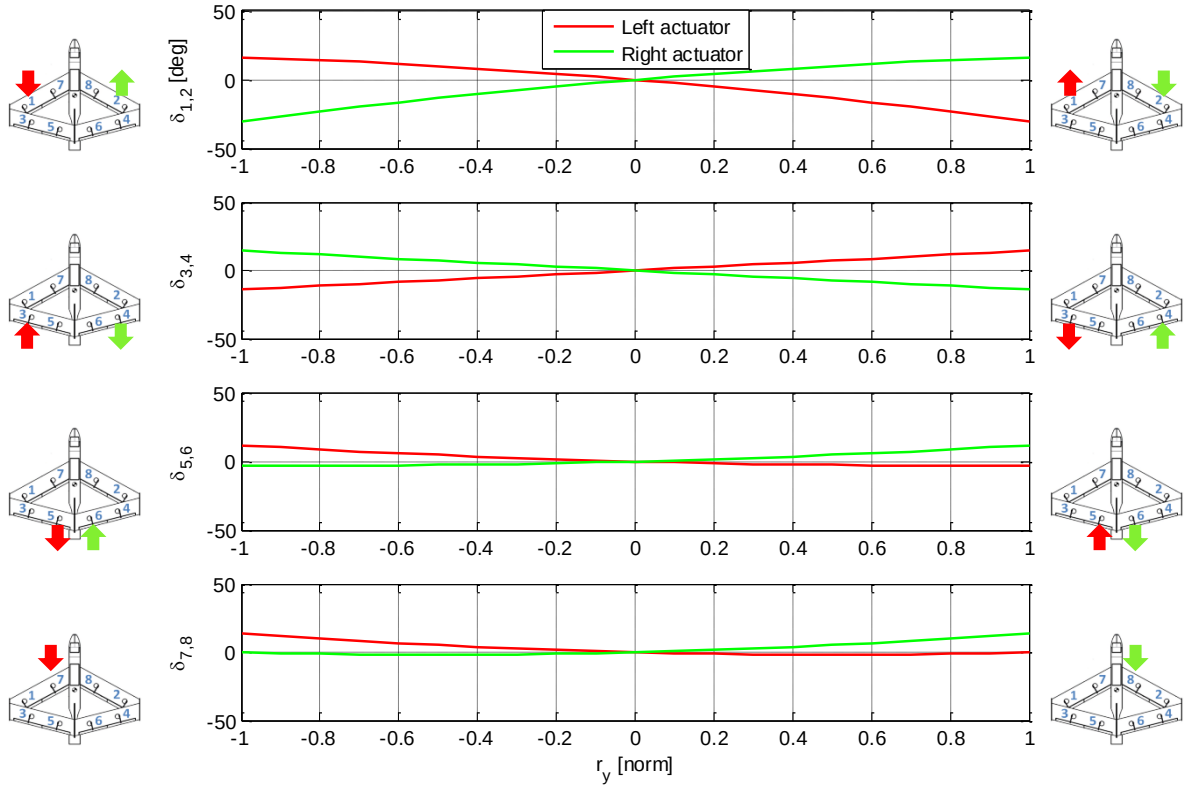

Figure 5.15: Yaw command control allocation for Configuration 3

As shown in Figure 5.15, the yaw control mixing was relatively complex and would have been very difficult to design manually, since the optimiser utilised all the available control surfaces. Control surfaces 1, 2, 3 and 4 were primarily used for yaw control. A fairly small number of control deflections was required from control surfaces 5 and 6, and 7 and 8 for yaw control.

5.4.3 Objective function solution

The optimal accelerations and optimal sideslip corresponding to the objective function terms obtained at Configuration 3 are shown in Table 5.20.

Table 5.20: Objective function solution obtained for Configuration 3

$\dot{p}$ [°/s^2]	88.2
β [°]	-1.16
$\dot{q}_{pos}$[°/s^2]	45.5
$\dot{q}_{neg}$[°/s^2]	-77.6
F(x)	-3.75

In Table 5.20, $\dot{p}$ denotes the maximum roll acceleration for a roll step input, β denotes the maximum sideslip for a yaw step input, $\dot{q}_{pos}$ denotes the maximum pitch acceleration for a nose-up pitch step input, $\dot{q}_{neg}$ denotes the maximum pitch acceleration for a nose-down pitch step input and F(x) denotes the objective function value at the optimal point.

5.4.4 Constraints at solution

The constraint requirements, as specified in section 3.4, state that the equality constraints need to be equal to zero and the inequality constraints need to be smaller than or equal to zero for an optimum point to exist. The six equality constraints for Phase 1 and the four equality constraints for Phase 2 were all equal to zero at the solution, which was a partial confirmation of convergence, as shown in Table 5.21 and Table 5.22.

Table 5.21: Phase 1 equality constraint results at optimum point for Configuration 3

h_final(1) = 0.00
h_final(2) = 0.00
h_final(3) = 0.00
h_final(4) = 0.00
h_final(5) = 0.00
h_final(6) = 0.00

Table 5.22: Phase 2 equality constraint results at optimum point for Configuration 3

h_final(1) = 0.00
h_final(2) = 0.00
h_final(3) = 0.00
h_final(4) = 0.00

The inequality constraint results at the solution for Configuration 3 are given in Table 5.23, and the inequality constraints that are active at the optimum point are highlighted in Table 5.23.

Table 5.23: Inequality constraint results at solution for Configuration 3

g (1) = -623.9	g (15) = -650.6	g (29) = -810.9	g (43) = -645.9
g (2) = 0.000	g (16) = -733.4	g (30) = -871.4	g (44) = -896.5
g (3) = -0.000	g (17) = -844.9	g (31) = -861.4	g (45) = 0.000
g (4) = -623.9	g (18) = -447.3	g (32) = -826.6	g (46) = -645.9
g (5) = -708.6	g (19) = -853.9	g (33) = -871.6	g (47) = -645.9
g (6) = -899.8	g (20) = -650.6	g (34) = -871.4	g (48) = 0.000
g (7) = -623.9	g (21) = 0.000	g (35) = -861.5	g (49) = -645.9
g (8) = -0.000	g (22) = -898.3	g (36) = -826.4	g (50) = -0.000
g (9) = 0.000	g (23) = -0.000	g (37) = -668.4	g (51) = -0.000
g (10) = -623.9	g (24) = -898.3	g (38) = 0.000	g (52) = -645.9
g (11) = -708.6	g (25) = -650.6	g (39) = -183.5	g (53) = -645.9
g (12) = -0.000	g (26) = -0.000	g (40) = -0.000	g (54) = -0.000
g (13) = -159.2	g (27) = -844.9	g (41) = -0.758	g (55) = -0.000
g (14) = -708.6	g (28) = 0.000	g (42) = 0.000	g (56) = -645.9

The active inequality constraints for Configuration 3 for the respective control surface pairs are provided in Table 5.24. The active inequality constraints highlighted in Table 5.23 for Configuration 3 for the respective control surface pairs are also given in Table 5.24. The first column in Table 5.24 represents the inequality constraints that are active at the optimum point. The control command combinations corresponding to the active constraint are given in the next three columns, together with a short description of the command in the last column.

Table 5.24: Active inequality constraints for Configuration 3

Active inequality constraints for control surface 1 and 2				
# g(x)	**r_p**	**r_r**	**r_y**	**Comment**
2	0	0	1	Right-yaw command
3	0	1	-1	Roll + yaw
8	0	-1	1	Roll + yaw
9	1	0	-1	Positive pitch + yaw
12	-1	0	0	Negative pitch
Active inequality constraints for control surface 3 and 4				
# g(x)	**r_p**	**r_r**	**r_y**	**Comment**
21	0	-1	-1	Roll + yaw
23	1	0	-1	Pitch + yaw
26	-1	0	0	Negative pitch
28	1	-1	0	Pitch + roll
Active inequality constraints for control surface 5 and 6				
# g(x)	**r_p**	**r_r**	**r_y**	**Comment**
38	1	0	1	Positive pitch + yaw
40	-1	0	0	Negative pitch
42	1	-1	0	Pitch + roll

Active inequality constraints for control surface 7 and 8				
# g(x)	**r_p**	**r_r**	**r_y**	**Comment**
45	0	1	-1	Roll + yaw
48	0	-1	0	Left-roll command
50	0	-1	1	Roll + yaw
51	1	0	-1	Pitch + yaw
54	-1	0	0	Negative pitch
55	1	1	0	Pitch + roll

The following command combinations were active for control surfaces 1 and 2 for configurations 1 and 2, but not for Configuration 3: full left-yaw command, right-roll and right-yaw command combination, left-roll and left-yaw command combination and nose-up pitch with right-yaw command combination. The active constraints for Configuration 3 for control surfaces 3 and 4 correlated either with Configuration 1 or with Configuration 2. There were no new active constraints. The nose-up pitch with right-yaw command combination was active for Configuration 3, but not for the lower airspeeds. The active constraints for Configuration 3 for control surfaces 7 and 8 correlated either with Configuration 1 or with Configuration 2. Note that almost all the constraints listed for configurations 1 and 2 for control surfaces 7 and 8 were active for Configuration 3. The number of active constraints decreased as the airspeed increased.

5.4.5 Simulated aircraft response

The aircraft dynamic responses were simulated to evaluate the results for a full roll and yaw command using Configuration 3. The aircraft lateral response for a pure roll command for Configuration 3 is illustrated in Figure 5.16.

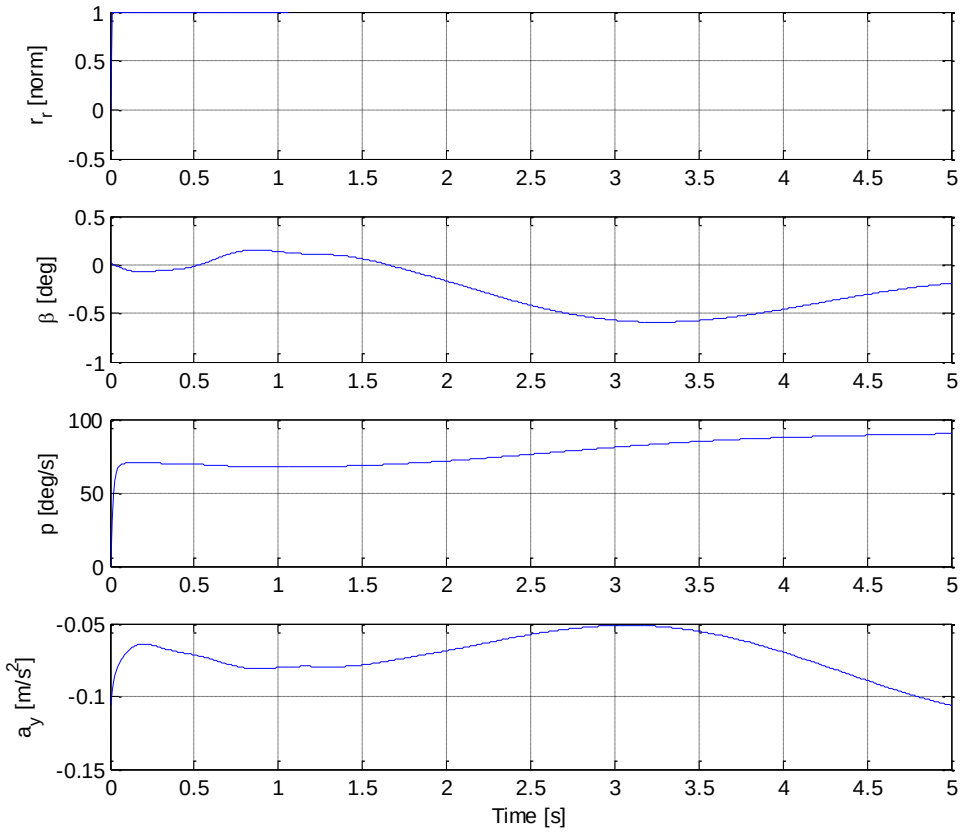

Figure 5.16: Dynamic response for a pure roll input for Configuration 3

A steady roll rate of 70°/s was reached within 0.1 seconds after the control input was given. Very little rudder control was needed to coordinate the aircraft for the small sideslip and lateral acceleration generated during a roll manoeuvre. A roll input command would excite the Dutch roll mode and therefore the sideslip was not constant.

The aircraft lateral response for a pure yaw command for Configuration 3 is illustrated in Figure 5.17. The controls were not particularly effective to yaw the aircraft, since a maximum yaw input was only able to generate an approximate steady-state sideslip angle of -2° in Figure 5.17. There was no initial roll response to a yaw input. The longer-term roll response to a yaw input was caused by the dihedral effect, a characteristic of the airframe. The yaw rate slowly increased after 1.7 seconds.

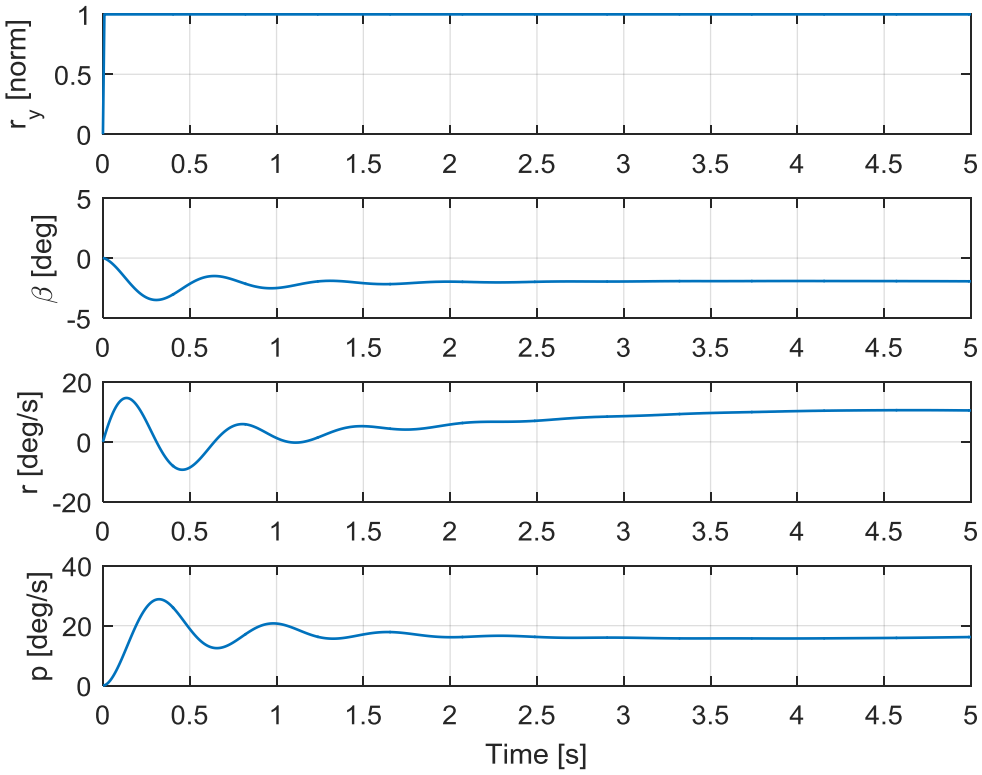

Figure 5.17: Dynamic response for a pure yaw input for Configuration 3

5.4.6 Off-design response

The amount of pitch input command required to trim the UAV using Configuration 3 over the entire flight envelope is shown in the figure below. The blue dot in Figure 5.18 represents the on-design condition for Configuration 3.

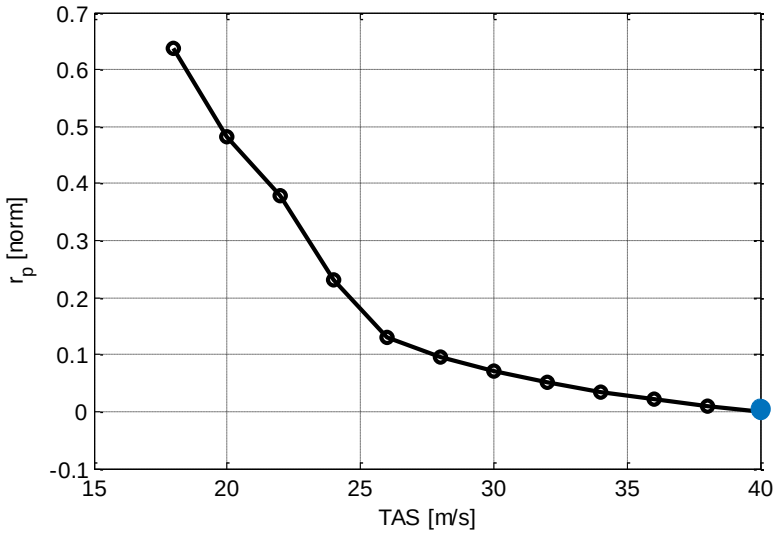

Figure 5.18: Pitch authority required to trim UAV over flight envelope for Configuration 3

Figure 5.18 shows that a maximum amount of 63% positive input at low speed was required to trim the aircraft. A sufficient control surface deflection margin remained for low speeds,

which was desired. An adequate amount of control authority therefore remains to trim the aircraft throughout the speed envelope.

The maximum pitch rate (q) the aircraft can achieve over the flight envelope using Configuration 3 is shown in Table 5.25 below. The first column represents the respective airspeeds at which the pitch rates were determined and the second column contains the maximum pitch rates achieved at the respective airspeeds. The third column contains the pitch commands (r_p) required to reach the respective pitch rates and the last column indicates the load factor (n_z) experienced by the airframe at the respective pitch rates.

Table 5.25: Maximum obtainable pitch rate using Configuration 3 over the flight envelope

TAS [m/s]	**q [°/s]**	**r_p [norm]**	**n_z [g]**
18	5.60	1	-1.16
20	12.50	1	-1.42
25	28.33	1	-2.21
30	42.25	1	-3.18
35	55.10	1	-4.33
40	67.29	1	-5.66
45	79.00	1	-7.16

5.5 Scheduling

The mixing function was scheduled against airspeed to evaluate the aircraft response for two different scenarios: Scenario 1, where there was no scheduling, compared to Scenario 2, where the mixing function was scheduled. The first scenario involved using one mixing function over the entire flight envelope, and the second scenario involved using various mixing functions designed at the respective airspeeds.

The aircraft response in the two scenarios was compared to determine whether scheduling was necessary. The control surface scheduling was done against airspeed in order to investigate various strategies to deal with off-design performance. The mixing functions were implemented in the 6DOF locally developed simulation to evaluate the aircraft behaviour in off-design conditions. The off-design conditions in this thesis refer to any airspeed for which the mixing function was not designed.

The three configurations mentioned in section 5.1 were tested over the entire airspeed range to determine the feasibility of using one mixing function throughout the entire flight envelope. The aircraft response was evaluated to ensure that the handling qualities remained satisfactory when using the mixing functions in off-design conditions. The results are discussed in the sections below.

5.5.1 Aircraft response at 20 m/s

The aircraft responses at an airspeed of 20 m/s in the three different configurations are compared below. If the aircraft response is evaluated at the same airspeed as the one for which the mixing function was designed, it is referred to as the on-design condition, whereas any airspeed for which the mixing function was not designed is the off-design condition. The aircraft response in this section was evaluated in the on-design condition and in two off-design conditions. The on-design condition can be viewed as the aircraft baseline response against which the off-design response is compared. Figure 5.19 illustrates the aircraft response to a full right-roll command ($r_r = 1$), using Configuration 1 as the on-design response, compared to the aircraft off-design response, using configurations 2 and 3. The respective configurations' mixing functions were designed at the following airspeeds:

- Configuration 1 was performed at an airspeed of 20 m/s
- Configuration 2 was performed at an airspeed of 30 m/s
- Configuration 3 was performed at an airspeed of 40 m/s

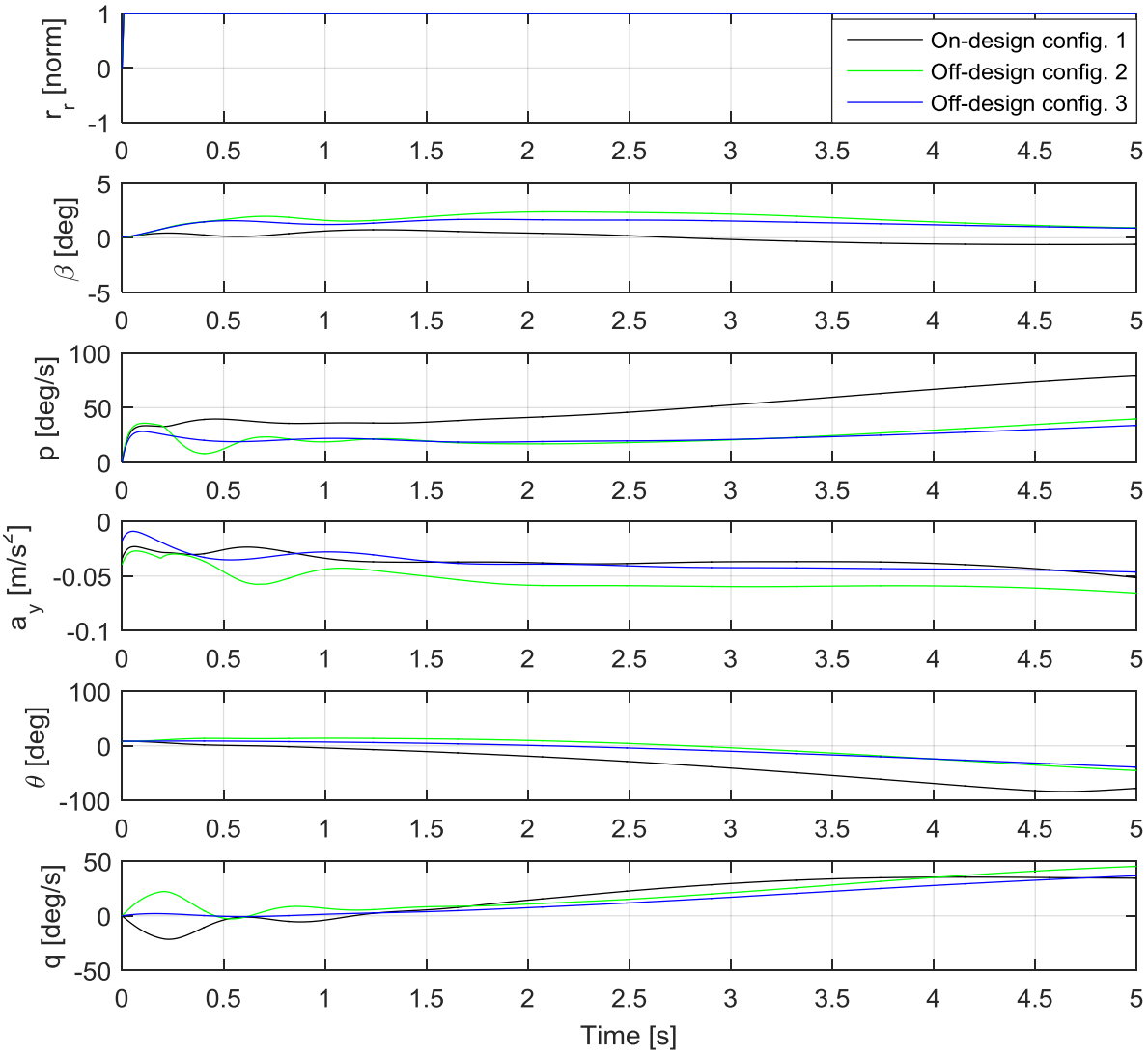

Figure 5.19: Dynamic response for a pure roll input at 20 m/s, comparing all three configurations

Figure 5.19 shows that the adverse yaw effect is higher at 30 and 40 m/s, compared to 20 m/s. A roll rate of about 35°/s was reached within 0.1 seconds after the control input was given for 20 and 30 m/s. The generated roll rate using the mixing function at 40 m/s was smaller, compared to the other two configurations. The long-term off-design effects on the roll rate were very similar, whereas a greater long-term roll rate was generated at 20 m/s.

The side force accelerations for 20 and 40 m/s were similar, although a higher side force acceleration was produced with the 30 m/s control allocation function. The pitch angles for 30 and 40 m/s were similar and smaller than the pitch angle for 20 m/s.

The 30 m/s mixing function produced a positive initial pitch rate, whereas the 20 m/s produced a negative initial pitch rate. A very small initial pitch rate was produced at 40 m/s. The longer-term pitch rates produced by the three configurations all showed a positive increase at similar rates, but a negative pitch angle. The pitch angle indicated that a nose-up pitch command would be required to maintain level flight during a roll to some angle and

subsequent turn. The qualitative pilot-in-the-loop simulations demonstrated that the pitch effects were controllable with normal pitch inputs.

Figure 5.20 illustrates the aircraft response to a full right-yaw command (r_y = 1) when the control allocation function is implemented at 20, 30 and 40 m/s. All three configurations generated an approximate steady-state sideslip angle of -2.0°. There was no initial roll response to a yaw input for any of the three configurations. However, the maximum roll rate that was generated was 20°/s, using the 20 and 30 m/s mixing functions. The roll rate produced at 40 m/s was slightly less than that produced at 20 m/s. The heading angle for all three configurations increased approximately parabolically with time, whereas the pitch rate increased approximately linearly with time. The roll rates produced by all three configurations were similar and increased with time.

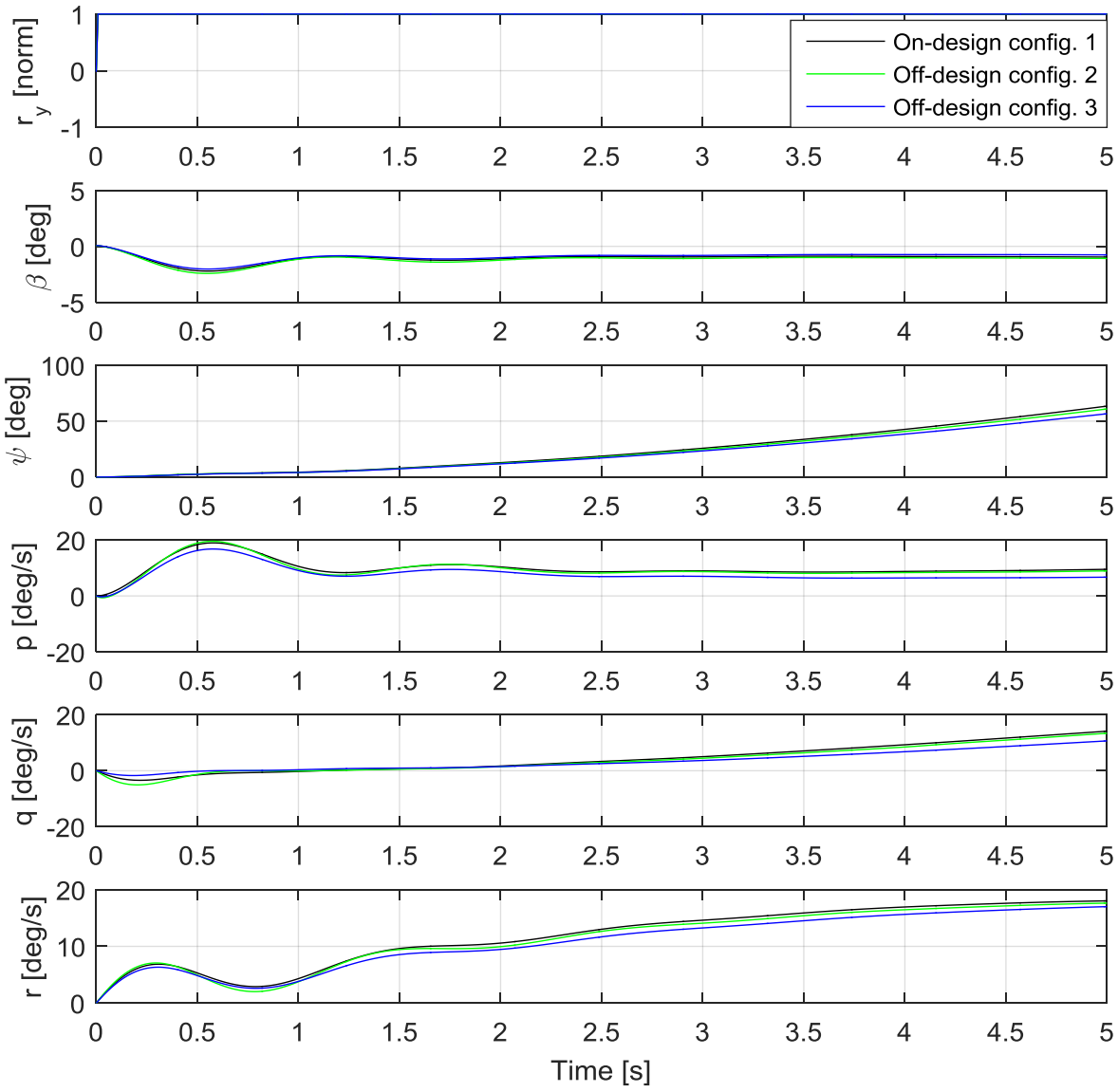

Figure 5.20: Dynamic response for a pure yaw input at 20 m/s, comparing all three configurations

5.5.2 Aircraft response at 30 m/s

The aircraft responses at an airspeed of 30 m/s, using the three configurations, are compared below. The aircraft response in this section was evaluated at the on-design condition, which was 30 m/s and at two off-design conditions which were 20 and 40 m/s respectively. The 30 m/s mixing function results can be seen as the aircraft baseline response with which the off-design response can be compared. Figure 5.21 illustrates the aircraft response to a full right-roll command ($r_r = 1$), using 30 m/s as the on-design response, compared to the aircraft off-design response of the 20 and 40 m/s mixing functions. The configurations in this section are defined as follows:

- Off-design configuration 1: Mixing function designed at 20 m/s
- On-design configuration 2: Mixing function designed at 30 m/s
- Off-design configuration 3: Mixing function designed at 40 m/s

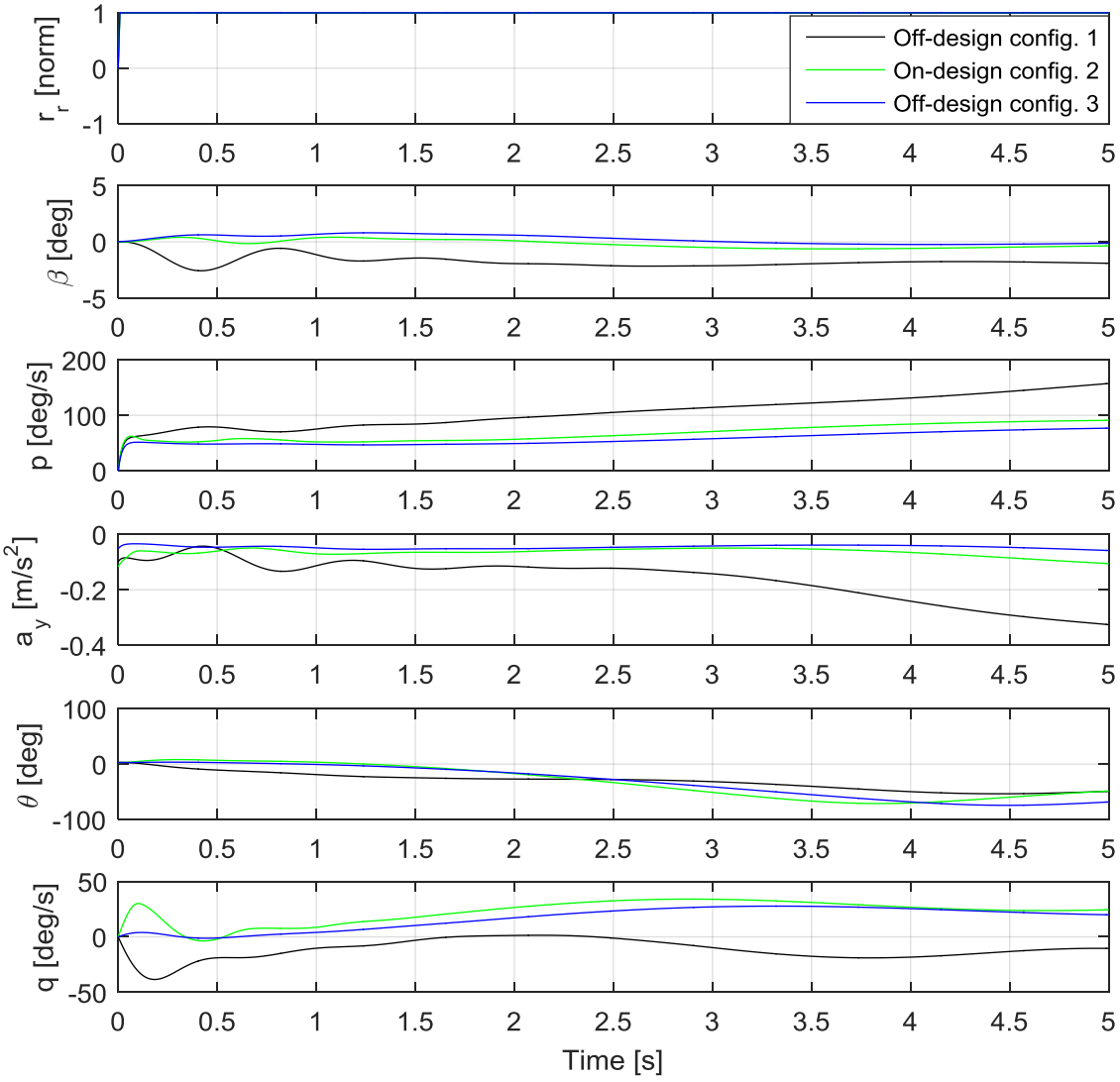

Figure 5.21: Dynamic response for a pure roll input at 30 m/s, comparing all three configurations

Figure 5.21 shows that the adverse yaw effect is slightly higher at 20 m/s than at 30 m/s. A roll rate of about 57°/s was reached within 0.1 seconds after the control input was given for 30 and 20 m/s. The initial roll rate produced at 40 m/s was about 50°/s.

The side force accelerations for the three configurations were very similar, although a higher side force acceleration was produced in the case of the 20 m/s control allocation function.

The pitch angles for the three configurations showed very similar behaviour. A positive initial pitch rate was generated at 30 m/s, whereas a negative initial pitch rate was generated at 20 m/s. A very small initial pitch rate was produced at 40 m/s.

Figure 5.22 illustrates the aircraft response to a full right-yaw command (r_y = 1), using Configuration 2 as the on-design response, compared to the aircraft off-design response using configurations 1 and 3.

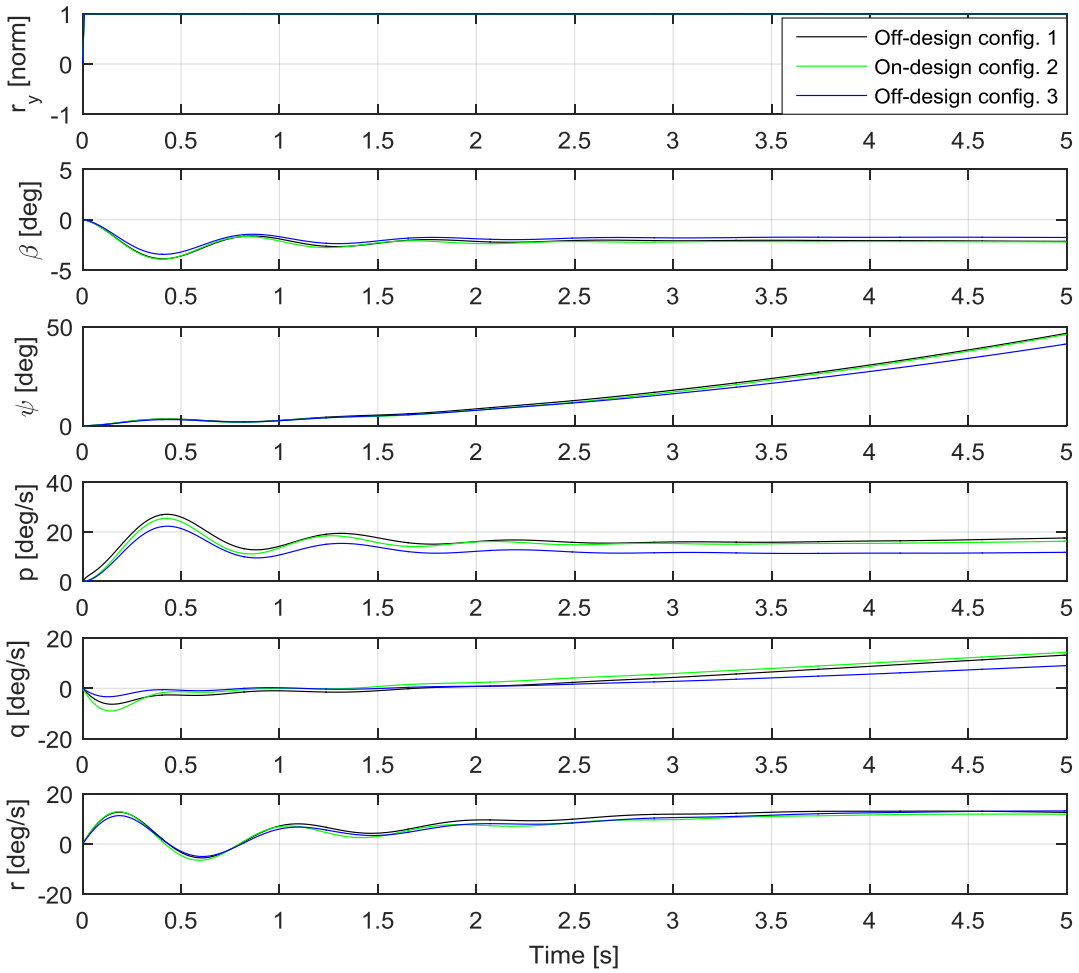

Figure 5.22: Dynamic response for a pure yaw input at 30 m/s, comparing all three configurations

The three configurations all generated a negative steady-state sideslip angle of about -2.4°. The heading angle for all three configurations increased approximately parabolically with time. There was no initial roll response to a yaw input for any of the three configurations. However, the maximum roll rate generated was 25°/s. The configuration at 20 m/s produced the biggest roll rate, and the generated roll rate decreased as the airspeed increased. The

highest pitch rate was generated at 0.1 seconds at 30 m/s. The longer-term pitch rate for all three configurations increased linearly with time. The yaw rates produced by all three configurations were very similar and sufficient.

5.5.3 Aircraft response at 40 m/s

The aircraft responses at an airspeed of 40 m/s, using the three configurations, are compared below. The aircraft response in this section was evaluated at an on-design condition of 40 m/s and at two off-design conditions of 20 and 30 m/s. The 40 m/s configuration results can be seen as the aircraft baseline response against which the off-design response can be compared. Figure 5.23 illustrates the aircraft response to a full right-roll command ($r_r = 1$) at 20, 30 and 40 m/s. The legend in Figure 5.23 can be interpreted using the following information:

- Off-design configuration 1: Mixing function designed at 20 m/s
- Off-design configuration 2: Mixing function designed at 30 m/s
- On-design configuration 3: Mixing function designed at 40 m/s

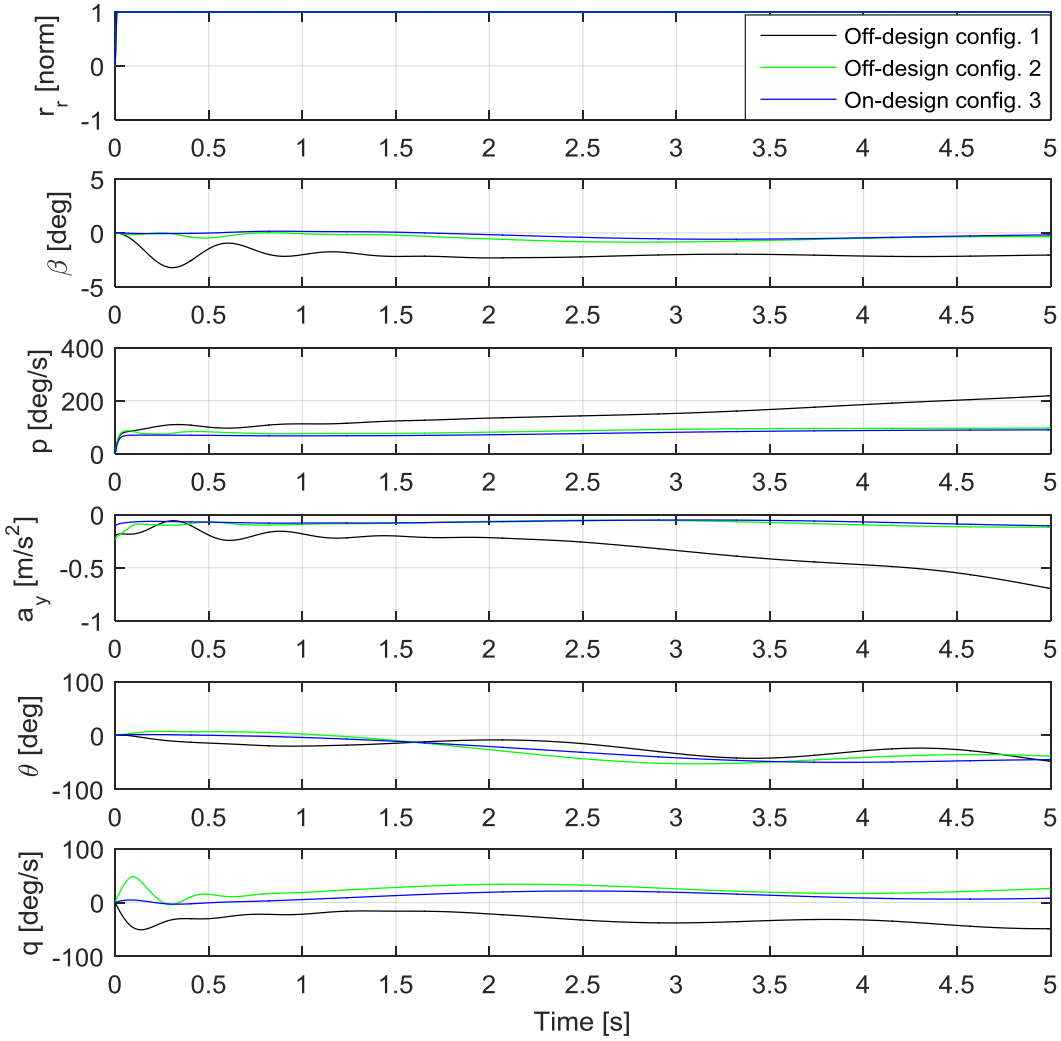

Figure 5.23: Dynamic response for a pure roll input at 40 m/s, comparing all three configurations

As shown in Figure 5.23, the adverse yaw effect was remarkably higher at 20 m/s, compared to 30 and 40 m/s. A roll rate of about 65°/s was reached within 0.1 seconds after the control

input was given at 40 m/s; the 20 and 30 m/s configurations produced slightly higher roll rates at the same time.

The side force accelerations generated at 20 and 30 m/s were slightly higher than at 40 m/s.

The pitch angles for all three configurations showed very similar behaviour. The 30 m/s configuration produced a positive initial pitch rate, whereas the 20 m/s configuration produced a negative initial pitch rate. A very small initial pitch rate was produced at 40 m/s.

Figure 5.24 illustrates the aircraft response to a full right-yaw command ($r_y = 1$) at 20, 30 and 40 m/s. The three configurations generated a negative steady-state sideslip angle of about -2.4°. The heading angle for all three configurations increased approximately parabolically with time. There was no initial roll response to a yaw input for any of the three configurations. However, the maximum roll rate generated was 36°/s. The biggest roll rate was produced at 20 m/s, and the generated roll rate decreased as the airspeed increased. The 40 m/s configuration produced the smallest pitch rate at 0.1 seconds. The longer-term pitch rate for all three configurations increased linearly with time. The yaw rates produced by all three configurations were very similar.

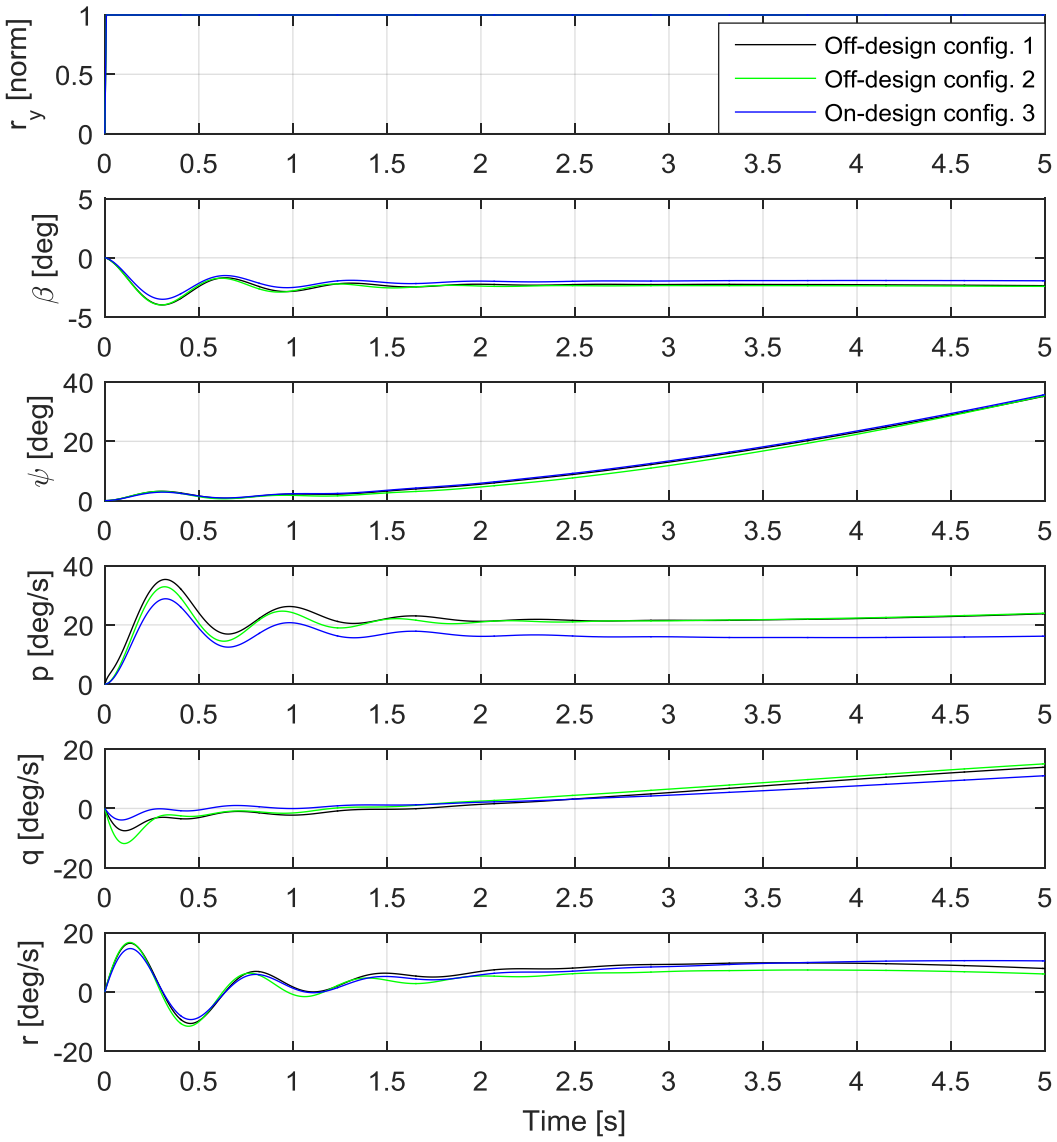

Figure 5.24: Dynamic response for a pure yaw input at 40 m/s, comparing all three configurations

5.5.4 Aircraft response using Configuration 1

The aircraft responses over the speed envelope using Configuration 1, which was designed for 20 m/s, are compared below. Figure 5.25 illustrates the aircraft responses to a full right-roll command ($r_r = 1$) for Configuration 1 over the speed envelope.

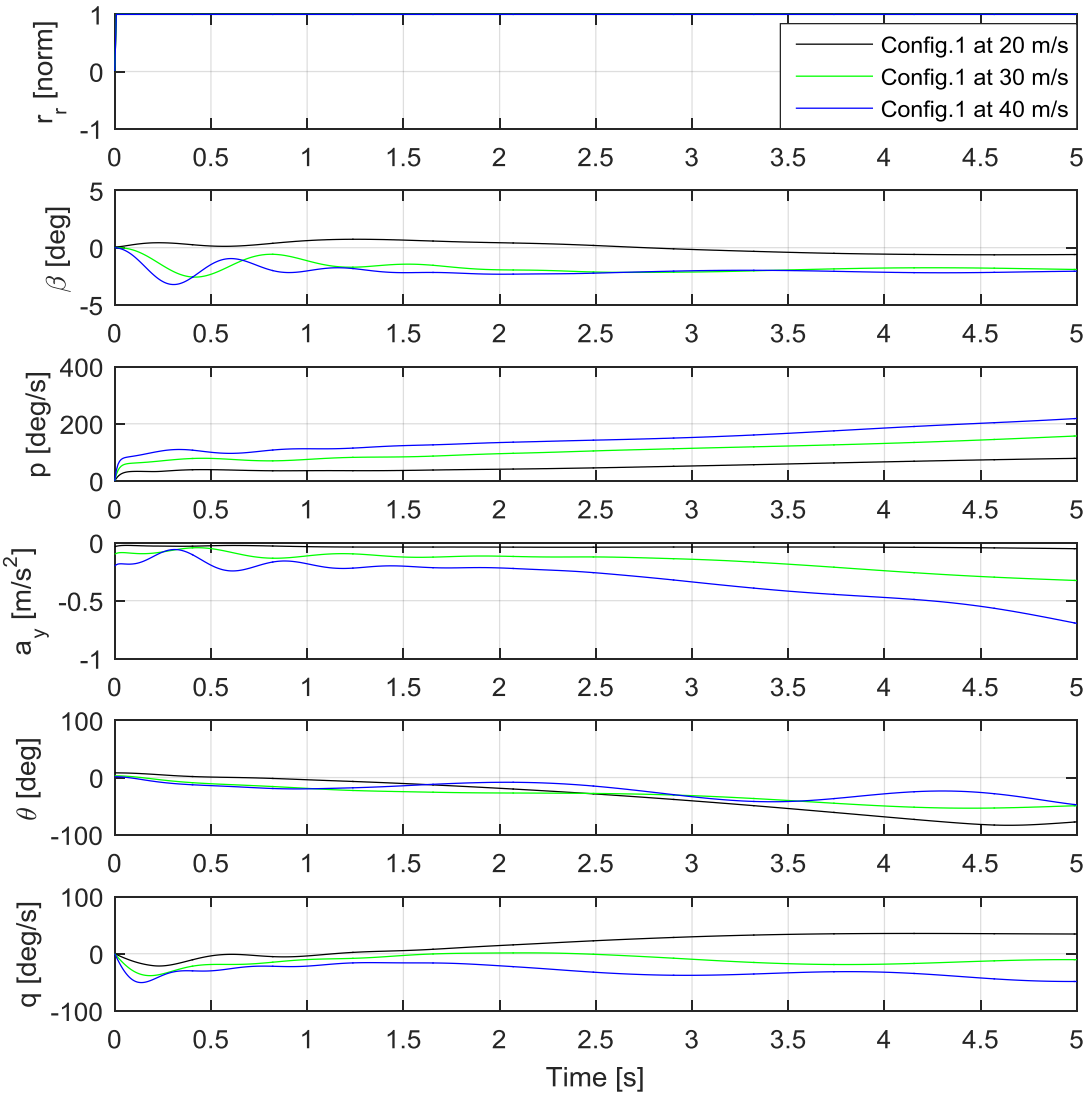

Figure 5.25: Dynamic response for a pure roll input over speed envelope, using Configuration 1

Figure 5.25 illustrates the case for a full roll input command. It was desired to minimise the adverse yaw, which was at a minimum using the mixing function that was designed at 20 m/s. It is clear that slightly higher sideslips were generated when this control allocation function was implemented at 30 and 40 m/s. The pitch coupling illustrated in Figure 5.25 was controllable. The initial pitch angle responses were very similar in the configuration over the entire flight envelope, but the longer-term responses showed different behaviour.

Figure 2.29illustrates the aircraft response to a full right-yaw command (r_y = 1), using Configuration 1 over the speed envelope. Figure 2.29illustrates a full right-yaw command, and it can be seen that Configuration 1 produced higher sideslip angles at 30 and 40 m/s. The initial yaw angles were very similar, but the steady-state sideslips were higher at 30 and 40 m/s, compared to the sideslip at 20 m/s. The biggest roll rates were produced with. Configuration 1 at 30 and 40 m/s. As the airspeed increased, the roll and pitch rate responses increased. This was expected, since the airspeed increased, which resulted in an increase in dynamic pressure. The longer-term pitch rate responses for the envelope of flight increased approximately linearly with time. The biggest yaw rates were generated at 30 and 40 m/s, and

the amount of yaw rate generated increased as the airspeed increased. Most of the differences observed in the results were due to higher dynamic pressure. The directions for the roll, yaw and pitch commands were all conventional, regardless of the airspeed, and the aircraft response was predictable and consistent for a range of airspeeds.

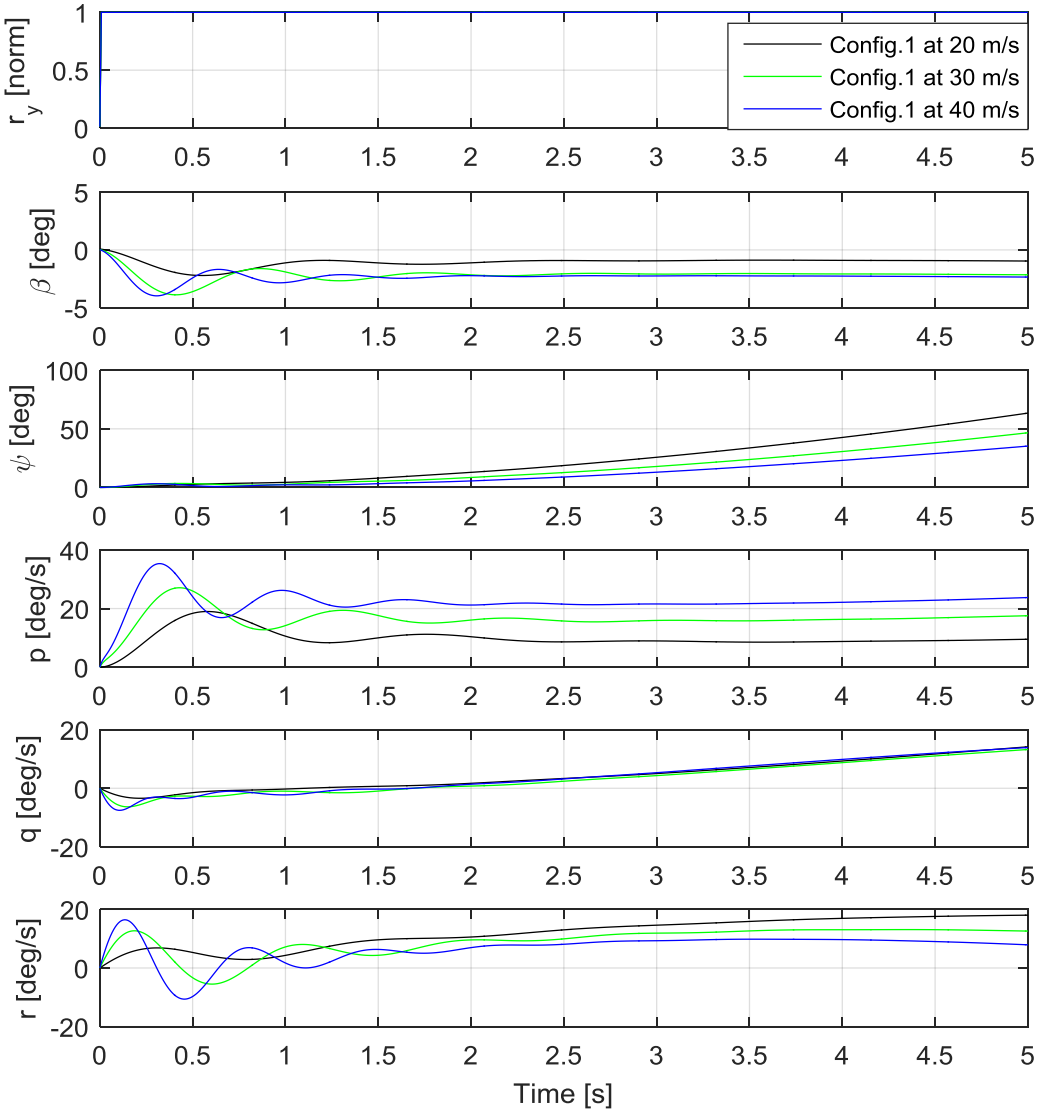

Figure 5.26: Dynamic response for a pure yaw input over speed envelope, using Configuration 1

5.5.5 Aircraft response using Configuration 2

The aircraft responses over the speed envelope using Configuration 2, which was the mixing function designed at 30 m/s, are compared below. Figure 5.27 illustrates the aircraft response to a full right-roll command ($r_r = 1$), using Configuration 2 over the speed envelope.

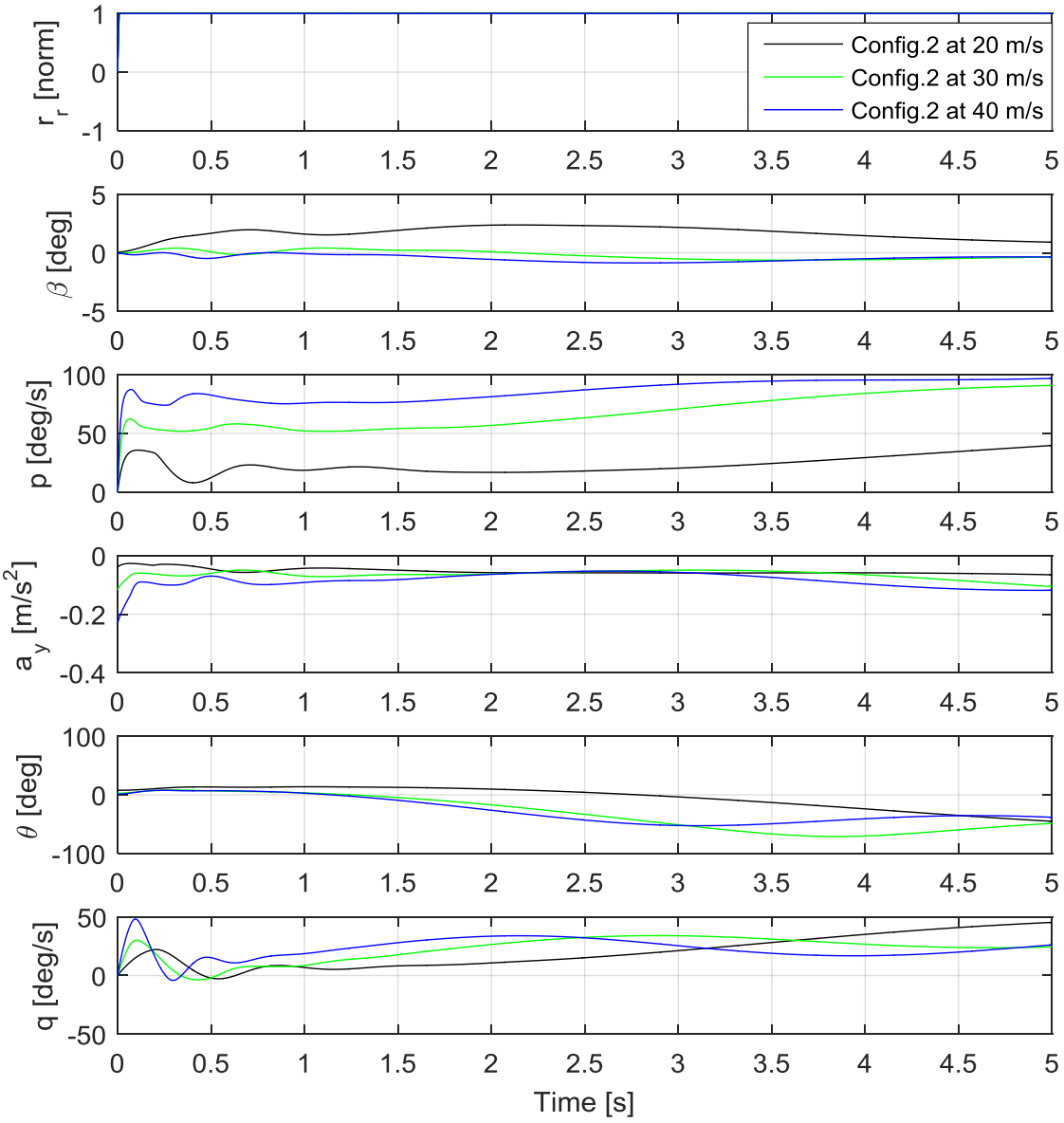

Figure 5.27: Dynamic response for a pure roll input over speed envelope, using Configuration 2

Figure 5.27 indicates that implementing Configuration 2 at 20 m/s generated a greater adverse yaw, compared to 40 m/s. The roll rates generated increased as the airspeed increased when Configuration 2 was implemented. The initial side force acceleration was smallest at 20 m/s and increased as the airspeed increased. However, the longer-term side force acceleration effects decreased and were of a similar magnitude at all three airspeeds. The initial pitch angles at all three airspeeds were very similar. The initial pitch rate generated at 20 m/s was lower than at the other two airspeeds, and a slight lag in reaching the initial maximum value was observed. The highest pitch rate was generated at 40 m/s, which was expected due to a higher dynamic pressure. However, positive initial pitch rates were generated at all three airspeeds. The rates produced by the aircraft increased as the airspeed increased, due to an increase in dynamic pressure.

Figure 5.28 illustrates the aircraft response to a full right-yaw command (r_y = 1), using Configuration 1 over the speed envelope. As shown in Figure 5.28, a negative sideslip was generated for a full right-yaw command, using Configuration 2 over the flight envelope. The sideslips generated increased as the airspeed increased. The sideslips generated at 30 and 40 m/s were very similar, whereas the sideslip generated at 20 m/s was remarkably lower. The initial heading angles for all three airspeeds were very small and only started increasing parabolicly after 1 second. The initial roll rates generated at all three airspeeds were zero. Configuration 2 generated the highest roll rate at 40 m/s, and the smallest roll rate at 20 m/s, and a slight lag in reaching the maximum initial roll rate was observed as the airspeed decreased. The biggest pitch rate was generated at 0.1 seconds after the control input command was given at 40 m/s. The pitch rate decreased as the airspeed decreased. The longer-term pitch rate increased approximately linearly with time for all three airspeeds. The biggest yaw rate was generated at 40 m/s with Configuration 2, and the yaw rate decreased as the airspeed decreased. The initial maximum yaw rate generated at 20 m/s lagged the initial maximum yaw rates generated at 30 and 40 m/s. The figure showed that more rapid responses were obtained for a yaw control input at higher airspeeds using Configuration 2.

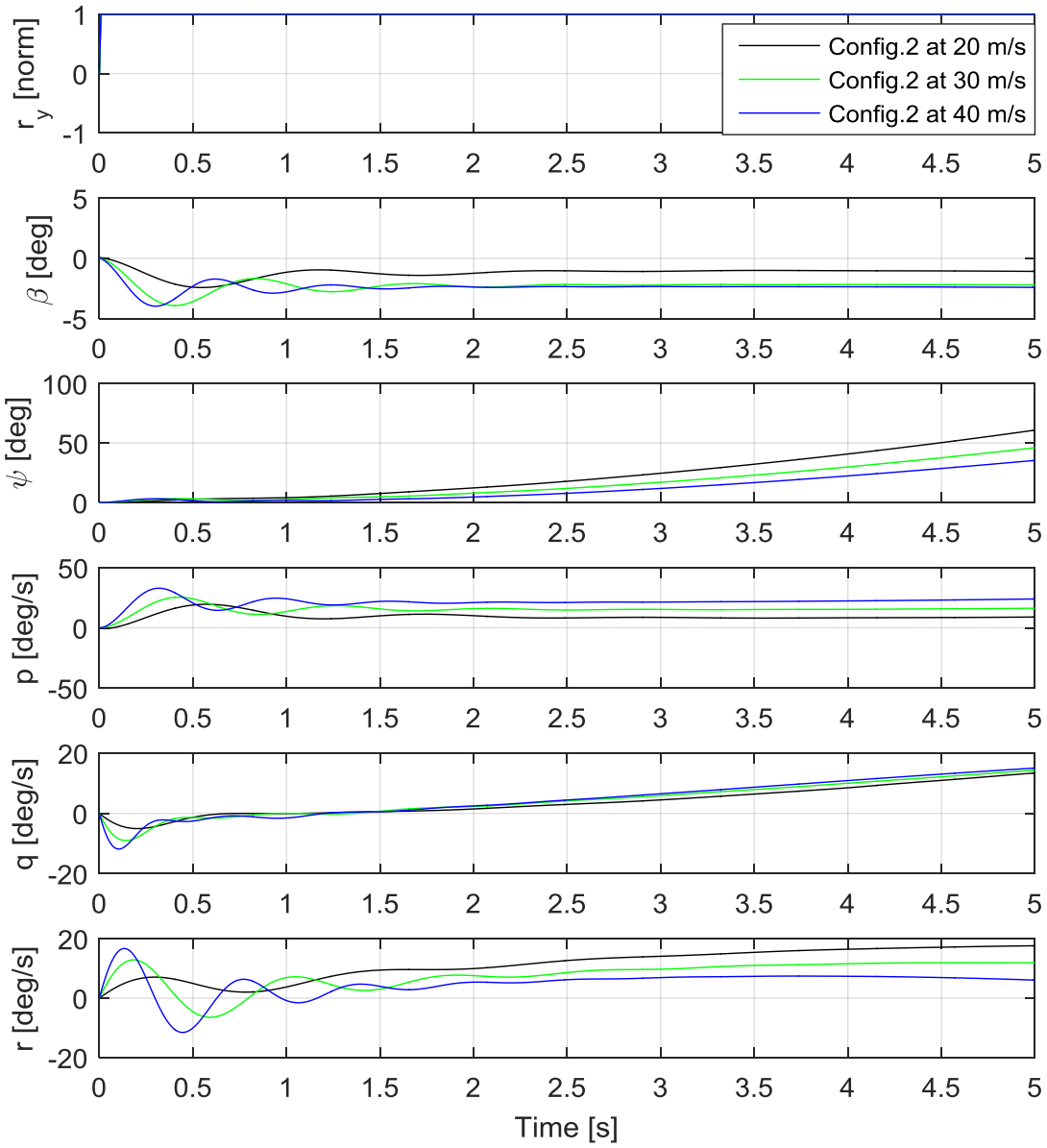

Figure 5.28: Dynamic response for a pure yaw input over speed envelope, using Configuration 2

5.5.6 Aircraft response using Configuration 3

The aircraft responses over the speed envelope using Configuration 3, which was designed at 40 m/s, are compared below. Figure 5.29 illustrates the aircraft response to a full right-roll command ($r_r = 1$) using Configuration 3 over the speed envelope.

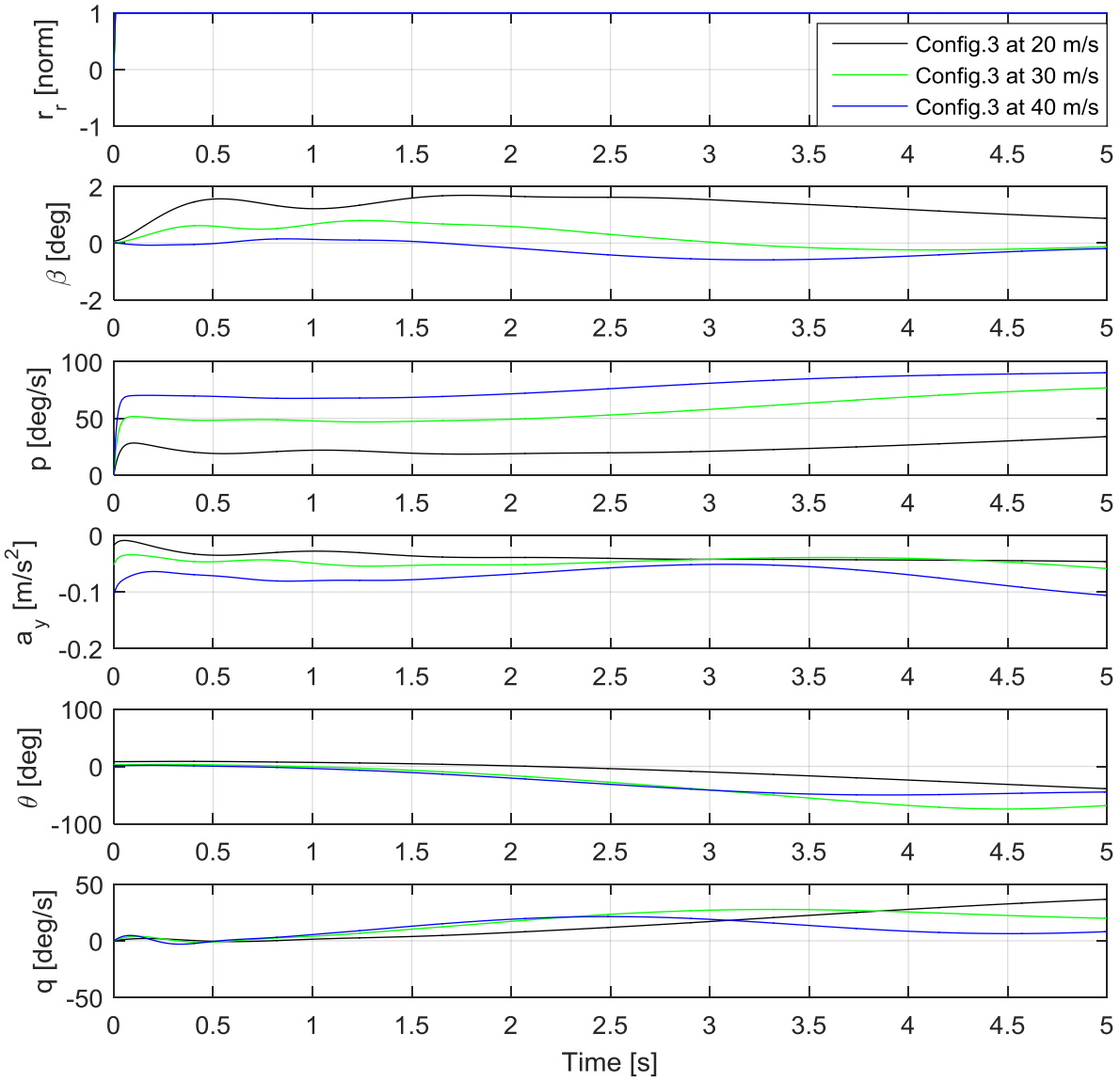

Figure 5.29: Dynamic response for a pure roll input over speed envelope, using Configuration 3

Figure 5.29 illustrates the scenarios when Configuration 3 was implemented. Greater adverse yaws were generated at 20 and 30 m/s, than at 40 m/s. The roll rate increased as the airspeed increased when Configuration 3 was implemented. The initial side force acceleration was the smallest at 20 m/s, and increased with an increase in airspeed. The longer-term side acceleration effect remained relatively constant with minor changes as the time increased. The initial pitch angles at all three airspeeds were very similar, and decreased with time. The initial pitch rates generated were very small at all three airspeeds, with the longer-term effect increasing slightly over time.

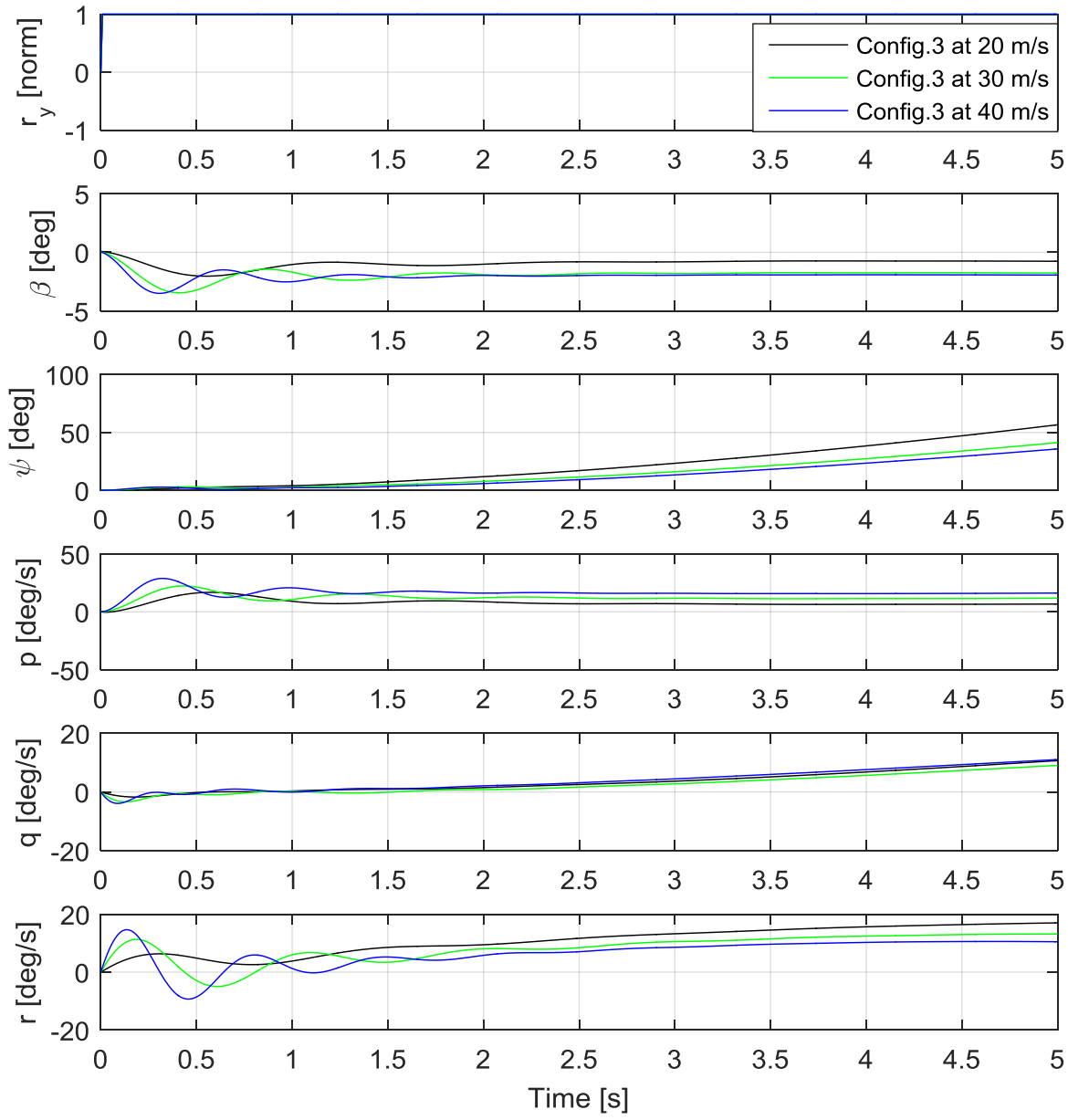

Figure 5.30: Dynamic response for a pure yaw input over speed envelope, using Configuration 3

Figure 5.30 illustrates the aircraft responses to a full right-yaw command (r_y = 1) using Configuration 1 over the speed envelope. As shown in Figure 5.30, a negative sideslip was generated for a full right-yaw command using Configuration 3 over the flight envelope. The sideslips generated at 30 and 40 m/s were very similar, whereas the sideslip generated at 20 m/s was slightly lower. The initial heading angles for all three airspeeds were zero and only started increasing parabolically after about 1 second. The initial roll rates generated at all three airspeeds were zero. Configuration 3 generated the highest roll rate at 40 m/s, and the smallest roll rate at 20 m/s. A slight lag in reaching the maximum initial roll rate was observed as the airspeed decreased. The initial pitch rates generated at 30 and 40 m/s were very similar, with a very small initial pitch rate generated at 20 m/s. The longer-term pitch rate increased approximately linearly with time for all three airspeeds. The biggest yaw rate was generated at 40 m/s using Configuration 3. The yaw rate decreased as the airspeed

decreased, due to a decrease in dynamic pressure. The initial maximum yaw rate generated at 20 m/s lagged behind the initial maximum yaw rates generated at 30 and 40 m/s. The figure showed that a more rapid response was obtained for a yaw control input at higher airspeed, due to higher dynamic pressure.

5.6 Robustness study

The actuator failures were tested in the simulation environment and then compared to flight tests conducted in FlightGear. Sufficient control authority and controllability were the main concerns when investigating the actuator failures for this open-loop system. The following assumptions were made regarding the actuator failures:

- Single actuator failure at a time
- Actuator fail at zero-degree deflection ($\delta = 0°$)

The control authority and aircraft response when experiencing an actuator failure are evaluated below for Configuration 2. The pitch input needed to trim the aircraft at various airspeeds was first evaluated, followed by the simulated aircraft response. The simulations were conducted using Configuration 2, as it appeared to produce the best results throughout the envelope. The sensitivity to actuator failures on the left front and rear wings is provided in this section. The control surfaces on the corresponding left and right side were combined to operate as pairs, and therefore the results are identical for left and right control surface failures due to symmetry.

5.6.1 Simulated failure of inner actuator, front wing

The first simulated failure consisted of the inner actuator failing on the left front wing; the control surface is shown in Figure 5.31 as control surface 7.

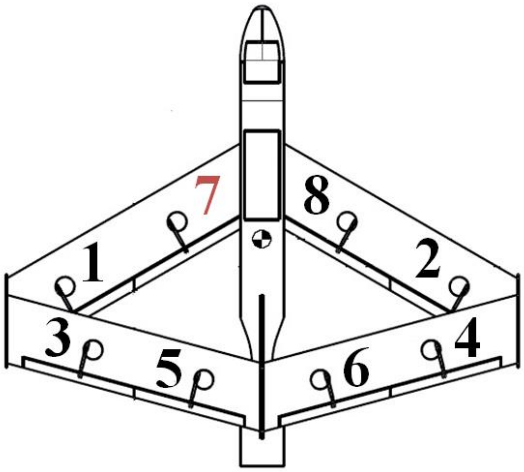

Figure 5.31: Inner left front wing control surface actuator failure

The pitch command required to trim the aircraft as a function of airspeed is illustrated in Figure 5.32. The black line represents the amount of pitch command necessary to trim the aircraft without an actuator failure, whereas the red line illustrates the amount of pitch command necessary to trim the aircraft with the actuator failure.

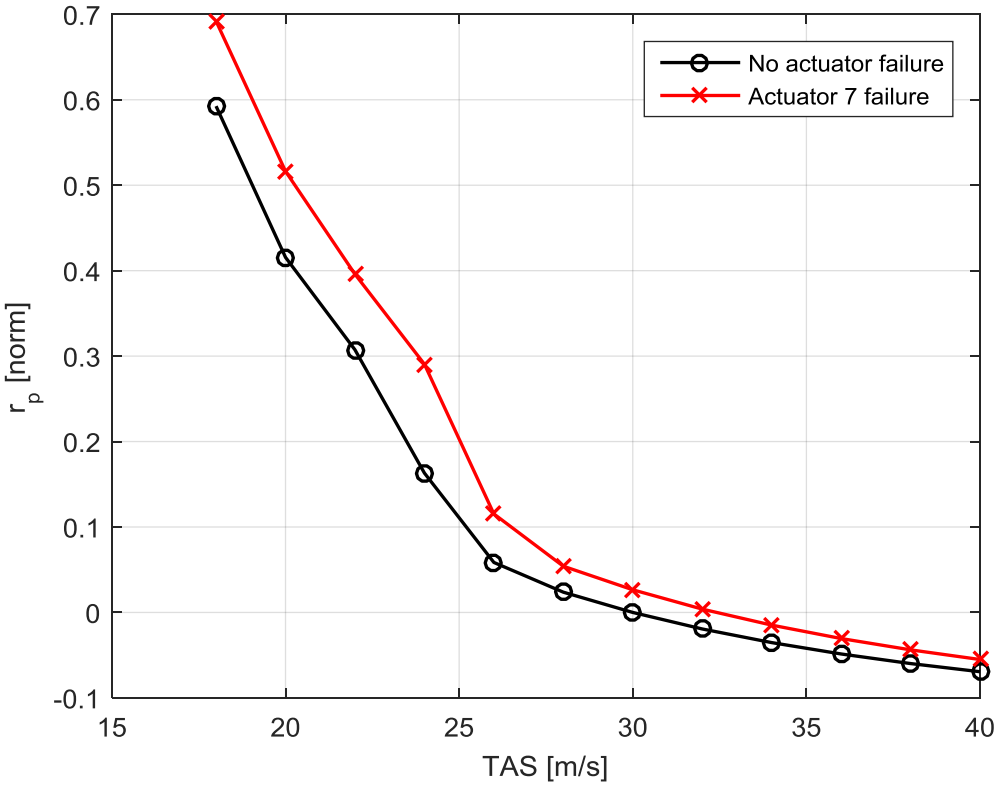

Figure 5.32: Pitch authority required to trim the aircraft with actuator 7 failing

Figure 5.32 shows that only a 10% pitch command increase was required to trim the aircraft at the lowest flyable airspeed when experiencing an actuator failure on control surface 7. A sufficient amount of control authority remained, which indicates that the aircraft was not sensitive to this actuator failure. The dynamic aircraft responses at 18 and 30 m/s were simulated to evaluate the rates obtainable when experiencing an actuator failure – the goal was to determine whether the aircraft was still flyable and controllable.

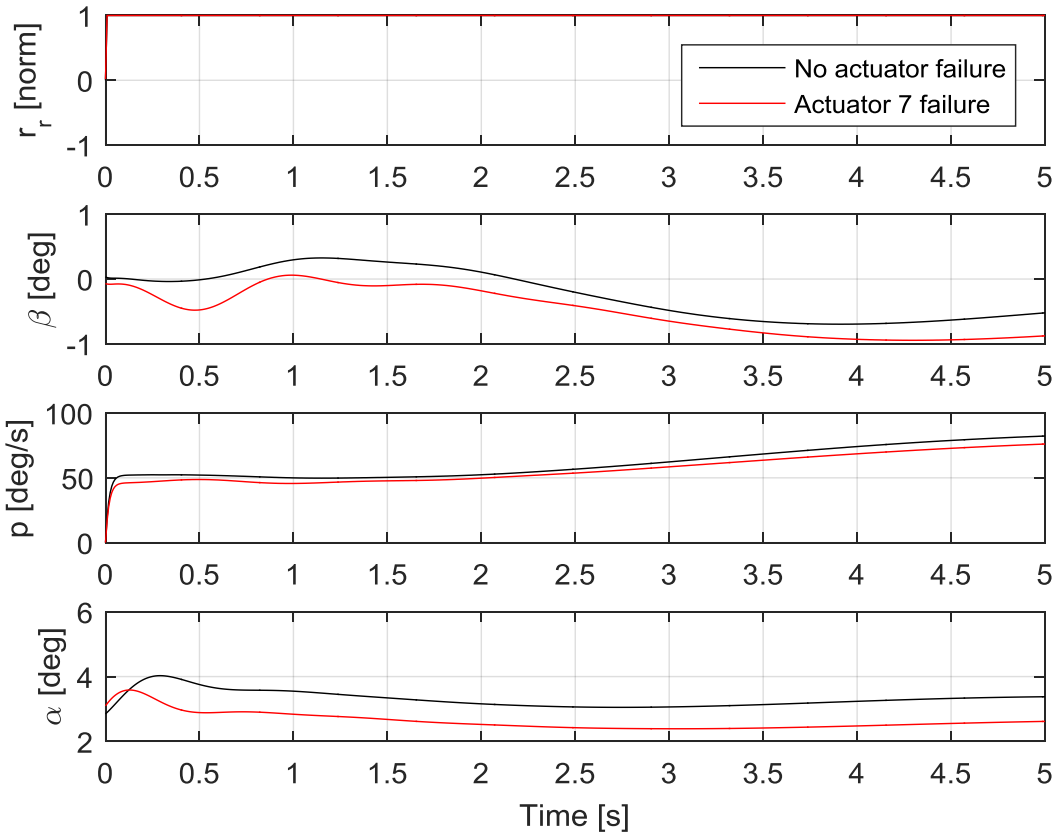

Figure 5.33: Roll response for actuator failure on control surface 7 at 30 m/s

Figure 5.33 illustrates the aircraft dynamic response to a full right-roll command *(r_r = 1)* at 30 m/s. In Figure 5.33, it can be seen that the sideslip amplitude remained the same, although the aircraft initially experienced slightly more oscillations in sideslip. As expected, the roll performance has been slightly degraded due to the failed actuator, but it still appears to be adequate to control the aircraft.

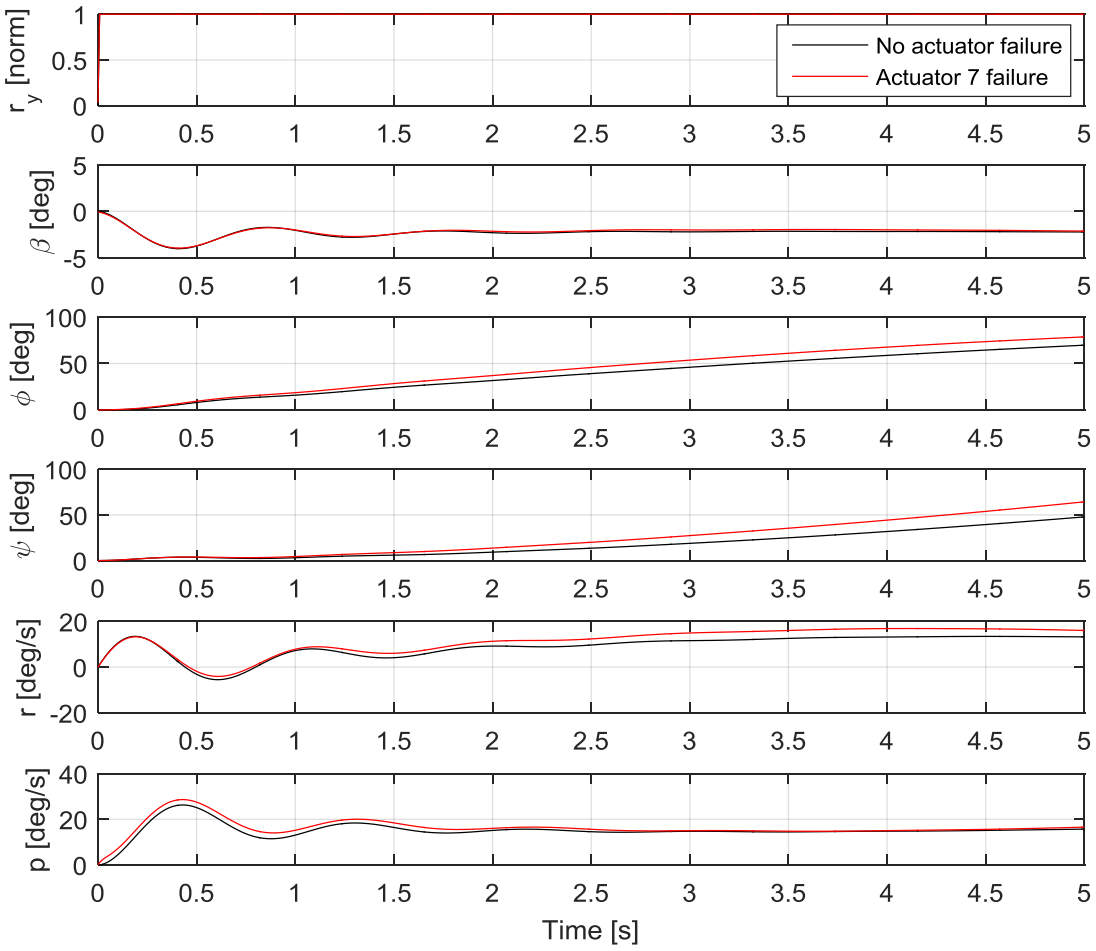

Figure 5.34: Yaw response for actuator failure on control surface 7 at 30 m/s

Figure 5.34 indicates the aircraft dynamic response to a full right-yaw command *(r_y = 1)* at 30 m/s. It is clear that the actuator failure had a negligible effect on the sideslip, although a slightly higher roll rate was generated.

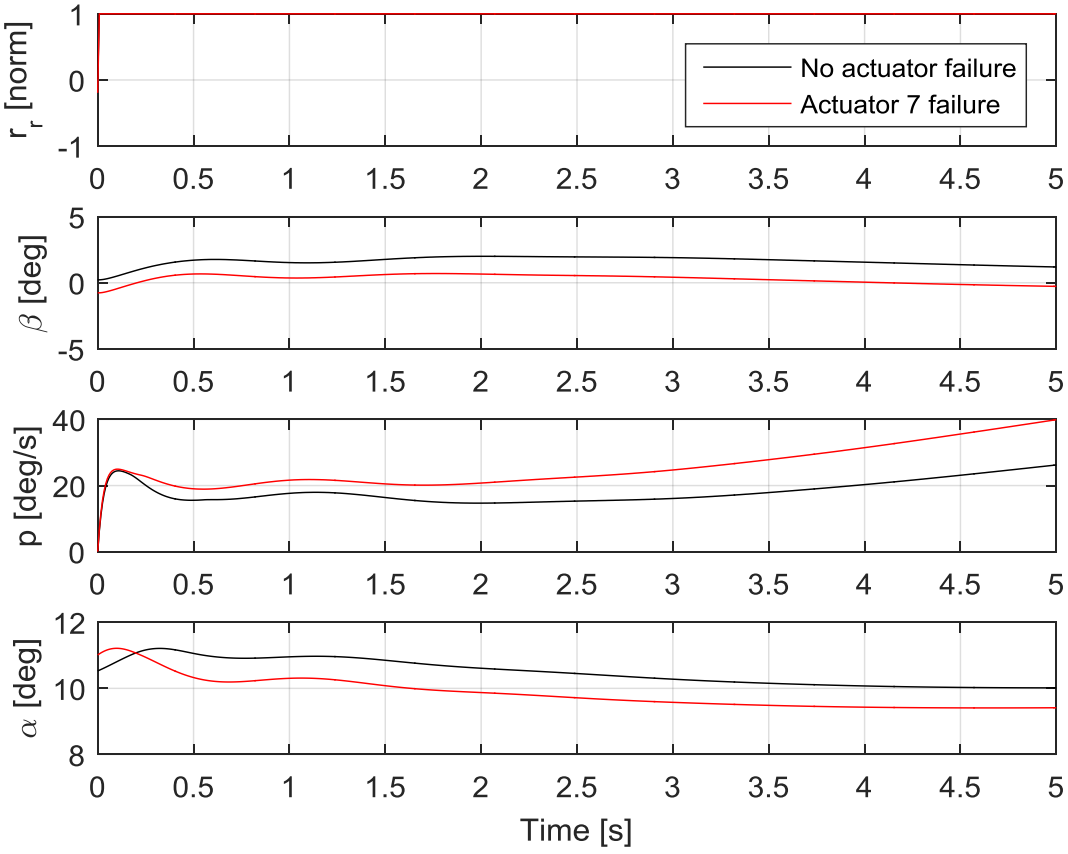

Figure 5.35: Roll response for actuator failure on control surface 7 at 18 m/s

Figure 5.35 illustrates the aircraft dynamic response to a full right-roll command *(r_r = 1)* at 18 m/s. It shows that the sideslip amplitude and trend remained the same. The roll rate was slightly higher for the first two seconds, after which it increased at a higher rate than when experiencing actuator failure. The angle of attack the aircraft maintained while rolling was almost 1° less than when experiencing actuator failure.

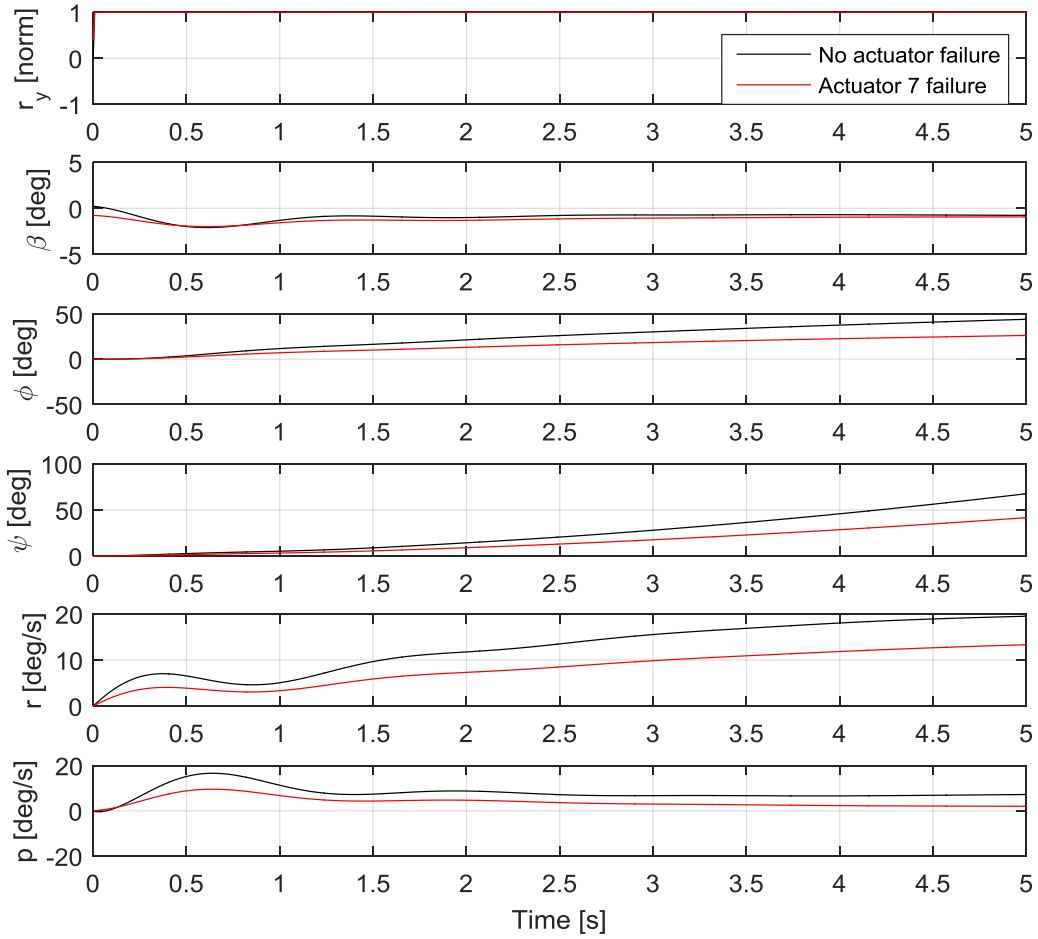

Figure 5.36: Yaw response for actuator failure on control surface 7 at 18 m/s

Figure 5.36 shows the aircraft dynamic response to a full right-yaw command *(r_y = 1)* at 18 m/s. In Figure 5.36, it can be seen that the sideslip generated at 18 m/s with a failure was slightly less than without a failure, but it might go unnoticed when remotely flown by a pilot. The heading and roll angles were slightly less when experiencing a failure. The roll rate generated for a yaw input was less for an actuator failing on control surface 7.

The results provided above show that the inner actuator failing on the left front wing did not have a remarkable impact on the aircraft response. The aircraft was still flyable, since the dynamic responses obtained were only slightly worse than before the failure, and no objectionable oscillations or adverse behaviour was observed, indicating that the aircraft would still be controllable after experiencing this failure.

5.6.2 Simulated failure of outer actuator, front wing

The second simulated failure consisted of the outer actuator failing on the left front wing; the control surface is indicated in Figure 5.37 as control surface 1.

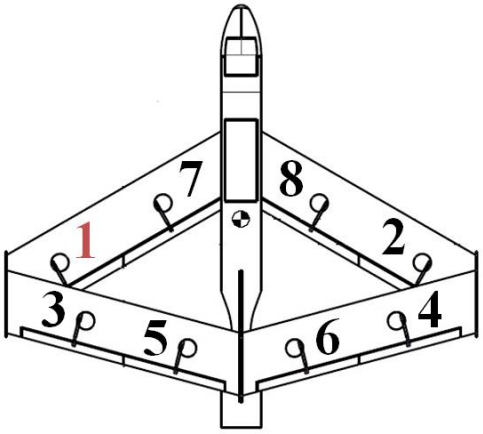

Figure 5.37: Outer left front wing control surface actuator failure

The pitch command required to trim the aircraft as a function of airspeed is illustrated in Figure 5.38. The black line represents the amount of pitch command necessary to trim the aircraft without actuator failure, whereas the red line illustrates the amount of pitch command necessary to trim the aircraft with actuator failure.

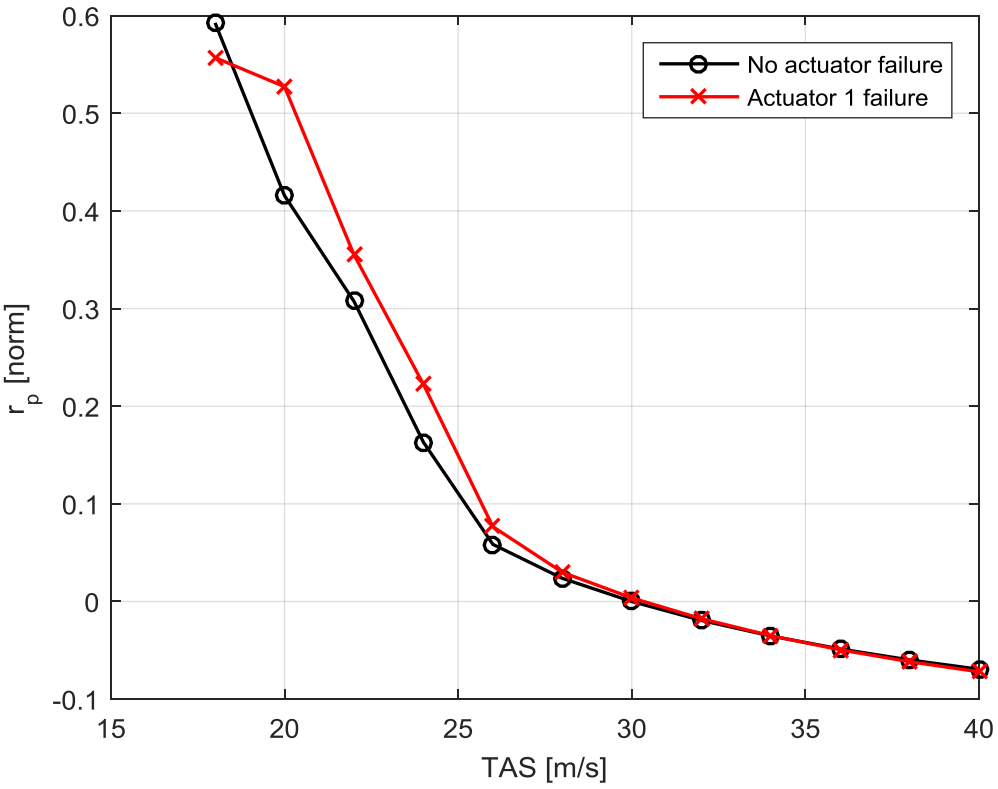

Figure 5.38: Pitch authority required to trim the aircraft with actuator 1 failing

Figure 5.38 shows that less pitch command was required to trim the aircraft at the lowest flyable airspeed after experiencing failure on actuator 1. The required pitch command to trim the aircraft remained more or less the same between 30 and 40 m/s, with an increasing amount of pitch command required as the airspeed decreased to 20 m/s. The results for an actuator failure at 30 m/s are provided below.

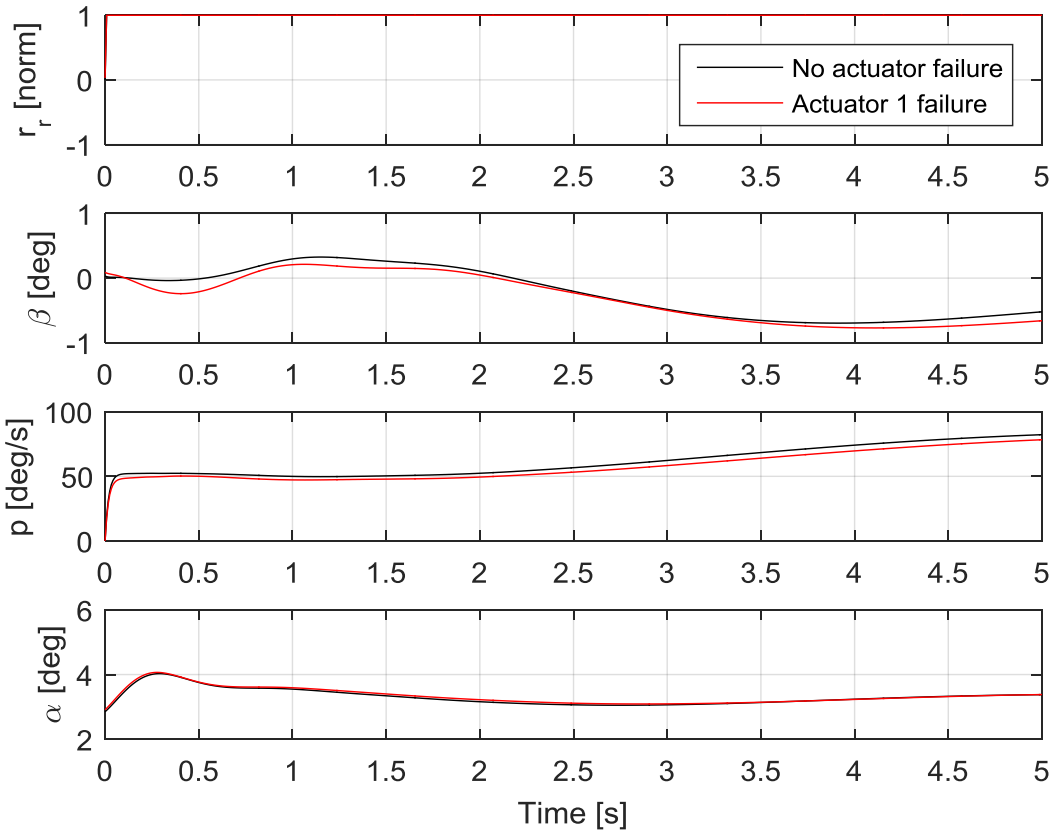

Figure 5.39: Roll response for actuator failure on control surface 1 at 30 m/s

Figure 5.39 illustrates the aircraft dynamic response to a full right-roll command *(r_r = 1)* at 30 m/s. It shows that the aircraft response was almost the same when experiencing actuator failure on control surface 1. The sideslip deviated slightly, but the amplitude remained the same.

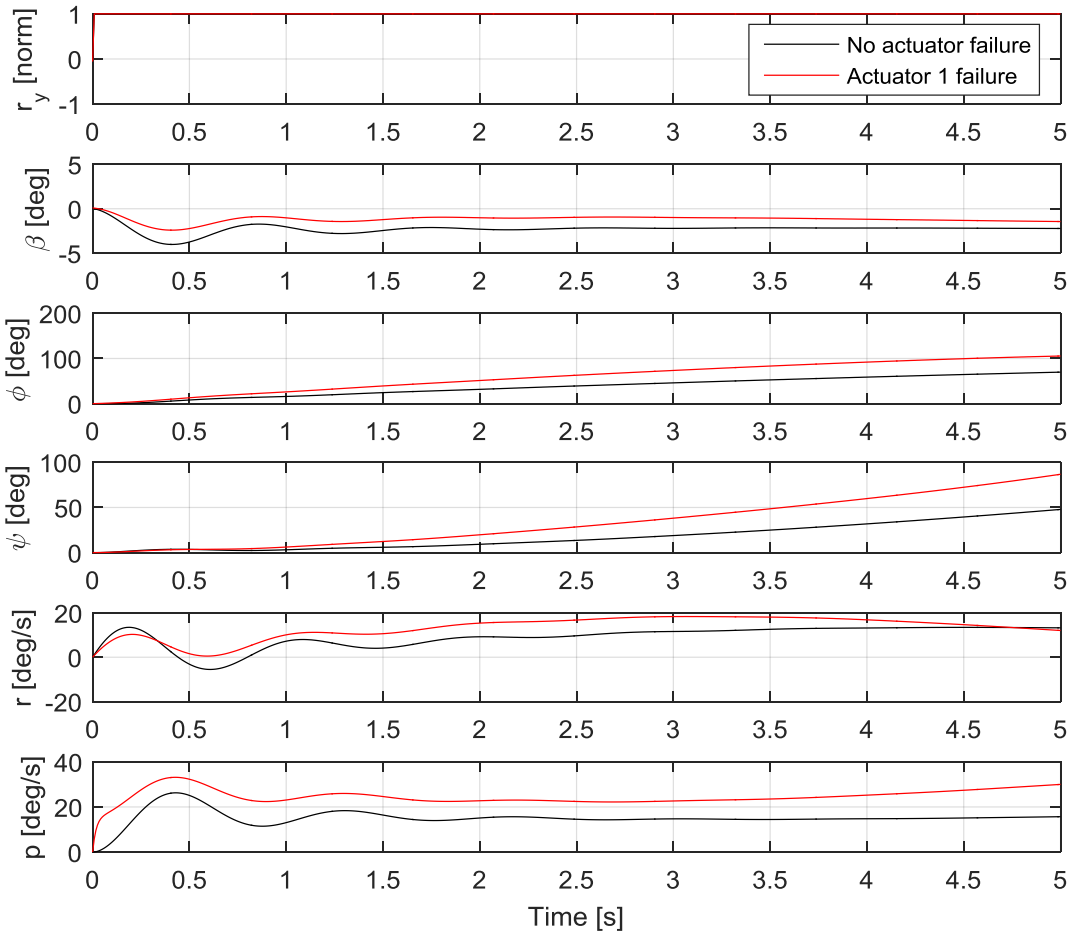

Figure 5.40: Yaw response for actuator failure on control surface 1 at 30 m/s

Figure 5.40 illustrates the aircraft dynamic response to a full right-yaw command *(r_y = 1)* at 30 m/s. Control surfaces 1 and 2 were mostly responsible for yaw control, as mentioned in section 5.2.2, which is why a smaller sideslip for this failure is apparent in Figure 5.40. The roll rate was considerably higher for actuator failure on control surface 1. The optimiser used this control surface to reduce the roll/yaw coupling that existed and therefore an increase in roll rate was observed. A slight increase in roll and heading angle rates was observed.

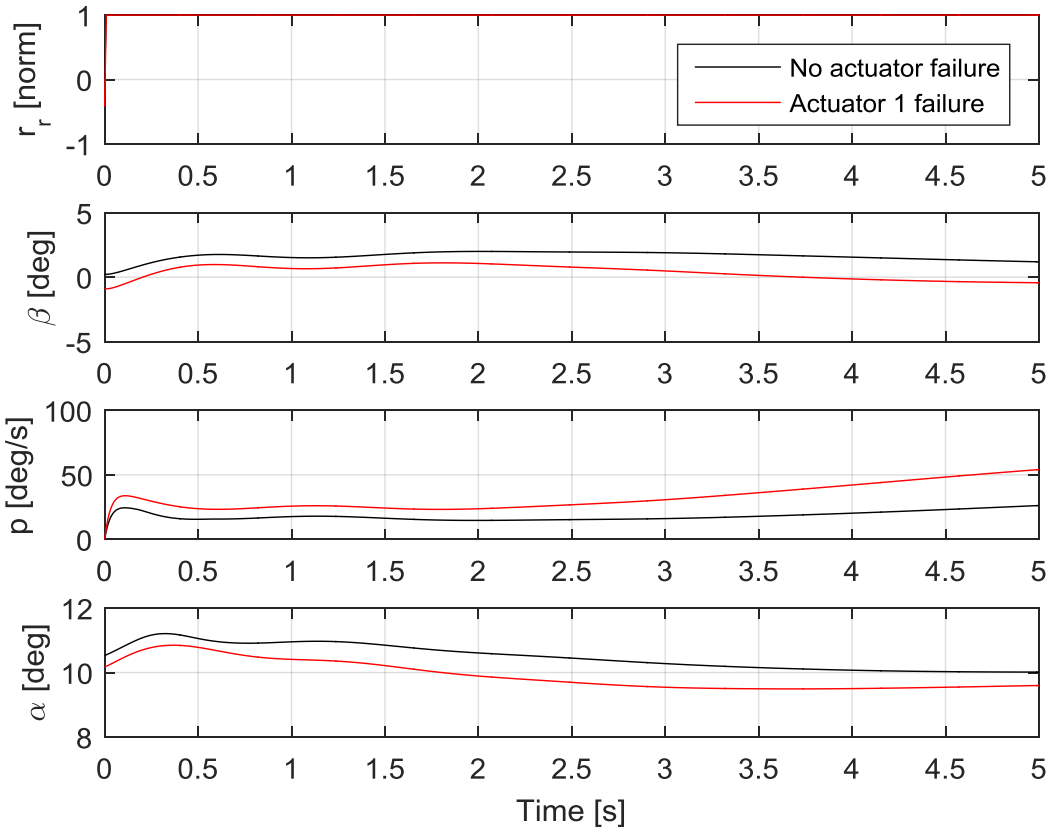

Figure 5.41: Roll response for actuator failure on control surface 1 at 18 m/s

Figure 5.41 illustrates the aircraft dynamic response to a full right-yaw command *(r_y = 1)* at 18 m/s. As shown in Figure 5.41, the sideslip generated was smaller for actuator failure at 18 m/s. However, a higher roll rate was generated for actuator 1 failure.

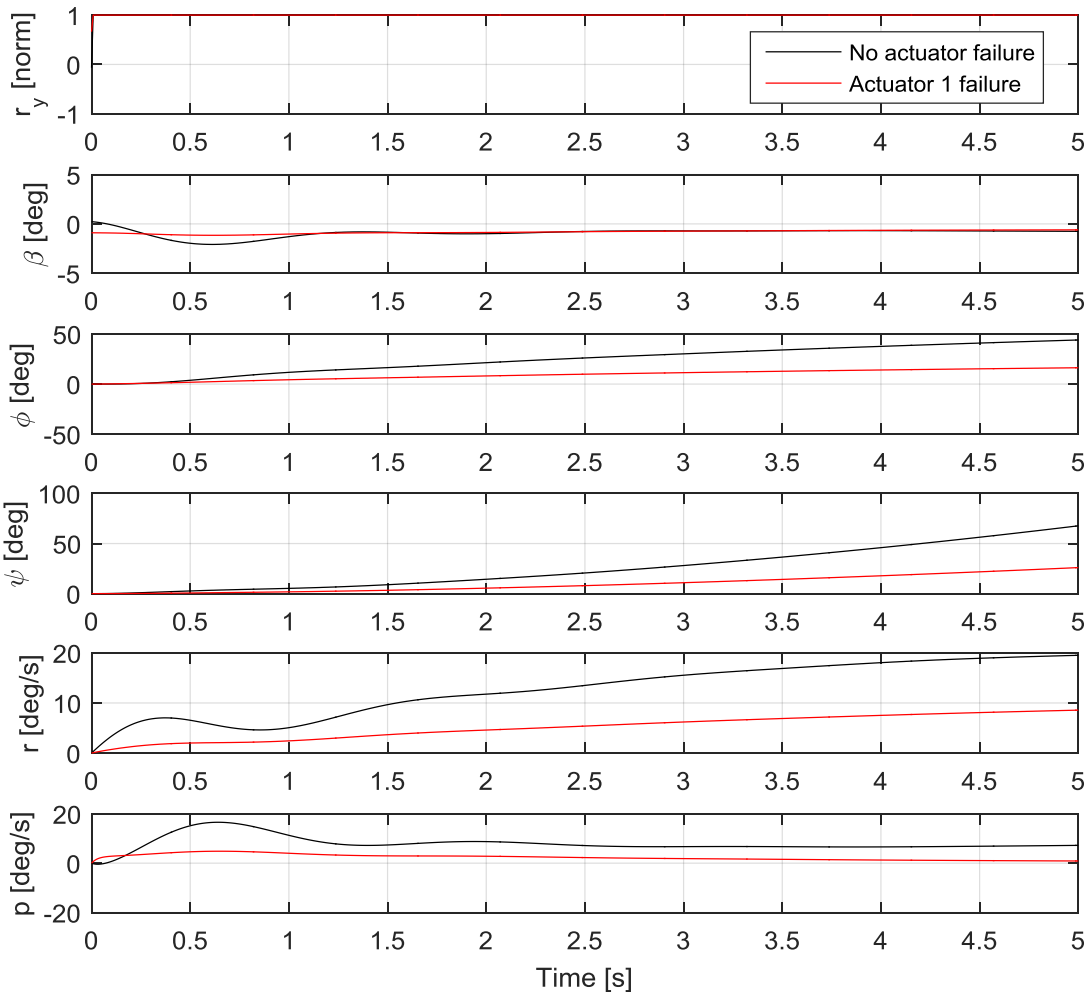

Figure 5.42: Yaw response for actuator failure on control surface 1 at 18 m/s

Figure 5.42 indicates the aircraft dynamic response to a full right-yaw command *(r_y = 1)* at 18 m/s. It shows that the sideslip is constant the entire time. This implies that the simulation program had to use sideslip to trim the aircraft before the dynamic response part started. The yaw command produced virtually no sideslip response during this failure, since control surfaces 1 and 2 were mostly reserved for yawing the aircraft. Little to no response was thus expected for this failure.

5.6.3 Simulated failure of outer actuator, rear wing

The third simulated failure consisted of the outer actuator failing on the left rear wing; the control surface is indicated in Figure 5.43 as control surface 3.

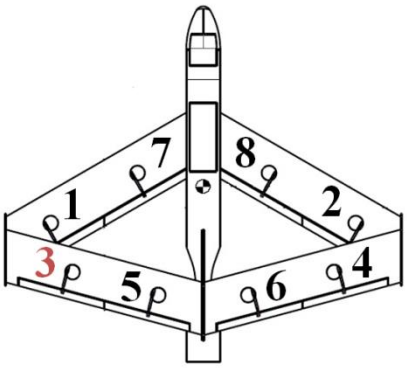

Figure 5.43: Outer left rear wing control surface actuator failure

The pitch command required to trim the aircraft as a function of airspeed is illustrated in Figure 5.44. The black line represents the amount of pitch command necessary to trim the aircraft without actuator failure, whereas the red line illustrates the amount of pitch command necessary to trim the aircraft with actuator failure.

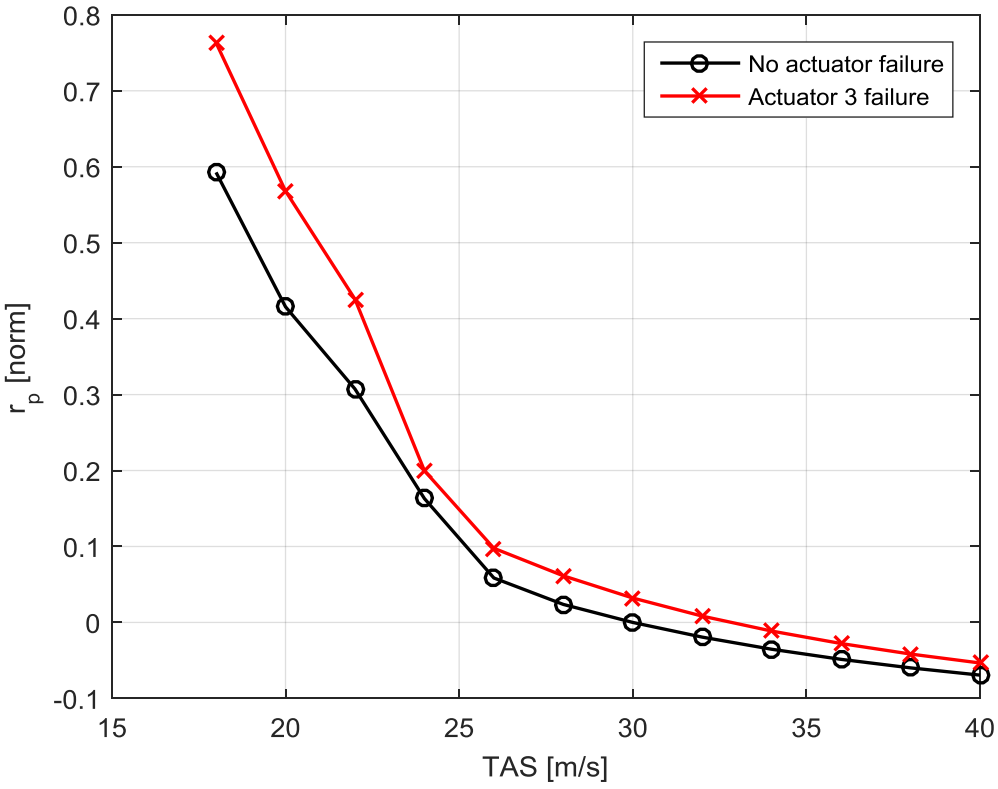

Figure 5.44: Pitch authority required to trim the aircraft with actuator 3 failing

In Figure 5.44, it can be seen that a 17% pitch command increase was required to trim the aircraft at the lowest flyable airspeed when experiencing actuator failure on control surface 3. The dynamic aircraft responses at 18 and 30 m/s were simulated to evaluate the rates obtainable when experiencing actuator failure; the goal was to determine whether the aircraft was still flyable and controllable.

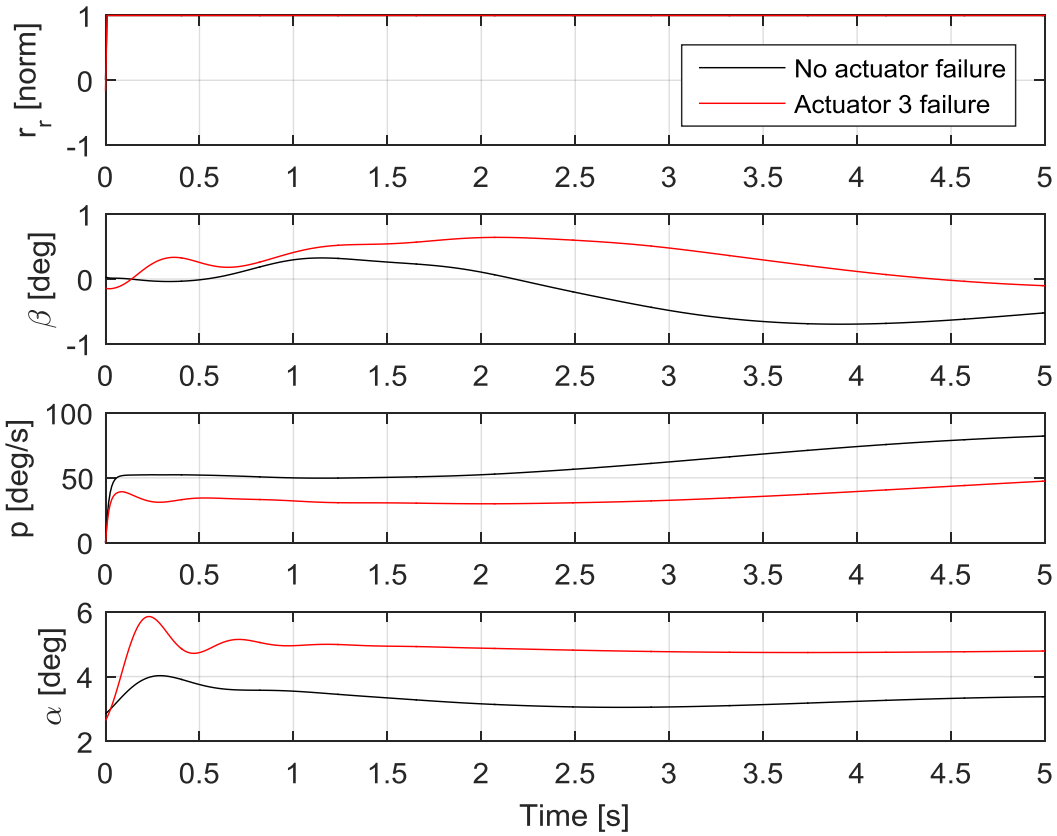

Figure 5.45: Roll response for actuator failure on control surface 3 at 30 m/s

Figure 5.45 illustrates the aircraft dynamic response to a full right-roll command *(r_r = 1)* at 30 m/s. The roll command produced a bigger and more oscillatory sideslip – indicated in Figure 5.45 – when the actuator on control surface 3 failed. The roll rate produced by the aircraft was considerably lower for this failure, but this was expected, as the optimiser mainly allocated control surfaces 3 and 4 to roll the aircraft. The roll command caused a larger angle-of-attack excursion in the presence of this failure. Control surfaces 3 and 4 were also used to pitch the aircraft, and the loss of control surface 3 therefore resulted in a larger angle-of-attack excursion.

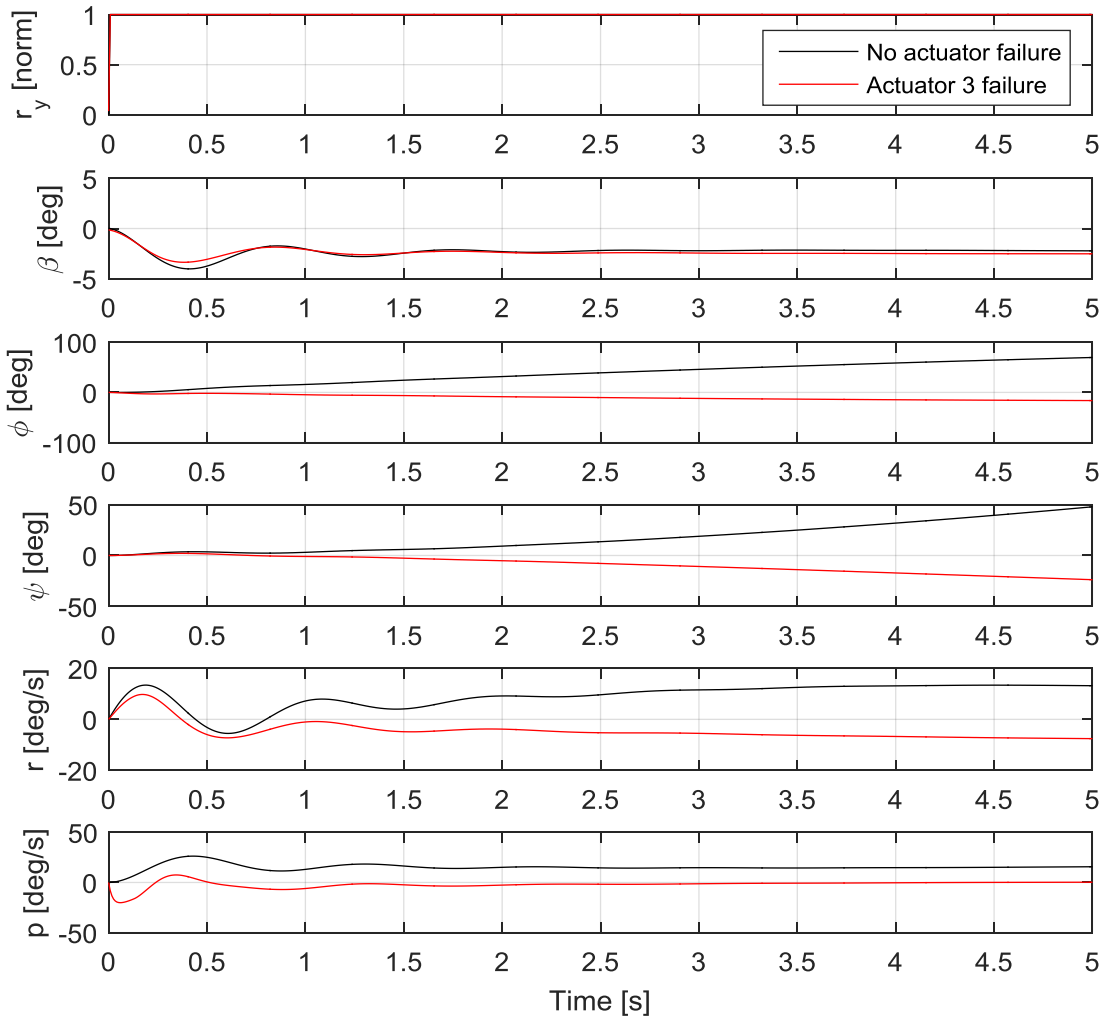

Figure 5.46: Yaw response for actuator failure on control surface 3 at 30 m/s

Figure 5.46 shows the aircraft dynamic response to a full right-yaw command *(r_y = 1)* at 30 m/s. As seen in this figure, a full right-yaw command produced a negative sideslip, which was expected, although the heading and roll angle response was predictable. The no-failure case produced a rolling moment to the right, which would be conventional for a positive dihedral effect, whereas a very small rolling moment to the left was produced in the case of failure. The same response was seen for the heading; a yawing moment to the right was produced for the no-failure case, whereas a yawing moment to the left was produced for the failure case. The heading angle was reduced, because the anhedral effect rolled the wings to the left, which initiated a poorly coordinated left-hand turn.

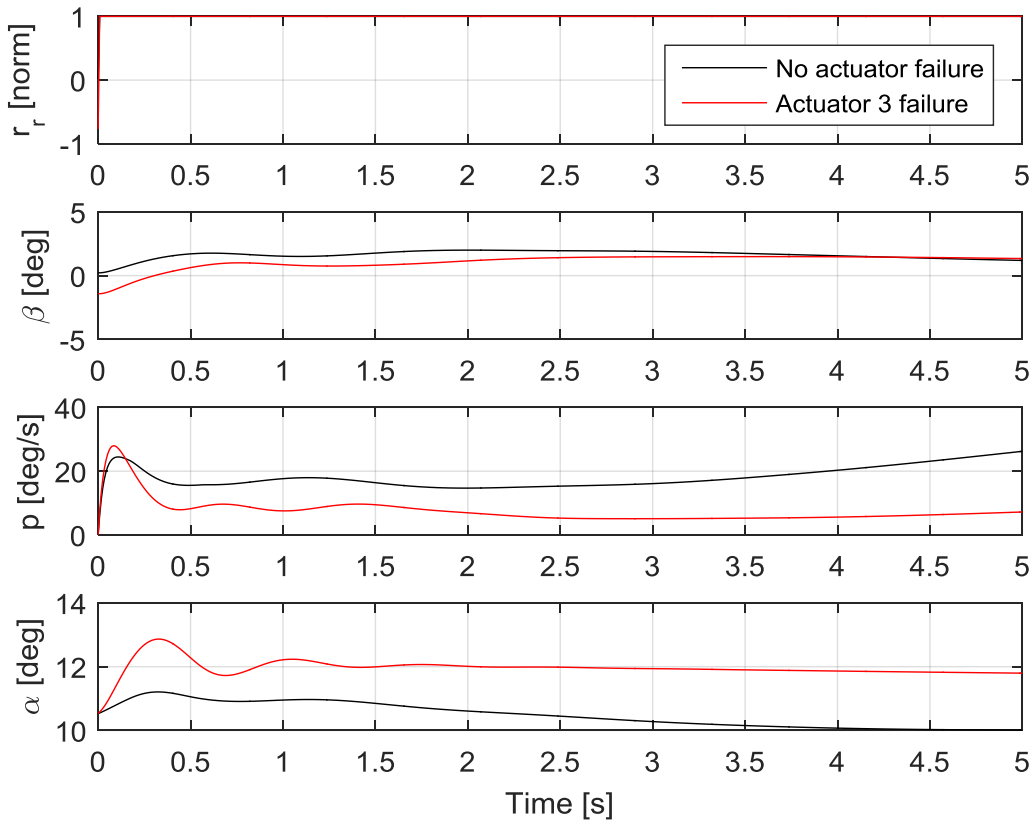

Figure 5.47: Roll response for actuator failure on control surface 3 at 18 m/s

Figure 5.47 illustrates the aircraft dynamic response to a full right-roll command *(r_r = 1)* at 18 m/s. The roll command shown in Figure 5.47 produced a large negative initial sideslip, but it progressed to a positive sideslip similar to that in the case of no actuator failure. The initial roll rate generated by the aircraft rapidly increased within the first 0.1 seconds, but reduced rapidly within 0.5 seconds after the input command was given. The longer-term roll rate was considerably lower for this failure, but it was expected, as the optimiser allocated control surfaces 3 and 4 to mainly roll the aircraft. An opposing rolling moment was produced for this failure; the sideslip caused a type of dihedral effect that created an opposing rolling response.

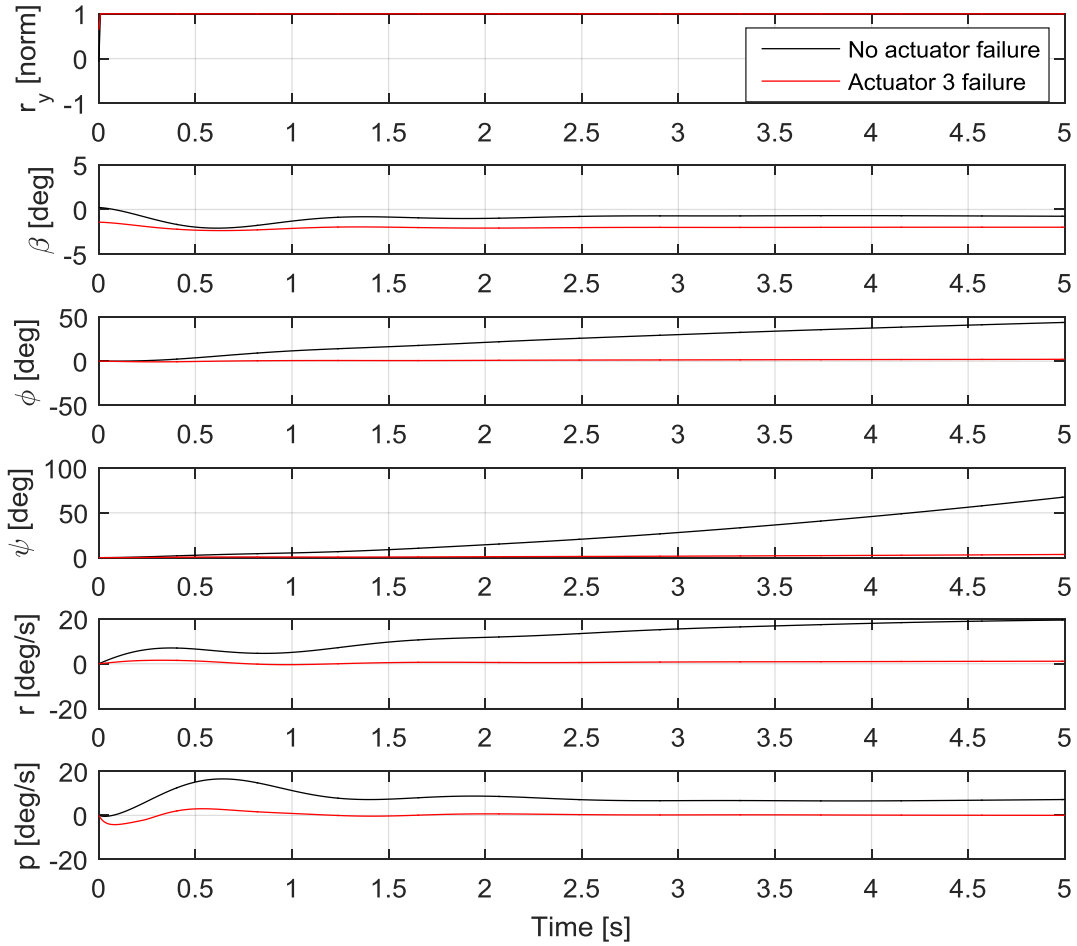

Figure 5.48: Yaw response for actuator failure on control surface 3 at 18 m/s

Figure 5.48 indicates the aircraft dynamic response to a full right-yaw command *(r_y = 1)* at 18 m/s. In this figure, it is clear that the sideslip starts with a negative value. This is due to the assumption that the control surface failed at 0° deflection, which resulted in the aircraft starting with an asymmetric deflection of control surfaces in trim. The roll and yaw angles remained unchanged, which implies that there was no yaw control for this failure. The optimiser allocated control surfaces 1, 2, 3 and 4 to primarily yaw the aircraft, with the control surfaces on the rear wing having a greater effect on the aircraft response. Therefore there was no yaw control for this failure.

The opposite control surface failure is illustrated in Figure 5.50. This was the only case in which the corresponding control surface failures were illustrated. Due to the results illustrated in Figure 5.48, the opposite control surface failure was simulated to determine whether the results obtained would be the same for both failures. The roll and yaw angles also remained unchanged for this control surface failure. There was no yaw response for this control surface failure pair. This was therefore a result of the differential effect designed as part of the mixing function.

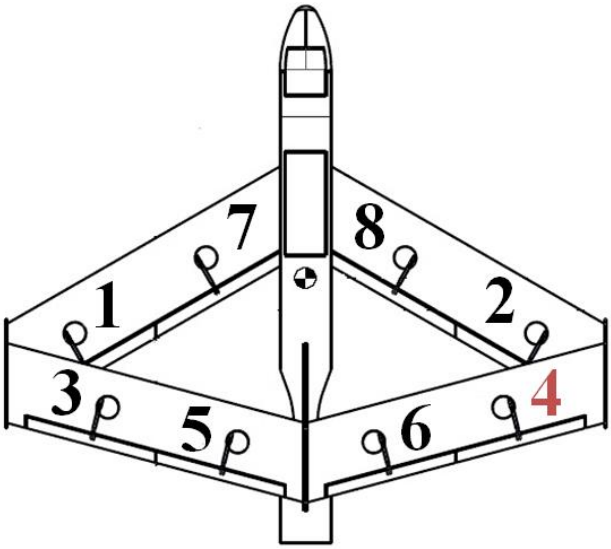

Figure 5.49: Outer right rear wing control surface actuator failure

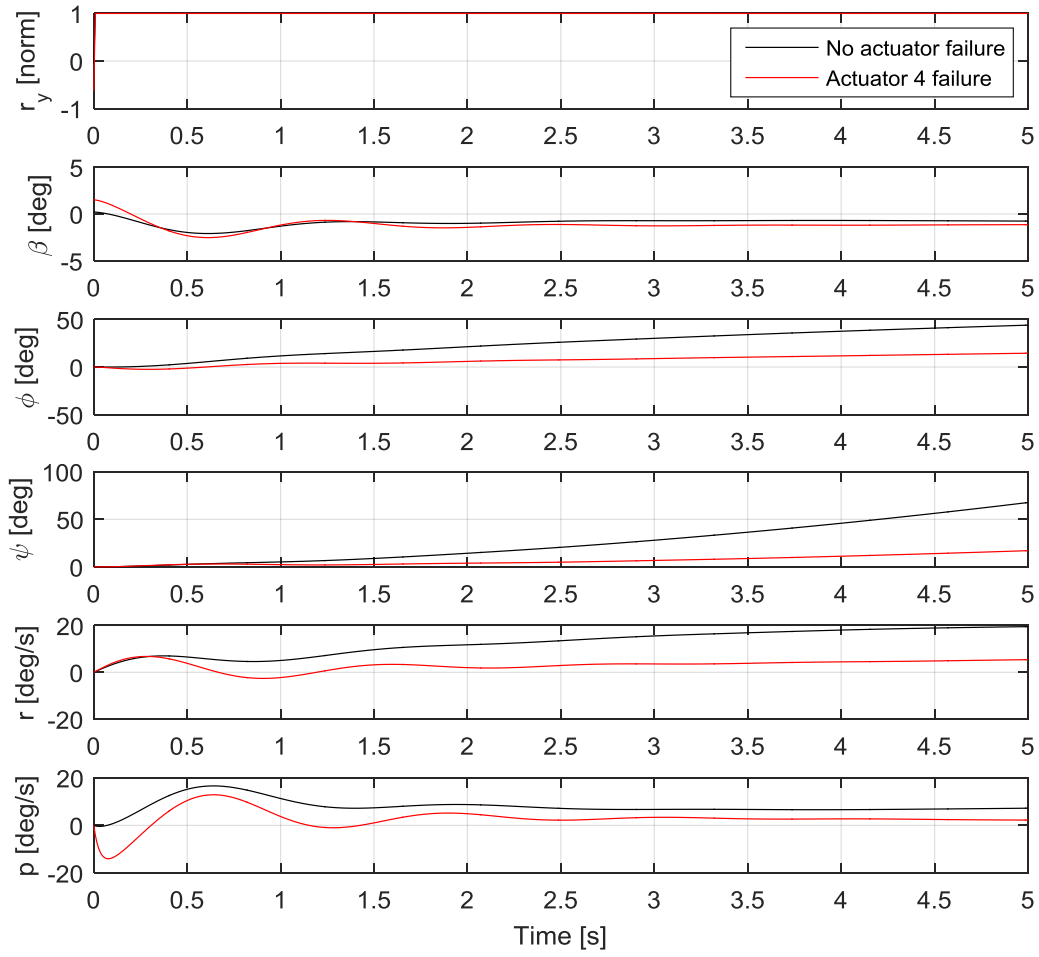

Figure 5.50: Yaw response for actuator failure on control surface 4 at 18 m/s

5.6.4 Simulated failure of inner actuator, rear wing

The fourth simulated failure consisted of the inner actuator failing on the left rear wing; the control surface is indicated in Figure 5.51 as control surface 5.

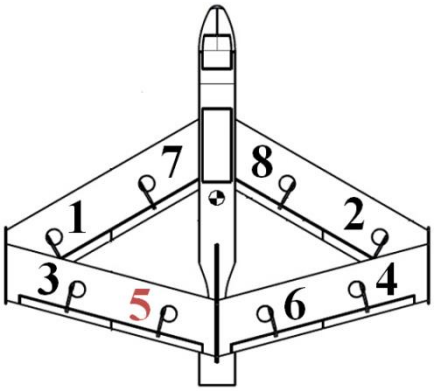

Figure 5.51: Inner left rear wing control surface actuator failure

The pitch command required to trim the aircraft as a function of airspeed is illustrated in Figure 5.52. The black line represents the amount of pitch command necessary to trim the aircraft without actuator failure, whereas the red line illustrates the amount of pitch command necessary to trim the aircraft with actuator failure.

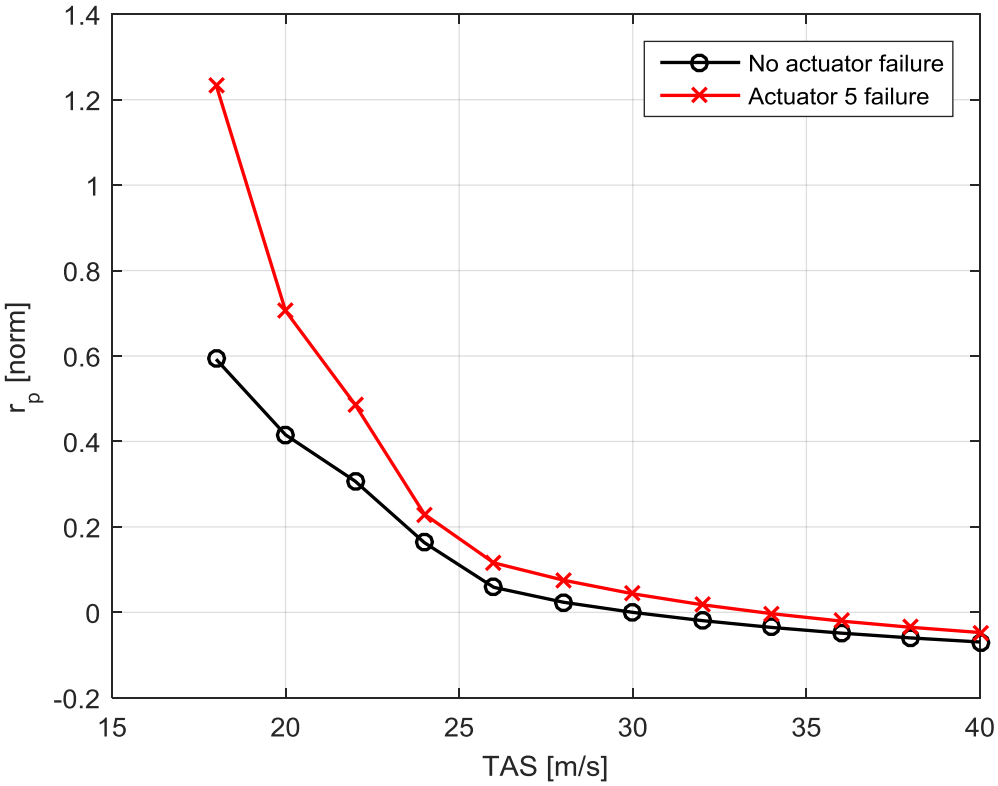

Figure 5.52: Pitch authority required to trim the aircraft with actuator 5 failing

Figure 5.52 shows that a pitch command increase of more than 50% was required to trim the aircraft at the lowest flyable airspeed when experiencing failure on actuator 5. The pitch

control was mainly affected by actuators 5 and 6, since the optimiser mainly reserved them to pitch the aircraft. The aircraft was therefore very sensitive to actuator failures on control surfaces 5 and 6. The aircraft would in reality not be able to be trimmed below approximately 19 m/s using this mixing function when experiencing a failure on either actuator 5 or 6, since the control surfaces would be saturated. However, the aircraft could be trimmed during the optimisation simulation, because the control surfaces were allowed to exceed the deflection restriction. During the simulated response, the control surfaces were restricted and therefore exceeded the maximum pitch authority required to trim the aircraft below 19 m/s.

5.6.5 Robustness study summary

The required pitch command to trim the aircraft was effected by actuator failures, as there was less control authority available to trim the aircraft. The amount of pitch authority, however, was sensitive to actuator failure of the inner control surfaces on the rear wing. The aircraft could not be trimmed below 19 m/s when actuator failure on actuator 5 or 6 occurred, due to the way the optimiser allocated controls. In the simulation, the aircraft could be trimmed, but the control surfaces were not restricted in the simulation. In the case of the real aircraft, the control surfaces would have been saturated, and therefore it would not have been possible to trim the aircraft. The optimiser mainly reserved actuators 5 and 6 for pitch control, and therefore the aircraft could not be trimmed below 19 m/s if either of these actuators failed.

The optimiser allocated certain control surfaces to be mainly responsible for rolling or yawing the aircraft. This resulted in a decrease in roll rate or sideslip generated when one of the respective actuators failed. The aircraft was relatively robust against actuator failures. This was due to the availability of eight control surfaces. The aircraft dynamic behaviour plots indicated that for certain failures, the aircraft's desired responses to control inputs were greatly reduced.

5.7 Qualitative testing

The qualitative tests consisted of loading the validated JSBSim data model into FlightGear to perform real-time pilot testing in the loop simulations. The aim was to qualitatively evaluate the control allocation/mixing function design to demonstrate that the constraints and requirements listed in section 4.2 were valid and that the evaluation results and the man-in-the-loop assessment corresponded to an acceptable extent.

The open-loop simulations appeared to demonstrate satisfactory flying qualities, but these had to be verified for the closed-loop case, with a human pilot conducting various predefined tasks. The results were still dependent on the accuracy of the simulation model, and final verification could only occur in actual flight. However, in a real-time simulation or, even better, during a flight test, the aircraft might respond differently despite indications that the handling qualities complied with the specifications. The ideal would be to perform an in-flight demonstration, but given the time constraints and availability of an airframe, this was outside the scope of the current research.

The simulation was performed using the mixing function designed at 30 m/s, since the off-design study indicated that it appeared to result in satisfactory flying qualities throughout the whole flight envelope. The aircraft was flown by an aeronautical engineer with considerable experience in flying model aircraft. The pilot flew the aircraft in the graphical flight simulator (FlightGear) using a 3G Logitech joystick. The numerical tests executed before were repeated in FlightGear to assess the aircraft behaviour and dynamic responses from a man-in-the-loop perspective. The man-in-the-loop inputs consisted of the following:

- Flying a set pattern in the form of the figure 8
- Performing a pitch doublet (neutral – down – up – neutral pitch command)
- Performing a yaw doublet (neutral – left – right – neutral yaw command)
- Coordinated turn
- General flying
    - Steep turns
    - Climbing
    - Descending
    - Stalling

Seven flight tests were conducted to assess the aircraft's sensitivity to actuator failures and responses to the inputs described above. The flight tests were executed at the airspeeds corresponding to the mixing function designs, *i.e.* 20 m/s (38.9 knots), 30 m/s (58.3 knots) and 40 m/s (78 knots). The man-in-the-loop results are discussed below. Note that the hub displayed on the screen in FlightGear is in non-SI units, and the airspeed on the hub is given in knots.

5.7.1 Pilot-in-the-loop evaluation: normal

First flight test

The first flight was conducted at 58 knots (30 m/s), and a specified pattern was flown to evaluate the aircraft path control ability. Slight deviations from the flight path were observed, but minor adjustments were required to correct the error without the aircraft feeling sluggish. The aircraft was sensitive in pitch, meaning that any small control input in pitch resulted in a very quick nose-up or -down response.

Pitch doublet

A pitch doublet was created to assess the stability of the aircraft. The short-period mode damped out quickly. The left wing dropped, inducing a small rolling moment due to a sort of gyroscopic effect, when a pitch doublet was created, although it was very easy for the pilot to correct.

Yaw doublet

The Dutch roll mode was well damped. During a pure yaw command, the aircraft tended to roll more than it yawed, although a coordinated turn was easily maintained, indicating that there was a sufficient amount of yaw authority. The aircraft had a slight tendency to restore

itself back to the trim position when a sideslip was induced through the yaw command, implying a slight positive lateral stability.

Second flight test

The second flight was conducted at approximately 39 knots (20 m/s), and the pilot was required to fly a set pattern to evaluate the aircraft path control ability. The pilot was able to control the flight path without the aircraft feeling sluggish, although it appeared to respond slower when rolling to the left than to the right. It was easy to bank the aircraft at this speed, and it did not require a lot of up pitch command to maintain level flight. In general, the aircraft felt relatively responsive at this speed.

Pitch doublet

The short-period mode damped out quickly, as before. The speed stability of the aircraft was quite good and it returned to the trim speed fairly quickly without pilot input.

Yaw doublet

Yaw damped out quickly; once again, a large amount of roll accompanied the yaw. There was no noticeable difference in lateral stability between 38 and 58 knots; it seemed to stay constant.

Third flight test

The third flight was conducted at 78 knots (40 m/s), and the pilot was required to fly a set pattern to evaluate the aircraft path control ability. The pilot was able to control the flight path without the aircraft feeling sluggish, although the pitch sensitivity seemed to increase as the airspeed increased, and the control response did not feel linear in pitch.

Pitch doublet

Both the short-period and phugoid mode damped out, as expected. The aircraft felt over-sensitive to small pitch command inputs, but more normal for larger pitch command inputs.

Yaw doublet

The dihedral effect appeared to be more significant at higher airspeeds. The roll rate induced with a yaw command was higher, compared to lower airspeeds, although it damped out quickly. The aircraft's tendency to return to its trimmed position at higher airspeeds was greater than at lower airspeeds.

5.7.2 Pilot-in-the-loop evaluation: simulated failures

The actuator failures were simulated in FlightGear to assess to which extent the aircraft response was influenced. The following assumptions were made regarding the actuator failures:

- Single actuator failure at a time
- Actuator fail at zero-degree deflection ($\delta = 0°$)

5.7.2.1 The first simulated failure

The first simulated failure consisted of the inner actuator failing on the left front wing. The observations made by the pilot at the three airspeeds are discussed below.

TAS of 58 knots

The reduced sensitivity made it easier to control the aircraft in pitch. No remarkable change in roll rate was observed, although a full yaw command generated less sideslip when a failure was present.

TAS of 39 knots

The pitch control felt more sluggish at this airspeed for the inner actuator failure on the left front wing. The roll response was more sluggish, although reasonably controllable. A negligible amount of sideslip was generated for a yaw command at this configuration.

TAS of 78 knots

The pitch control was more sensitive; it felt like the aircraft was more sensitive to airspeed changes with failure. The roll rate for a roll command was much higher than before. Once again, very little sideslip was generated for a yaw command, mostly rolling the aircraft.

5.7.2.2 The second simulated failure

The second simulated failure consisted of the outer actuator failing on the left front wing.

TAS of 58 knots

The pitch control was very sensitive, with a strong tendency to roll the aircraft to the left when a pitch command was given. There were no changes observed on the roll command, although the amount of sideslip generated for a yaw command was less.

TAS of 39 knots

The pitch control was less effective at this airspeed. The roll control was a lot more sluggish at the lower airspeed, but perfectly adequate for controllable flight. The yaw control was less effective, producing less roll for a yaw input.

TAS of 78 knots

The controls were a lot more sensitive with speed; the aircraft response was a lot quicker as the airspeed increased.

5.7.2.3 The third simulated failure

The third simulated failure consisted of the outer actuator failing on the left rear wing.

TAS of 58 knots

The pitch control seemed similar as before, apart from an additional right roll that existed when creating a pitch doublet, although it was easily trimmed out. A definite roll moment to

the right with a pitch-up command existed, compared to pitch down. The roll command was more sluggish than before, with the yaw control remaining the same.

TAS of 39 knots

The pitch-up command induced a noticeable roll to the right. The roll control was more sluggish at lower airspeeds, with the roll to the left being more sluggish than the roll to the right. The yaw control remained very similar, with slightly less roll response accompanying yaw to the left.

TAS of 78 knots

The aircraft quickly responded to pitch input commands, and small command inputs resulted in large pitching moments. A pitch-up command produced a roll to the right and a pitch-down command produced a left roll. The roll control improved as the airspeed increased, although it was a little more sluggish, compared to no failures. The yaw control was largely the same, although the roll accompanying the yaw was less.

The following interesting observation was made: in the case of a right-yaw command, the aircraft strongly rolled to the left, and on a left-yaw command, the aircraft strongly rolled to the right. This corresponds with the simulated failures described in section 5.6.3. A remarkable decrease in aircraft performance was experienced, although the aircraft was still reasonably controllable. This means that if such a failure had to occur, the pilot would not find it difficult to safely return the aircraft.

5.7.2.4 The fourth simulated failure

The fourth simulated failure consisted of the inner actuator failing on the left rear wing.

TAS of 58 knots

The pitch control was very sensitive to this failure. It was interesting to observe that no coupling was experienced between roll and pitch. The roll was more effective, although there was slightly less roll authority to the left, when compared to the right. The yaw control was largely the same with a strong roll-yaw coupling like before.

TAS of 38 knots

The aircraft was less responsive in pitch, although it seemed to be more of an airspeed dependency than actuator failure sensitivity. The roll response was unaffected by actuator failure at this airspeed, although a decrease in yaw response was observed with an increase in roll-yaw coupling for a yaw command.

TAS of 78 knots

The pitch control was less sensitive with actuator failure, with a significant left roll that existed for a pitch-up command. The roll response was unaffected by actuator failure, although a strong roll-yaw coupling was experienced for a yaw command.

5.7.3 Comments on the general flying qualities

The aircraft was easy to land without actuator failures, although it felt like it ran out of pitch authority during the flair with actuator failing on control surfaces 5 or 6. The pilot was not able to stall or spin the aircraft during normal flight, and the nose-up pitch authority seemed to be insufficient with and without actuator failure. The aircraft recovered itself to the designed airspeed after a stall was attempted, and all controls were neutralised by the pilot.

The aircraft was very easy to control in general; most of the characteristics seemed to be identical with actuator failure compared to without failure. Although only a small amount of sideslip was generated for a full yaw command, the aircraft still had a sufficient amount of yaw authority to balance the turn. The pitch control sensitivity increased with an increase in airspeed, with very little pitch authority available during flair with actuator failures present.

The aircraft flew like a conventional aircraft in most aspects, apart from the pilot being able to stall the aircraft. A sufficient amount of control authority throughout the entire flight envelope was noted. The aircraft speed stability was very good – if the trim condition was disturbed, it would recover and return to the speed it was flying before the disturbance. Having eight control surfaces contributed to the robustness of the aircraft. Due to the availability of these eight control surfaces, it was expected that the remaining control surfaces would allow satisfactory control. This was demonstrated during the testing.

5.8 Impact of relative objective weightings

The impact of the relative objective function term weightings was investigated using configurations 1, 2 and 3 as a weighting baseline. The goal was to determine whether the expected outcome would be obtained if the weights were adjusted intuitively to meet the desired requirements according to the methodology developed in the project. The control allocation design methodology was implemented and evaluated in three flight conditions, resulting in three control configurations, as defined below, but in this case different weights were used for the objective function terms:

- Configuration 4: mixing function designed at 20 m/s, adjusted weighting
- Configuration 5: mixing function designed at 30 m/s, adjusted weighting
- Configuration 6: mixing function designed at 40 m/s, adjusted weighting

Configurations 1, 2 and 3 were used as a universal baseline, whereas configurations 4, 5 and 6 were specific to the aircraft application. The relative weights for configurations 4, 5 and 6 were adjusted, based on the aircraft application. In this case, the designer decided to increase the importance of the sideslip term in the optimisation objective function to obtain an acceptable sideslip response from the aircraft. The same logic should be applied when adjusting the weights on other aircraft when using this methodology, since the weight adjustment should be applied as a function of the aircraft application and desired response.

The optimisation methodology was designed in such a way that the weights could be adjusted intuitively. If the designer wanted to increase the associated effect of one of the terms, the weight for that term would thus simply be increased. The optimisation simulations were re-

run at the same airspeeds with the adjusted weights. The results are discussed in the subsections that follow.

5.8.1 Control configuration 4

The objective function weights for Configuration 1 were all equal to 1. As the flight conditions are the same for configurations 4 and 1, the results obtained for adjusting the weights are compared in this section. The baseline weights, together with the adjusted weights, are provided in Table 5.26 below. This table shows that the nose-up pitch rate and sideslip objective weights were increased to emphasise their importance, and that the roll rate and nose-down pitching moment weights remained unchanged.

Table 5.26: Baseline and adjusted weights for control configuration 4

	w_1	w_2	w_3	w_4
Configuration 1	1.0	1.0	1.0	1.0
Configuration 4	1.0	1.2	2.0	1.0

A comparison between the baseline and adjusted weights, based on the amount of pitch command to trim the aircraft, is reflected in Figure 5.53. The weight for the nose-up pitching moment was increased. Although it cannot be seen in the figure, a slightly smaller pitch command is required to trim the aircraft at the same speeds – the difference is more noticeable at higher airspeeds. The aircraft was not very sensitive to weight adjustments at low airspeeds, and the results presented below were practically the same for configurations 1 and 4. As the aircraft was not sensitive to weight adjustments, the weights should be increased by using bigger values.

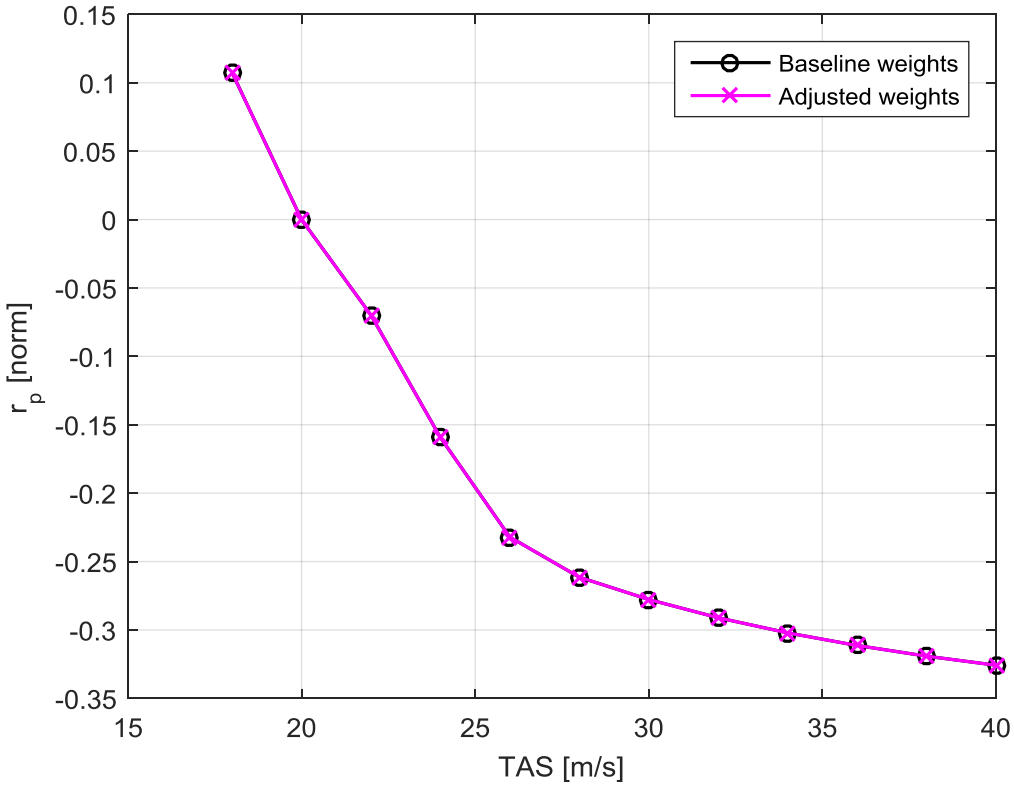

Figure 5.53: Pitch authority required to trim UAV, comparing baseline and adjusted weights at 20 m/s

Figure 5.54 illustrates a full right rudder command. It was expected that a slighter bigger sideslip would be generated for the adjusted weight, since the sideslip term weight in the objective function was increased. A very small difference in sideslip was seen, although the difference at this airspeed was not very obvious. A comparison between the yaw rates of the two configurations indicates that the adjusted weight results produced a slightly bigger yaw rate, which was expected, as the weight for the sideslip term was increased.

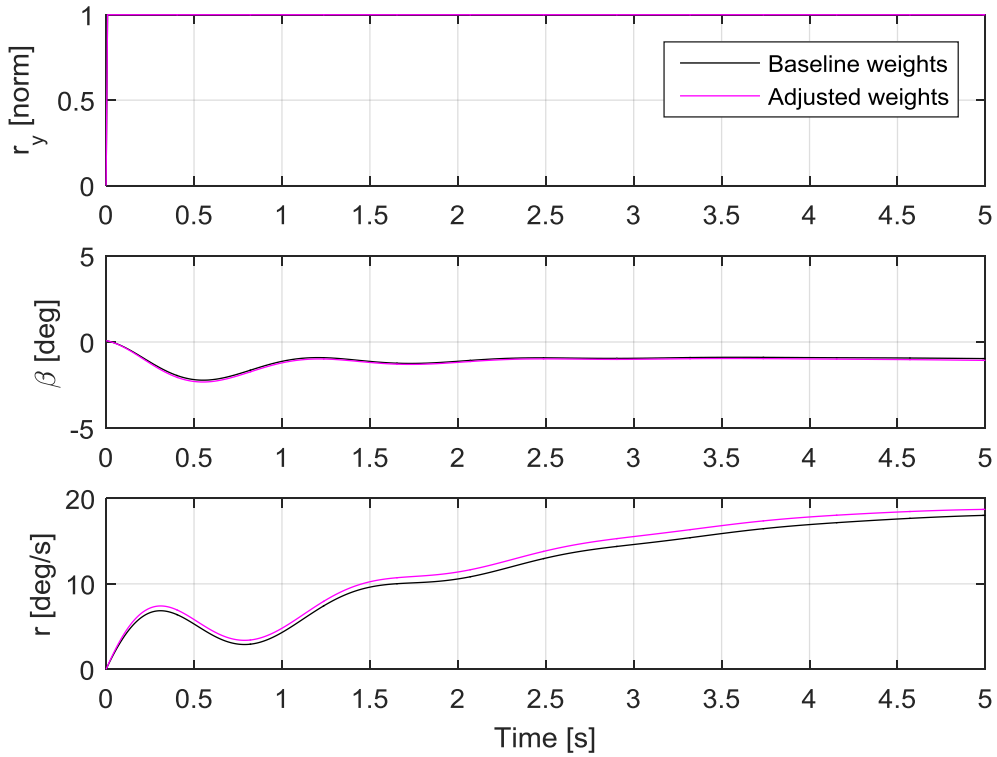

Figure 5.54: Dynamic response for a pure yaw input, comparing baseline and adjusted weights at 20 m/s

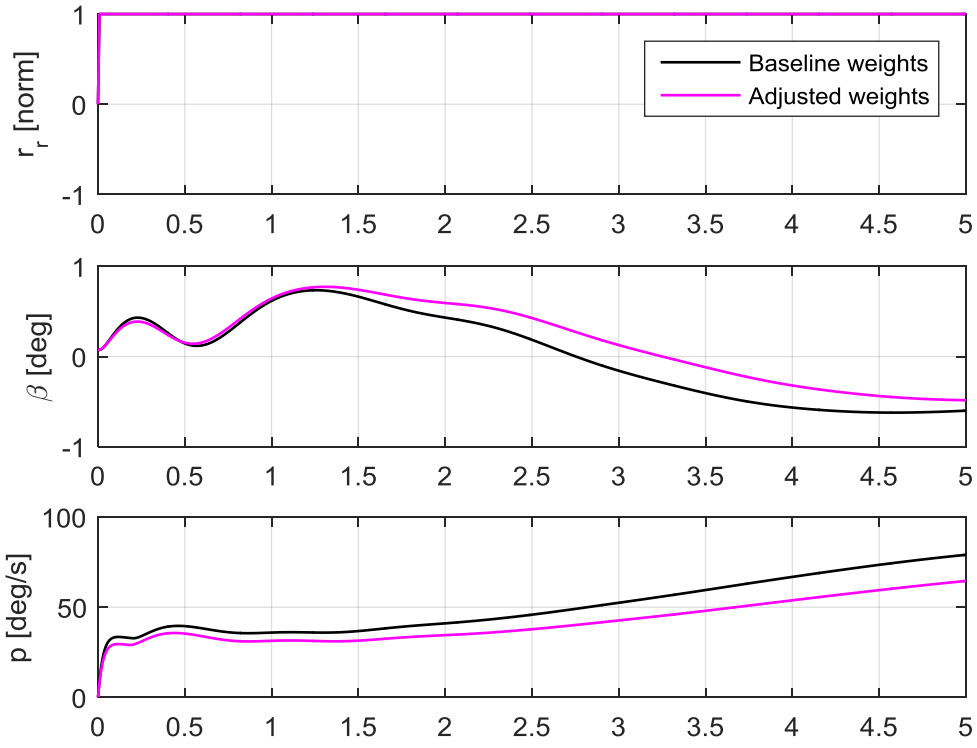

Figure 5.55: Dynamic response for a pure roll input, comparing baseline and adjusted weights at 20 m/s

Figure 5.55 illustrates the case for a full right-roll command. It is clear that the initial sideslips generated for the two configurations were identical, but the longer-term effect differed. The roll rate generated for the adjusted weight configuration was slightly less than that for the baseline weight case.

5.8.2 Control configuration 5

The objective function weights for Configuration 2 were all equal to 1, since the flight conditions were the same for configurations 5 and 2. The results obtained after adjusting the weights are compared in this section. The baseline weights, together with the adjusted weights, are shown in Table 5.27 below. This table indicates that the nose-up pitch rate and sideslip objective weights were increased to emphasise their importance, and the roll rate and nose-down pitching moment weights remained unchanged.

Table 5.27: Baseline and adjusted weights for control configuration 5

	w_1	w_2	w_3	w_4
Configuration 2	1.0	1.0	1.0	1.0
Configuration 5	1.0	1.2	1.8	1.0

A comparison between the baseline and adjusted weights, based on the amount of pitch command to trim the aircraft, is indicated in Figure 5.56. The weight for the nose-up pitching moment was increased, and therefore less pitch command is required to trim the aircraft at lower airspeeds. As the airspeed increased, the amount of pitch command required was approximately the same.

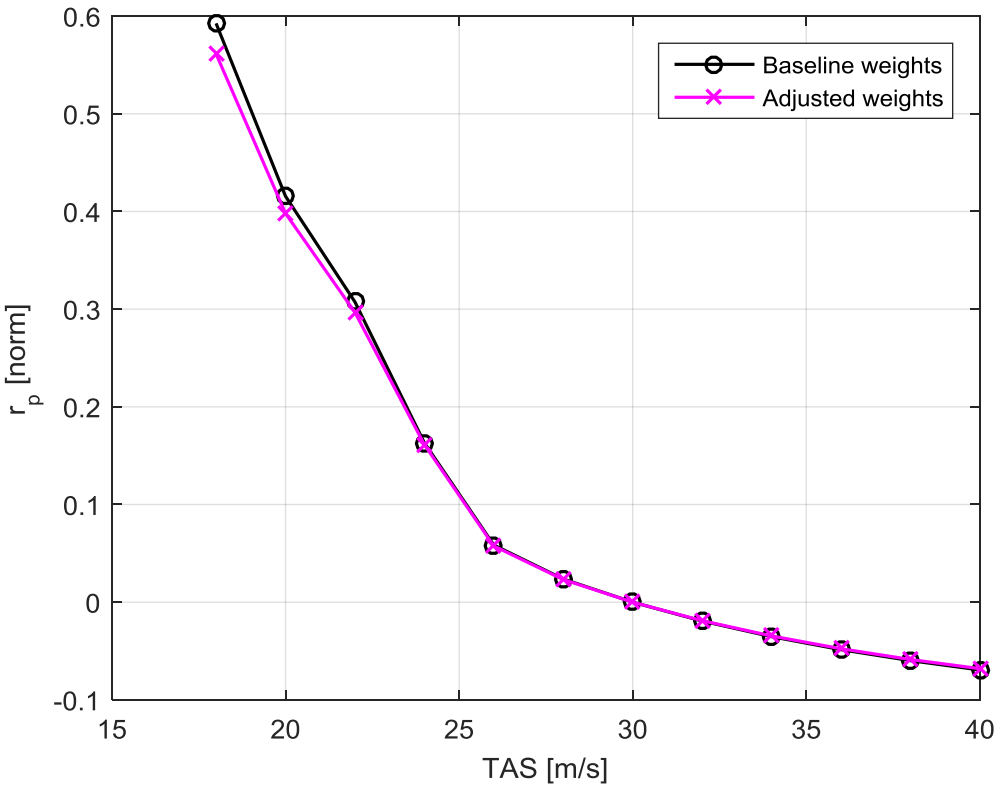

Figure 5.56: Pitch authority required to trim UAV, comparing baseline and adjusted weights at 30 m/s

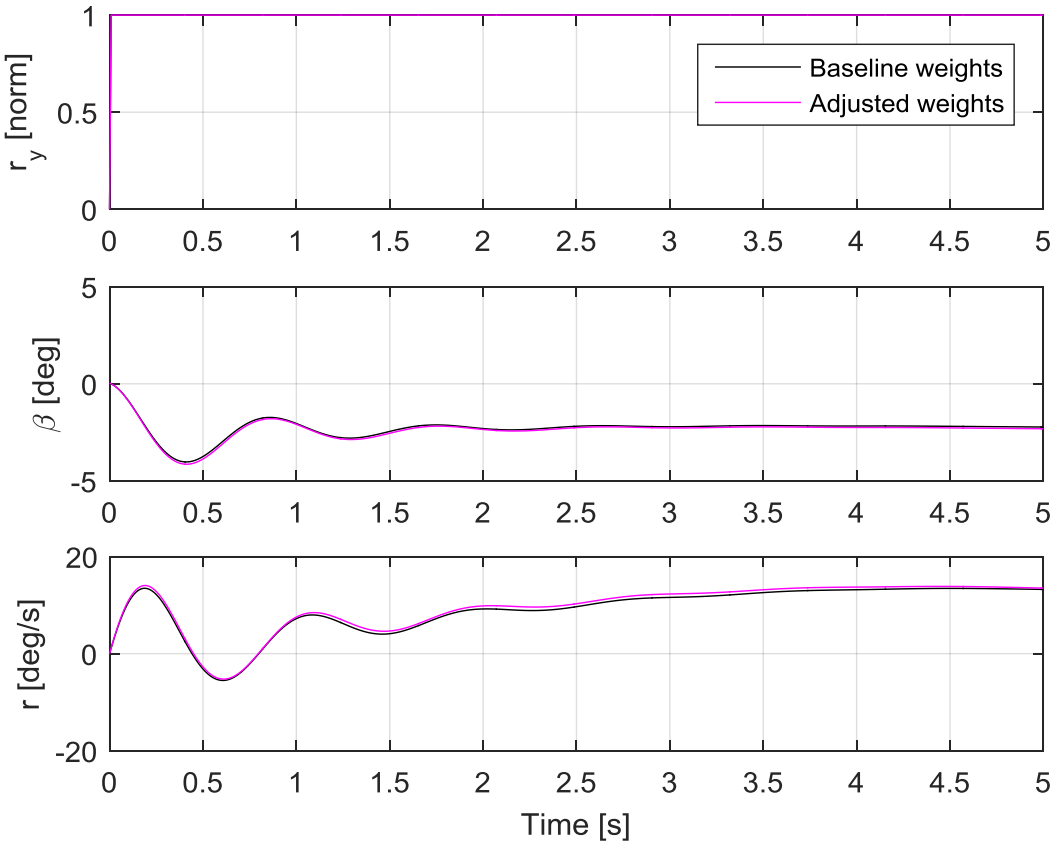

Figure 5.57: Dynamic response for a pure yaw input, comparing baseline and adjusted weights at 30 m/s

Figure 5.54 shows the case for a full right rudder command. It was expected that a slighter bigger sideslip would be generated for the adjusted weight, as the sideslip term weight in the objective function was increased. A very small difference in the sideslips generated can be seen. If the yaw rates of the two configurations are compared, it is clear that the adjusted weight produced a slightly bigger yaw rate, which was expected, since the weight for the sideslip term was increased.

The differences between the two configurations were less evident for the roll and yaw, compared to the differences observed in the amount of pitch command required. The weights almost had a negligible impact on the results, and the weights of relevant objectives should therefore be increased heavily. Although the weight had no impact on the aircraft response, it could still help with decreasing the convergence time.

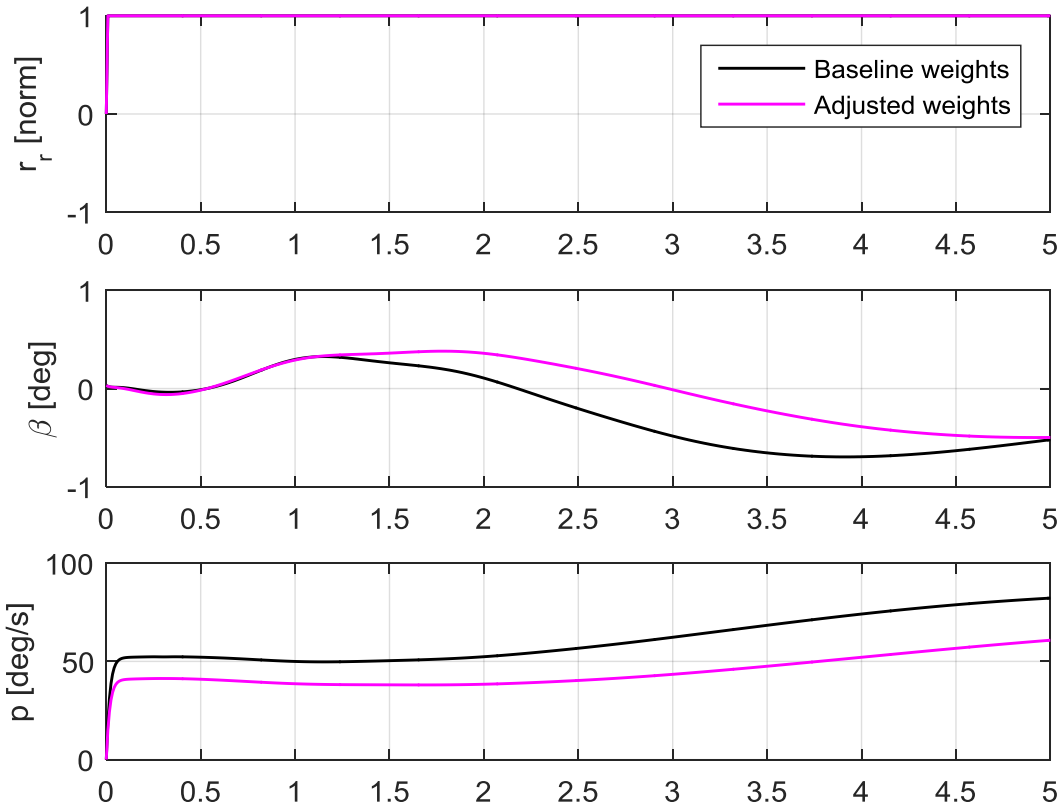

Figure 5.58: Dynamic response for a pure roll input, comparing baseline and adjusted weights at 30 m/s

A full right-roll command is illustrated in Figure 5.58. It can be seen that the initial sideslips generated for the two configurations were similar, but the longer-term effects differed. The roll rate generated for the adjusted weight configuration was significantly less than that for the baseline weight case. The optimiser focused on increasing the sideslip and nose-up pitch authority, and stopped at a solution that satisfied these two requirements without ensuring that the roll rate remained unchanged.

5.8.3 Control configuration 6

The objective function weights for Configuration 3 were all equal to 1. As the flight conditions were the same for configurations 6 and 3, the results obtained for adjusting the weights are compared in this section. The baseline weights, together with the adjusted weights, are reflected in Table 5.28 below. This table shows that the nose-up pitch rate and sideslip objective weights were increased to emphasise their importance, and the roll rate and nose-down pitching moment weights remained unchanged.

Table 5.28: Baseline and adjusted weights for control configuration 6

	w_1	w_2	w_3	w_4
Configuration 3	1.0	1.0	1.0	1.0
Configuration 6	1.0	1.2	1.5	1.0

A comparison between the baseline and adjusted weights, based on the amount of pitch command to trim the aircraft, is provided in Figure 5.59. The weight for the nose-up pitching moment was increased, and therefore it can be seen that less pitch command is required to trim the aircraft at airspeeds between 18 and 22 m/s. As the airspeed increased, the amount of pitch command required remained approximately the same.

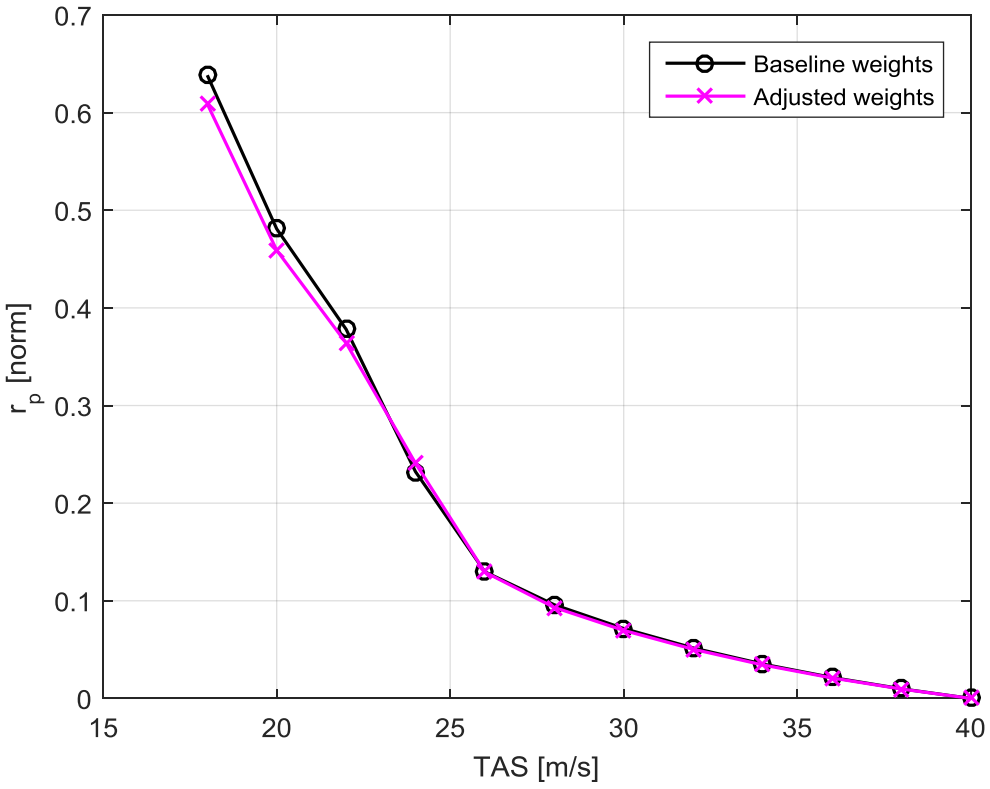

Figure 5.59: Pitch authority required to trim UAV, comparing baseline and adjusted weights at 40 m/s

A full right rudder command is illustrated in Figure 5.54. It was expected that a slightly bigger sideslip would be generated for the adjusted weight, as the sideslip term weight in the objective function was increased. A noticeable difference in the sideslips was seen – a bigger sideslip was generated using the adjusted weight configuration. When the yaw rates of the two configurations were compared, it was seen that the periods of the two rates were very similar, but that the amplitude of the adjusted weight yaw rate was bigger than the baseline weight configuration. The differences between the two configurations were less evident for the yaw rate, but could clearly be seen by the amount of sideslip generated.

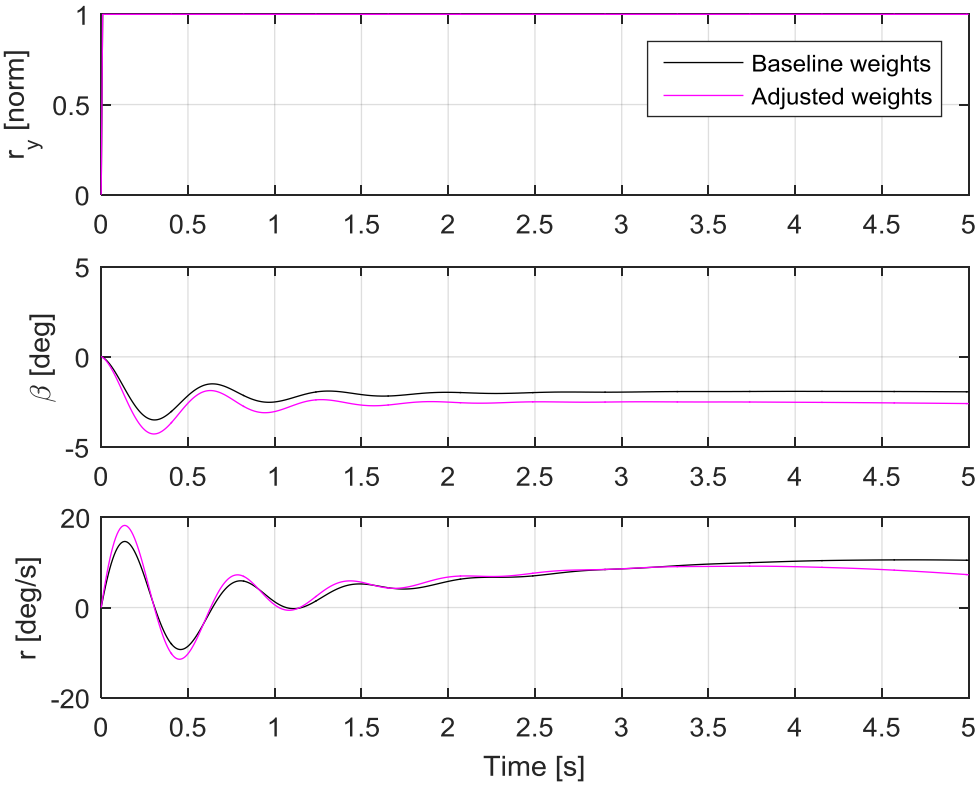

Figure 5.60: Dynamic response for a pure yaw input, comparing baseline and adjusted weights at 40 m/s

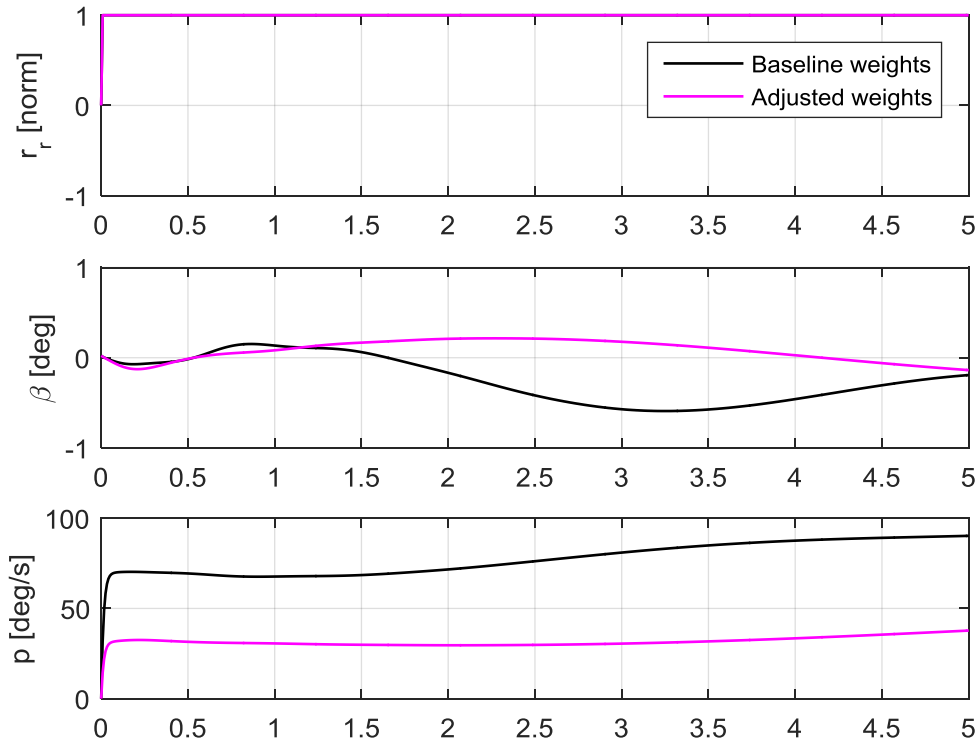

Figure 5.61: Dynamic response for a pure roll input, comparing baseline and adjusted weights at 40 m/s

A full right-roll command is illustrated in Figure 5.61. The initial sideslips generated for the two configurations were similar, but after 0.1 seconds, the two configurations produced different results. The roll rate generated for the adjusted weight configuration was significantly less than that for the baseline weight case.

In summary, the results presented in section 5.8 indicate that the impact of relative weighting was more obvious at 30 and 40 m/s than at 20 m/s. The nose-up pitch command and sideslip weightings were increased for the adjusted weight configurations. The impact of the weights on the pitch command required to trim the aircraft was clearly seen in configurations 5 and 6, but not in Configuration 4. The impact of the weightings on the sideslip was clearly seen in Configuration 6, where the adjusted weights produced a noticeable increase in the sideslip than in the baseline configurations. The impact of the weightings on configurations 4 and 5 was negligible – the aircraft was not sensitive to an adjustment in weightings at low airspeeds. In order to obtain a significant impact on the aircraft response, the weightings should be adjusted using larger numbers.

5.9 Summary

In this chapter, the control allocation methodology was implemented and the results were presented. The general optimisation results, such as the number of function evaluations and iterations for Phase 1 and Phase 2, were first reported. Various plots were provided to illustrate how the mixing function performed control allocation for full pitch, roll and yaw commands. The pitch and roll responses were shown to be conventional, but the yaw mixing was less intuitive and would have been difficult to allocate in an optimal way without optimisation. The optimisation runs were firstly conducted at three control configurations, which consisted of the following:

- Configuration 1: mixing function designed at 20 m/s, baseline weighting
- Configuration 2: mixing function designed at 30 m/s, baseline weighting
- Configuration 3: mixing function designed at 40 m/s, baseline weighting

These were designed at the respective airspeeds with all the objective function weightings equal to 1. The maximum roll rates, sideslips, nose-up and nose-down pitch rates that the aircraft could achieve at the respective configurations were provided. The active constraints related to the solution were provided, followed by descriptions of the input command combinations that represented each active constraint.

The dynamic response of the aircraft was illustrated through a step roll and a step yaw input, and the resulting aircraft responses were demonstrated to be conventional and satisfactory with enough authority to control a typical UAV in manual or automated flight. The yaw authority was closely examined, as the aircraft had no vertical control surfaces, and it was found that a sufficient amount of yaw authority would be available to coordinate the aircraft throughout the entire flight envelope. Very little rudder control was needed to coordinate the aircraft for the small sideslip and lateral acceleration (a_y) generated during a turning manoeuvre for the respective configurations.

One of the off-design responses of the mixing function was investigated by calculating the amount of pitch command required to trim the aircraft for level flight over the flight envelope. A sufficient amount of pitch control authority was available to trim the aircraft over the entire flight envelope for all three configurations, and enough authority remained to also manoeuvre the aircraft.

The control allocation function was scheduled against airspeed and it was found that a single function could be used over the entire flight envelope, since the aircraft performance was satisfactory in off-design conditions. However, although the off-design characteristics were judged to be satisfactory, handling qualities could be improved by using dedicated mixing functions for different airspeeds. The designer can therefore make a compromise between the complexities of the mixing function implementation and improved handling qualities, depending on the application.

The robustness of the control allocation design was investigated by simulating actuator failures and studying the aircraft responses. A man-in-the-loop flight test was also conducted with the JSBSim flight dynamics module in FlightGear, as FlightGear is able to use several different flight dynamics modules.

Extensive tests were conducted to evaluate the effect of individual failures, where the control surfaces were eliminated one by one and the assumptions that were made stated that an actuator failure occurred at a zero control surface deflection, or that the control surface would return to the neutral position following the failure. The aircraft response was evaluated and it was found that the aircraft could still be trimmed in all cases, except at very low speeds when actuator failure occurred on the inner control surfaces on the rear wing (control surfaces 5 and 6). At all speeds, however, a larger control command was required to trim the aircraft once the failure occurred, and the impact of this failure became larger at lower airspeeds.

Three further configurations were designed using different objective function weightings:

- Configuration 4: mixing function designed at 20 m/s, adjusted weighting
- Configuration 5: mixing function designed at 30 m/s, adjusted weighting
- Configuration 6: mixing function designed at 40 m/s, adjusted weighting

The goal was to investigate the impact of relative objective weighting to determine whether a designer could change the weights intuitively and obtain the desired handling characteristic as a function of the aircraft application. The adjusted weightings were compared to the results from the baseline weight assignments, as obtained for configurations 1 to 3. The control allocation design was shown to be capable of changing the importance of specified terms by adjusting the assigned weights at high airspeeds. The impact of small adjustments to the weights at low airspeeds was negligible. In order to obtain a significant impact on the aircraft response, the weights at low airspeeds, in particular, should be adjusted using larger numbers.

6. Conclusion

This study investigated the development of a control allocation methodology for unconventional aircraft using mathematical optimisation techniques. The primary goal was to design an open-loop control allocation program that could serve as the foundation for a closed-loop program to simplify autopilot design.

A conventional autopilot expects a command input from elevator, aileron and rudder, whereas various aircraft that have unconventional control setups do not have dedicated elevators, ailerons and rudders. The control allocation program was therefore designed to take conventional input commands such as pitch, roll and yaw, and map these to the unconventional control surfaces in order to operate like conventional aircrafts. The autopilot design on the unconventional aircraft could therefore follow the same approach as for a conventional aircraft with dedicated elevators, ailerons and rudders when this mixing approach is followed, which should simplify the autopilot design to a great extent.

A 6DOF simulation model was developed as part of this work, and implemented in a locally developed MATLAB® simulation environment. The 6DOF simulation model was used to demonstrate the control allocation program capabilities through various simulations. Note that it was outside the scope of the project to develop a 6DOF simulation environment, and therefore a locally developed simulation environment was made available.

The control allocation program design made use of multiple-objective constrained optimisation. A second-order mixing function was selected to perform the control allocation. This mixing function consisted of a constant term, a linear term and a quadratic term. The constant term was used to store the trim control surface deflections, and the linear and quadratic terms were used to obtain optimal control mixing for manoeuvring, control and trim in other states. The control allocation design therefore comprised two phases:

- Phase 1 was used to obtain the constant trim bias vector that could be solved independently from Phase 2.
- Phase 2 was used to obtain the linear and quadratic terms responsible for the control allocation required to manoeuvre the aircraft.

The primary aim of Phase 1 was to obtain a set of control surface deflections at trim, where each individual control surface still remained as close as possible to neutral. The primary aim of Phase 2 was to maximise the aircraft response in all three axes without saturating the controls.

The selection of relevant objective function terms that would result in satisfactory handling qualities was investigated through various optimisation runs. In order to maximise the responses, secondary effects such as adverse yaw and control coupling were eliminated or reduced through equality constraints, and control saturation was prevented through inequality constraints. The inequality constraints were defined in an intuitive and systematic approach that could readily be adjusted, depending on the application in which the aircraft would operate. Preventing control saturation for all possible input commands resulted in too many constraints, which would unnecessarily reduce the performance of the aircraft.

A method to determine the relevant optimisation constraints based on the user's specific requirements was demonstrated. It was then demonstrated how to eliminate all the unnecessary constraints in order to prevent an artificial reduction of the design space. The identified combined input commands related to the aircraft application were posed as inequality constraints. Various optimisation runs were executed after the problem formulation process had been completed. These runs consisted of several changes to evaluate the impact of the following:

- Using different variables in the objective function
- Using different inequality constraints
- Using different weightings for the objective function terms

The impact of the relative weighting of the objective function terms was investigated in the following manner: The first configuration/design consisted of setting all the weights equal to 1 in order to use the result as a baseline. The weights were then adjusted to shift the emphasis in order to give specified terms more importance than others. The results obtained at 40 m/s showed that the desired outcomes would be reached if weights were changed intuitively. Larger variations in the weights were required at lower airspeeds, as the impact of changing the weights at low airspeeds were not as significant as expected. The weights could only be changed intuitively if the objective function terms were normalised. The methodology used for this normalisation was also described. The optimisation results obtained were used for further investigation.

Scheduling against airspeed was investigated and it was determined that scheduling was not required. However, it was demonstrated that better results at off-design conditions were obtained in some cases. Using a single mixing function is beneficial in the case of sensor failure. The mixing function required no feedback, because it is an open-loop function and all the functions demonstrated satisfactory aircraft responses over the flight envelope. The mixing function can be implemented once without the aircraft knowing the airspeed to perform scheduling.

The robustness of the control allocation design was investigated by simulating actuator failures and inspecting the corresponding aircraft responses. Extensive tests were conducted to investigate the effect of individual failures where the control surfaces were eliminated one at a time. The aircraft responses were considered and it was found that the aircraft could still be trimmed in all cases, except when actuator failure occurred on the inner control surfaces on the rear wing. The aircraft could not be trimmed for airspeeds below 19 m/s when failures on these control surfaces occurred. The aircraft remained fully controllable for recovery, although reduced control effectiveness was experienced. The control authority was reduced for almost all the failures, as expected.

In conclusion, a methodology to efficiently allocate controls on an unconventional aircraft by using mathematical optimisation was developed and demonstrated. The resulting aircraft response was demonstrated to be conventional and satisfactory, with enough authority to control a typical UAV in manual or automated flight. All the design requirements were met, and a few recommendations were identified, which are discussed in the next chapter.

7. Recommendation

Through the use of alternative combinations of constraints and objectives, it will be possible to implement unconventional or special control modes, such as high-lift devices or direct force control. The eight control surfaces contributed to robustness, especially when actuator failures occurred, but among the questions raised were whether all eight control surfaces were needed. Therefore, some of the recommendations include the following:

- Some of the control surfaces should be fixed to act as high-lift devices, and then it should be investigated whether satisfactory control could still be achieved with the remaining surfaces.
- A change in weightings should be investigated and it should be determined whether this could improve the ability to trim the aircraft with actuator failures.

It is recommended that the designer always start the optimisation process by obtaining a baseline set of results with all the weightings equal to 1 before adjusting the weightings to meet further requirements. During the optimisation process, 56 inequality constraints were defined, based on the identified realistic input command combinations. The results revealed that only a few of these were active at the optimum solution. A further study to determine whether the number of constraints can be reduced is recommended. This would entail investigating the use of a different set of inequality constraints.

The optimisation computational times were very long, and it is therefore recommended to investigate the effects of the following:

- Using a different optimiser
- Using a different step size for the objective function evaluations
- Using a different step size for the equality constraint evaluations

The aircraft performance at the off-design conditions was satisfactory for the application it was designed for, but it could be improved by designing the control allocation for a specific speed. The method described in this thesis gives the designer the ability to compare the effectiveness of scheduling, which will allow him to make an informed decision about whether scheduling is needed or not.

Bibliography

[1] J. Wolkovitch, "Joined wing aircraft", United States of America Patent 4,365,773, 28 December 1982.

[2] D. Schiktanz and D. Scholz, "Box Wing Fundamentals - An Aircraft Design Perspective", *Proceedings of the DGLR Conference*, Bremen, 2011.

[3] P. O. Jemitola and J. P. Fielding, "Box Wing Aircraft Conceptual Design", *Proceedings of the 28th ICAS Congress*, Brisbane, 2012.

[4] J. Corneille, "Wind Tunnel Investigation Of Joined Wing Configurations", MEng Thesis, Air Force Institute of Technology, Ohio, 1999.

[5] D. Zafirov, "Closed Wing Aircraft Classification", *International Journal of Engineering Research & Technology*, vol. 3, no. 1, pp. 10-15, 2014.

[6] I. Kroo, J. McMasters and S. C. Smith, "Highly Nonplanar Lifting Systems", Presented at: Transportation Beyond 2000: Technologies Needed for Engineering Design NASA Langley Research Center, September 26-28, 1995.

[7] A. Frediani, M. Gasperini, G. Saporito and A. Rimondi, "Development of a Prandtlplane aircraft configuration", Department of Aerospace Engineering "Lucio Lazzarino" Pisa University, Italy.

[8] Airbender, "Online School of Aerospace Engineering," 11 December 2014. [Online]. Available: http://discovernewinfo.com/familiarization-of-cessna-182-rg-aircraft-using-microsoft-flight-simulator/. [Accessed 19 05 2015].

[9] P. M. Bowers, *Unconventional aircraft*, New York, NY: TAB Books, 1984.

[10] L. R. Newcome, *Unmanned aviation: a brief history of unmanned aerial vehicles*, Reston, VA: American Insititute of Aeronautics and Astronautics, 2004.

[11] M. Armitage, *Unmanned aircraft*, London: Brassey's Defence Publisher, 1988.

[12] J. B. Davidson, F. J. Lallman and T. W. Bundick, "Real-Time Adaptive Control Allocation applied to a High Performance Aircraft", *Proceedings of the 2001 5th SIAM Conference on Control & Its Applications*, 2001.

[13] Y. Zhang, S. V. Suresh, B. Jiang and D. Theilliol, "Reconfigurable Control Allocation against Aircraft Control Effector Failure", *Proceedings of the IEEE International Conference on Control Applications*, Singapore, 2007.

[14] J. M. Buffington, "Tailless Aircraft Control Allocation", USAF Wright Laboratory, Report number WL-TM-97-3060, Ohio, 1997.

[15] O. Härkegård and T. S. Glad, "Resolving actuator redundancy-optimal control vs. control allocation", *Automatica*, no. 41, pp. 137-144, 2005.

[16] M. W. Oppenheimer and D. B. Doman, "Control allocation for overactuated systems", Air Force Research Laboratory, Report number AFRL-VA-WP-TP-2006-321, Ohio, 2006.

[17] D. B. Doman and M. W. Oppenheimer, "Improving Control Allocation for Nonlinear Aircraft Dynamics", Wright-Patterson Air Force Laboratory, Report number AFRL-VA-WP-TP-2002-302, Ohio, 2002.

[18] V. L. Poonamallee, S. Yurkovich, A. Serrani, D. B. Doman and M. W. Oppenheimer, "A Nonlinear Programming Approach for Control Allocation", *Proceedings of the American Control Conference*, Boston, Massachusetts, 2004.

[19] L. Basson, "Control allocation as part of a fault-tolerant control architecture for UAV's", MSc Thesis, Department of Electrical and Electronic Engineering, Stellenbosch University, 2011.

[20] S. F. Wu, C. J. Engelen, Q. P. Chu, R. Babuska, J. A. Mulder and G. Ortega, "Fuzzy logic based attitude control of the spacecraft X-38 along a nominal re-entry tragectory", *Control Engineering Practice,* no. 9, pp. 699-707, 2001.

[21] H. Alwi and C. Edwards, "Fault tolerant control using sliding modes with on-line control allocation", *Automatica*, vol. 44 (2008), pp. 1859-1866, 2008.

[22] M. Voskuijl, G. La Rocca and F. Dircken, "Controllability of Blended Wing Body Aircraft", in *International Congress of the Aeronautical Sciences*, Anchorage, Alaska, 2008.

[23] J. A. Petersen and M. Bodson, "Constrained quadratic programming techniques for control allocation", in *IEEE Transactions on Control Systems Technology*, Hawaii USA, 2006.

[24] O. Härkegård, "Dynamic control allocation using constrained quadratic programming", Linköping University, Report number LiTH-ISY-R-2594, Sweden, 2004.

[25] O. Härkegård, "Efficient active set algorithms for solving constrained least squares problems in aircraft control allocation," Linköping University, Report number LiTH-ISY-R-2426, Sweden, 2002.

[26] D. Dang-Vu and D. Brocas, "Closed-Loop Constrained Control Allocation for a

Supermanoeuvrable Aircraft", *Proceedings of the 21st ICAS Congress and the Proceedings of the AIAA Guidance and Control Conference*, Melbourne Australia, 1998.

[27] A. Johansen, T. I. Fossen and S. P. Berge, "Constrained Nonlinear Control Allocation With Singularity Avoidance Using Sequential Quadratic Programming", *IEEE Transactions on control systems technology*, vol. 12, no. 1, pp. 211-216, 2004.

[28] Y. Luo, A. Serrani, S. Yurkovich, D. B. Doman and M. W. Oppenheimer, "Model Predictive Dynamic Control Allocatin with Actuator Dynamics", *Proceedings of the American Control Conference*, Boston, Massachusetts, 2004.

[29] B. Etkin, *Dynamics of Flight Stability and Control*, Hoboken, NY: Wiley, 1982.

[30] W. F. Phillips, *Mechanics of Flight* (2nd ed.), Hoboken, NY: Wiley, 2010.

[31] I. Peddle, "Autonomous Flight of a Model Aircraft", Lecture notes, Department of Electrical and Electronic Engineering, Stellenbosch University, 2004.

[32] R. F. Stengel, *Flight Dynamics*, Princeton, NJ, Princeton University Press, 2004, pp. 15,215.

[33] M. R. Waszak, L. N. Jenkins and P. Lfju, "Stability and Control Properties of an Aeroelastic Fixed Wing Micro Aerial Vehicle", *Proceedings of the AIAA Atmospheric Flight Mechanics Conference*, Montreal, 2001.

[34] P. group, "Paramount group website", Paramount Advance Technologies, September 2014. [Online]. Available: http://www.paramountgroup.com/capabilities/air/roadrunner/. [Accessed 10 02 2016].

[35] B. L. Stevens and F. L. Lewis, *Aircraft control and simulation* (2nd ed.), Hoboken, NJ: Wiley, 2003.

[36] N. A. a. S. A. U. A. F. National Oceanic and Atmospheric Administration, *U. S. Standard Atmosphere 1976*, Washington, DC: U. S. Government Printing Office, 1976.

[37] R. L. Burden and J. D. Faires, *Numerical Analysis* (9th ed.), Canada: Richard Stratton, 2011.

[38] G. F. Franklin, J. D. Powell and A. Emami-Naeini, *Feedback control of dynamic systems*, Upper Saddle River, NJ: Prentice Hall, 2010.

[39] B. T. Kulakowski, J. F. Gardner and J. L. Shearer, *Dynamic modeling and control of engineering systems*, New York, NY: Cambridge University Press, 2010.

[40] R. F. Stengel, *Flight dynamics*, Princeton, NJ: Princeton University Press, 2004.

[41] P. Skinner, "Low-speed Wind Tunnel Test of the Roadrunner Joined Wing Configuration", Report number DPSS-ASC2014/054, Council for Scientific and Industrial Research, Pretoria, 2014.

[42] R. DeLoach, "Application of Modern Experiment Design to Wind Tunnel Testing at NASA Langley Research Centre", *Proceedings of the 36th AIAA Aerospace Sciences Meeting and Exhibit*, vol. 0713, p. 98, 1998.

[43] A. Giunta, S. J. Wojtkiewicz and M. Eldred, "Overview of Modern Design of Experiments Methods for Computational Simulations", *Proceedings of the 41st AIAA Aerospace Sciences Meeting and Exhibit*, vol. 0649, 2003.

[44] J. Dias and B. Broughton, "Aircraft Wind Tunnel Characterisation Using Modern Design of Experiments", *Proceedings of the 54th AIAA/ASME/ASCE/AHS/ASC Strustures, Structural Dynamics, and Material Conference*, vol. 1502, 2013.

[45] D. Landman, J. Simpson, R. Mariani, F. Ortiz and C. Brithcher, "Hybrid Design for Aircraft Wind-Tunnel Testing Using Response Surface Methodologies", *Journal of Aircraft*, vol. 44, no. 4, pp. 1214-1221, 2007.

[46] Y. H. Drela M, "AVL (Athena Vortex LAttice)", 2004. [Online]. Available: http://web.mit.edu/drela/Public/web/avl. [Accessed 07 01 2014].

[47] E. Stackpole, "OpenROV", 4 November 2013. [Online]. Available: http://openrov.com/forum/topics/brushless-motor-calculation. [Accessed 1 April 2014].

[48] J. S. Berndt, "JSBSim, An open source, platform-independent, flight dynamics model in C++", 1996. [Online]. Available: http://www.jsbsim.org.. [Accessed 18 02 2014].

[49] J. S. Arora, *Introduction to optimum design* (3rd ed.), Atlanta, GA: Elsevier, 2012.

[50] J. Snyman, "A new and dynamic method for unconstrained minimization", *Appl. Math. Modelling*, vol. 6, pp. 449-462, 1982.

[51] J. Snyman, "An improved version of the original leap-frog dynamic method for unconstrained minimization: LFOP1(b)", *Appl. Math. Modelling*, vol. 7, pp. 216-218, 1983.

[52] Department of Defence, "Flying Qualities of Piloted Airplanes", *MIL-F-8785C*, 5 November 1980.

Appendix A: Static derivatives

The results obtained from AVL, together with the wind tunnel test results, are tabulated below. Each model's results were compared to the wind tunnel test results to determine which model would be most accurate.

Roadrunner 1 fuselage is vertical "lifting panel"						
Alpha	0	10	0	0	0	0
Beta	0	0	10	0	0	0
dr	0	0	0	10	0	0
da	0	0	0	0	10	0
de	0	0	0	0	0	10
CX	-0.02309	0.05267	-0.02044	-0.02493	-0.02455	-0.02426
CY	0	0.00004	-0.02697	-0.01098	0.00703	-0.00478
CZ	-0.03266	-0.61623	-0.03328	-0.03257	-0.03264	-0.0817
Cl	0	0.00002	0.0074	0.02065	0.01153	0.00521
Cm	0.00024	-0.06047	-0.00236	0.00034	-0.00003	-0.03704
Cn	0	-0.00002	-0.001	0.0022	-0.00103	0.00107
CL	0.03266	0.61601	0.03328	0.03257	0.03264	0.0817
CD	0.02309	0.05513	0.02044	0.02493	0.02455	0.02426

Roadrunner 2 fuselage is modelled using sources and doublets						
Alpha	0	10	0	0	0	0
Beta	0	0	10	0	0	0
dr	0	0	0	10	0	0
da	0	0	0	0	10	0
de	0	0	0	0	0	10
CX	-0.0267	0.05091	-0.0249	-0.02855	-0.02817	-0.02788
CY	0	0.00004	-0.02598	-0.01129	0.00733	-0.00582
CZ	-0.02492	-0.61524	-0.02495	-0.02483	-0.0249	-0.07405
Cl	0	-0.00002	0.00732	0.02068	0.01154	0.00521
Cm	-0.0114	-0.06473	-0.01181	-0.01129	-0.01166	-0.04874
Cn	0	-0.00002	-0.00108	0.00228	-0.00106	0.00137
CL	0.02492	0.61473	0.02495	0.02483	0.0249	0.07405
CD	0.0267	0.0567	0.0249	0.02855	0.02817	0.02788

Roadrunner 3 fuselage nose is modelled using sources and doublets and the rest lifting panel						
Alpha	0	10	0	0	0	0
Beta	0	0	10	0	0	0
dr	0	0	0	10	0	0
da	0	0	0	0	10	0
de	0	0	0	0	0	10
CX	-0.02672	0.05043	-0.02359	-0.02856	-0.02818	-0.02789
CY	0	0.00004	-0.0339	-0.01096	0.00701	-0.00466
CZ	-0.02467	-0.61636	-0.02609	-0.02458	-0.02465	-0.07379
Cl	0	-0.00002	0.00748	0.02069	0.01153	0.00522
Cm	-0.01173	-0.0637	-0.01294	-0.01162	-0.01199	-0.04906
Cn	0	-0.00002	-0.00244	0.0022	-0.00104	0.00104
CL	0.02467	0.61576	0.02609	0.02458	0.02465	0.07379
CD	0.02672	0.05737	0.02359	0.02856	0.02818	0.02789

Roadrunner 4 has no fuselage						
Alpha	0	10	0	0	0	0
Beta	0	0	10	0	0	0
dr	0	0	0	10	0	0
da	0	0	0	0	10	0
de	0	0	0	0	0	10
CX	-0.02309	0.05267	-0.02117	-0.02493	-0.02455	-0.02426
CY	0	0.00004	-0.02138	-0.01127	0.00732	-0.00581
CZ	-0.03266	-0.61623	-0.03417	-0.03257	-0.03264	-0.0817
Cl	0	-0.00002	0.00743	0.02065	0.01153	0.0052
Cm	0.00024	-0.06047	-0.0014	0.00034	-0.00003	-0.03704
Cn	0	-0.00002	0.00197	0.00228	-0.00105	0.00137
CL	0.03266	0.61601	0.03417	0.03257	0.03264	0.0817
CD	0.02309	0.05513	0.02117	0.02493	0.02455	0.02426

Roadrunner wind tunnel results						
Alpha	0	10	0	0	0	0
Beta	0	0	10	0	0	0
dr	0	0	0	10	0	0
da	0	0	0	0	10	0
de	0	0	0	0	0	10
CX	-0.0229	0.0272	-0.0218	-0.0192	-0.0225	-0.0211
CY	-4.69E-04	-0.0044	-0.076	-0.0102	0.0093	-0.0014
CZ	-0.048	-0.6078	-0.0614	-0.0509	-0.0493	-0.1116
Cl	-0.0017	-4.81E-04	-0.0472	0.017	0.0056	-0.0017
Cm	-0.0055	-0.1609	-0.0216	-0.0064	-0.0056	-0.0569
Cn	-4.15E-05	6.10E-04	0.0041	0.0025	-0.0016	2.40E-04
CL	0.048	0.6033	0.0614	0.0509	0.0493	0.1116
CD	0.0229	0.0788	0.0218	0.0192	0.0225	0.0211

Appendix B: Dynamic derivatives

The dynamic derivatives obtained from AVL are provided in the tables below. These derivatives were used to model the 6DOF aircraft.

Roadrunner 4 without fuselage			
Clr			
beta			
alpha	-10	0	10
-6	-0.07799	-0.07919	-0.07799
0	-0.02163	-0.02196	-0.02162
6	0.034973	0.035514	0.034977
12	0.09119	0.092599	0.091194
18	0.146409	0.148669	0.146413
Cnr			
beta			
alpha	-10	0	10
-6	-0.00686	-0.00697	-0.00686
0	-0.00767	-0.00779	-0.00767
6	-0.00839	-0.00852	-0.00839
12	-0.00902	-0.00915	-0.00902
18	-0.00954	-0.00969	-0.00955
Cxq			
beta			
alpha	-10	0	10
-6	-0.2828	-0.28715	-0.28278
0	-0.02132	-0.02164	-0.0213
6	-0.0083	0.244109	0.240412
12	0.499468	0.507184	0.499489
18	0.753073	0.764701	0.753094
Cyp			
beta			
alpha	-10	0	10
-6	-0.08815	-0.08951	-0.08814
0	0.05987	0.060795	0.059873
6	0.207229	0.210428	0.207232
12	0.352319	0.357756	0.352322
18	0.493548	0.501164	0.493551
Cyr			
beta			
alpha	-10	0	10
-6	0.045023	0.045716	0.04502
0	0.041814	0.042457	0.041811
6	0.038146	0.038733	0.038143

12	0.034061	0.034585	0.034058
18	0.029603	0.030058	0.029599
Czq			
beta			
alpha	-10	0	10
-6	-3.80746	-3.86599	-3.80706
0	-3.85242	-3.91165	-3.85202
6	-3.85517	-3.91444	-3.85477
12	-3.81569	-3.87435	-3.81529
18	-3.73441	-3.79181	-3.73401
Clp			
beta			
alpha	-10	0	10
-6	-0.33733	-0.34253	-0.33732
0	-0.33846	-0.34368	-0.33846
6	-0.33589	-0.34107	-0.33588
12	-0.32963	-0.33472	-0.32963
18	-0.31977	-0.3247	-0.31976
Cmq			
beta			
alpha	-10	0	10
-6	-2.45885	-2.49666	-2.45861
0	-2.47519	-2.51325	-2.47495
6	-2.46441	-2.5023	-2.46416
12	-2.42663	-2.46394	-2.42638
18	-2.36227	-2.39858	-2.36202
Cnp			
beta			
alpha	-10	0	10
-6	0.048482	0.049224	0.04847
0	-0.01777	-0.01805	-0.01778
6	-0.08383	-0.08513	-0.08384
12	-0.14897	-0.15128	-0.14898
18	-0.21248	-0.21576	-0.21249

Appendix C: Blending function

The polynomial equations were joined using an interpolation function between the low, high and post-stall angle-of-attack regions, respectively. An extract of how the alpha regions for the axial-force coefficient were blended is illustrated in the figure below. Note that all the force and moment coefficients were blended using the same approach.

```
if alpha <= 4
    val = CA1;
elseif alpha <= 6
    t = (alpha - 4)/(6-4);
    val = (1-t)*CA1 + t*CA2;
elseif alpha <= 11
        val = CA2;
elseif alpha <= 14
    CA_l = CA2;
    CA_r = CA3;
    val = (((alpha - 11)/(14-11))*(CA_r - CA_l)) + CA_l;
else
    val = CA3;
end
```

In the figure above, ‘CA1’ represents the polynomial equation for the low alpha region, ‘CA2’ the polynomial equation for the high alpha region and ‘CA3’ the polynomial equation for the post-stall alpha region. The output of the blending function illustrated in the figure is represented by ‘Val’.

Appendix D: Inequality constraints

The inequality constraints for control surface pairs 3 and 4, 5 and 6, and 7 and 8 are indicated below.

Inequality constraints for control surfaces 3 and 4 are provided below:

$$g(15) = (x(6) - x(18) + T34)^2 - 30^2$$

$$g(16) = (x(6) + x(18) + T34)^2 - 30^2$$

$$g(17) = (x(5) + x(6) + x(17) - x(18) + T34)^2 - 30^2$$

$$g(18) = (x(5) + x(6) + x(17) + x(18) + T34)^2 - 30^2$$

$$g(19) = (x(5) + x(17) + T34)^2 - 30^2$$

$$g(20) = (x(5) - x(17) + T34)^2 - 30^2$$

$$g(21) = (x(5) + x(6) - x(17) - x(18) + T34)^2 - 30^2$$

$$g(22) = (x(5) + x(6) - x(17) + x(18) + T34)^2 - 30^2$$

$$g(23) = (x(4) + x(6) + x(16) - x(18) + T34)^2 - 30^2$$

$$g(24) = (x(4) + x(6) + x(16) + x(18) + T34)^2 - 30^2$$

$$g(25) = (x(4) + x(16) + T34)^2 - 30^2$$

$$g(26) = (x(4) - x(16) + T34)^2 - 30^2$$

$$g(27) = (x(4) + x(5) + x(16) + x(17) + T34)^2 - 30^2$$

$$g(28) = (x(4) + x(5) + x(16) - x(17) + T34)^2 - 30^2$$

Inequality constraints for control surfaces 5 and 6 are provided below:

$$g\,(29) = (x(9) - x(21) + T56)^2 - 30^2$$

$$g\,(30) = (x(9) + x(21) + T56)^2 - 30^2$$

$$g\,(31) = (x(8) + x(9) + x(20) - x(21) + T56)^2 - 30^2$$

$$g\,(32) = (x(8) + x(9) + x(20) + x(21) + T56)^2 - 30^2$$

$$g\,(33) = (x(8) + x(20) + T56)^2 - 30^2$$

$$g\,(34) = (x(8) - x(20) + T56)^2 - 30^2$$

$$g\,(35) = (x(8) + x(9) - x(20) - x(21) + T56)^2 - 30^2$$

$$g\,(36) = (x(8) + x(9) - x(20) + x(21) + T56)^2 - 30^2$$

$$g\,(37) = (x(7) + x(9) + x(19) - x(21) + T56)^2 - 30^2$$

$$g\,(38) = (x(7) + x(9) + x(19) + x(21) + T56)^2 - 30^2$$

$$g\,(39) = (x(7) + x(19) + T56)^2 - 30^2$$

$$g\,(40) = (x(7) - x(19) + T56)^2 - 30^2$$

$$g\,(41) = (x(7) + x(8) + x(19) + x(20) + T56)^2 - 30^2$$

$$g\,(42) = (x(7) + x(8) + x(19) - x(20) + T56)^2 - 30^2$$

Inequality constraints for control surfaces 7 and 8 are provided below:

$$g\,(43) = (x(12) - x(24) + T78)^2 - 30^2$$

$$g\,(44) = (x(12) + x(24) + T78)^2 - 30^2$$

$$g\,(45) = (x(11) + x(12) + x(23) - x(24) + T78)^2 - 30^2$$

$$g\,(46) = (x(11) + x(12) + x(23) + x(24) + T78)^2 - 30^2$$

$$g\,(47) = (x(11) + x(23) + T78)^2 - 30^2$$

$$g\,(48) = (x(11) - x(23) + T78)^2 - 30^2$$

$$g\,(49) = (x(11) + x(12) - x(23) - x(24) + T78)^2 - 30^2$$

$$g\,(50) = (x(11) + x(12) - x(23) + x(24) + T78)^2 - 30^2$$

$$g\,(51) = (x(10) + x(12) + x(22) - x(24) + T78)^2 - 30^2$$

$$g\,(52) = (x(10) + x(12) + x(22) + x(24) + T78)^2 - 30^2$$

$$g\,(53) = (x(10) + x(22) + T78)^2 - 30^2$$

$$g\,(54) = (x(10) - x(22) + T78)^2 - 30^2$$

$$g\,(55) = (x(10) + x(11) + x(22) + x(23) + T78)^2 - 30^2$$

$$g\,(56) = (x(10) + x(11) + x(22) - x(23) + T78)^2 - 30^2$$

Appendix E: Optimisation summary

The optimisation process consisted of 72 runs. A short description of each run is provided below, with a mathematical expression of the objective function, equality and inequality constraints. The optimisation results used in this thesis are identified later in the section.

Description of Optimisation Run 1:

The first optimisation run consisted of maximising the roll rate:

$$f\_val = -\dot{p}$$

The six steady-state equations were implemented as equality constraints in order to trim the aircraft:

$$h\_vec(1) = \dot{p}$$

$$h\_vec(2) = \dot{q}$$

$$h\_vec(3) = \dot{r}$$

$$h\_vec(4) = \dot{V}_t$$

$$h\_vec(5) = \dot{\beta}$$

$$h\_vec(6) = \dot{\alpha}$$

The control surface deflections were limited by using the first eight inequality constraints, and the remaining four constraints were implemented to limit the output control commands:

$$g_{vec(1)} = x(1).^2 + x(2).^2 + x(3).^2 - 15^2$$

$$g_{vec(2)} = x(4).^2 + x(5).^2 + x(6).^2 - 15^2$$

$$g_{vec(3)} = x(7).^2 + x(8).^2 + x(9).^2 - 15^2$$

$$g_{vec(4)} = x(10).^2 + x(11).^2 + x(12).^2 - 15^2$$

$$g_{vec(5)} = x(13).^2 + x(14).^2 + x(15).^2 - 15^2$$

$$g_{vec(6)} = x(16).^2 + x(17).^2 + x(18).^2 - 15^2$$

$$g_{vec(7)} = x(19).^2 + x(20).^2 + x(21).^2 - 15^2$$

$$g_{vec(8)} = x(22).^2 + x(23).^2 + x(24).^2 - 15^2$$

$$g_{vec(9)} = x(25).^2 - 1$$

$$g_{vec(10)} = x(26).^2 - 1$$

$$g_{vec(11)} = x(27).^2 - 1$$

$$g\_vec(12) = x(28) - 1$$

Description of Optimisation Run 2:

The second optimisation run consisted of the same equality and inequality constraints, but the objective function given below was used with the goal of optimising six of the rates:

$$f_{val} = \dot{V_t}^2 + \dot{\alpha}^2 + \dot{\beta}^2 + \dot{p}^2 + \dot{q}^2 + \dot{r}^2$$

Description of Optimisation Run 3:

The results for the first two runs were insufficient, and the designer therefore redefined the optimisation process so that it consisted of two phases, as reported in the thesis. The first phase was to obtain the trim bias vector. The eight design variables in the objective function were therefore the control surface deflection positions at trim:

$$f\_val = x(1)^2 + x(2)^2 + x(3)^2 + x(4)^2 + x(5)^2 + x(6)^2 + x(7)^2 + x(8)^2$$

Optimisation Phase 1 had no inequality constraints. The equality constraints consisted of the six steady-state equations required to trim the aircraft:

$$h\_vec(1) = \dot{p}$$

$$h\_vec(2) = \dot{q}$$

$$h\_vec(3) = \dot{r}$$

$$h\_vec(4) = \dot{V_t}$$

$$h\_vec(5) = \dot{\beta}$$

$$h\_vec(6) = \dot{\alpha}$$

Description of Optimisation Run 4:

The objective was to optimise the roll rate and yaw rate of the aircraft with both weights equal to 1:

$$w1 = 1$$

$$w2 = 1$$

$$f\_val = -(w1 \cdot pdot + w2 \cdot rdot)$$

The control surface deflections were limited by restricting each one individually, using an inequality constraint:

$$g\_vec(1) = \left(T(1) + x(1) + x(2) + x(3) + x(13) + x(14) + x(15)\right)^2 - 15^2$$

$$g\_vec(2) = \left(T(2) + x(1) + x(2) + x(3) + x(13) - x(14) - x(15)\right)^2 - 15^2$$

$$g\_vec(3) = \left(T(3) + x(4) + x(5) + x(6) + x(16) + x(17) + x(18)\right)^2 - 15^2$$

$$g\_vec(4) = \left(T(4) + x(4) + x(5) + x(6) + x(16) - x(17) - x(18)\right)^2 - 15^2$$

$$g\_vec(5) = \left(T(5) + x(7) + x(8) + x(9) + x(19) + x(20) + x(21)\right)^2 - 15^2$$

$$g\_vec(6) = \left(T(6) + x(7) + x(8) + x(9) + x(19) - x(20) - x(21)\right)^2 - 15^2$$

$$g\_vec(7) = \left(T(7) + x(10) + x(11) + x(12) + x(22) + x(23) + x(24)\right)^2 - 15^2$$

$$g\_vec(8) = \left(T(8) + x(10) + x(11) + x(12) + x(22) - x(23) - x(24)\right)^2 - 15^2$$

Description of Optimisation Run 5:

The same objective function was used for runs 4 and 5. The only difference between the two runs was the number of inequality constraints implemented. Each control surface was now restricted by two inequality constraints to limit the positive and negative deflection instead of squaring the equation:

$$g_{vec(1)} = T(1) + [|x_1| + |x_2| + |x_3| + |x_{13}| + |x_{14}| + |x_{15}|] - 15$$

$$g_{vec(2)} = -T(1) - [|x_1| + |x_2| + |x_3| + |x_{13}| + |x_{14}| + |x_{15}|] - 15$$

$$g_{vec(3)} = T(2) + [|x_1| + |x_2| + |x_3| + |x_{13}| + |x_{14}| + |x_{15}|] - 15$$

$$g_{vec(4)} = -T(2) - [|x_1| + |x_2| + |x_3| + |x_{13}| + |x_{14}| + |x_{15}|] - 15$$

$$g_{vec(5)} = T(3) + [|x_4| + |x_5| + |x_6| + |x_{16}| + |x_{17}| + |x_{18}|] - 15$$

$$g_{vec(6)} = -T(3) - [|x_4| + |x_5| + |x_6| + |x_{16}| + |x_{17}| + |x_{18}|] - 15$$

$$g_{vec(7)} = T(4) + [|x_4| + |x_5| + |x_6| + |x_{16}| + |x_{17}| + |x_{18}|] - 15$$

$$g_{vec(8)} = -T(4) - [|x_4| + |x_5| + |x_6| + |x_{16}| + |x_{17}| + |x_{18}|] - 15$$

$$g_{vec(9)} = T(5) + [|x_7| + |x_8| + |x_9| + |x_{19}| + |x_{20}| + |x_{21}|] - 15$$

$$g_{vec(10)} = -T(5) - [|x_7| + |x_8| + |x_9| + |x_{19}| + |x_{20}| + |x_{21}|] - 15$$

$$g_{vec(11)} = T(6) + [|x_7| + |x_8| + |x_9| + |x_{19}| + |x_{20}| + |x_{21}|] - 15$$

$$g_{vec(12)} = -T(6) - [|x_7| + |x_8| + |x_9| + |x_{19}| + |x_{20}| + |x_{21}|] - 15$$

$$g_{vec(13)} = T(7) + [|x_{10}| + |x_{11}| + |x_{12}| + |x_{22}| + |x_{23}| + |x_{24}|] - 15$$

$$g_{vec(14)} = -T(7) - [|x_{10}| + |x_{11}| + |x_{12}| + |x_{22}| + |x_{23}| + |x_{24}|] - 15$$

$$g_{vec(15)} = T(8) + [|x_{10}| + |x_{11}| + |x_{12}| + |x_{22}| + |x_{23}| + |x_{24}|] - 15$$

$$g_{vec(16)} = -T(8) - [|x_{10}| + |x_{11}| + |x_{12}| + |x_{22}| + |x_{23}| + |x_{24}|] - 15$$

Description of Optimisation Run 6:

The same objective function was used for runs 4, 5 and 6. The only difference between the runs was the inequality constraints implemented. Each control surface was restricted by only one inequality constraint to limit the positive and negative deflection:

$$g_{vec(1)} = [|x_1| + |x_2| + |x_3| + |x_{13}| + |x_{14}| + |x_{15}|]^2 - 15^2$$

$$g_{vec(2)} = -[|x_1| + |x_2| + |x_3| + |x_{13}| + |x_{14}| + |x_{15}|]^2 - 15^2$$

$$g_{vec(3)} = +[|x_4| + |x_5| + |x_6| + |x_{16}| + |x_{17}| + |x_{18}|]^2 - 15^2$$

$$g_{vec(4)} = -[|x_4| + |x_5| + |x_6| + |x_{16}| + |x_{17}| + |x_{18}|]^2 - 15^2$$

$$g_{vec(5)} = +[|x_7| + |x_8| + |x_9| + |x_{19}| + |x_{20}| + |x_{21}|]^2 - 15^2$$

$$g_{vec(6)} = -[|x_7| + |x_8| + |x_9| + |x_{19}| + |x_{20}| + |x_{21}|]^2 - 15^2$$

$$g_{vec(7)} = +[|x_{10}| + |x_{11}| + |x_{12}| + |x_{22}| + |x_{23}| + |x_{24}|]^2 - 15^2$$

$$g_{vec(8)} = -[|x_{10}| + |x_{11}| + |x_{12}| + |x_{22}| + |x_{23}| + |x_{24}|]^2 - 15^2$$

Description of Optimisation Run 7:

The objective function for the seventh run consisted of maximising the roll, yaw and pitch rates of the aircraft.

$$w_1 = 1$$

$$w_2 = 1$$

$$w_3 = 1$$

$$f\_val = -(w_1 * pdot + w_2 * rdot + w_3 * qdot)$$

The inequality constraints consisted of the set defined below:

$$g_{vec(1)} = \left(0.5 * \left(T(1) + T(2)\right) + |x_1| + a|x_{13}|\right)^2 - 10^2$$

$$g_{vec(2)} = \left(0.5 * \left(T(3) + T(4)\right) + |x_4| + a|x_{16}|\right)^2 - 10^2$$

$$g_{vec(3)} = \left(0.5 * \left(T(5) + T(6)\right) + |x_7| + |x_{19}|\right)^2 - 10^2$$

$$g_{vec(4)} = \left(0.5 * \left(T(7) + T(8)\right) + |x_{10}| + |x_{21}|\right)^2 - 10^2$$

$$g_{vec(5)} = \left(0.5 * \left(T(1) + T(2)\right) + |x_2| + |x_{14}|\right)^2 - 10^2$$

$$g_{vec(6)} = \left(0.5 * \left(T(3) + T(4)\right) + |x_5| + |x_{17}|\right)^2 - 10^2$$

$$g_{vec(7)} = \left(0.5 * \left(T(5) + T(6)\right) + |x_8| + |x_{20}|\right)^2 - 10^2$$

$$g_{vec(8)} = \left(0.5 * \left(T(7) + T(8)\right) + |x_{11}| + |x_{23}|\right)^2 - 10^2$$

$$g_{vec(9)} = \left(0.5 * \left(T(1) + T(2)\right) + |x_3| + |x_{15}|\right)^2 - 10^2$$

$$g_{vec(10)} = \left(0.5 * \left(T(3) + T(4)\right) + |x_6| + |x_{18}|\right)^2 - 10^2$$

$$g_{vec(11)} = \left(0.5 * \left(T(5) + T(6)\right) + |x_9| + |x_{21}|\right)^2 - 10^2$$

$$g_{vec(12)} = \left(0.5 * \left(T(7) + T(8)\right) + |x_{12}| + |x_{24}|\right)^2 - 10^2$$

Description of Optimisation Run 8:

The objective function for the eighth run consisted of maximising the roll, yaw and pitch rates of the aircraft:

$$w_1 = 1$$

$$w_2 = 1$$

$$w_3 = 1$$

$$f\_val = -(w_1 * pdot + w_2 * rdot + w_3 * qdot)$$

The inequality constraints consisted of the set defined below:

$$g_{vec(1)} = \left(\frac{1}{2}(T_1 + T_2)\right)^2 + x(1).^2 + x(2).^2 + x(3).^2 + x(13).^2 + x(14).^2 + x(15).^2 - 15^2$$

$$g_{vec(2)} = \left(\frac{1}{2}(T_1 + T_2)\right)^2 + x(1).^2 + x(2).^2 + x(3).^2 + x(13).^2 - x(14).^2 - x(15).^2 - 15^2$$

$$g_{vec(3)} = \left(\frac{1}{2}(T_3 + T_4)\right)^2 + x(4).^2 + x(5).^2 + x(6).^2 + x(16).^2 + x(17).^2 + x(18).^2 - 15^2$$

$$g_{vec(4)} = \left(\frac{1}{2}(T_3 + T_4)\right)^2 + x(4).^2 + x(5).^2 + x(6).^2 + x(16).^2 - x(17).^2 - x(18).^2 - 15^2$$

$$g_{vec(5)} = \left(\frac{1}{2}(T_5 + T_6)\right)^2 + x(7).^2 + x(8).^2 + x(9).^2 + x(19).^2 + x(20).^2 + x(21).^2 - 15^2$$

$$g_{vec(6)} = \left(\frac{1}{2}(T_5 + T_6)\right)^2 + x(7).^2 + x(8).^2 + x(9).^2 + x(19).^2 - x(20).^2 - x(21).^2 - 15^2$$

$$g_{vec(7)} = \left(\frac{1}{2}(T_7 + T_8)\right)^2 + x(10).^2 + x(11).^2 + x(12).^2 + x(22).^2 + x(23).^2 + x(24).^2 - 15^2$$

$$g_{vec(8)} = \left(\frac{1}{2}(T_7 + T_8)\right)^2 + x(10).^2 + x(11).^2 + x(12).^2 + x(22).^2 - x(23).^2 - x(24).^2 - 15^2$$

Description of Optimisation Run 9:

The objective function and constraints of the ninth run were exactly the same as for Optimisation Run 8. The only difference was that equality constraints were also defined for Optimisation Run 9.

The equality constraints are defined below:

$$h\_vec(1) = rdot$$

$$h\_vec(2) = qdot$$

$$h\_vec(3) = pdot$$

$$h\_vec(4) = qdot2$$

Description of Optimisation Run 10:

The same objective function and equality constraints were used for optimisation runs 9 and 10. However, the inequality constraints were increased to two constraints per control surface in order to restrict the up and down deflection of the control surfaces:

$$g_{vec(1)} = \left(\frac{1}{2}(T_1 + T_2)\right)^2 + x(1).^2 + x(2).^2 + x(3).^2 + x(13).^2 + x(14).^2 + x(15).^2 - 15^2$$

$$g_{vec(2)} = \left(\frac{1}{2}(T_1 + T_2)\right)^2 + x(1).^2 + x(2).^2 + x(3).^2 + x(13).^2 - x(14).^2 - x(15).^2 - 15^2$$

$$g_{vec(3)} = \left(\frac{1}{2}(T_3 + T_4)\right)^2 + x(4).^2 + x(5).^2 + x(6).^2 + x(16).^2 + x(17).^2 + x(18).^2 - 15^2$$

$$g_{vec(4)} = \left(\frac{1}{2}(T_3 + T_4)\right)^2 + x(4).^2 + x(5).^2 + x(6).^2 + x(16).^2 - x(17).^2 - x(18).^2 - 15^2$$

$$g_{vec(5)} = \left(\frac{1}{2}(T_5 + T_6)\right)^2 + x(7).^2 + x(8).^2 + x(9).^2 + x(19).^2 + x(20).^2 + x(21).^2 - 15^2$$

$$g_{vec(6)} = \left(\frac{1}{2}(T_5 + T_6)\right)^2 + x(7).^2 + x(8).^2 + x(9).^2 + x(19).^2 - x(20).^2 - x(21).^2 - 15^2$$

$$g_{vec(7)} = \left(\frac{1}{2}(T_7 + T_8)\right)^2 + x(10).^2 + x(11).^2 + x(12).^2 + x(22).^2 + x(23).^2 + x(24).^2 - 15^2$$

$$g_{vec(8)} = \left(\frac{1}{2}(T_7 + T_8)\right)^2 + x(10).^2 + x(11).^2 + x(12).^2 + x(22).^2 - x(23).^2 - x(24).^2 - 15^2$$

$$g_{vec(9)} = -\left[\left(\frac{1}{2}(T_1 + T_2)\right)^2 + x(1).^2 + x(2).^2 + x(3).^2 + x(13).^2 + x(14).^2 + x(15).^2\right] - 15^2$$

$$g_{vec(10)} = -\left[\left(\frac{1}{2}(T_1 + T_2)\right)^2 + x(1).^2 + x(2).^2 + x(3).^2 + x(13).^2 - x(14).^2 - x(15).^2\right] - 15^2$$

$$g_{vec(11)} = -\left[\left(\frac{1}{2}(T_3 + T_4)\right)^2 + x(4).^2 + x(5).^2 + x(6).^2 + x(16).^2 + x(17).^2 + x(18).^2\right] - 15^2$$

$$g_{vec(12)} = -\left[\left(\frac{1}{2}(T_3 + T_4)\right)^2 + x(4).^2 + x(5).^2 + x(6).^2 + x(16).^2 - x(17).^2 - x(18).^2\right] - 15^2$$

$$g_{vec(13)} = -\left[\left(\frac{1}{2}(T_5 + T_6)\right)^2 + x(7).^2 + x(8).^2 + x(9).^2 + x(19).^2 + x(20).^2 + x(21).^2\right] - 15^2$$

$$g_{vec(14)} = -\left[\left(\frac{1}{2}(T_5 + T_6)\right)^2 + x(7).^2 + x(8).^2 + x(9).^2 + x(19).^2 - x(20).^2 - x(21).^2\right] - 15^2$$

$$g_{vec(15)} = -\left[\left(\frac{1}{2}(T_7 + T_8)\right)^2 + x(10).^2 + x(11).^2 + x(12).^2 + x(22).^2 + x(23).^2 + x(24).^2\right] - 15^2$$

$$g_{vec(16)} = -\left[\left(\frac{1}{2}(T_7 + T_8)\right)^2 + x(10).^2 + x(11).^2 + x(12).^2 + x(22).^2 - x(23).^2 - x(24).^2\right] - 15^2$$

Description of Optimisation Run 11:

The same objective function, equality and inequality constraints were used for optimisation runs 10 and 11, apart from the weights that were adjusted for the eleventh run, as illustrated below:

$$w_1 = 1$$

$$w_2 = 1$$

$$w_3 = 0.3$$

Description of Optimisation Run 12:

The objective function for the twelfth run consisted of maximising the roll, yaw and pitch rates of the aircraft:

$$w_1 = 1$$

$$w_2 = 1$$

$$w_3 = 0.3$$

$$f\_val = -(w_1 \cdot pdot + w_2 \cdot rdot + w_3 \cdot qdot)$$

The equality constraints are defined below:

$$h\_vec(1) = rdot$$

$$h\_vec(2) = qdot$$

$$h\_vec(3) = pdot$$

$$h\_vec(4) = qdot2$$

The control surface deflections were limited by restricting each one individually, using an inequality constraint:

$$g\_vec(1) = \left(T(1) + x(1) + x(2) + x(3) + x(13) + x(14) + x(15)\right)^2 - 15^2$$

$$g\_vec(2) = \left(T(2) + x(1) + x(2) + x(3) + x(13) - x(14) - x(15)\right)^2 - 15^2$$

$$g\_vec(3) = \left(T(3) + x(4) + x(5) + x(6) + x(16) + x(17) + x(18)\right)^2 - 15^2$$

$$g\_vec(4) = \left(T(4) + x(4) + x(5) + x(6) + x(16) - x(17) - x(18)\right)^2 - 15^2$$

$$g\_vec(5) = \left(T(5) + x(7) + x(8) + x(9) + x(19) + x(20) + x(21)\right)^2 - 15^2$$

$$g\_vec(6) = \left(T(6) + x(7) + x(8) + x(9) + x(19) - x(20) - x(21)\right)^2 - 15^2$$

$$g\_vec(7) = \left(T(7) + x(10) + x(11) + x(12) + x(22) + x(23) + x(24)\right)^2 - 15^2$$

$$g\_vec(8) = \left(T(8) + x(10) + x(11) + x(12) + x(22) - x(23) - x(24)\right)^2 - 15^2$$

Description of Optimisation Run 13:

The objective function terms were slightly changed by separating the nose-up and nose-down pitch rates. A symmetrical response for roll and yaw is desired, but for pitch up and down, an asymmetrical response is desired. Therefore, the two rates were separated and each was given its own weight, as illustrated below:

$$w_1 = 1$$

$$w_2 = 15$$

$$w_3 = 1$$

$$w_4 = 0.3$$

$$f\_val = -(2w1 \cdot pdot + 2w2 \cdot rdot + w3 \cdot qdot - w4 \cdot qdotn)$$

The equality constraints are defined below:

$$h\_vec(1) = rdot$$

$$h\_vec(2) = qdot$$

$$h\_vec(3) = pdot$$

$$h\_vec(4) = qdot2$$

The inequality constraints consisted of the set defined below:

$$g_{vec(1)} = \left(\frac{1}{2}(T_1 + T_2)\right)^2 + x(1).^2 + x(2).^2 + x(3).^2 + x(13).^2 + x(14).^2 + x(15).^2 - 25^2$$

$$g_{vec(2)} = \left(\frac{1}{2}(T_1 + T_2)\right)^2 + x(1).^2 + x(2).^2 + x(3).^2 + x(13).^2 - x(14).^2 - x(15).^2 - 25^2$$

$$g_{vec(3)} = \left(\frac{1}{2}(T_3 + T_4)\right)^2 + x(4).^2 + x(5).^2 + x(6).^2 + x(16).^2 + x(17).^2 + x(18).^2 - 25^2$$

$$g_{vec(4)} = \left(\frac{1}{2}(T_3 + T_4)\right)^2 + x(4).^2 + x(5).^2 + x(6).^2 + x(16).^2 - x(17).^2 - x(18).^2 - 25^2$$

$$g_{vec(5)} = \left(\frac{1}{2}(T_5 + T_6)\right)^2 + x(7).^2 + x(8).^2 + x(9).^2 + x(19).^2 + x(20).^2 + x(21).^2 - 25^2$$

$$g_{vec(6)} = \left(\frac{1}{2}(T_5 + T_6)\right)^2 + x(7).^2 + x(8).^2 + x(9).^2 + x(19).^2 - x(20).^2 - x(21).^2 - 25^2$$

$$g_{vec(7)} = \left(\frac{1}{2}(T_7 + T_8)\right)^2 + x(10).^2 + x(11).^2 + x(12).^2 + x(22).^2 + x(23).^2 + x(24).^2 - 25^2$$

$$g_{vec(8)} = \left(\frac{1}{2}(T_7 + T_8)\right)^2 + x(10).^2 + x(11).^2 + x(12).^2 + x(22).^2 - x(23).^2 - x(24).^2 - 25^2$$

The objective function, equality constraints and inequality constraints for the following few optimisation runs remained the same; only the weights were adjusted to obtain the desired aircraft response.

Description of Optimisation Run 14:

$$w_1 = 1$$

$$w_2 = 30$$

$$w_3 = 1$$

$$w_4 = 0.3$$

Description of Optimisation Run 15:

$$w_1 = 1$$

$$w_2 = 100$$

$$w_3 = 1$$

$$w_4 = 0.3$$

Description of Optimisation Run 16:

$$w_1 = 0.5$$

$$w_2 = 30$$

$$w_3 = 1.25$$

$$w_4 = 0.55$$

Description of Optimisation Run 17:

$$w_1 = 0.5$$

$$w_2 = 40$$

$$w_3 = 1.25$$

$$w_4 = 0.55$$

Description of Optimisation Run 18:

$$w_1 = 0.5$$

$$w_2 = 30$$

$$w_3 = 1.25$$

$$w_4 = 0.55$$

Description of Optimisation Run 19:

$$w_1 = 0.7$$

$$w_2 = 30$$

$$w_3 = 1.23$$

$$w_4 = 0.55$$

Description of Optimisation Run 20:

$$w_1 = 0.8$$

$$w_2 = 30$$

$$w_3 = 1.22$$

$$w_4 = 0.55$$

Description of Optimisation Run 21:

$$w_1 = 1.0$$

$$w_2 = 30$$

$$w_3 = 1.25$$

$$w_4 = 0.5$$

Description of Optimisation Run 22:

The remaining optimisation runs were all conducted using the inequality constraints expressed in section 4.5.4:

$$w_1 = 0.8$$

$$w_2 = 30$$

$$w_3 = 1.22$$

$$w_4 = 0.55$$

The objective function remained unchanged:

$$f\_val = -(2w1 \cdot pdot + 2w2 \cdot rdot + w3 \cdot qdot - w4 \cdot qdotn)$$

The equality constraints are defined below:

$$h\_vec(1) = rdot$$

$$h\_vec(2) = qdot$$

$$h\_vec(3) = pdot$$

$$h\_vec(4) = qdot2$$

Description of Optimisation Run 23:

Note that the inequality constraints remained unchanged for the remaining optimisation runs. Since a poor response was obtained for optimising the yaw rate, it was replaced in the objective function with the maximum sideslip that could be generated:

$$w_1 = 0.8$$

$$w_2 = 30$$

$$w_3 = 1.22$$

$$w_4 = 0.55$$

$$f\_val = -(2w1 \cdot pdot + 2w2 \cdot \beta + w3 \cdot qdot - w4 \cdot qdotn)$$

Description of Optimisation Run 24:

The objective function, equality and inequality constraints remained unchanged. The only adjustment made for this optimisation run was the weights assigned to each objective function term:

$$w_1 = 0.8$$

$$w_2 = 30$$

$$w_3 = 3$$

$$w_4 = 0.55$$

Description of Optimisation Run 25:

$$w_1 = 0.6$$

$$w_2 = 100$$

$$w_3 = 5$$

$$w_4 = 0.3$$

Description of Optimisation Run 26:

$$w_1 = 0.8$$

$$w_2 = 100$$

$$w_3 = 5$$

$$w_4 = 0.03$$

Description of Optimisation Run 27:

The sideslip in the objective function was optimised at 1.5 seconds, due to previous results revealing the time step where the sideslip features:

$$f\_val = -(2w1 \cdot pdot + 2w2 \cdot \beta_{t=1.5s} + w3 \cdot qdot - w4 \cdot qdotn)$$

$$w_1 = 0.8$$

$$w_2 = 30$$

$$w_3 = 1.22$$

$$w_4 = 0.55$$

Description of Optimisation Run 28:

$$w_1 = 0.8$$

$$w_2 = 250$$

$$w_3 = 5$$

$$w_4 = 0.01$$

Description of Optimisation Run 29:

The objective function term for sideslip was changed back to maximising the initial sideslip generated:

$$f\_val = -(2w1 \cdot pdot + 2w2 \cdot \beta + w3 \cdot qdot - w4 \cdot qdotn)$$

$$w_1 = 0.8$$

$$w_2 = 100$$

$$w_3 = 5$$

$$w_4 = 0.03$$

Description of Optimisation Run 30:

The best optimisation results using the optimisation problem defined above were obtained using the weights given below. These results were used for the first publication:

$$w_1 = 0.8$$

$$w_2 = 1000$$

$$w_3 = 5$$

$$w_4 = 0.01$$

The weights illustrated above were not intuitive and various optimisation runs were required to obtain these results. The objective function terms were then normalised to provide the user with weights of a similar order magnitude. This is recommended when the objective function terms have different units.

Description of Optimisation Run 31:

The optimisation process was performed at three flight conditions to obtain the maximum rates the aircraft can achieve in order to normalise the objective function terms using those values. The first run consisted of obtaining the maximum roll rate the aircraft could achieve:

$$V_t = 30\,m/s$$

$$w_1 = 1.0$$

$$w_2 = 0.00001$$

$$w_3 = 0.00001$$

$$w_4 = 0.00001$$

$$f\_val = -(2w1 \cdot pdot + 2w2 \cdot \beta + w3 \cdot qdot - w4 \cdot qdotn)$$

Description of Optimisation Run 32:

The second run consisted of obtaining the maximum sideslip the aircraft could achieve:

$$V_t = 30\,m/s$$

$$w_1 = 0.00001$$

$$w_2 = 1.0$$

$$w_3 = 0.00001$$

$$w_4 = 0.00001$$

$$f\_val = -(2w1 \cdot pdot + 2w2 \cdot \beta + w3 \cdot qdot - w4 \cdot qdotn)$$

Description of Optimisation Run 33:

The third run consisted of obtaining the maximum nose-up pitch rate the aircraft could achieve:

$$V_t = 30\,m/s$$

$$w_1 = 0.00001$$

$$w_2 = 0.00001$$

$$w_3 = 1.0$$

$$w_4 = 0.00001$$

$$f\_val = -(2w1 \cdot pdot + 2w2 \cdot \beta + w3 \cdot qdot - w4 \cdot qdotn)$$

Description of Optimisation Run 34:

The fourth run consisted of obtaining the maximum nose-down pitch rate the aircraft could achieve:

$$V_t = 30\,m/s$$

$$w_1 = 0.00001$$

$$w_2 = 0.00001$$

$$w_3 = 0.00001$$

$$w_4 = 1.0$$

$$f\_val = -(2w1 \cdot pdot + 2w2 \cdot \beta + w3 \cdot qdot - w4 \cdot qdotn)$$

Description of Optimisation Run 35:

The objective function was normalised using the results obtained from the runs described above:

$$V_t = 30\,m/s$$

$$f1 = \dot{p}/135.6089$$

$$f2 = \beta/(-0.0627)$$

$$f3 = \dot{q}/36.4457$$

$$f4 = \dot{q_n}/(-46.5958)$$

$$w_1 = 1.0$$

$$w_2 = 1.0$$

$$w_3 = 1.0$$

$$w_4 = 1.0$$

$$f\_val = -(2w1 \cdot f1 - 2w2 \cdot f2 + w3 \cdot f3 - w4 \cdot f4)$$

Description of Optimisation Run 36:

The optimisation process was performed at three flight conditions to obtain the maximum rates the aircraft could achieve in order to normalise the objective function terms using those values. The first run consisted of obtaining the maximum roll rate the aircraft could achieve:

$$V_t = 20\,m/s$$

$$w_1 = 1.0$$

$$w_2 = 0.00001$$

$$w_3 = 0.00001$$

$$w_4 = 0.00001$$

$$f\_val = -(2w1 \cdot pdot + 2w2 \cdot \beta + w3 \cdot qdot - w4 \cdot qdotn)$$

Description of Optimisation Run 37:

The second run consisted of obtaining the maximum sideslip the aircraft could achieve:

$$V_t = 20\,m/s$$

$$w_1 = 0.00001$$

$$w_2 = 1.0$$

$$w_3 = 0.00001$$

$$w_4 = 0.00001$$

$$f\_val = -(2w1 \cdot pdot + 2w2 \cdot \beta + w3 \cdot qdot - w4 \cdot qdotn)$$

Description of Optimisation Run 38:

The third run consisted of obtaining the maximum nose-up pitch rate the aircraft could achieve:

$$V_t = 20\,m/s$$

$$w_1 = 0.00001$$

$$w_2 = 0.00001$$

$$w_3 = 1.0$$

$$w_4 = 0.00001$$

$$f\_val = -(2w1 \cdot pdot + 2w2 \cdot \beta + w3 \cdot qdot - w4 \cdot qdotn)$$

Description of Optimisation Run 39:

The fourth run consisted of obtaining the maximum nose-down pitch rate the aircraft could achieve:

$$V_t = 20\,m/s$$

$$w_1 = 0.00001$$

$$w_2 = 0.00001$$

$$w_3 = 0.00001$$

$$w_4 = 1.0$$

$$f\_val = -(2w1 \cdot pdot + 2w2 \cdot \beta + w3 \cdot qdot - w4 \cdot qdotn)$$

Description of Optimisation Run 40:

The objective function was normalised using the results obtained from the runs above:

$$V_t = 20\,m/s$$

$$f1 = \dot{p}/48.3046$$

$$f2 = \beta/(-0.0389)$$

$$f3 = \dot{q}/9.5877$$

$$f4 = \dot{q_n}/(-23.3096)$$

$$w_1 = 1.0$$

$$w_2 = 1.0$$

$$w_3 = 1.0$$

$$w_4 = 1.0$$

$$f\_val = -(2w1 \cdot f1 - 2w2 \cdot f2 + w3 \cdot f3 - w4 \cdot f4)$$

Description of Optimisation Run 41:

The optimisation process was performed at three flight conditions to obtain the maximum rates the aircraft could achieve in order to normalise the objective function terms using those values. The first run consisted of obtaining the maximum roll rate the aircraft could achieve:

$$V_t = 40\,m/s$$

$$w_1 = 1.0$$

$$w_2 = 0.00001$$

$$w_3 = 0.00001$$

$$w_4 = 0.00001$$

$$f\_val = -(2w1 \cdot pdot + 2w2 \cdot \beta + w3 \cdot qdot - w4 \cdot qdotn)$$

Description of Optimisation Run 42:

The second run consisted of obtaining the maximum sideslip the aircraft could achieve:

$$V_t = 40\,m/s$$

$$w_1 = 0.00001$$

$$w_2 = 1.0$$

$$w_3 = 0.00001$$

$$w_4 = 0.00001$$

$$f\_val = -(2w1 \cdot pdot + 2w2 \cdot \beta + w3 \cdot qdot - w4 \cdot qdotn)$$

Description of Optimisation Run 43:

The third run consisted of obtaining the maximum nose-up pitch rate the aircraft could achieve:

$$V_t = 40\,m/s$$

$$w_1 = 0.00001$$

$$w_2 = 0.00001$$

$$w_3 = 1.0$$

$$w_4 = 0.00001$$

$$f\_val = -(2w1 \cdot pdot + 2w2 \cdot \beta + w3 \cdot qdot - w4 \cdot qdotn)$$

Description of Optimisation Run 44:

The fourth run consisted of obtaining the maximum nose-down pitch rate the aircraft could achieve:

$$V_t = 40\,m/s$$

$$w_1 = 0.00001$$

$$w_2 = 0.00001$$

$$w_3 = 0.00001$$

$$w_4 = 1.0$$

$$f\_val = -(2w1 \cdot pdot + 2w2 \cdot \beta + w3 \cdot qdot - w4 \cdot qdotn)$$

Description of Optimisation Run 45:

The objective function was normalised using the results obtained from the runs described above.

$$V_t = 40\,m/s$$

$$f1 = \dot{p}/222.626$$

$$f2 = \beta/(-0.0622)$$

$$f3 = \dot{q}/68.6286$$

$$f4 = \dot{q_n}/(-77.6347)$$

$$w_1 = 1.0$$

$$w_2 = 1.0$$

$$w_3 = 1.0$$

$$w_4 = 1.0$$

$$f\_val = -(2w1 \cdot f1 - 2w2 \cdot f2 + w3 \cdot f3 - w4 \cdot f4)$$

Description of Optimisation Run 46:

The weights were adjusted to evaluate the impact of relative weighting on the aircraft's response:

$$V_t = 20\,m/s$$

$$f1 = \dot{p}/48.3046$$

$$f2 = \beta/(-0.0389)$$

$$f3 = \dot{q}/9.5877$$

$$f4 = \dot{q_n}/(-23.3096)$$

$$w_1 = 1.0$$

$$w_2 = 1.0$$

$$w_3 = 1.5$$

$$w_4 = 0.5$$

$$f\_val = -(2w1 \cdot f1 - 2w2 \cdot f2 + w3 \cdot f3 - w4 \cdot f4)$$

Description of Optimisation Run 47:

The weights were adjusted to evaluate the impact of relative weighting on the aircraft's response:

$$V_t = 30\,m/s$$

$$f1 = \dot{p}/135.6089$$

$$f2 = \beta/(-0.0627)$$

$$f3 = \dot{q}/36.4457$$

$$f4 = \dot{q_n}/(-46.5958)$$

$$w_1 = 1.0$$

$$w_2 = 1.0$$

$$w_3 = 1.5$$

$$w_4 = 0.5$$

$$f\_val = -(2w1 \cdot f1 - 2w2 \cdot f2 + w3 \cdot f3 - w4 \cdot f4)$$

Description of Optimisation Run 48:

The weights were adjusted to evaluate the impact of relative weighting on the aircraft's response:

$$V_t = 40\,m/s$$

$$f1 = \dot{p}/222.626$$

$$f2 = \beta/(-0.0622)$$

$$f3 = \dot{q}/68.6286$$

$$f4 = \dot{q_n}/(-77.6347)$$

$$w_1 = 1.0$$

$$w_2 = 1.0$$

$$w_3 = 1.5$$

$$w_4 = 0.5$$

$$f\_val = -(2w1 \cdot f1 - 2w2 \cdot f2 + w3 \cdot f3 - w4 \cdot f4)$$

Description of Optimisation Run 49:

The weights were adjusted to evaluate the impact of relative weighting on the aircraft's response:

$$V_t = 20\,m/s$$

$$f1 = \dot{p}/48.3046$$

$$f2 = \beta/(-0.0389)$$

$$f3 = \dot{q}/9.5877$$

$$f4 = \dot{q_n}/(-23.3096)$$

$$w_1 = 1.0$$

$$w_2 = 1.0$$

$$w_3 = 1.1$$

$$w_4 = 0.9$$

$$f\_val = -(2w1 \cdot f1 - 2w2 \cdot f2 + w3 \cdot f3 - w4 \cdot f4)$$

Description of Optimisation Run 50:

The weights were adjusted to evaluate the impact of relative weighting on the aircraft's response:

$$V_t = 30\,m/s$$

$$f1 = \dot{p}/135.6089$$

$$f2 = \beta/(-0.0627)$$

$$f3 = \dot{q}/36.4457$$

$$f4 = \dot{q_n}/(-46.5958)$$

$$w_1 = 1.0$$

$$w_2 = 1.0$$

$$w_3 = 1.1$$

$$w_4 = 0.9$$

$$f\_val = -(2w1 \cdot f1 - 2w2 \cdot f2 + w3 \cdot f3 - w4 \cdot f4)$$

Description of Optimisation Run 51:

The weights were adjusted to evaluate the impact of relative weighting on the aircraft's response:

$$V_t = 40\,m/s$$

$$f1 = \dot{p}/222.626$$

$$f2 = \beta/(-0.0622)$$

$$f3 = \dot{q}/68.6286$$

$$f4 = \dot{q_n}/(-77.6347)$$

$$w_1 = 1.0$$

$$w_2 = 1.0$$

$$w_3 = 1.1$$

$$w_4 = 0.9$$

$$f\_val = -(2w1 \cdot f1 - 2w2 \cdot f2 + w3 \cdot f3 - w4 \cdot f4)$$

Description of Optimisation Run 52:

The weights were adjusted to evaluate the impact of relative weighting on the aircraft's response:

$$V_t = 20\,m/s$$

$$f1 = \dot{p}/48.3046$$

$$f2 = \beta/(-0.0389)$$

$$f3 = \dot{q}/9.5877$$

$$f4 = \dot{q_n}/(-23.3096)$$

$$w_1 = 1.0$$

$$w_2 = 1.0$$

$$w_3 = 1.2$$

$$w_4 = 0.8$$

$$f\_val = -(2w1 \cdot f1 - 2w2 \cdot f2 + w3 \cdot f3 - w4 \cdot f4)$$

Description of Optimisation Run 53:

The weights were adjusted to evaluate the impact of relative weighting on the aircraft's response:

$$V_t = 30\,m/s$$

$$f1 = \dot{p}/135.6089$$

$$f2 = \beta/(-0.0627)$$

$$f3 = \dot{q}/36.4457$$

$$f4 = \dot{q_n}/(-46.5958)$$

$$w_1 = 1.0$$

$$w_2 = 1.0$$

$$w_3 = 1.2$$

$$w_4 = 0.8$$

$$f\_val = -(2w1 \cdot f1 - 2w2 \cdot f2 + w3 \cdot f3 - w4 \cdot f4)$$

Description of Optimisation Run 54:

The weights were adjusted to evaluate the impact of relative weighting on the aircraft's response:

$$V_t = 40\,m/s$$

$$f1 = \dot{p}/222.626$$

$$f2 = \beta/(-0.0622)$$

$$f3 = \dot{q}/68.6286$$

$$f4 = \dot{q_n}/(-77.6347)$$

$$w_1 = 1.0$$

$$w_2 = 1.0$$

$$w_3 = 1.2$$

$$w_4 = 0.8$$

$$f\_val = -(2w1 \cdot f1 - 2w2 \cdot f2 + w3 \cdot f3 - w4 \cdot f4)$$

Description of Optimisation Run 55:

The weights were adjusted to evaluate the impact of relative weighting on the aircraft's response:

$$V_t = 20\,m/s$$

$$f1 = \dot{p}/48.3046$$

$$f2 = \beta/(-0.0389)$$

$$f3 = \dot{q}/9.5877$$

$$f4 = \dot{q_n}/(-23.3096)$$

$$w_1 = 0.9$$

$$w_2 = 1.0$$

$$w_3 = 1.2$$

$$w_4 = 0.9$$

$$f\_val = -(2w1 \cdot f1 - 2w2 \cdot f2 + w3 \cdot f3 - w4 \cdot f4)$$

Description of Optimisation Run 56:

The weights were adjusted to evaluate the impact of relative weighting on the aircraft's response:

$$V_t = 30\,m/s$$

$$f1 = \dot{p}/135.6089$$

$$f2 = \beta/(-0.0627)$$

$$f3 = \dot{q}/36.4457$$

$$f4 = \dot{q_n}/(-46.5958)$$

$$w_1 = 0.9$$

$$w_2 = 1.0$$

$$w_3 = 1.2$$

$$w_4 = 0.9$$

$$f\_val = -(2w1 \cdot f1 - 2w2 \cdot f2 + w3 \cdot f3 - w4 \cdot f4)$$

Description of Optimisation Run 57:

The weights were adjusted to evaluate the impact of relative weighting on the aircraft's response:

$$V_t = 40\,m/s$$

$$f1 = \dot{p}/222.626$$

$$f2 = \beta/(-0.0622)$$

$$f3 = \dot{q}/68.6286$$

$$f4 = \dot{q_n}/(-77.6347)$$

$$w_1 = 0.9$$

$$w_2 = 1.0$$

$$w_3 = 1.2$$

$$w_4 = 0.9$$

$$f\_val = -(2w1 \cdot f1 - 2w2 \cdot f2 + w3 \cdot f3 - w4 \cdot f4)$$

Description of Optimisation Run 58:

The weights were adjusted to evaluate the impact of relative weighting on the aircraft's response:

$$V_t = 20\,m/s$$

$$f1 = \dot{p}/48.3046$$

$$f2 = \beta/(-0.0389)$$

$$f3 = \dot{q}/9.5877$$

$$f4 = \dot{q_n}/(-23.3096)$$

$$w_1 = 0.9$$

$$w_2 = 1.0$$

$$w_3 = 1.4$$

$$w_4 = 0.7$$

$$f\_val = -(2w1 \cdot f1 - 2w2 \cdot f2 + w3 \cdot f3 - w4 \cdot f4)$$

Description of Optimisation Run 59:

The weights were adjusted to evaluate the impact of relative weighting on the aircraft's response:

$$V_t = 30\,m/s$$

$$f1 = \dot{p}/135.6089$$

$$f2 = \beta/(-0.0627)$$

$$f3 = \dot{q}/36.4457$$

$$f4 = \dot{q_n}/(-46.5958)$$

$$w_1 = 0.9$$

$$w_2 = 1.0$$

$$w_3 = 1.4$$

$$w_4 = 0.7$$

$$f\_val = -(2w1 \cdot f1 - 2w2 \cdot f2 + w3 \cdot f3 - w4 \cdot f4)$$

Description of Optimisation Run 60:

The weights were adjusted to evaluate the impact of relative weighting on the aircraft's response:

$$V_t = 40\,m/s$$

$$f1 = \dot{p}/222.626$$

$$f2 = \beta/(-0.0622)$$

$$f3 = \dot{q}/68.6286$$

$$f4 = \dot{q_n}/(-77.6347)$$

$$w_1 = 0.9$$

$$w_2 = 1.0$$

$$w_3 = 1.4$$

$$w_4 = 0.7$$

$$f\_val = -(2w1 \cdot f1 - 2w2 \cdot f2 + w3 \cdot f3 - w4 \cdot f4)$$

Description of Optimisation Run 61:

The weights were adjusted to evaluate the impact of relative weighting on the aircraft's response:

$$V_t = 20\,m/s$$

$$f1 = \dot{p}/48.3046$$

$$f2 = \beta/(-0.0389)$$

$$f3 = \dot{q}/9.5877$$

$$f4 = \dot{q_n}/(-23.3096)$$

$$w_1 = 0.8$$

$$w_2 = 1.2$$

$$w_3 = 1.2$$

$$w_4 = 0.8$$

$$f\_val = -(2w1 \cdot f1 - 2w2 \cdot f2 + w3 \cdot f3 - w4 \cdot f4)$$

Description of Optimisation Run 62:

The weights were adjusted to evaluate the impact of relative weighting on the aircraft's response:

$$V_t = 30\,m/s$$

$$f1 = \dot{p}/135.6089$$

$$f2 = \beta/(-0.0627)$$

$$f3 = \dot{q}/36.4457$$

$$f4 = \dot{q_n}/(-46.5958)$$

$$w_1 = 0.8$$

$$w_2 = 1.2$$

$$w_3 = 1.2$$

$$w_4 = 0.8$$

$$f\_val = -(2w1 \cdot f1 - 2w2 \cdot f2 + w3 \cdot f3 - w4 \cdot f4)$$

Description of Optimisation Run 63:

The weights were adjusted to evaluate the impact of relative weighting on the aircraft's response:

$$V_t = 40\,m/s$$

$$f1 = \dot{p}/222.626$$

$$f2 = \beta/(-0.0622)$$

$$f3 = \dot{q}/68.6286$$

$$f4 = \dot{q_n}/(-77.6347)$$

$$w_1 = 0.8$$

$$w_2 = 1.2$$

$$w_3 = 1.2$$

$$w_4 = 0.8$$

$$f\_val = -(2w1 \cdot f1 - 2w2 \cdot f2 + w3 \cdot f3 - w4 \cdot f4)$$

Description of Optimisation Run 64:

The weights were adjusted to evaluate the impact of relative weighting on the aircraft's response:

$$V_t = 20\,m/s$$

$$f1 = \dot{p}/48.3046$$

$$f2 = \beta/(-0.0389)$$

$$f3 = \dot{q}/9.5877$$

$$f4 = \dot{q_n}/(-23.3096)$$

$$w_1 = 0.5$$

$$w_2 = 1.5$$

$$w_3 = 1.5$$

$$w_4 = 0.5$$

$$f\_val = -(2w1 \cdot f1 - 2w2 \cdot f2 + w3 \cdot f3 - w4 \cdot f4)$$

Description of Optimisation Run 65:

The weights were adjusted to evaluate the impact of relative weighting on the aircraft's response:

$$V_t = 30\,m/s$$

$$f1 = \dot{p}/135.6089$$

$$f2 = \beta/(-0.0627)$$

$$f3 = \dot{q}/36.4457$$

$$f4 = \dot{q_n}/(-46.5958)$$

$$w_1 = 0.5$$

$$w_2 = 1.5$$

$$w_3 = 1.5$$

$$w_4 = 0.5$$

$$f\_val = -(2w1 \cdot f1 - 2w2 \cdot f2 + w3 \cdot f3 - w4 \cdot f4)$$

Description of Optimisation Run 66:

The weights were adjusted to evaluate the impact of relative weighting on the aircraft's response:

$$V_t = 40\,m/s$$

$$f1 = \dot{p}/222.626$$

$$f2 = \beta/(-0.0622)$$

$$f3 = \dot{q}/68.6286$$

$$f4 = \dot{q_n}/(-77.6347)$$

$$w_1 = 0.5$$

$$w_2 = 1.5$$

$$w_3 = 1.5$$

$$w_4 = 0.5$$

$$f\_val = -(2w1 \cdot f1 - 2w2 \cdot f2 + w3 \cdot f3 - w4 \cdot f4)$$

Description of Optimisation Run 67:

The weights were adjusted to evaluate the impact of relative weighting on the aircraft's response:

$$V_t = 20\,m/s$$

$$f1 = \dot{p}/48.3046$$

$$f2 = \beta/(-0.0389)$$

$$f3 = \dot{q}/9.5877$$

$$f4 = \dot{q_n}/(-23.3096)$$

$$w_1 = 0.9$$

$$w_2 = 1.1$$

$$w_3 = 1.1$$

$$w_4 = 0.9$$

$$f\_val = -(2w1 \cdot f1 - 2w2 \cdot f2 + w3 \cdot f3 - w4 \cdot f4)$$

Description of Optimisation Run 68:

The weights were adjusted to evaluate the impact of relative weighting on the aircraft's response:

$$V_t = 30\,m/s$$

$$f1 = \dot{p}/135.6089$$

$$f2 = \beta/(-0.0627)$$

$$f3 = \dot{q}/36.4457$$

$$f4 = \dot{q_n}/(-46.5958)$$

$$w_1 = 0.9$$

$$w_2 = 1.1$$

$$w_3 = 1.1$$

$$w_4 = 0.9$$

$$f\_val = -(2w1 \cdot f1 - 2w2 \cdot f2 + w3 \cdot f3 - w4 \cdot f4)$$

Description of Optimisation Run 69:

The weights were adjusted to evaluate the impact of relative weighting on the aircraft's response:

$$V_t = 40\,m/s$$

$$f1 = \dot{p}/222.626$$

$$f2 = \beta/(-0.0622)$$

$$f3 = \dot{q}/68.6286$$

$$f4 = \dot{q_n}/(-77.6347)$$

$$w_1 = 0.9$$

$$w_2 = 1.1$$

$$w_3 = 1.1$$

$$w_4 = 0.9$$

$$f\_val = -(2w1 \cdot f1 - 2w2 \cdot f2 + w3 \cdot f3 - w4 \cdot f4)$$

Description of Optimisation Run 70:

The weights were adjusted to evaluate the impact of relative weighting on the aircraft's response:

$$V_t = 20\,m/s$$

$$f1 = \dot{p}/48.3046$$

$$f2 = \beta/(-0.0389)$$

$$f3 = \dot{q}/9.5877$$

$$f4 = \dot{q_n}/(-23.3096)$$

$$w_1 = 0.8$$

$$w_2 = 1.0$$

$$w_3 = 1.0$$

$$w_4 = 0.5$$

$$f\_val = -(2w1 \cdot f1 - 2w2 \cdot f2 + w3 \cdot f3 - w4 \cdot f4)$$

Description of Optimisation Run 71:

The weights were adjusted to evaluate the impact of relative weighting on the aircraft's response:

$$V_t = 30\,m/s$$

$$f1 = \dot{p}/135.6089$$

$$f2 = \beta/(-0.0627)$$

$$f3 = \dot{q}/36.4457$$

$$f4 = \dot{q_n}/(-46.5958)$$

$$w_1 = 0.8$$

$$w_2 = 1.0$$

$$w_3 = 1.0$$

$$w_4 = 0.5$$

$$f\_val = -(2w1 \cdot f1 - 2w2 \cdot f2 + w3 \cdot f3 - w4 \cdot f4)$$

Description of Optimisation Run 72:

The weights were adjusted to evaluate the impact of relative weighting on the aircraft's response:

$$V_t = 40\,m/s$$

$$f1 = \dot{p}/222.626$$

$$f2 = \beta/(-0.0622)$$

$$f3 = \dot{q}/68.6286$$

$$f4 = \dot{q_n}/(-77.6347)$$

$$w_1 = 0.8$$

$$w_2 = 1.0$$

$$w_3 = 1.0$$

$$w_4 = 0.5$$

$$f\_val = -(2w1 \cdot f1 - 2w2 \cdot f2 + w3 \cdot f3 - w4 \cdot f4)$$